Efficient radio channel modeling for urban wireless sensors networks

Taha Al-Wajeeh

Université de Poitiers
— Sciences Fondamentales et Appliquées —

THÈSE

pour l'obtention du Grade de
DOCTEUR DE L'UNIVERSITÉ DE POITIERS
(Faculté des Sciences Fondamentales et Appliquées)
(Diplôme National - Arrêté du 25 Avril 2002)

École Doctorale **: Sciences et Ingénierie pour l'Information, Mathématiques (S2IM)**
Secteur de Recherche **: Électronique, microélectronique, nanoélectronique et micro-ondes**

présentée par
ALWAJEEH Taha

Modélisation efficace du canal radio pour les réseaux de capteurs urbains.

Efficient radio channel modeling for urban wireless sensor networks.

Soutenue le 13 Décembre 2018 devant la Commission d'Examen composée de :

M. UGUEN Bernard, Professeur, Université de Rennes 1 ..... Rapporteur
M. KHENCHAF Ali, Professeur, ENSTA Bretagne ..... Rapporteur

M. RAOOF Kosaï, Professeur, Université du Maine ..... Examinateur
M. BERNARD Loïc, Docteur, HDR, Institut de recherche de Saint-Louis ..... Examinateur
M. MARC Olivier, Ingénieur, Virtualys, Brest ..... Examinateur

M. VAUZELLE Rodolphe, Professeur, Université de Poitiers ..... Directeur de Thèse
M. COMBEAU Pierre, Maître de Conférences, Université de Poitiers ..... Co-encadrant de Thèse
M. BOUNCEUR Ahcène, Maître de Conférences, Université de Bretagne Occidentale Co-encadrant de Thèse

God blessed me with a
wonderful daughter
to whom this dissertation is dedicated.

Acknowledgments

First and foremost, I would like to express my deepest gratitude and appreciation to Mr. Rodolphe VAUZELLE, Mr. Pierre Combeau, and Mr. Ahcène Bounceur for their invaluable guidance, immense knowledge, constant support, consistent encouragement, and patient advice throughout this journey. Thank you all for your unwavering support at all times. A special gratitude goes to Pierre Combeau who, besides his academic support, shared my personal concerns throughout my dissertation.

I also wish to sincerely thank Mr. Bernard UGUEN, Professor at the University of Rennes 1, and Mr. Ali KHENCHAF, Professor at ENSTA Bretagne, for their interest in this work by accepting to be reporters on this thesis.

I would like to thank Mr. Kosaï RAOOF, Professor at the University of Maine, Mr. Loïc BERNARD, Doctor, HDR, at the research institute of Saint-Louis, and Mr. Olivier MARC, Engineer at Virtualys, for the honor that has been conferred on me by agreeing to chair the thesis committee.

On a personal level, I would like to express my profound gratitude to my GREAT parents, my lovely wife, my supportive siblings, my little princess, who provided me with moral and emotional support all along the way, and I undoubtedly could not have done this accomplishment without them.

Finally, I conclude by expressing my thanks to my friends and to every single member of XLIM research institute of the University of Poitiers for their hospitality, collaboration, assistance, and the fruitful discussions.

Table of contents

List of figures

List of tables

General introduction

This thesis is a part of a national research project funded by the French National Research Agency (ANR) and supported by the National Center for Scientific Research (CNRS). The work presented in this thesis was carried out at XLIM research institute of the University of Poitiers under the direction of Mr. Rodolphe Vauzelle, Professor at the University of Poitier, Mr. Pierre Combeau, Senior Lecturer at the University of Poitiers, and Mr. Ahcène Bounceur Associate Professor at the University of Brest (UBO).

Nowadays, urban services are presented in a different way because new approaches of managing cities are replacing the conventional ones. In fact, the vision of managing cities was reshaped due to the wirelessly connected elements offered by new technologies. These new technologies improved the quality and efficiency of urban services for a wide range of applications in various domains. Wireless Sensor Networks and Internet of Things are the leading technologies that introduced the concept of "Smart City".

The radio channel is an unavoidable element in any wireless systems. Signals passing via the radio channel are subjected to impairments introduced by the channel. Modeling the radio channel for the wirelessly connected nodes within the wireless network simulators is the key point of the here presented thesis. The objective of this thesis is therefore to develop radio methods for modeling electromagnetic waves for outdoor urban environments. These models should guarantee a high degree of precision in a city-wide scale under tight time constraints. The models should also expect a large number of connected nodes.

The thesis consists of five chapters. The first chapter presents the general context, in which this thesis was carried out. It also discusses : the concept of the "Smart Cities" and their application domains, Wireless Sensor Networks, Internet of Things, and wireless network simulators and protocols. It also outlines the required specifications and the expected outcome of this work.

Chapter 2 provides a detailed summary of the relevant literature of : the radio channel fundamentals, radio wave interactions with the environment, channel modeling approaches, and the advantages and disadvantages of each method. Accordingly, it formulates the research problem, and then it concludes with a proposal for answering the research problem in an efficient way.

Chapter 3 will focus on developing a radio model for the configurations where the predominant propagation mechanism is occurring in the horizontal plane *i.e* the antennas height is lower than the average height of the surrounding environment. The adopted approach will be based on the visibility technique between the transmitter and the obstacles in the propagation environment. It will also be based on new acceleration techniques in order to ensure the rapidity and accuracy of the model. Results will be evaluated in terms of precision and execution time.

Chapter 4 starts by evaluating the validity of the radio model of chapter 3 when the antennas height is higher than the surroundings. Consequently, the objective of chapter 4 is to extend the existing model to be valid for all urban configurations. Therefore, it will integrate an appropriate radio model in the vertical plane. Simulation results will be compared with measurements conducted within a European project.

Chapter 5 will focus on the integration of the radio models into the final platform (*i.e* wireless sensor simulator). It first starts by introducing the platform to which the radio models are going to be integrated. It also details the integration process, and then it lists the encountered problems during this phase, especially due to the geometry databases. It also shows how these issues will be resolved. Chapter 5 concludes with a real case study of a number of sensors in an urban configuration. The study evaluates the impact on of integrating accurate radio channel to the wireless sensor simulator.

Chapter 1

Context and motivation

Contents

1.1 Introduction

This introductory chapter intends to present the context, objectives, and expected outcomes for the here presented thesis. In this regard, it will be important to start by introducing a set of general concepts and definitions that will seen throughout this chapter.

The discussion in chapter 1 attempts to address three main aspects. To that end, this chapter consists of three parts : the first part introduces the concept of the "Smart Cities", wireless sensor networks (WSNs), and wireless sensor network simulators. Then, the second part intends to present the research project "PERSEPTEUR", in which this thesis was carried out. Furthermore, this part presents the project partners and a brief description of their main roles in the project. Finally, part three will focus on the thesis itself, specifically, on objectives and contributions.

1.2 Smart cities

It was estimated in 2014 that 54% of the world population lived in urban areas, roughly 3.3 billion people. This percentage is expected to increase to 66% by 2030, or roughly to 5 billion people[Lea17]. This massive increase leads to new avenues of research for new approaches to manage cities and to offer urban services in a different way. Moreover, the increase of interconnected elements in cities' infrastructure due to new technologies has also reshaped the vision of managing cities[Ers17]. This, in turn, leads to the concept of "Smart City".

There are many angles from which smart cities can be defined. Generally speaking, a smart city refers to a city which uses new technologies and innovative ideas to improve the quality and efficiency of urban services in order to improve the lives of people. New solutions and new approaches are intended to improve public transportation, city traffic, energy resources, water management, environmental protection, surveillance, urban services, etc.

Technically speaking, smart cities involve three elements : information and communication technologies (ICTs) that collect data ; analytical tools that convert the collected data into useful information ; and an application to analyze that real-time information.

Smart city concept involves a wide range of applications in various domains. A simple practical example of these applications is the smart parking project, called "Connected Parking", carried out with Libelium World in Montpellier city to quickly find a parking, reducing considerably searching time for a free parking space [Lib]. A recent research published by the American University with the National League of Cities [DS16] presents graphically a number of applications for smart cities as shown in figure 1.1, which lists some interesting applications such as :

1. Smart transportation systems.
2. Water monitoring.
3. Smart parking.
4. Bridge systems.

5. Autonomous cars.
6. Waste management.
7. Lighting management.
8. Fire detection.
9. Energy management.
10. Solar panels monitoring.
11. Smart freight/tracking systems.
12. Vehicle fleet communication.
13. Drone applications.
14. Surveillance camera.
15. Body cameras.
16. Wearable detection sensors so that people can be a part of system.

Figure 1.1 – *Smart city applications. Image source : Trends in smart city development : Case studies and recommendations [DS16].*

Currently, smart city solutions are mainly based on communication technologies such as Wireless Sensor Networks (WSN) and the Internet of Things (IoT) [GMM+17]. However, in the very near future, smart city solutions will rely on 5G networks. In fact, 5G networks have a new vision. 5G networks intend to target every single element of future life because 5G networks define three service categories : enhanced mobile broadband (eMBB), massive machine-type communication (mMTC), and ultra-reliable and low latency communication (uRLLC) [XZS16]. Anyway, the discussion here will be limited to the current vision of smart cities.

1.3 Wireless sensor networks

Recently, several sensor-based technologies are being widely used in a wide range of domains, particularly in monitoring and surveillance. A wireless sensor network is simply a deployment of a large number of autonomous and self-configured devices equipped with sensors to monitor a number of different phenomena of interest. These devices, which are called sensor nodes, are typically tiny, low-cost, and battery-operated devices. The data collected by these sensors are collaboratively passed through the network to a central point (*i.e.* a base station) that gathers data from all sensor nodes for further processing. Through this definition, it is important to identify the following key elements : a physical sensor to collect the desired data, a protocol to communicate that data, an end-user application where data could be observed and analyzed. As is well known, WSN applications include, but are not limited to, surveillance and monitoring such as humidity, temperature, light, dust, pressure, motion detection, air pollution, fire detection, acoustic sensors, optical sensors, *etc.*

Internet of Things (IoT) is another important concept. IoT is a recent communication model in which everyday life objects are equipped with transceiver units, communication protocols, and microcontrollers. These objects are able to communicate with the network and with one another, becoming a part of the Internet [Tan16]. As a matter of fact, wireless sensor network concept was an important building block for the IoT vision[Jac15]. In addition, urban IoTs enhanced the vision of smart cities [ZBC+14]. According to [CIS15], it is estimated that the number of devices, which will be connected to the network, will reach about 50 billion devices by 2020. Other less pessimistic predictions estimate that the total number will be in the range of 20 - 30 billion connected things [KMF+14]. Regardless of the exact number, a huge growth in the number of the connected devices is expected over the next few years.

Let us take a closer look at the main blocks of a sensor node. A sensor node is composed of four main units [KAMH17] : sensing unit, processing unit, radio transceiver unit, and power unit as shown in figure 1.2. The sensing unit consists of a physical sensor which collects the desired data from the environment. The processing unit, which is composed of a processor and a specific operating system, processes data captured from nodes and transmits them to the network via the radio unit. The radio unit is responsible for all transmissions and receptions of data via defined communication protocols. The power unit supplies the energy to feed the different components.

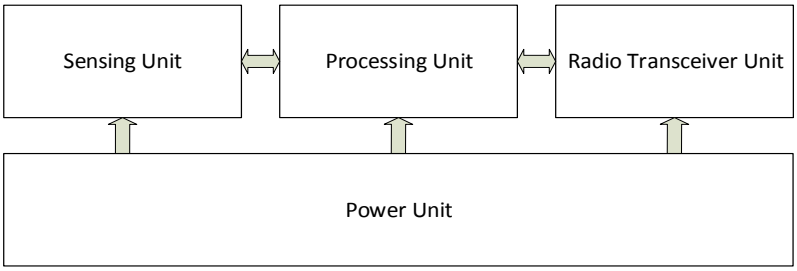

Figure 1.2 – *Block diagram of a sensor node.*

Energy consumption, that is due to data sensing, processing, and communication, is one of the major challenges in wireless sensor networks. Sensor nodes have very limited energy resources, that imposes severe restrictions on processing capabilities, storage capacities, and transmit power. Consequently, the transmit power is very moderate to reduce the transmission energy consumption since most of the energy usage is related to radio communications, which will, therefore, lead to short-range wireless communication links (depending on the communication protocol). This fact is exploitable in our context, as will be shown later on.

1.4 WSN protocols

One protocol cannot, indeed, cover all of the projected applications for WSNs and IoT. A large number of protocols are designed to satisfy a set of requirements based on the applications. As shown in figure 1.3, WSN protocols can roughly be classified into three categories according to the following parameters : data rate, radio range, and power consumption (battery lifetime). The first category is widely adopted to serve the applications that need to transmit moderate data rates over short ranges at low power consumption. The most well-known protocols for this category are the communication protocols that use the IEEE 802.15.4 standard (*cf.* subsection 1.4.1.1). The Second category offers a very long battery lifetime to serve the applications that need to send very limited amounts of data over long distances. This type of wireless networks is called a Low-Power Wide-Area Network (LPWAN). The most notable LPWAN technologies are SigFox (*cf.* subsection 1.4.2.1) and LoRA (*cf.* subsection 1.4.2.2) radio standards. The third category uses the existing cellular technologies to serve the applications that need high data rates, but it is not widely used due to the high power consumption.It is important to underline that these categories should be considered separately when modeling radio propagation models, as will be shown in the next chapters.

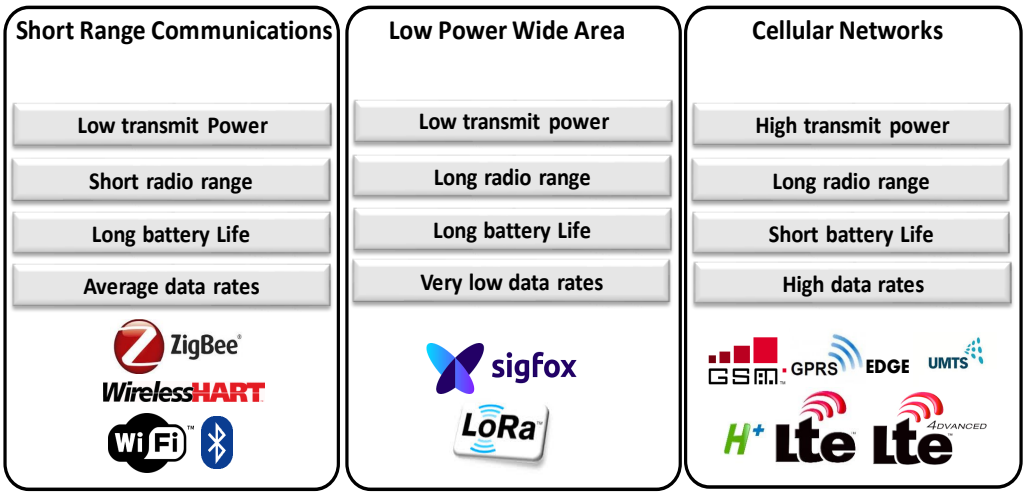

Figure 1.3 – *Classification of WSN protocols.*

1.4.1 Short range communication protocols

1.4.1.1 IEEE Std 802.15.4

IEEE 802.15.4 is a simple, low rate, low cost, short-range, flexible, and low power consumption standard for the lower layers of the OSI model. It defines the specifications of the physical layer (PHY) and also the medium access control (MAC) layer for a communication protocol which is designed to satisfy a set of simple needs for wireless communications with limited power and moderate throughput requirements. The standard was first defined in 2003 by the IEEE 802.15.4 working group, yet new variants of the original IEEE 802.15.4-2003 such as IEEE 802.15.4-2006, IEEE 802.15.4-2011, and IEEE 802.15.4-2015 were released afterward to add new features and clarifications to the existing versions.

The technical specifications are fully detailed in the document defining the IEEE 802.15.4 - 2003 standard [IEE03], but it is important to mention some of the characteristics of the IEEE 802.15.4 - 2003 that will be needed later on. The main characteristics of the standard can be summarized as follows :

- Layers : Physical and MAC layers.
- Data rates : 20 kb/s, 40 kb/s, and 250 kb/s.
- Frequency bands :
  - 868 MHz (1 channel)
  - 915 MHz (10 channels)
  - 2450 MHz (16 channels).
- Nominal transmit power of 0 dBm.
- Receiver sensitivity :
  - -92 dBm @ 868/915 MHz .
  - -85 dBm @ 2450 MHz.
- Modulation schemes : BPSK and O-QPSK.
- Low power consumption and short-range communications.
- Peer-to-peer or star topology.
- Two different device types :
  - Full-function device (FFD) : a node that can perform all the functions defined by the standard (*i.e.* send, receiver, and route data).
  - Reduced-function device (RFD) : a node that can perform only a certain number of functions so they are considered as low power consumption devices since these nodes do not participate in traffic routing (*i.e.* end nodes).

1.4.1.2 IEEE 802.15.4 derived standards

IEEE 802.15.4 is the basis for a number of various higher layer standards such as ZigBee, WirelessHart, ISA100.11a, OCARI, 6LoWPAN, and MiWi. Although these standards share the same physical and MAC layers that have been defined in IEEE 802.15.4, they extend the protocol by developing the upper layers in the OSI model.

ZigBee : is one the most popular WSN protocols that is an IEEE 802.15.4-based protocol. The full ZigBee protocol stack defines the upper layers of the system all the way to the application layer.

WirelessHart : is an open industrial communication technology based on the HART Communication protocol (Highway Addressable Remote Transducer). As its name indicates, it is as the wireless extension to the HART protocol. The protocol stack of WirelessHart implements IEEE 802.15.4 physical layer at 2.4 GHz.

ISA100.11a : is a wireless communication technology developed by the International Society of Automation (ISA) to provide a secure and reliable wireless system for industrial applications. Like WirelessHart, ISA100.11a is also based on IEEE 802.15.4 standard, implementing the 2.4 GHz physical layer. However, ISA100.11a standard modifies the IEEE 802.15.4 MAC layer, rather than adopting it in its entirety.

6LoWPAN : stands for IPv6 over Low-Power Wireless Personal Area Networks. 6LoWPAN has defined the mechanisms for the upper layers that allow IPv6 packets to be transferred over IEEE 802.15.4-based protocol.

MiWi : is an IEEE 802.15.4-based protocol designed by Microchip Technology, a well-known micro-controller manufacturer. The main feature of MiWi protocol is that it offers a smaller footprint, which makes microcontrollers perform opertaions with smaller memory.

OCARI : is a wireless communication protocol that was developed during the OCARI project that is funded by the French National Research Agency (ANR). The main goal of the project was to optimize the wireless communications for industrial networks. The project adopted the physical layer proposed a new MAC layer.

IEEE 802.15.4 derived standards					
Standard	ZigBee	WirelessHart	ISA100.11a	OCARI	6LoWPAN
IEEE	802.15.4 2003	802.15.4 2006	802.15.4 2006	802.15.4 2006	802.15.4 2003
Frequency bands	868 MHz 915 MHz 2450 MHz	2450 MHz	2450 MHz	2450 MHz	868 MHz 915 MHz 2450 MHz
Data rates	20 kbps 40 kbps 250 kbps	250 kbps	250 kbps	250 kbps	20 kbps 40 kbps 250 kbps
Modulation	BPSK O-QPSK	O-QPSK	O-QPSK	O-QPSK	BPSK O-QPSK
Receiver sensitivity	-92 dBm @915MHz -85 dBm @2450MHz	-85 dBm	-85 dBm	-85 dBm	-92 dBm @915MHz -85 dBm @2450MHz
Nominal transmit power	0 dBm	0 dBm	0 dBm	0 dBm	0 dBm
Radio range (roughly)	150 m	150 m	150 m	150 m	150 m

Table 1.1 – IEEE 802.15.4 derived standards

1.4.2 Low-Power Wide-Area Network (LPWAN) protocols

As was mentioned earlier, the number of connected nodes is expected to reach tens of billions of nodes over the few next years. However, some of these nodes need only very limited bandwidth to transmit small amounts of data over large distances. For many of these applications, the existing cellular systems are not well adapted to the specific needs of these applications because of the high power consumption, and the costly equipment. To this end, alternative communication systems are proposed to provide communications with the required objectives : long radio range, low data rates, and very low power consumption (*i.e.* a Low-Power Wide-Area Network (LPWAN)). SigFox and LoRA are the most well-known LPWAN technologies.

1.4.2.1 Sigfox

Sigfox is a proprietary protocol developed by the French company Sigfox [Sig]. It is a wide-range communication system that has been designed to offer a very low bitrate with significantly low power for remotely connected nodes using Ultra-Narrow Band (UNB) technology. In fact, transmitting through UNB channels makes it possible to send data over large distances with low transmit power levels. The main features of the protocol are summarized as follows :

- UNB technology (BW = 100 Hz).
- Modulation scheme :
  - Uplink : D-BPSK.
  - Downlink :GFSK.
- Bitrate :
  - Uplink : 100 bps or 600 bps (depends on the operation region).
  - Downlink : 600 bps.
- Frequency bands (depends on the operation region and the local regulations) :
  - 868 - 868.2 MHz.
  - 902 - 928 MHz.
- Low radiated Power :
  - 25mW = 14dBm @ 100bps.
  - 150mW = 22dBm @ 600bps.
- Receiver sensitivity :
  - -142 dBm @ 100bps.
  - -134 dBm @ 600bps.
- Link budget : $\approx$ 160 dB.
- Uplink messages :
  - Payload size for each message is from 0 to 12 bytes + 14 bytes of header.
  - Maximum 140 uplink messages per object per day to extend battery life.
- Downlink messages :
  - Payload size for each message is static : 8 bytes.
  - Maximum 4 downlink messages per object per day.
- Low power consumption :
  - 50 Microwatt with standby time of 20 years [PC15].
- Network System Architecture :

– Sigfox objects.
– Sigfox base stations.
– Sigfox cloud.
– Customer service (End-user).

1.4.2.2 LoRa

LoRa, an abbreviation for "Long Range", is a proprietary comunication protocol for a LPWAN that is designed to achieve long-range and low power communication links. It is important to point out that LoRa is the physical layer for the protocol, while LoRaWAN defines the whole communication protocol and network architecture. LoRaWAN specifications vary depending on the operation region and on the local regulations. A brief summary of the LoRaWAN specifications [Lor15] can be given as follows :

LoRaWAN specifications		
	Europe	North America
Frequency bands	863 - 870 MHz	902 - 928 MHz
Channel BW downlink	125 kHz	500kHz
Channel BW uplink	125/250kHz	125/500kHz
Modulation scheme	FSK	FSK**
Transmit power downlink	14 dBm	27 dBm
Transmit power uplink	14 dBm	20 dBm
Data rate	250 bps - 50 kbps	980 bps - 21.9 kbps
Link budget downlink	155 dB	157 dB
Link budget uplink	155 dB	154 dB
Maximum number of messages per day	Unlimited	
Battery lifetime (2000 mAh)	105 months	
Network architecture	- LoRa Sensors - Base Station (LoRaWAN Gateway) - Network Server - End-user application	

Table 1.2 – LoRaWAN specifications

1.5 Simulation tools for wireless sensor networks

It is crucial for researchers and engineers to study, develop, test, and evaluate new deployments, protocols, algorithms, and applications. These performance tests can be conducted through test-beds or simulation. Although test-beds are more realistic and more reliable as they conduct real experiments, they are fairly complex, time-consuming, costly, or even practically unfeasible for deploying a large number of nodes [AFAHN13]. Simulation is an appropriate alternative to examine, evaluate, and study network parameters before deployment especially for large-scale WSNs. In fact, simulations provide a cost-effective, fast-deployable, and fairly reliable solution. A comparison between simulation tools and testbeds is given

in [TWCM10] in order to provide a reference for choosing between them according to the research requirements. In fact, simulation is the research tool used by the majority of the research community as revealed by an investigation conducted through the papers published in SENSORCOMM conference [AAFA+12].

A WSN simulator allows constructing virtual and interactive networks in order to observe and evaluate the operation of the network. A wide range of available WSN simulators is presented in the literature. Exhaustive surveys of WSN simulation tools are given in [NS15, Yur16, AAFA+12]. However, this subsection intends to give a short description of some widely used network simulators with a particular focus on the integrated radio propagation models, which have a major impact on the reliability and quality of the simulation results. The main idea, therefore, is to present the most widely used network simulators in order to identify the radio propagation models used in these simulators. It is important to note that those models will not be presented here, but rather they will be discussed in detail in chapter 2.

There follows a brief summary of some well-known WSN simulators :

Network simulator 2 (NS-2)

NS-2 is one of the most popular WSN simulators [JZD09]. It is a discrete event open source network simulation tool which is written in object-oriented programming languages (*i.e.* C++ with OTcl). It is important to underline that NS-2 offers three simple non-realistic radio models [ns2a] [ns2b].

MannaSim

MannaSim is regarded as an extension for NS-2. This later extension takes the main features of NS-2 and adds ones to develop and analyze different WSN applications [Man]. MannaSim inherits the radio models from NS-2 [PRG15].

Network simulator 3 (NS-3)

NS-3 a is well-known, discrete-event, and open-source network simulator targeted mainly for educational and research purposes. NS-3 integrates a number of simple radio models for urban, suburban, and open environments [np16]. In fact, despite the fact that NS-3 offers a number of models that are widely used in the literature, these models are still not accurate enough or even not applicable in some circumstances.

TOSSIM

TOSSIM is a discrete-event simulator dedicated to networks running on the operating system TinyOS, which is an operating system designed specifically for WSNs [TOSb]. TOSSIM offers simple radio propagation models with the possibility to add additive white Gaussian noise (AWGN) [TOSa].

Cooja

Cooja is a simulation tool specifically designed for WSNs. Cooja offers a simple unit-disc

radio propagation model which abstracts the radio range simply as circles. It also includes a more sophisticated model *i.e.* a 2D site-specific radio propagation model [WGG10]. Although site-specific modeling provides accurate results, the computational complexity of this family of models is often not tolerable because simulation results should be obtained under time constraints.

Worldsens

Worldsens simulation environment is an integrated platform dedicated to designing applications for sensor networks. The Worldsens environment consists of two simulation tools (WSim and WSNet) that are used independently or together during the application design [FCF07] :

— WSNet is an event-driven large-scale wireless sensor network simulator. WSNet offers a number of basic radio propagation models : disk model (range), simple radio propagation models, or even probability distribution (statistical characterizations of the radio channel) [WSN].
— WSim is a hardware platform simulator that uses microcontroller binary codes.

QualNet

QualNet a commercial simulation platform developed by Scalable Network Technologies, Inc. Although it is not dedicated to WSN simulations, it supports WSN simulations using 802.15.4 library. The manual of the model library index of QualNet 8.0 [Inc17] shows that the urban propagation library includes a number of simple propagation models.

OMNeT++

OMNeT++ is an extensible component-based platform for building network simulators [omn]. Independent plugins are developed to provide specific functionality for the platform such support for WSNs :

— Castalia is a plugin for OMNeT++ platform developed by the National ICT Australia. It was designed for simulating WSNs and body area networks (BANs). Castalia users manual [Cas13] gives an overview of the radio models supported by this simulator. It shows that Castalia integrates simple radio propagation models. In addition, it also offers temporal models to describe the temporal variation of the channel.
— MiXiM is a plugin for OMNeT++ platform designed for WSNs, BAN, vehicular networks, etc. MiXiM includes the simple radio propagation models that are widely used by the presented network simulators [KSW+08, MiX].

OPNET

OPNET Modeler Wireless Suite supports a wide range of wireless networks such as cellular networks, ad-hoc networks, wireless LAN (IEEE 802.11), WSNs, and satellite communications [Beu12]. Like other presented simulators, OPNET provides also several simple propagation models [HBVP17]. It is necessary to underline that OPNET is now part of Riverbed company,

the new name of OPNET Modeler Suite is Riverbed Modeler.

CNET

CNET is an open source network simulator developed for research purposes at the University of Western Australia. It implements the IEEE 802.11 standard, which makes it able to simulate wireless networks. It integrates a simple radio propagation model, but it allows the users to define their own radio propagation models [CNE].

Since our main aim was, as mentioned earlier, not to make an exhaustive list of all the WSN simulators, but rather to give an overview of the radio models implemented in that network simulators. In fact, the review leads to the conclusion that well-known network simulators are implementing either simple radio propagation models which are environment independent and often not accurate enough ; or sophisticated site-specific radio propagation models which can give more accurate simulation results, but on the other hand, these simulators do not address time constraints. Hence, a new effective way for radio channel modeling for network simulators is required, taking into account the addressed problem.

1.6 PERSEPTEUR project

As mentioned in the introduction, this thesis is a part of a national project called **"PERSEPTEUR"**. The project's name is an abbreviation for the complete French name of the project "PlateformE viRtuelle 3D pour la Simulation des rEseaux de caPTEURs" which can be translated as a 3D Virtual Platform for Wireless Sensor Network Simulation. PERSEPTEUR is a research project funded by the French National Research Agency (ANR) and supported by the National Center for Scientific Research (CNRS).

1.6.1 Project objectives

The primary objective of this project is to construct realistic simulation platforms for WSNs and IoT for outdoor smart city applications using free 3D city models. The simulation tools of this project must satisfy the following global requirements :

— Provide fairly accurate simulation results within reasonable computational time.
— Take into account the geometrical details of the simulation environment.
— Able to represent mobile nodes and dynamic environments.
— Able to support large-scale wireless sensor networks.

The final simulation platform should include the following features :

- Simulation and visualization of WSNs services in a 2D/3D environment.
- Improving the quality of sensor deployment in terms of communication links feasibility and reliability by :
  – Providing accurate radio propagation predictions.
  – Detecting potential interference areas among the network in order to improve the link quality by placing sensor nodes in an optimal way.

  – Considering real environments.
- Visualization of the simulation results in public GIS platforms such as OpenStreetMap.
- Considering node mobility (*i.e.* public transport).
- Providing support for academic staff to illustrate the concept of WSNs using 3D virtual environments.

1.6.2 Project parteners

PERSEPTEUR project involves academic and corporate partners. More precisely, it is a collaboration between three research laboratories and a R&D engineering company specializing in 3D virtual representations. Each partner will provide an essential building block for constructing the final platform. To this end, the project is structured around four major axes that correspond to four different tasks. It should be pointed out that the aforementioned global project requirements will be reflected in each task. For the sake of brevity, the project partners will be listed with a brief description of the main role of each partner :

XLIM research institute is responsible for modeling the radio channel between the nodes. Channel modeling must surely take into account the global project specifications presented in 1.6.1, which are regarded technically as a set of constraints.
IEMN research institute is responsible for developing interference models in order to evaluate the impact of a set of nodes on a given link.
Lab-STICC is responsible for providing the main kernel of the project, which is a simulation tool for sensor networks (called CupCarbon). CupCarbon is a multi-agent and discrete-event WSN and IoT simulator for both educational and research purposes [MLBK14].
Virtualys is responsible for providing a 3D model of the city of Brest in the form of a virtual 3D environment.

The architecture of simulation platform consists of many modules as shown in figure 1.4 :

— **City model module :** it represents the city in digital form (2D or 3D). It includes information about the simulation scene (buildings, objects, roads, bridges, *etc.*).
— **Mobility module :** it defines the routes and trajectories of the mobile nodes.
— **Network module :** it defines the scenario and the parameters of the WSN to be simulated.
— **Communication Script module :** this module interprets the SenScript language (*i.e.* the script used to program the sensor nodes in CupCarbon simulator) in order to allow the simulator to understand and execute the instructions of the script.
— **Radio Propagation module :** it models the radio channel between the communicating nodes in the network. The radio channel between each pair of nodes could be represented in matrix form (*i.e.* propagation and connection matrix), which estimates the quality of radio links between the communicating nodes.
— **Interference module :** this module is models the effect of the network nodes on a given link used to determine if the sent message could be received by the receiver.
— **Simulation module :** this module is based on a discrete event simulation.

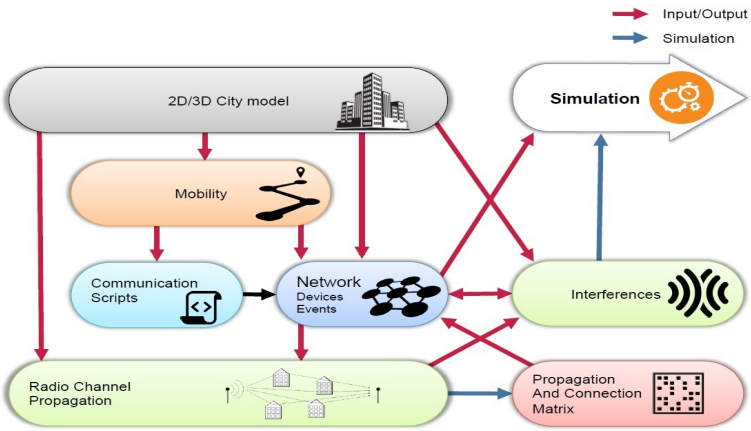

Figure 1.4 – *Simulator structure.*

1.7 Thesis motivation and objectives

Up to now, the first two parts have tended to present the context of the thesis. Henceforth, the discussion will focus on the research question of the here presented thesis.

As mention earlier, simulations provide a cheaper and more practical way to test and explore different deployment scenarios. For researchers and engineers, simulation is an essential tool to verify the behavior and performance of the designed network before moving towards live implementation. On the other hand, simulation results could give deceptive results. In fact, simulation results obtained by WSN simulators are affected by several factors, one of which is by modeling the radio channel. Although the simulation results are considerably affected by the radio channel characterization, well-know WSN simulation tools (*cf.* section 1.5) use simple and non-realistic radio propagation models, which can lead to erroneous results. Consequently, it is inevitable to integrate more accurate radio models into simulation tools in order to get more realistic results.

The quality of radio simulation results strongly depends on the degree of realism of modeling the propagation environment and also on the numerical methods that are used to characterize the propagation mechanisms. On the one hand, increasing the number of modeled elements will considerably increase the computational complexity and will occupy the available physical resources. This could be prohibitive due to the lack of available resources (physical constraints or time constraints).

It is difficult or even infeasible, under strict time constraints, to give realistic performance, to deal with realistic propagation environment, to execute numerical methods, and to treat a large number of nodes some of which are mobile. To that end, it is necessary to simplify the simulation scenario by excluding certain level of details (propagation scene, propagation mechanisms) in order to reduce the computational complexity. This can be done by reducing the complexity of the propagation scene, using less greedy numerical methods, adopting acceleration techniques, or sacrificing less significant propagation mechanisms but within a

manageable margin of error. Nevertheless, this brings up the question of how to define a trade-off between accuracy, complexity, and execution time for the radio propagation models.

Let us formulate the research problem, the thesis intends to propose radio propagation models that can accurately and quickly predict radio propagation behavior for wireless sensor networks and smart city applications. To this end, a set of trade-offs between accuracy and computational time will be defined to meet the following requirements :

– Models that are able to provide accurate results under severe time constraints.
– Models that consider the propagation environment –> that requires site-specific models.
– Models that are able to deal with large-scale networks (*i.e.* up to thousands of nodes) –> that requires very fast models.
– Models that are able to support mobile nodes –> that requires quasi-instantaneous models.

In the literature, a very large number of radio models has been proposed to predict radio waves behavior. Radio propagation models are broadly classified into two families [GMM+17] :

Empirical models

Empirical propagation models are a set of equations extracted for a particular environment and in particular conditions (*i.e.* antenna heights, frequency range, indoor/outdoor, urban/suburban/rural, etc.). These models are derived from extensive and time-consuming field measurements. Despite the fact that the empirical propagation models can be regarded as environment-dependent but non-site-specific, they do not require detailed information about the propagation environment but rather some indicative information. Empirical models are attractive because they are extremely fast and easily implementable. On the other hand, they fail to provide accurate results.

Deterministic models

Unlike empirical propagation models, deterministic propagation models do not require field measurements. On the other hand, deterministic modeling requires detailed information about the propagation environment [KM16]. This class of models depends on exact or approximate numerical solution of Maxwell's equations. Therefore, they require high computational time.

According to project requirements, site-specific (*i.e.* deterministic) radio propagation models are required. It is important to underline that the computational complexity for site-specific models is a critical issue especially for large-scale simulations because this class of models needs a huge amount of data related to the information of the propagation environment. In addition, It solves complex numerical methods. Hence, classical deterministic propagation models cannot be directly adopted in the research problem. On the other hand, the empirical class is extremely fast and can easily be implemented but it does not provide accurate estimations in such environments, which leads to exclude also this class of models. In fact, it is difficult to guarantee an ultimate degree of precision under such severe time constraints. Hence, the core issue of the here presented thesis is to place the cursor at the

most suitable trade-offs that give the best balance between accuracy and computational time as shown in figure 1.5.

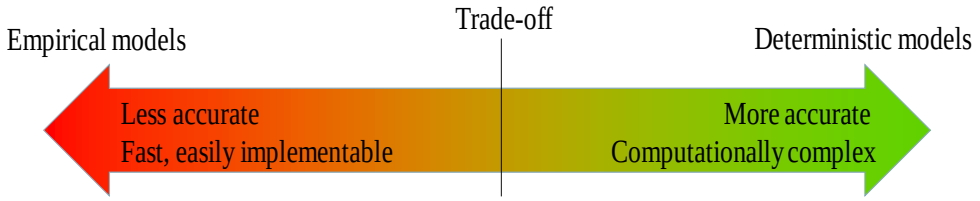

Figure 1.5 – *Accuracy computational time trade-off.*

1.8 Thesis Contributions

This dissertation proposes efficient, fast and accurate numerical methods for computing/modeling electromagnetic waves in realistic environments. The proposed models are adapted to meet the expected project specifications to the maximum extent possible by taking advantage of the specificity of the radio channels in this context. The final models are deterministic models that adopt a set of effective acceleration techniques in order to reduce the computational complexity with a minimal loss of accuracy. These models will be integrated into a WSN simulation platform in order to provide a more realistic and more reliable platform.

1.9 Conclusion

In this chapter, the smart city concept was introduced. Smart cities offer several important applications and diverse interesting uses that facilitate people's everyday life. Wireless sensor networks are an important element in smart cities. Many communication protocols for WSNs were proposed to cover a wide range of requirements. The simulation of sensor networks is an indispensable tool for testing and validating before real deployment. The simulation tools are also important to the researchers in order to test and validate their protocols and algorithms. In fact, real experiments are costly, time-consuming and difficult, especially when talking about a large number of nodes distributed over large areas. For this reason, network simulators should be reliable, accurate, and fast.

PERSEPTEUR project was presented in this chapter. Its objective is to construct a realistic and accurate simulator. An important element of the project's requirements is the radio propagation models since they affect considerably the simulation results. In fact, it was shown that existing well-known WSN simulators offer simple radio propagation models. Moreover, existing radio propagation models cannot be directly adapted to the simulator required by the project because they do not satisfy the project requirements in terms of accuracy and time constraints. A set of trade-offs will be proposed to address this problem.

Chapter 2

Background and state of the art

Contents

2.1 Introduction

Chapter 1 outlined the context, motivation and expected outcomes of the thesis. Chapter 2 aims to provide a synopsis of the relevant literature in order to suggest the most efficient proposition for the research problem. To that end, chapter 2 will cover several aspects such as radio channel fundamentals, a review of empirical channel modeling for WSNs, deterministic modeling principles. The chapter concludes by formulating the research problem and then by explaining the adopted proposal.

2.2 Radio Channel fundamentals

Radio propagation channel is the medium where the electromagnetic waves propagate between the transmitter and the receiver. It is an inevitable element for any radio communication system. Through the radio channel, information is transmitted over a given bandwidth by establishing point-to-point or point-to-zone radio links. However, real radio channels introduce a variety of impairments and disturbances to the signal. Understanding the radio channel is thus a key element in the implementation and design of wireless communication systems. It is necessary here to clarify what is the difference between the radio channel and the transmission channel. A transmission channel refers to the radio channel but it includes also the antenna radiation patterns of the transmitter and receiver.

For any radio communication system, radio channel characterization is a crucial issue for system design, because the quality of radio links is the main limiting factor of the end-to-end communication quality. One possible way to obtain exact information about the radio channel is to perform field measurements. However, field measurements for complex test scenarios could be prohibitively expensive and very time-consuming because all transmitters, receivers, and all other equipment must be deployed over a large area, including possibly a relatively large number of test locations. It is, therefore, essential to develop effective and accurate radio propagation models as a viable alternative to field measurements.

2.2.1 Multipath propagation

Radio propagation is the behavior of radio waves as they move from one point to another in the propagation environment. When the radio waves travel from the transmitter to the receiver, they encounter many obstacles in their propagation way, especially in urban environments. Knowing the phenomena that influence radio waves is indispensable for characterizing the behavior of the radio channel. The principal phenomena can generally be described by four basic mechanisms or interactions : reflection, diffraction, refraction (also called transmission), and scattering. At the receiver side, the signal will be received via a set of different paths undergone multiple interactions, as depicted in figure 2.1. These interactions can affect the direction, amplitude, phase, and polarization of the initial radio wave. Consequently, the received signal is composed of a number of attenuated, phase shifted, and time-delayed replicas of the transmitted signal. This propagation mechanism is known as multipath propagation, which can guarantee a good-quality radio communication over non line of sight (NLOS) configurations.

Reflection occurs when radio waves encounter relatively large objects (*i.e.* greater than the wavelength such as buildings, walls, grounds, *etc.*). When a radio wave travels through one medium and hits another medium having electrical properties different from that of the first medium, part of the energy is reflected into the initial medium and another part is transmitted into the second medium. In outdoor environments, It is generally assumed that the transmitted field is totally absorbed by the building. It is therefore considered as non-significant propagation phenomenon in outdoor scenarios.

Diffraction occurs when radio waves encounter edges, corners, or sharp obstacles. Diffraction allows signal propagation behind obstacles in the shadowed regions. Signal field strength becomes more attenuated, as the receiver goes deeper behind the shadowed (obstructed) region. Diffraction can be understood by the *Huygens' principle* [SS99] that says that each point on a wavefront is regarded as a point source to produce secondary spherical wavelets and the sum of those wavelets forms another spherical wavefront at the same direction.

Scattering occurs when radio waves encounter rough surfaces, small objects, or atmosphere particles [HHC06], so that the reflected wave is diffused in all directions. Trees, signpost, lamppost, and other similar small objects tend to scatter the incident waves in all directions.

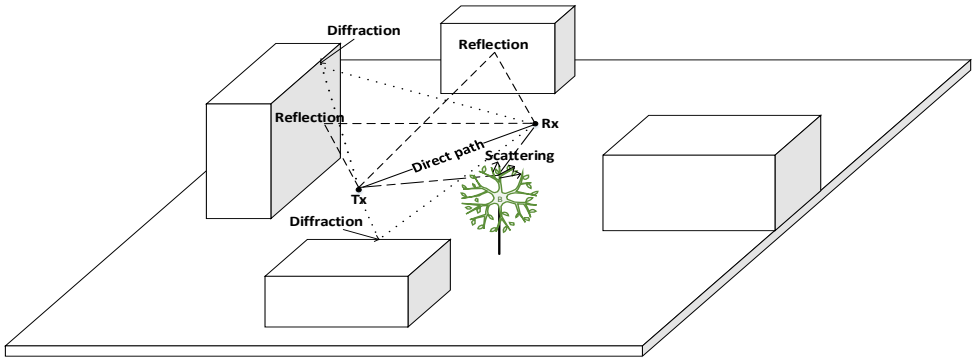

Figure 2.1 – *Urban propagation scenario.*

Mathematical model for multipath radio channel :

It is fundamental to characterize the wideband multipath channels by mathematical models, for many purposes. The key purpose is to understand how the channel behaves and how it does affect the transmitted signals. An additional crucial purpose is to use these models for computer simulations. Finally, it is possible through these models to quantify the radio channel by some parameters such as the rms delay spread, coherence time, coherence bandwidth, and Doppler spread (*cf.* section 2.3). These parameters are useful in comparing different multipath radio channels and in developing broad guidelines for wireless networks designers.

As indicated previously, the received signal in multipath environments is composed of a set of attenuated, phase shifted, and time-delayed replicas of the transmitted signal. Hence, it is convenient to view the radio propagation channel as a filter, which can be characterized

by its impulse response [Ham13]. The complex impulse response $h(\tau)$ of a radio channel can be modeled (assuming that the channel is time-independent over the interval of interest) by a time-invariant linear filter and is expressed as :

$$h(\tau) = \sum_{n=1}^{N_T} a_n e^{-j\theta_n} \delta(\tau - \tau_n) \tag{2.1}$$

where N_T is the total number of paths between a given transmitter/receiver pair, a_n is the amplitude of the n^{th} path, τ_n is the delay of the n^{th} path (depends on its length), and finally θ_n is the phase of the n^{th} path (depends on its length, on the frequency, and on the electromagnetic interactions that occurred during the propagation).

Spatial variability : is due to the mobility of the receiver and/or transmitter in the propagation environment. In typical multipath environments, the received signal fluctuates rapidly over small distances, because as the receiver and/or the transmitter moves, the received paths are not the same anymore. Hence, the received signal depends on the properties of the new/modified paths at the receiving side.

Time variability : is due in part to the mobility in the propagation environment, modifying the characteristics of the paths. New paths may appear, other existing paths may disappear, even the persevered paths are subject to change. The transmitter and receiver are assumed to be fixed.

Thus, the channel time-variant impulse response $h(t, \tau)$ is modeled by a time-variant linear filter and is expressed as :

$$h(t, \tau) = \sum_{n=1}^{N_T(t)} a_n(t) e^{-j\theta_n(t)} \delta(\tau - \tau_n(t)) \tag{2.2}$$

where $N_T(t)$, $a_n(t)$, $\tau_n(t)$, and $\theta_n(t)$ are defined as before but they are time-dependent parameters.

Although the radio channel can be characterized by the complex impulse response $h(t, \tau)$, it can also be modeled by other system functions, which are called Bello's functions. These functions are related through Fourier transforms as shown in figure 2.2 :

— **Delay spread function** $h(t, \tau)$ **:** is the time-variant impulse response, which is called by Bello the input delay spread function.
— **Time-variant transfer function** $H(t, f)$ **:** is simply the Fourier transform of the delay spread function $h(t, \tau)$ with respect to the time delay τ. It is interpreted as the time evolution of the transfer function, given by

$$H(t, f) = \int_{-\infty}^{\infty} h(t, \tau) \cdot e^{(-j2\pi f\tau)} d\tau \tag{2.3}$$

— **Delay Doppler spread function** $S(\tau, v)$ **:** represents the spreading of the input signal in the delay and Doppler domains, given by

$$S(\tau, v) = \int_{-\infty}^{\infty} h(t, \tau) \cdot e^{(-j2\pi vt)} dt \tag{2.4}$$

— **Doppler spread function** $D(f, v)$ **:** is the Fourier transform of the delay Doppler spread function with respect to τ, that is

$$D(f, v) = \int_{-\infty}^{\infty} S(\tau, v) \cdot e^{(-j2\pi f\tau)} d\tau \tag{2.5}$$

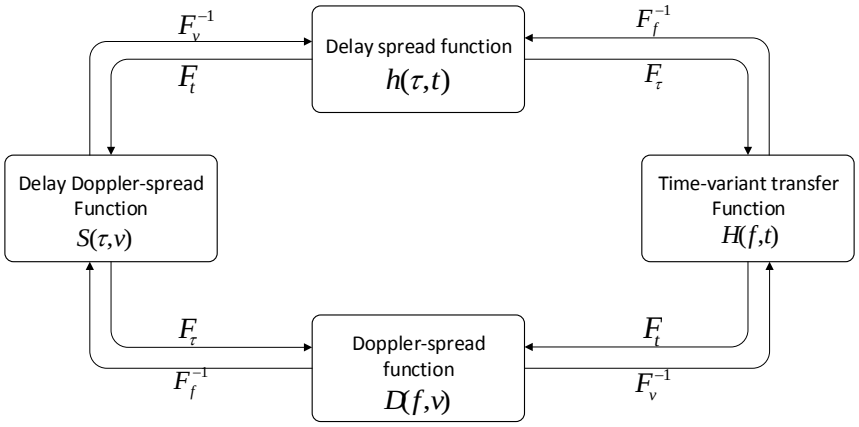

Figure 2.2 – *Bello functions.*

where τ is the time delay, t denotes the time, v designates the Doppler shift, and f is the carrier frequency. A detailed description of Bello functions is given in [Bel63].

2.2.2 Different Scales of Attenuation

In[Lee10], Lee has shown that the received signal strength can be expressed as the product of two terms :

$$r(t) = m(t) \cdot r_0(t) \tag{2.6}$$

where $r(t)$ is the received signal strength, $m(t)$ characterizes the large-scale fading, and $r_0(t)$ characterizes the small-scale fading.

Large-scale fading : describes the average attenuation of signal power over relatively large distances (*i.e.* it gives the envelope of the received signal over large distances). Large-scale fading can be further classified according to its cause into path loss and shadowing. Path loss is the mean attenuation that depends mainly on the frequency and on the distance between the transmission point and the reception point, while shadowing occurs when the signal is obstructed by an obstacle in the propagation environment, which can attenuate the signal power.

Small-scale fading describes the fast fluctuations of the signal power around its local mean value due to the constructive or destructive sum of multipath components. These fluctuations occur over short time intervals and/or over short distances because of the mobility of the communicating terminals, and/or because of the movement of the objects in the propagation environment. Small-scale fading is typically modeled by statistical distributions such as

Rayleigh and Rician distributions. Other statistical models for multipath channels models are presented in [S.R10].

Accordingly, the total signal attenuation $A_{t[dB]}$ can be decomposed into three parts :

$$A_{t[dB]} = A_{pl[dB]} + A_{sh[dB]} + A_{ff[dB]} \tag{2.7}$$

where $A_{pl[dB]}$ is the path loss attenuation, $A_{sh[dB]}$ is the attenuation due to the shadowing, and $A_{ff[dB]}$ represents fast fading fluctuations as depicted in figure 2.3.

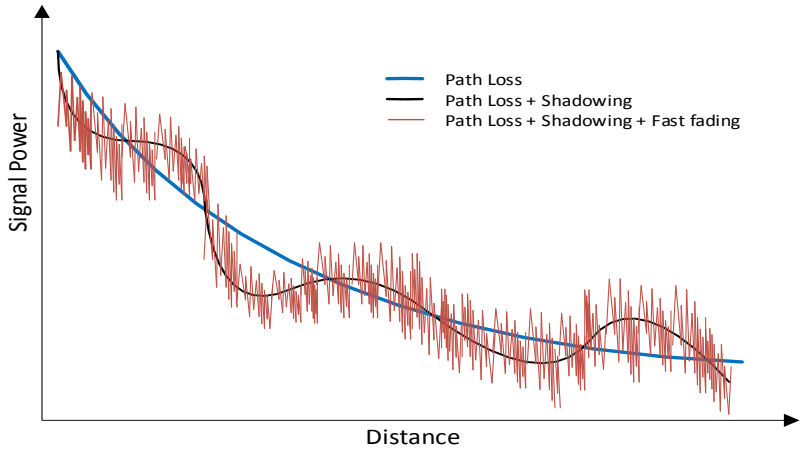

Figure 2.3 – *Path loss, shadowing and fast fading.*

2.3 Parameters of Multipath Radio Channels

As discussed earlier, in the propagation environments, there are a large number of obstacles and dynamic objects between the transmitter and the receiver. These obstacles cause the multipath phenomenon. In fact, it is important to quantify the multipath radio channel by certain parameters in order to give an indication of the channel effect on the radio signal. These parameters are defined in the time domain such as the delay spread and coherence time, and in the frequency domain such as the coherence bandwidth and Doppler spread.

2.3.1 Time dispersion parameters

In multipath channels, the power delay profile $P(\tau)$ represents the power intensity of the received signal in function of time delay (τ) (*i.e.* $P(\tau) = |h(\tau)|^2$). Important multipath channel parameters, which quantify the multipath channel, are determined from the power delay profile such as : the mean excess delay ($\bar{\tau}$) and *rms* delay spread (τ_{rms}). The *rms* delay spread gives an indication about the multipath richness of the radio channel. These delay parameters are calculated relative to a time reference which is the time at which the first perceptible signal arrives at the receiver (denoted by τ_0).

The mean excess delay is defined as :

$$\bar{\tau} = \frac{\int_{-\infty}^{\infty} \tau P(\tau)\,\mathrm{d}\tau}{\int_{-\infty}^{\infty} P(\tau)\,\mathrm{d}\tau} \tag{2.8}$$

The mean excess delay $\bar{\tau}$ is used to calculate the rms delay spread τ_{rms} as follows :

$$\tau_{rms} = \sqrt{\frac{\int_{-\infty}^{\infty} (\tau - \bar{\tau})^2 P(\tau)\,\mathrm{d}\tau}{\int_{-\infty}^{\infty} P(\tau)\,\mathrm{d}\tau}} \tag{2.9}$$

An additional time delay parameter is the maximum excess delay (τ_{max}), which is defined as the time difference between the time of the first arriving signal (τ_0) and the time at which the power delay profile falls to a certain threshold level $X(dB)$ below the maximum value (denoted by τ_X). That is,

$$\tau_{max} = \tau_X - \tau_0 \tag{2.10}$$

2.3.2 Coherence bandwidth

A radio channel can be considered "flat" over a range of frequencies if the channel treats all frequency components with nearly equal amplitude and linear phase. Coherence bandwidth (B_c) is basically a measure of the frequency range over which the radio channel can be considered as flat. In other words, if two different frequency components are separated by frequency separation ($> B_c$), the radio channel will affect them differently. Coherence bandwidth is inversely related to the rms delay spread ($B_c \propto 1/\tau_{rms}$). Mathematically, coherence bandwidth is expressed through the correlation between the end frequency components of the interval of interest[Ban06, S.R10]. Coherence bandwidth for 90% correlation (corresponding to 0.5 dB channel variation) is given by :

$$B_c \approx \frac{1}{50\tau_{rms}} \tag{2.11}$$

Similarly, coherence bandwidth for 50% correlation (corresponding to 3 dB channel variation) is given by :

$$B_c \approx \frac{1}{5\tau_{rms}} \tag{2.12}$$

2.3.3 Doppler spread and coherence time

The two channel parameters discussed above give information about the time dispersion of the radio channel but they do not give any information about the channel time variability caused by the movement of either the scatterers of the environment or the terminals themselves. Doppler spread and coherence time are introduced to give information about the time variability of the radio channel.

Doppler spread (B_D) is a measure of the frequency broadening caused by the shift in the carrier frequency. Doppler spread has a dual parameter in the time domain which is the

coherence time. Coherence time is defined as the time interval over which the signal does not experience time fluctuations (*i.e.* the channel impulse response can be regarded as time-invariant over this interval). The coherence time is inversely proportional to Doppler spread. Mathematically, coherence time is described as the time interval for which the time correlation function is $> 50\%$ [S.R10], and is given by :

$$T_c \approx \frac{9}{16\pi f_m} \tag{2.13}$$

where, f_m is the Doppler shift.

2.3.4 Narrowband and wideband channels

Radio channels can be described as either narrowband or wideband. The difference between them depends on the transmitted signal parameters (signal bandwidth B_s and signal symbol period T_s) with respect to the radio channel parameters (coherence bandwidth and B_c and rms delay spread τ_{rms}). In narrowband systems, all multipath contributions arrive within time delays that are smaller than the symbol time ($T_s >> \tau_{rms}$). This means that the signal bandwidth B_s with respect to the channel bandwidth. In wideband systems, some multipath contributions arrive with delays greater or comparable with the symbol time ($T_s < \tau_{rms}$). Table 2.2 specifies four possible fading scenarios as a result of the time and frequency dispersion nature of the radio channel.

Fading type	Channel type
Flat fading	Narrowband : • $B_s << B_c$ • $T_s >> \tau_{rms}$
Frequency selective fading	Wideband : • $B_s > B_c$ • $T_s < \tau_{rms}$
Fast Fading	Narrowband : • $B_s < B_c$. • $T_s > T_c$
Slow Fading	Wideband : • $B_s >> B_c$. • $T_s << T_c$

Table 2.2 – *Fading types*

2.3.5 Macro, Micro, Pico, and Femto Cells

Broadly speaking, radio base stations (BSs) are often categorized according to cell size into different types (*i.e.* macro, micro, pico, and femto cells). The main factors that define such classification are : cell purpose (*i.e.* coverage, capacity), radiated power, and antenna height. It would be useful to give a brief overview of all cell types in general before talking about the different configurations of WSNs. Figure 2.4 illustrates the general concept of cell types :

Macro cells : are deployed to provide radio coverage over large distances. Macro cells are characterized by their high radiated power and their antenna heights (higher than the average height of the surrounding buildings). This configuration can provide wide coverage up to several kilometers, depending on the environment (*i.e.* urban, suburban, or rural).

Micro cells : are designed to provide radio coverage and additional capacity for relatively small distances, particularly in areas with high traffic density. Micro cells are characterized by their low transmit power with low antenna heights (lower than the surrounding buildings), giving a cell radius of a few hundreds of meters.

Pico cells : are designed mainly to provide capacity for hotspots that have high traffic densities. Pico cells have smaller configurations with a cell radius of several tens of meters (*e.g.* train stations).

Femto cells : are deployed inside buildings to provide radio coverage/capacity (*e.g.* offices, shopping malls, *etc.*).

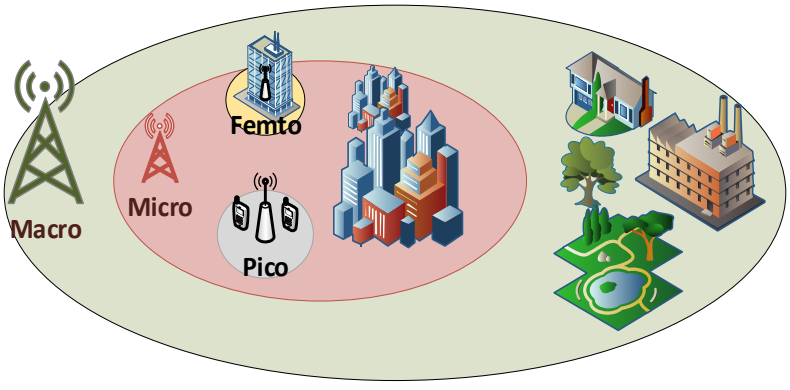

Figure 2.4 – *Macro, Micro, Pico, and Femto Cells.*

It is important to note that configuration of the short-range communication protocols of WSNs such as Zigbee, WirelessHART, *etc.* could be considered mainly as micro cells, while the LPWAN protocols such as LoRa and Sigfox are mainly considered as macro cells. Hence, micro or macro cell configurations will be assumed for channel modeling.

2.4 Review of empirical propagation radio models for WSNs

Many empirical radio propagation models have been developed in the literature. However, not all models are applicable to WSNs. To this end, this section intends to give an overview of the most widely used outdoor physical and empirical propagation models for short-range communication protocols of WSNs that were presented in chapter 1. As mentioned previously, short-range communication protocols are widely used in smart city applications. However, they have some constraints that should be taken into account when modeling the radio channel, these constraints can be summarized as follows [SKPP09a, SKPP08, KT13] :

— Low transmit power : the energy consumption is one of restricting factors in WSNs. For this reason, the transmission power is very low compared to other communication systems. The nominal transmit power defined by the IEEE 802.15.4 physical layer - 2003 is 1 mW (0 dBm) [IEE03], giving a radio range of at most a few hundred meters.
— Low antenna heights : in some WSN scenarios for smart cities, the sensor nodes are relatively close to the ground level.
— Directivity of antennas : perfect omnidirectional antennas are usually assumed in WSNs simulations. However, the assumption of perfect omnidirectional antennas is not very accurate, so antenna radiation patterns should be considered for more realistic models.

In the next subsections, the most widely used outdoor propagation models for short-range communication protocols will be described. However, other propagation models for LPWAN protocols will be discussed in chapter 4.

2.4.1 Free Space Model

The free space model is one of the most widely used propagation models in WSN simulators. It assumes ideal propagation conditions as it considers only one unobstructed line of sight path between the transmitter and receiver. The propagation environment is totally neglected, hence reflections and diffraction are not considered. This model calculates simply the attenuation of a direct electromagnetic wave taking account of the distance and frequency. Free space path loss is given by Friis equation as

$$P_r(d, f) = P_t G_t G_r \left(\frac{\lambda}{4\pi d}\right)^2 \tag{2.14}$$

where,

— d is the distance between the transmitter and receiver,
— f is the frequency,
— λ is the wavelength ($\lambda = c/f$),
— G_t, G_r are the transmitter and receiver antenna gains in dBi respectively.

The Free path loss is generally expressed in dB

$$L[dB] = 10 \log \frac{P_t}{P_r} = -10 \log \left(G_t G_r \left(\frac{\lambda}{4\pi d}\right)^2\right) \tag{2.15}$$

where L is the path loss in dB.

Despite the fact that free space model considers only the direct clear path, it is still commonly used in visibility scenarios because the direct path is the predominant one.

2.4.2 Adapted Free Space Model

Path loss exponent (n) in the free space model equals 2, but the adapted free space model makes it possible to use an empirical value for the path loss exponent according to the propagation environment. For example, in [SEGD11], for an urban unobstructed scenario, it was found that the measurements match the model if a path loss exponent of $n = 2.2$ is assumed. The path loss exponent can grossly take into account the multipath effect. Figure 2.5 depicts the path losses for $n = 2$ and $n = 2.2$ for . It can be shown that at a distance of 150 m, the adapted model predicts a path loss of about 90 dB at 2.4 GHz. In fact, this model suggests that the radio range of wireless sensors operating at 2.4 GHz and having a link budget of 90 dB is about 150 m.

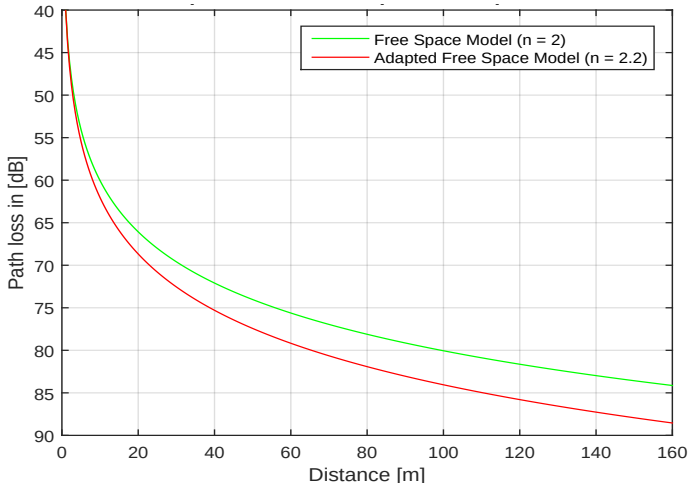

Figure 2.5 – *Free space model vs. adapted model.*

2.4.3 Simplified Two-Ray Ground Reflection Model

Free space model does not consider any obstacle. When the nodes are placed close to the ground, we have an unavoidable obstacle, which is the ground. Wireless sensors are probably placed near to the ground, thus we have to take into account the ground reflected ray because it carries significant power. Two-ray model estimates the path loss of the received signal considering the two predominant paths in such scenarios, which are the direct path (LOS) and the ground reflected rays as shown in figure 2.6.

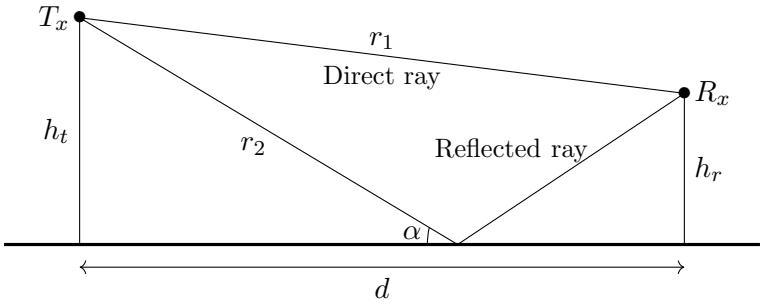

Figure 2.6 – *Two-ray ground reflection model.*

The interaction between the direct path and the reflected path is simplified [SD11], by assuming a large distance d between the transmitter and receiver, and a perfect reflection coefficient. Thus, the simplified Two-Ray Ground equation is given by

$$L[dB] = 20 \log \left(\frac{d^2}{h_t h_r} \right) \tag{2.16}$$

where h_t and h_r are the transmitter and receiver antenna heights respectively.

In point of fact, if $d >> h_t h_r$, the phase difference between the two rays becomes very small and cancels out, which makes the expression frequency independent. Hence, equation 2.16 depends only on the antenna heights and on the distance.

Figure 2.7 shows the simulation results of this model using the IEEE 802.15.4 default parameters (transmit power = 0 dBm, receiver sensitivity = - 90 dB, and frequency = 2.4 GHz). Sensor nodes' heights were assumed to be close to the ground *i.e.* $h_t = h_r = 0.3m$. Simulation results show that the maximum radio range for that configuration is about 55 m, which is confirmed and validated in [SJK07], by using a real test platform.

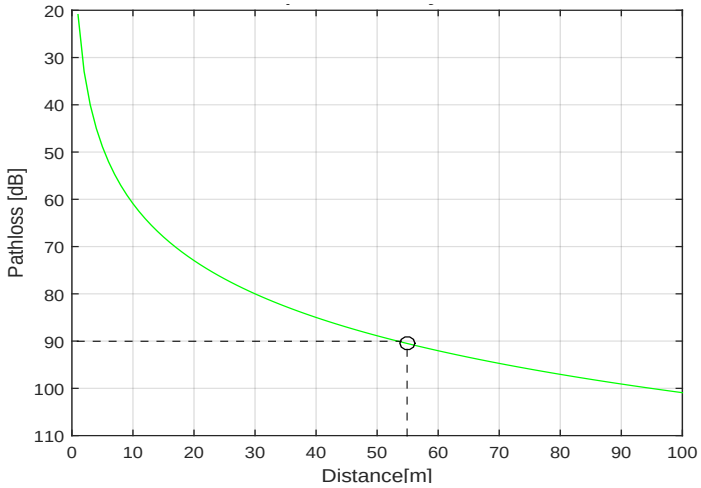

Figure 2.7 – *Simplified two-ray ground reflection Model.*

2.4.4 Free Space and Simplified Two-Ray Hybrid Model

As mentioned earlier, the simplified two ray ground model was simplified for large distances relative to antenna heights. The simplified two-ray model does not, therefore, give accurate results for short distances because it assumes that the two rays are in phase. For this reason, the authors in [SD11] and [KT13] propose to use the free space model until a certain distance, which is called the cross-over distance and is given by equation 2.18, after that distance the simplified two-ray ground reflection model is used as follows

$$L[dB] = \begin{cases} L_{Free\ space\ model} & d \leq d_b \\ L_{Simplified\ two-ray\ ground\ reflection\ model} & d > d_b \end{cases} \tag{2.17}$$

$$d_b = \frac{4h_t h_r}{\lambda} \tag{2.18}$$

2.4.5 Two-Ray Ground Reflection Model

As mentioned above, the two-ray model considers two significant paths in near-ground scenarios, which are the direct and the ground reflected rays. The simplified version assumes some simplifying hypotheses such as perfect reflection coefficient which is not true because the ground is not a perfect conductor. The here presented model integrates the ground reflection coefficient. Considering only the direct and reflected rays, the expression of the two-ray ground reflection model may be written as [KGNM06] :

$$\bar{P_r}(d) = P_t \left(\frac{\lambda}{4\pi d}\right)^2 \left| \frac{1}{r_1} e^{-jkr_1} + \frac{\Gamma_2(\alpha)}{r_2} e^{-jkr_2} \right|^2 \tag{2.19}$$

where,

— $\bar{P_r}$ is the received power,
— P_t is the transmit power,
— d is the distance between the transmitter and receiver,
— r_1 and r_2 are the length of the direct and reflected paths respectively,
— λ is wavelength,
— k is the wavenumber,
— α is the angle of incidence of the ground ray,
— Γ_2 is the ground reflection coefficient, given in [KGNM06].

Figure 2.8 shows the simulation results for the simplified two-ray, two-ray, and free space models. Simulations were conducted at 2.4 GHz, and at heights $h_t = h_r = 1.5m$. It is obvious that the simplified model underestimates the path loss if the distance is less than the cross-over distance. The curve of the two-ray model shows that the direct and reflected rays add up constructively or destructively (oscillations around the free space model). It is important to note that the received signal experiences deep fades due to the combination of two out-of-phase rays.

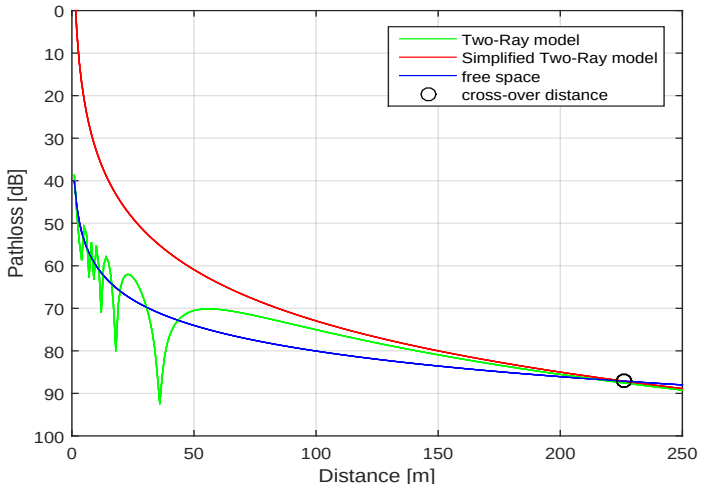

Figure 2.8 – *Simplified two-ray, two-ray, and free space models.*

Although this model is more accurate than the simplified version, it does not include some relatively important factors such as the antenna radiation pattern and the variation of the received signal. These factors will be taken into consideration in the next model.

2.4.6 Free Outdoor Model (FOM)

This model combines the four most significant path loss factors for WSN [SKPP09a]. These factors are : free space path loss, ground reflection path loss, it adds a Gaussian random variable to represent the uncertainty of the estimated received signal level due to multiple less significant paths, and finally, it includes two factors to represent the antenna radiation pattern gains along the direct and reflected paths respectively. The received power (taking all the mentioned factors into account) is, therefore, given by

$$\bar{P_r}(d) = P_t\left(\frac{\lambda}{4\pi d}\right)^2\left(K_1^2 + K_2^2\Gamma^2 + 2K_2\Gamma\cos(\frac{2\pi}{\lambda}\Delta L)\right) + X_{\sigma(\bar{P_r})} \tag{2.20}$$

where,

— Δ L is the path difference between direct and reflected paths,
— K_1 and K_2 are coefficients to represent the difference in the antennas' gain, along the direct and reflected paths respectively, due to the antennas' radiation pattern,
— $X_{\sigma(\bar{P_r})}$ is a Gaussian distribution with a mean of $\bar{P_r}$ and a variance of σ given in [SKPP09a].

Figure 2.9 shows the predicted signal attenuation obtained by this model (blue curve) versus the attenuation obtained without considering the reflected ray (green curve). It shows that direct and reflected rays add up constructively or destructively when they are out of phase [SWS12]. The red points around the free outdoor model represent the uncertainty range or the margin of error that was introduced by the Gaussian distribution.

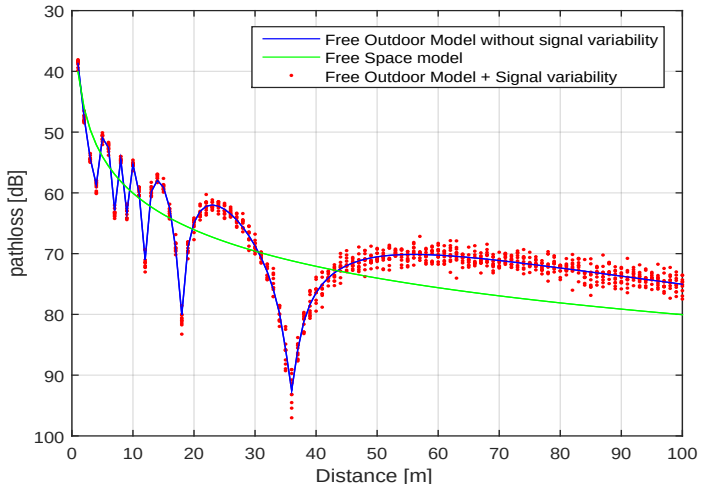

Figure 2.9 – *Free outdoor model.*

This model was validated in [SKPP09a] through actual measurements for some test scenarios. To address the problem of the deep fades, which is called energy holes (caused when the two rays are completely out of phase), figure 2.10 traces the distance-height relationship at 2.4 GHz. It shows the signal attenuation in function of the distance (between the transmitter node and receiver node), and in function of the nodes' heights. Figure 2.10 shows the energy holes areas (yellow areas). Ideally, sensors should be placed neither in an area of potential energy hole, nor at very low heights [SKPP08].

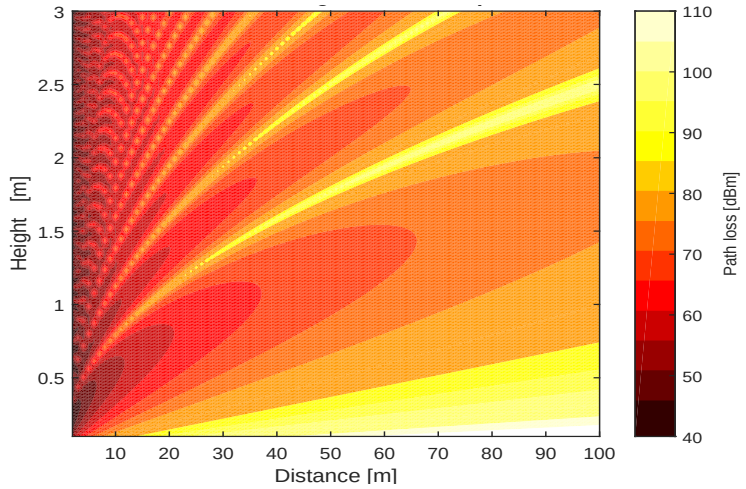

Figure 2.10 – *Distance-height relationship.*

2.4.7 Log Normal Model Shadowing Model

Log-Normal shadowing model is a general extension to the free space model. It estimates the path loss for a wide range of environments, whereas, the free space is restricted to the unobstructed path. The log-normal shadowing model consists of two parts ; the first one is the adapted free model that uses a path loss exponent determined by field measurements. The second part is the shadowing model to reflect the variation of the received power due

to obstacles. Some typical values of path loss exponent and shadowing deviation are given in table 2.3. The overall relationship between the path loss and the distance is expressed as follows

$$L(d_i) = L(d_0) + 10n \log\left(\frac{d_i}{d_0}\right) + X_\sigma \tag{2.21}$$

where,

— $L(d_i)$ is the path loss in dB at a distance d_i, $d_i > d_0$,
— $L(d_0)$ is the path loss in dB at a distance d_0,
— n is the path loss exponent,
— n is a zero-mean Gaussian random variable with a standard deviation of σ.

Environment	n	$\sigma[dB]$
Free Space	2	3-12
Urban area	2.7-3.5	
Shadowed urban area	3-5	

Table 2.3 – *Some typical values of path loss exponent and shadowing deviation*

In [WSKZ12], it was proposed to use the log-normal model with two different slopes and deviation values. A break-point distance separates the two slopes of this model. It was proved in [WSKZ12] that prediction accuracy of a two-slope log-normal model is superior to that of the one-slope model in near ground scenarios. The two-slope model is expressed as follows

$$L(d_i) = \begin{cases} L(d_b) + 10n_1 \log\left(\frac{d_i}{d_b}\right) + X_{\sigma 1} & d_i \leq d_b \\ L(d_{b+1}) + 10n_2 \log\left(\frac{d_i}{d_{b+1}}\right) + X_{\sigma 2} & d_i > d_b \end{cases} \tag{2.22}$$

where $d_b = \frac{4h_r h_t}{\lambda}$

Table 2.4 shows the simulation parameters for a plaza side given in [WSKZ12]. The simulation results obtained are given in figure 2.11 (a), which shows the two slopes separated at the break-point distance = 32 m. The red samples represent the variations of the received power of the first piece of the model while the black ones represent the variations of the received power of the second piece. Figure 2.11 (b) shows the same results but with a logarithmic scale on the Y-axis. It depicts two linear slopes, the first slope value is 15.2 dB/decade, while the second slope is 37.4 dB/decade.

Environment	h_t	h_r	n_1	n_2	σ_1	σ_2	d_b
Plaza	1 m	1 m	1.52	3.74	2.49	1.85	32

Table 2.4 – *Two-slope log-normal model parameters*

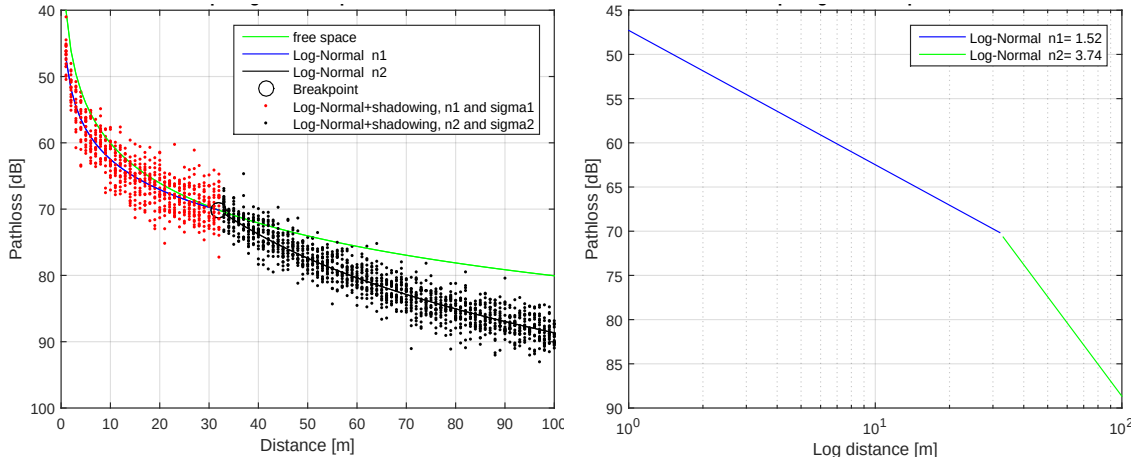

(a) (b)

Figure 2.11 – *Simulation results for the two-slope log normal model.*

2.4.8 Survey of radio propagation models in WSN Simulators

As mentioned in the previous chapter, well-known network simulators are mainly implementing simple empirical radio propagation models, without giving further detail about the nature of these models. Therefore, this subsection intends to provide an overview of the radio models that are integrated into those network simulators. Table 2.5 lists the radio models implemented in the WSN simulators presented in section 1.5. It should be noted that 2.5 lists also some radio propagation models that have not been presented in the previous subsections.

Simulator	Propagation models
ns-2	— Free space model. — Two-ray ground reflection model. — Log-normal shadowing model.
MannaSim	— Free space model — Two-ray ground reflection model. — Log-normal shadowing model.
TOSSIM	— Simplified two-ray ground reflection model. — Log-normal shadowing model.

Cooja	— Disk model. — 2D Ray-tracing.
Worldsens	— Disk model. — Free space model. — Simplified two-ray ground reflection model. — Log-normal shadowing model. — Rayleigh. — Nakagami.
QualNet	— Free space model. — Lee's street Microcell [LL00]. — Street-Mobile-to-Mobile. — COST231 Hata [DC99]. — COST231 Walfish-Ikegami [DC99].
OMNet++	— Free space model. — Two-ray ground reflection model. — Temporal variation.
OPNET	— Free space model. — TIREM propagation models. — COST231 Hata [DC99]. — COST231 Walfish-Ikegami [DC99]. — Longley-Rice model.
CNET	— Free space model. — User-defined radio propagation model.

ns-3[np16]	— Free space model. — Log-normal shadowing model. — Three log Distance Propagation Loss model. — Two-ray ground reflection loss model. — Cost 231 propagation loss model. — Fixed RSS Loss model. — ITU R1411 LOS Propagation loss model. — ITU R1411 NLOS over-rooftop propagation loss model. — Jakes propagation loss model. — Kun 2600 Mhz propagation Loss Model. — Matrix propagation loss model. — Nakagami propagation loss model. — Okumura Hata propagation loss model. — Random propagation loss model. — Range propagation loss model.

Table 2.5: *Propagation models implemented in some WSN simulators.*

2.5 Deterministic modeling

Deterministic models simulate radio propagation based on Maxwell's equations. They simulate mainly the significant physical phenomenon that occur to radio waves when traveling through the propagation environment, *e.g.* reflection, transmission (refraction), and diffraction. Deterministic models usually have a high degree of accuracy and they can provide both narrowband and wideband channel parameters. There are two main families of deterministic models. First category is based on rigorous numerical solutions to Maxwell's equations (*cf.* subsection 2.5.3) and the other category is based on asymptotic numerical solutions for high frequencies (*cf.* subsection 2.5.5). In order to understand these methods, it is necessary first to introduce briefly Maxwell's Equations.

2.5.1 Maxwell's Equations

In 1873, James Maxwell published a set of equations that describes how electromagnetic waves behave through a medium. In a homogeneous, uncharged, and isotropic medium, Maxwell's equations can be expressed in the differential form for a given frequency ($f = w/2\pi$) as :

$$\nabla \times \overrightarrow{\mathcal{H}} = \frac{\partial \overrightarrow{\mathcal{D}}}{\partial t} \tag{2.23}$$

$$\nabla \times \overrightarrow{\mathcal{E}} = - \frac{\partial \overrightarrow{\mathcal{B}}}{\partial t} \tag{2.24}$$

$$\nabla \cdot \overrightarrow{\mathcal{B}} = 0 \tag{2.25}$$

$$\nabla \cdot \overrightarrow{\mathcal{D}} = 0 \tag{2.26}$$

where,

— $\overrightarrow{\mathcal{H}}$ is the magnetic field intensity.
— $\overrightarrow{\mathcal{D}}$ is the electric flux density.
— $\overrightarrow{\mathcal{E}}$ is the electric field intensity.
— $\overrightarrow{\mathcal{B}}$ is the magnetic flux density.

The electric flux density $\overrightarrow{\mathcal{D}}$ is related to the electric field $\overrightarrow{\mathcal{E}}$, and the magnetic flux density $\overrightarrow{\mathcal{B}}$ is related to the magnetic field intensity $\overrightarrow{\mathcal{H}}$ by the following relations :

$$\overrightarrow{\mathcal{D}} = \epsilon \overrightarrow{\mathcal{E}} \tag{2.27}$$

$$\overrightarrow{\mathcal{B}} = \mu \overrightarrow{\mathcal{H}} \tag{2.28}$$

where ϵ is the electric permittivity and μ is the magnetic permeability, as defined in the next subsection.

2.5.2 Electrical properties of propagation medium

A propagation medium is mainly characterized by three parameters that define the response of that medium to the magnetic and electric fields :

— Permittivity (ϵ) : can be defined as a measure of how a dielectric medium can be affected by the application of an electric field. The permittivity is, therefore, a physical quantity that reflects the resistivity of a dielectric medium to the application of an electric field. Permittivity is given by $\epsilon = \epsilon_r \epsilon_0$, where ϵ_0 is the permittivity of free space ($\epsilon_0 = \frac{1}{\mu_0 c^2} = 8.854 \times 10^{-12}$ F/m), and ϵ_r is the relative permittivity, which is the ratio of the permittivity of the dielectric to that of free space ($\geqslant 1$).

— Permeability (μ) : represents the ability of a medium to magnetize due to the application of a magnetic field. Permeability is given by $\mu = \mu_r \mu_0$, where μ_0 permeability of free space ($\mu_0 = 4\pi \times 10^{-7}$ H/m), and μ_r is the relative permeability, which is the ratio of the permeability of the medium to that of free space.

— Conductivity (σ) : is defined as the ability of a medium to allow electrical charges to move through that medium, therefore it is the inverse of resistivity. In other words, the value of σ is a physical quantity that determines the conductivity of the medium (*i.e.* $\sigma = 0$ for a perfect dielectric, $\sigma = \infty$ for a perfect conductor, and $\frac{\sigma}{\omega\epsilon} \gg 1$ for a good conductor).

2.5.3 Rigorous solutions to Maxwell's equations

Rigorous numerical methods are based on a numerical resolution of Maxwell's equations using differential or integral equations. The most widely used numerical methods are as follows :

- Finite Difference Time-Domain (FDTD) : is one of the most popular differential methods that solves Maxwell's equations in the time domain. FDTD was first introduced by Yee [Yee66]. Maxwell's equations are discretized using both time and space discretization [TH05]. In order to have a stable algorithm, this method requires a minimum spatial spacing of 10-20 per wavelength and sufficiently small temporal spacing.
- Finite Element Method (FEM) : is a differential method in the frequency domain [Jin15].
- Method of Moments (MoM) : is a frequency domain method that is based on the numerical resolution of the integral form of Maxwell's equations. Frequency domain methods calculate the solution for a single frequency. Therefore, for a range of frequencies, the calculation must be repeated for each frequency.

Advantages : these methods can provide accurate results of the electric field.
Drawbacks : the discretization of the environment depends on the wavelength. Therefore, these approaches prove to be inapplicable in high-frequency problems as well as in large-scale environments. Consequently, they will not be used in the here presented thesis. Moreover, these methods give the total field, that is to say that one can not isolate the contributions of each interaction with the propagation environment.

2.5.4 Helmholtz wave Equation

In homogeneous media, propagation problems can be studied by using Helmholtz equation which can be derived from Maxwell's equations :

$$\nabla^2 \overrightarrow{U}(\overrightarrow{r}, w) + k^2 \overrightarrow{U}(\overrightarrow{r}, w) = \quad 0 \tag{2.29}$$

where,

- $\overrightarrow{U}(\overrightarrow{r}, w)$ is the electric or magnatic field at the point of observation.
- k is the wave number of the medium ($k = w\sqrt{\epsilon\mu} = \frac{w}{v} = \frac{2\pi}{\lambda_0}\sqrt{\epsilon_r \mu_r} = \frac{2\pi}{\lambda}$), λ_0 and λ are the wavelengths in free space and in the propagation medium respectively, v is the speed of the wave in the medium.
- ∇^2 is the Laplace operator, $\nabla^2 = \nabla\nabla = \frac{\partial^2}{\partial x^2} + \frac{\partial^2}{\partial y^2} + \frac{\partial^2}{\partial z^2}$

2.5.5 High frequency asymptotic methods

The asymptotic approach is based on the assumption that the wavelength is small with respect to the dimensions of the obstacles in the propagation environment (*i.e.* high frequency methods). According to this hypothesis, the interactions between the environment and waves at a given point can be considered independent of the neighborhood of this point. According to this principle, radio waves are assumed to propagate as rays undergoing a set of local interactions such as reflections on surfaces and diffraction by edges. To characterize the interactions between the rays and the environment, it is necessary to solve locally Helmholtz's equation, both from a physical point of view (*i.e.* amplitude and phase of the reflected or

diffracted wave) and also from a geometrical point of view (*i.e.* direction of the reflected or diffracted ray). In general, asymptotic methods involve three important phases : first, it is necessary, before performing any field calculation, to search for all possible paths joining a given transmitter with a given receiver. This requires a detailed description of the environment. Different path calculation algorithms will be discussed later. Secondly, physical models are needed to calculate the electric field carried by each path. These models require the geometrical and electrical properties of the obstacles in the propagation environment. Finally, results are processed to obtain the parameters that allow to characterize the channel : mean received power, channel impulse response, delay spread, etc.

— **Advantages :** asymptotic approaches give actuate results because they describe the real propagation process. Moreover, field polarization and antennas radiation patterns can be taken into account. These methods can give narrowband and wideband results. In addition, the contribution of each path can be studied separately, by separating the contributions of diffracted or reflected rays. Another advantage is that the calculation time is independent of the frequency.

— **Drawbacks :** it is necessary to fix beforehand a number of interactions between the wave and the environment. However, it not easy to predict the order of interactions from which the contribution will be negligible, especially in confined environments. In addition, asymptotic methods remain valid only if the wavelength is small compared to the dimensions of the obstacles present in the propagation environment. These methods are therefore only applicable in high-frequency regimes.

2.5.5.1 Geometric Optics and its extensions

The Geometric Optics (GO) is an important technique to obtain an approximate solution of the Helmholtz's equation (for a homogeneous, isotopic, and source free medium). The GO field is assumed to propagate along rays. In isotropic and lossless media, the energy carried by a ray is assumed to be conserved in a ray tube. The energy is persistent in magnitude and phase as well as in the space and time domains. The ray trajectories follow a path in accordance with the Fermat's principle. For homogeneous media, the rays are straight and propagating perpendicularly to the wavefront (*i.e.* a surface of points that have the same phase) as illustrated in figure 2.12. The GO field is expressed by Luneburg-Kline asymptotic series solution of the wave equation (Kline [Kli51] ; Luneberg [LH64]) :

$$\overrightarrow{U}(\overrightarrow{r},w) = e^{jkS(\overrightarrow{r})} \sum_{n=0}^{\infty} \frac{\overrightarrow{U_n}(\overrightarrow{r})}{(jk)^n} e^{-jwt} \tag{2.30}$$

where,

— $\overrightarrow{U}(\overrightarrow{r},w)$ is the electric or magnetic field at the point of observation,

— $S(\overrightarrow{r})$ is the phase function,

— $\overrightarrow{r}$ is the position vector of the field,

It was shown that the leading term of the Luneburg-Kline series ($n = 0$) corresponds to the GO field in high-frequency regimes. The series can then be reduced to :

$$\overrightarrow{U}(\overrightarrow{r},w) = \overrightarrow{U_0}(\overrightarrow{r}) e^{jkS(\overrightarrow{r})} e^{-jwt} \tag{2.31}$$

Thus, the general form of GO field along a ray at the observation point P at distance r from the reference point O (temporal variation is implicitly assumed) can be expressed as :

$$\overrightarrow{U}(P) = \overrightarrow{U}(O)A(r, \rho 1, \rho 2)e^{-jkr} \tag{2.32}$$

where

- $\overrightarrow{U}(P)$ is the field at the observation point P,
- $\overrightarrow{U}(O)$ is the field at the reference point O,
- r is the distance between the reference point O and the observation point P,
- ρ_1, ρ_2 are the radii of curvature of the wavefront of the surface that contains the reference point O,
- $A(r, \rho_1, \rho_2)$ is the divergence factor which corresponds to the ratio between $\overrightarrow{U}(P)$ and $\overrightarrow{U}(O)$ and is given by $A(r, \rho_1, \rho_2) = \sqrt{\frac{\rho_1 \rho_2}{(\rho_1 + r)(\rho_2 + r)}}$.

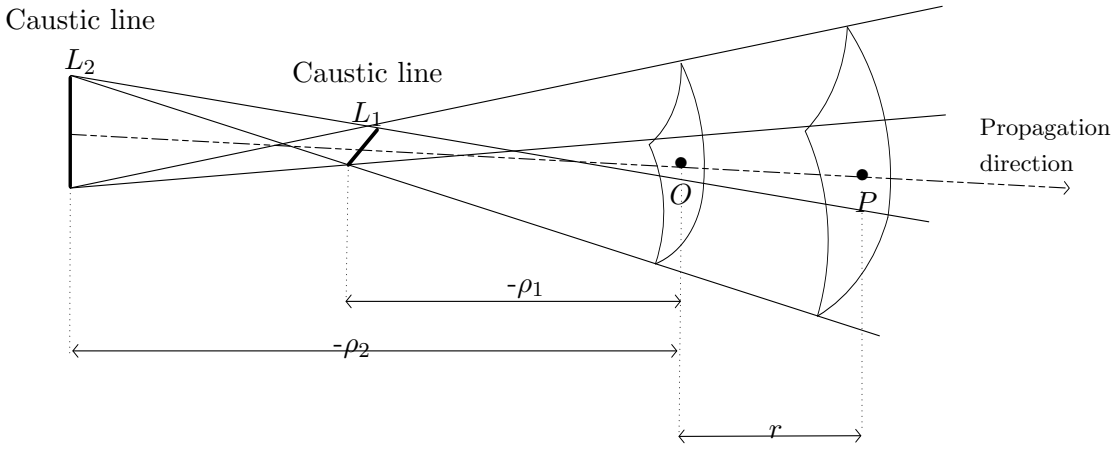

Figure 2.12 – *Astigmatic ray tube.*

The general configuration of a ray tube is the astigmatic ray tube as depicted in figure 2.12. It is obvious from figure 2.12 that all the rays pass through the same lines (L_1 and L_2), which are known as caustic lines. The GO field is in infinite at these lines, because, in theory, an infinite number of rays cross them. This behavior is also confirmed from equation 2.32 where the denominator of the divergence factor becomes zero at $r = -\rho_1$ or $r = -\rho_2$ and hence the GO field becomes infinite.

2.5.5.2 Wave types

Equation 2.32 is a familiar equation in the GO. In homogeneous media, the field at any point can be obtained from this equation provided that the field is known at a reference point. Equation 2.32 is usually written as

$$\overrightarrow{U}(P) = \overrightarrow{U}(O)\sqrt{\frac{\rho_1 \rho_2}{(\rho_1 + r)(\rho_2 + r)}}e^{-jkr} \tag{2.33}$$

The form of any wave is determined by its source and described by the shape of its wavefront. Four types of field can be distinguished according to the radii of curvature of the wavefront (values of ρ_1 and ρ_2), namely astigmatic, spherical, cylindrical, and plane front waves. Figure 2.13 depicts the spherical, cylindrical, and plane waves, they are all special cases of the astigmatic ray tube.

— Astigmatic wavefront : when $\rho_1 \neq \rho_2$, the field is given by equation 2.33.

— Spherical wavefront : when $\rho_1 = \rho_2$, the field is given by :

$$\overrightarrow{U}(P) = \overrightarrow{U}(O)\frac{\rho}{\rho + r}e^{-jkr} \tag{2.34}$$

— Cylindrical wavefront : when ρ_1 or $\rho_2 = \infty$, the field is given by :

$$\overrightarrow{U}(P) = \overrightarrow{U}(O)\sqrt{\frac{\rho}{\rho + r}}e^{-jkr} \tag{2.35}$$

— Plane wavefront : when $\rho_1 = \rho_2 = \infty$, the field is given by :

$$\overrightarrow{U}(P) = \overrightarrow{U}(O)e^{-jkr} \tag{2.36}$$

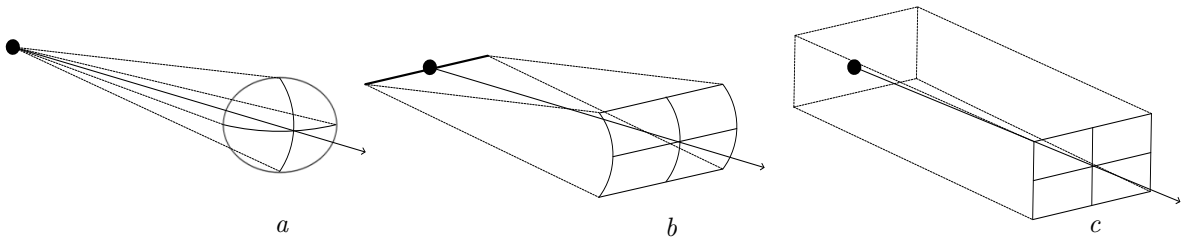

Figure 2.13 – *Wavefronts : a. spherical wave, b. cylindrical wave, c. plane wave.*

2.5.5.3 Reflection

Reflection is an important propagation mechanism in indoor and outdoor environments. It occurs when the radio wave traveling in one medium hits another medium with different electrical properties. The incident field is split into reflected and transmitted parts. In outdoor environments, only the contribution of the reflected rays is of importance, since the transmitted rays are assumed to be entirely absorbed by the buildings. Fresnel reflection coefficient relates the incident electric field with the reflected and transmitted fields.

The field at a point P (shown in figure 2.14) after being reflected at a point Q can be expressed in the same manner as the fundamental expression of the field in the GO (equation 2.33). The reflected field at the observation point P is thus given by :

$$\overrightarrow{E}^r(P) = \overrightarrow{E}^r(Q)\sqrt{\frac{\rho_1^r\rho_2^r}{(\rho_1^r + s_r)(\rho_2^r + s_r)}}e^{-jks_r} \tag{2.37}$$

where

— $\overrightarrow{E}^r(P)$ and $\overrightarrow{E}^r(Q)$ are the reflected fields at the reflection point P and the observation point Q respectively,

— ρ_1^r, ρ_2^r are the radii of curvature of the reflected wavefront (in the case of a planner surface $\rho_1^i = \rho_1^r$ and $\rho_2^i = \rho_2^r$),
— s_r is the distance between the reflection point Q and the observation point P .

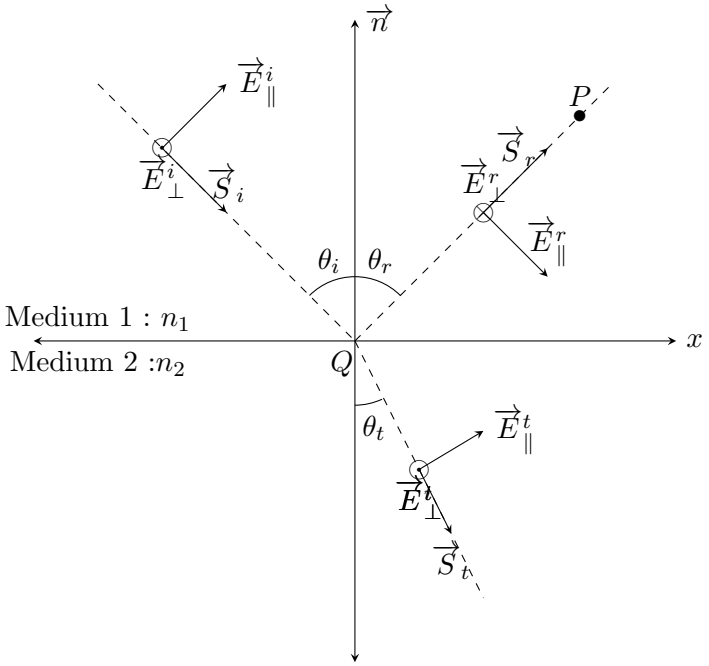

Figure 2.14 – *Incident, reflected, and transmitted wave at a smooth plane.*

In outdoor environments, refection normally occurs on the buildings' walls and on the ground. In addition, it is also very probable that multiple reflections (wall-wall or ground-wall) occur before the reflected wave arrives at the receiver. The incident wave is decomposed into two orthogonal components (parallel polarization ($\parallel$) and perpendicular polarization ($\perp$), which are treated separately as shown in figure 2.14. The superscripts i, r, and t refer to the incident, reflected, and transmitted waves respectively. The total reflected wave is the vector sum of the two polarizations and is given by :

$$\overrightarrow{E}^r(P) = E^r_{\parallel}(P)\,\overrightarrow{e}^r_{\parallel} + E^r_{\perp}(P)\,\overrightarrow{e}^r_{\perp} \tag{2.38}$$

where $\overrightarrow{e}^r_{\parallel}$ is a unit vector parallel to the plane of incidence and $\overrightarrow{e}^r_{\perp}$ is a unit vector perpendicular to the plane of incidence.

The reflected field and the incident field are related at the reflection point by the reflection coefficients $R_{\parallel,\perp}$ according to

$$\begin{bmatrix} E^r_{\parallel}(Q) \\ E^r_{\perp}(Q) \end{bmatrix} = \begin{bmatrix} R_{\parallel} & 0 \\ 0 & R_{\perp} \end{bmatrix} \begin{bmatrix} E^i_{\parallel}(Q) \\ E^i_{\perp}(Q) \end{bmatrix} \tag{2.39}$$

$$R_{\parallel,\perp} = \frac{E^r_{\parallel,\perp}(Q)}{E^i_{\parallel,\perp}(Q)} \tag{2.40}$$

The reflection coefficients are simply the ratio of the reflected field to the incident field at the reflection point. The Fresnel reflection coefficients for an infinite plane surface with

$$R_{\parallel} = \frac{n_i \cos\theta_t - n_t \cos\theta_i}{n_i \cos\theta_t + n_t \cos\theta_i} \tag{2.41}$$

$$R_{\perp} = \frac{n_i \cos\theta_i - n_t \cos\theta_t}{n_i \cos\theta_i + n_t \cos\theta_t} \tag{2.42}$$

The Fresnel reflection coefficients for an infinite plane surface with a permittivity ϵ_r are given as :

$$R_{\parallel} = \frac{\epsilon_r \cos\theta_i - \sqrt{\epsilon_r - \sin^2\theta_i}}{\epsilon_r \cos\theta_i + \sqrt{\epsilon_r - \sin^2\theta_i}} \tag{2.43}$$

$$R_{\perp} = \frac{\cos\theta_i - \sqrt{\epsilon_r - \sin^2\theta_i}}{\cos\theta_i + \sqrt{\epsilon_r - \sin^2\theta_i}} \tag{2.44}$$

In the case of a perfect conductor plane, the Fresnel coefficients become simply $R_{\parallel} = 1$ and $R_{\perp} = -1$, *i.e.* perfect conductors reflect entirely the incident field.

Finally the reflected field at the observation point P can be expressed in function of the incident wave at the reflection point Q as

$$\begin{bmatrix} E^r_{\parallel}(P) \\ E^r_{\perp}(P) \end{bmatrix} = \begin{bmatrix} R_{\parallel} & 0 \\ 0 & R_{\perp} \end{bmatrix} \begin{bmatrix} E^i_{\parallel}(Q) \\ E^i_{\perp}(Q) \end{bmatrix} \sqrt{\frac{\rho^r_1 \rho^r_2}{(\rho^r_1 + s_r)(\rho^r_2 + s_r)}} e^{-jks_r} \tag{2.45}$$

The refracted (or transmitted) also follows the same GO field expression. It is given by an expression analogous to equation 2.45. However, the Fresnel transmission coefficients are defined as

$$T_{\parallel} = \frac{2\sqrt{\epsilon_r}\cos\theta_i}{\epsilon_r \cos\theta_i + \sqrt{\epsilon_r - \sin^2\theta_i}} \tag{2.46}$$

$$T_{\perp} = \frac{2\cos\theta_i}{\epsilon_r \cos\theta_i + \sqrt{\epsilon_r - \sin^2\theta_i}} \tag{2.47}$$

As previously indicated, the transmitted wave is assumed to be absorbed in outdoor scenarios and hence it will not be discussed in this thesis.

2.5.5.4 Diffraction

Diffraction is a key phenomenon of radio propagation, especially in outdoor scenarios. The GO laws govern the reflection and refraction but they do not account for diffraction. In fact, the GO has two deficiencies [KMHMP16] : firstly, the field becomes infinite at $r = -\rho_1$ or $r = -\rho_2$ (caustic lines), whereas the real field at these points has a finite value. The second shortcoming is that at the shadow region, the field of the GO is zero, whereas the real field at that region has mostly a nonzero value. Consequently, the GO laws fail to account for diffraction. It is for these reasons that new extensions of the GO were proposed.

2.5.5.5 The geometrical theory of diffraction

Keller introduced the geometrical theory of diffraction (GTD) [Kel62] as an extension of the GO to account for diffraction. The GTD introduces diffracted rays in addition to the existing rays of the GO. These diffracted rays are generated if an incident ray hits edges, corners, or even graze such surfaces. Several laws were introduced to characterize the diffracted rays. When the incident ray hits an edge at point Q, a set of diffracted rays from the point of diffraction Q is generated, all laying on a cone as shown in figure 2.15. In addition, the incident angle and the corresponding diffraction angle are equal with respect to the edge axis.

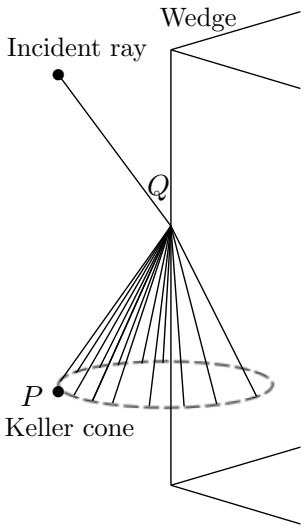

Figure 2.15 – *The cone of diffracted rays.*

The GTD was based on the several postulates [KMHMP16, LL13, God01] :
— Diffraction is a local phenomenon at high frequencies (*i.e.* small wavelengths). The value of the diffracted ray is related to the incident field at the point of diffraction by a coefficient [ST12].
— The diffracted rays follow trajectories defined by a generalized Fermat's principle for edge diffraction.
— The diffracted rays follow the ordinary GO laws away from the point of diffraction.

Based on the aforementioned postulates, the diffracted field can be expressed in a form analogous to reflection as (it should be mentioned that the GTD considers only perfectly conducting materials) :

$$\overrightarrow{E}^d(P) = \overrightarrow{E}^i(Q)\overline{D}\sqrt{\frac{\rho^d}{S_d(\rho^d + S_d)}}e^{-jkS_d} \tag{2.48}$$

where
— $\overrightarrow{E}^d(P)$ is the diffracted field at the observation point P,
— $\overrightarrow{E}^i(Q)$ is the incident field at the diffraction point Q,
— S_d is the distance from the diffraction point Q to the observation point P,

— $\overline{D}$ is the dyadic diffraction coefficient.
— ρ^d is a distance defined by equation (12) in [KP74],
— $\sqrt{\frac{\rho^d}{S_d(\rho^d+S_d)}}$ is the divergence factor.

Since the GTD is purely a ray optical method, the space is divided into regions differentiated by the nature of the existing rays in each one. Figure 2.16 identifies three regions separated by boundaries (reflection and diffraction boundaries). Region 1 includes incident, reflected, and diffracted fields ; region 2 contains incident and diffracted fields ; region 3 has only a diffracted field. It is important to emphasize that there are transition regions close to the boundaries as shown in figure 2.16.

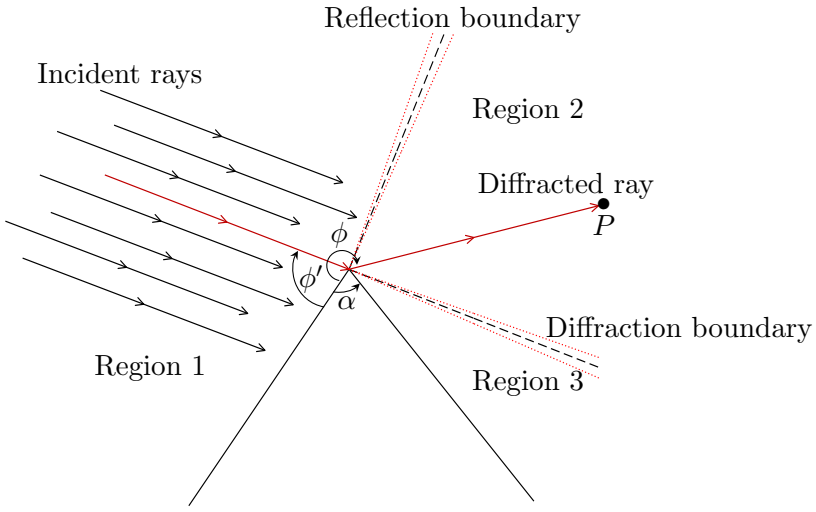

Figure 2.16 – *Geometry for diffraction by a wedge.*

If the observation point P is not in the transition regions, the diffraction coefficients are given by :

$$D_{\parallel,\perp}(\phi,\phi',\beta_0,n) = \frac{e^{-\frac{jk}{4}}\sin\frac{\pi}{n}}{n\sqrt{2\pi k}\sin\beta_0}\left[\frac{1}{(\cos\frac{\pi}{2}-\cos\frac{\phi-\phi'}{n})} \mp \frac{1}{(\cos\frac{\pi}{2}-\cos\frac{\phi+\phi'}{n})}\right] \tag{2.49}$$

where,
— $D_{\parallel,\perp}$ are the diffraction coefficient for parallel and perpendicular polarization respectively.
— ϕ and ϕ' are the angle of incident ray and the angle of diffracted ray respectively as defined in figure 2.16.
— n is a number related to the inner of the wedge ($n = \frac{2\pi-\alpha}{\pi}$), where α is the inner angle of the wedge.

2.5.5.6 The Uniform theory of diffraction

The expression given by the GTD (equation 2.49) becomes singular if the observation point is close to the reflection or shadow boundaries (*i.e.* in the transition regions). Kouyoumjian and

Pathak [KP74] solved the singularity problem by introducing new terms based on a Fresnel integral. This approach is called the Uniform Theory of Diffraction (UTD). For perfectly conducting wedges the diffraction coefficients are given by (it should be also noted that this form of the UTD considers only perfectly conducting materials) :

$$\begin{aligned} D_{\parallel,\perp}(\phi,\phi',\beta_0,n,L) = \frac{-e^{-\frac{jk}{4}}}{2n\sqrt{2\pi k}\sin\beta_0}\Bigg[& \cot\left(\frac{\pi+(\phi-\phi')}{2n}\right)F[kLa^+(\phi-\phi')] \\ & + \cot\left(\frac{\pi-(\phi-\phi')}{2n}\right)F[kLa^-(\phi-\phi')] \\ & \mp\Bigg(\cot\left(\frac{\pi+(\phi+\phi')}{2n}\right)F[kLa^+(\phi+\phi')] \\ & + \cot\left(\frac{\pi-(\phi+\phi')}{2n}\right)F[kLa^-(\phi+\phi')]\Bigg)\Bigg] \end{aligned} \tag{2.50}$$

Equation 2.50 is generally written as sum of four terms as :

$$D_{\parallel,\perp}(\phi,\phi',\beta_0,n,L) = D_1 + D_2 \mp (D_3 + D_4) \tag{2.51}$$

where,

— $F(X)$ is called the transition function, given by $F(X) = 2j\sqrt{X}e^{jX}\int_{\sqrt{X}}^{\infty} e^{-j\tau^2}d\tau$,

— L is a distance parameter, which depends on the wavefront of the incident wave, given by equation (32) in [KP74],

— $a^{\mp}$ depends on is the inner angle of the wedge α, given by equation (27) in [KP74].

The transfer function $F(X)$ plays an important role in the transition regions. In fact, the transfer function involves a Fresnel integral, which ensures the field continuity at those regions. As can be seen from figure 2.17 that this correction term approaches zero in the transition regions when the GTD gives infinite values. Otherwise, the term becomes 1 outside the transition regions so the expression of the UTD reduces to the GTD.

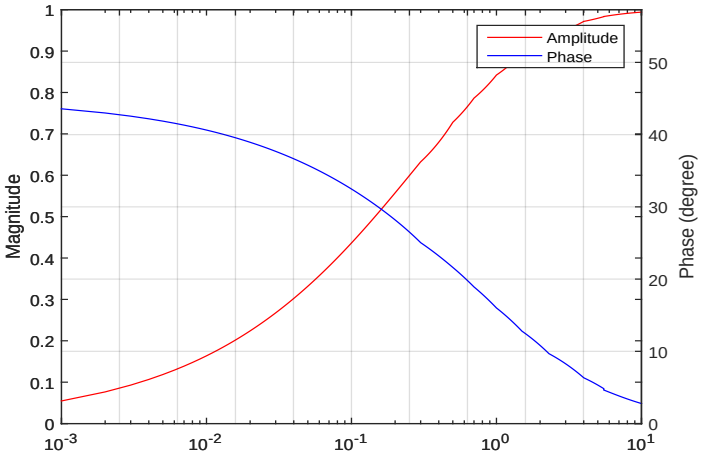

Figure 2.17 – *Transition Function.*

The UTD was further extended by Luebbers so that diffraction for dielectric wedges "lossy" can also be treated. In fact, Luebbers expression includes the reflection coefficients $R_{0(\parallel,\perp)}$ and $R_{n(\parallel,\perp)}$ for the appropriate polarization [Lue89] :

$$D_{\parallel,\perp}(\phi,\phi',\beta_0,n,L) = D_1 + D_2 + R_{n(\parallel,\perp)}D_3 + R_{0(\parallel,\perp)}D_4 \tag{2.52}$$

It should be mentioned that there are other coefficients (other than Luebbers [Lue89]) that have improved the diffraction coefficient. Some commonly used coefficients are Holm[Hol00] and Soni[SON10] diffraction coefficients. The common point is that all these coefficients are heuristic and they fail to predict the field for multiple diffraction problems where the edges are in the transition region of one another. This issue will be addressed in chapter 4.

2.6 Ray Tracing Techniques for Radio Propagation

Ray tracing is a commonly-used technique in propagation modeling. Ray tracing algorithms start by finding all the possible geometrical rays between a transmitter and a receiver for a given number of allowed interactions. Then, the calculation of the rays contributions is based on the GO and UTD. The most common ray tracing algorithms are described in the following subsections.

2.6.1 Ray-launching method

Ray-launching method (known also as the shoot-and-bounce method) was first introduced in [LCL89]. It involves mainly three steps as illustrated in figure 2.18. First, a large number of uniformly distributed rays are launched in all directions, separated with small angles. The second step consists in tracing each emitted ray by conducting intersection tests with the objects in the propagation environment in order to identify any possible reflection or diffraction. These ray-object intersection tests are very time-consuming (more than 90% of the total computational time of the algorithm [YI15]). In addition, each diffraction acts as a new secondary source which increases the computational load. The last step is the reception test to identify the rays that are received. In fact, a ray is represented usually by a rectangular ray tube or ray cone [IY02], and the receiver is represented by a sphere centered at the reception point with a radius defined in function of the angular separation and the length of the received ray. If a given ray tube includes the reception sphere, the ray is considered as being received.

The main drawbacks of this approach is that in order to obtain reasonable accuracy, the angular separation should be small enough (about 0.01 radians [CDB04]). Consequently, the number of rays tend to become extremely large leading to high processing time. On the other hand, when the angular separation is not fine, certain significant rays are likely to be missed.

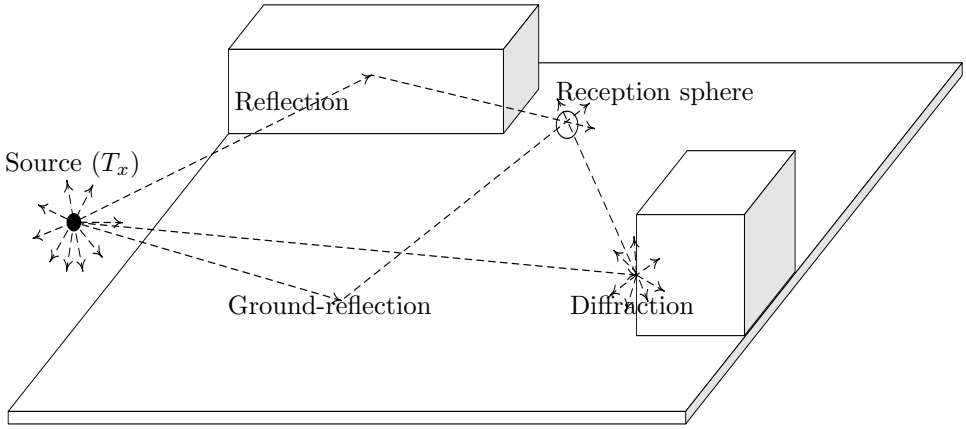

Figure 2.18 – *Ray-Launching method.*

2.6.2 Image method

The image method provides an accurate and simple approach to find the exact ray trajectory between two points (T_x,R_x). The concept can better be illustrated through an example of a multiple reflected ray as shown in figure 2.19, which depicts a simple environment with a transmitter T_x, a receiver R_x, and two walls (wall 1 and 2). First, the image of T_x with respect to wall 1 is located (by axial symmetry, since Fresnel law says that incident and reflected angles are equal), that is T'_x. Similarly, the image of T_x with respect to wall 2 is located, that is T''_x. The path trajectory can be determined recursively by connecting a segment form R_x to T''_x to find the point where the ray is reflected on wall 2, that is P_2. Similarly, another segment is traced between the obtained point P_2 with T'_x to find the point where the ray is reflected on wall 1, that is P_1. Now, the path trajectory can easily be traced through the points (T_x,P_1,P_2,R_x).

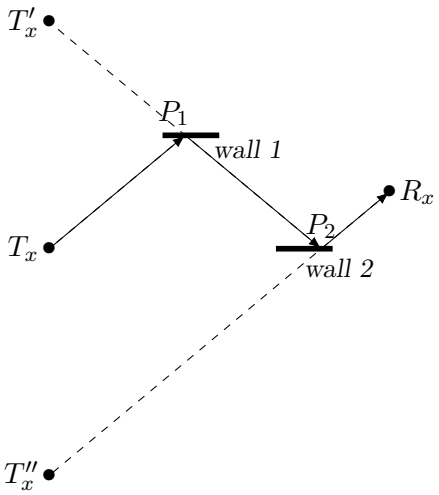

Figure 2.19 – *The image method.*

Typical urban environments have a large number of surfaces, so the computational time becomes prohibitively large especially if a large number of interactions (reflections and diffraction) is considered. Consequently, the image method cannot be adopted for time-restricted applications without efficient acceleration and optimization techniques.

2.6.3 Hybrid method

The ray-launching algorithm identifies the trajectories faster than the image method, on the other hand, the image method provides more accurate path trajectories. Thus it was proposed in [TT96] to take advantage of the two approaches by using first the ray launching method to determine a valid ray trajectory, then the image method intervenes to rectify this path trajectory. Since the surfaces and edges involved in this ray are now determined, the ray-object intersection tests are conducted for only those surfaces and edges.

2.6.4 Other methods

2.7 Ray-Tracing Acceleration Techniques

For certain applications, the computational time of a conventional 3D ray-tracing model is intolerable. To that end, some acceleration techniques are proposed in the literature to make the model more computationally efficient. Iskander and Yun provided a brief summary of several ways to accelerate ray-tracing algorithms [IY02, YI15]. The acceleration techniques can be roughly grouped into four categories :

2.7.1 Dimension Reduction

Ray tracing algorithms in non-full 3D propagation environments are much computationally efficient than those in full 3D environments, and still, they provide accurate results in non-full 3D geometries under certain circumstances. Dimension reduction tends to simplify the complexity of the propagation scene, that guarantees a considerable gain in terms of execution time. Dimension reduction includes approaches such as :

— **2D-H :** if the heights of the buildings in the propagation scene are greater than the heights of the transmitter and receiver, the propagation in the horizontal plane becomes dominant (*i.e.* around buildings) [RVF$^+$98]. In this case, the 3D scene can be amplified by a 2D scene in the horizontal plane. A horizontal 2D method was proposed and validated in [RWG97].
— **2D-V :** if the heights of the buildings in propagation scene are close to or less than heights of the transmitter and receiver, the over-rooftop contributions (*i.e.* rays in the vertical plane), become the most significant propagation mechanism [RVF$^+$98]. A well-known 2D method is the vertical plan launch (VPL), which was proposed in [LB98]. The VLP method uses a 2D horizontal ray tracing technique but each ray is represented by a vertical propagation plane to find the reflection and diffraction points as explained in [LB98].
— **2.5D :** this kind of methods uses a 2D model in the horizontal plane combined with another method in the vertical plane [Cor10].

2.7.2 Space Division

The main idea is to reduce the number of objects for which the intersection tests are performed. To this end, the space is divided into cells using a 2D or 3D grid. The objects in the propagation environment are then associated with the corresponding cell(s). In the same manner, when a ray travels in the scene, it traverses the cells. Consequently, the intersection tests will only be conducted for a limited number of candidate objects.

There are many space division approaches : uniform space division is best adapted if the objects have relatively the same size and are uniformly distributed. Otherwise adaptive or non-regular space division would be more efficient. The most widely used non-regular space division methods are : triangular partitioning [YZI02, ZYI00], angular Z-buffer [SH10], k-d tree [WH06]. Similar to k-d tree, there are other partition approaches such as octree, quadtree, and binary space partition (BSP). They are used for the same purpose but they are simpler to implement [YI15].

2.7.3 Visibility Graphs

The idea of the visibility graphs is that the intersection test should only be conducted with objects where rays are most likely to intersect. The visibility graphs include many layers. The first level contains the visible objects to the transmitter. The next level contains the visible objects to first layer. Further levels are constructed in the same manner.

2.7.4 GPU Acceleration

Graphics processing units are special processing units that possess multiple cores operating in parallel. They are more efficient than the central processing units (CPUs) for parallelizable algorithms. GPUs have also been exploited to accelerate tracing algorithms. In [STW17, SRK$^+$09, SRK$^+$11], tracing methods are developed on a GPU leading to a significant time gain from minutes to seconds [YI15]. However, this kind of parallel algorithms needs high-level programming skills.

2.8 Formulation of the research problem

The research problem can be formulated from a technical perspective as : 'Empirical radio propagation models are very fast but they cannot guarantee the desired performance under high accuracy requirements. On the other hand, conventional deterministic radio models are impractical under strict time constraints. Between these two extremes, how to propose deterministic models that can guarantee a high degree of accuracy in as little time as possible to be able to support large-scale wireless sensor networks, possibly including mobile nodes'.

2.9 Proposed Solution

As a matter of fact, the project "PERSEPTEUR" necessitates precise radio propagation model that respect the specificity of the propagation scene. Therefore, only site-specific models will be considered. The two deterministic families have already been presented. Since the ray-tracing methods are computationally more efficient than the rigorous numerical solutions,

the ray-tracing option will be considered. Still, full 3D ray-tracing models are computationally inefficient and the cannot satisfy the project requirements with regard to execution time. A number of acceleration strategies will be used and new acceleration techniques adapted to WSNs will also be proposed.

In fact, knowing the dominant propagation aspects for the targeted environments is the key element in developing efficient deterministic radio models because it helps in proposing the most realistic approximations and the best acceleration techniques. Risk et al. [RVF+98] compared between three propagation modes. Using the same terms, they are defined as :

Lateral propagation : When the buildings are much higher than the transmitter and receiver heights. The propagation occurs mainly in the horizontal plane around the buildings. Lateral propagation involves a combination of multiple reflected rays and diffracted rays from the buildings' vertical edges.

Vertical plane propagation : When the buildings heights are comparable or lower than the transmitter and receiver, over-roof diffracted rays become significant so they can contribute largely to the total field. In the regions far from the transmitter, over-roof multiple diffraction becomes the dominant mechanism.

Full 3D : It includes the lateral propagation as well as the rays diffracted from rooftops and their combinations.

WSN protocols for smart cities were classified (*cf.* section 1.4) into categories. From the radio point of view, the dominant propagation contributions are different for each category. Accordingly, the research problem is split into two parts, each of them will be treated differently :

— Short Range Communication protocols such as ZigBee and its competitors are characterized by their low transmit power and low antenna heights, which implies that the propagation occurs mainly in the horizontal plane within a limited radio range. Consequently, the proposed solution is based on a ray-tracing method that integrates novel optimization and acceleration strategies to find the best time-accuracy trade-off. A plan of the proposed solution for the horizontal plane is depicted in figure 2.20 and will be discussed thoroughly in chapter 3.

— Low-Power Wide-Area Network (LPWAN) protocols such as SigFox and Lora have a large link budget ($\approx$ 160 dB) and they were designed to cover wide areas (a few km in urban areas and more in rural areas). Therefore, rooftop diffraction is the dominant mechanism. Hence, another deterministic radio propagation model in the vertical plane that integrates novel optimization and acceleration strategies will be proposed. This will be covered thoroughly in chapter 4.

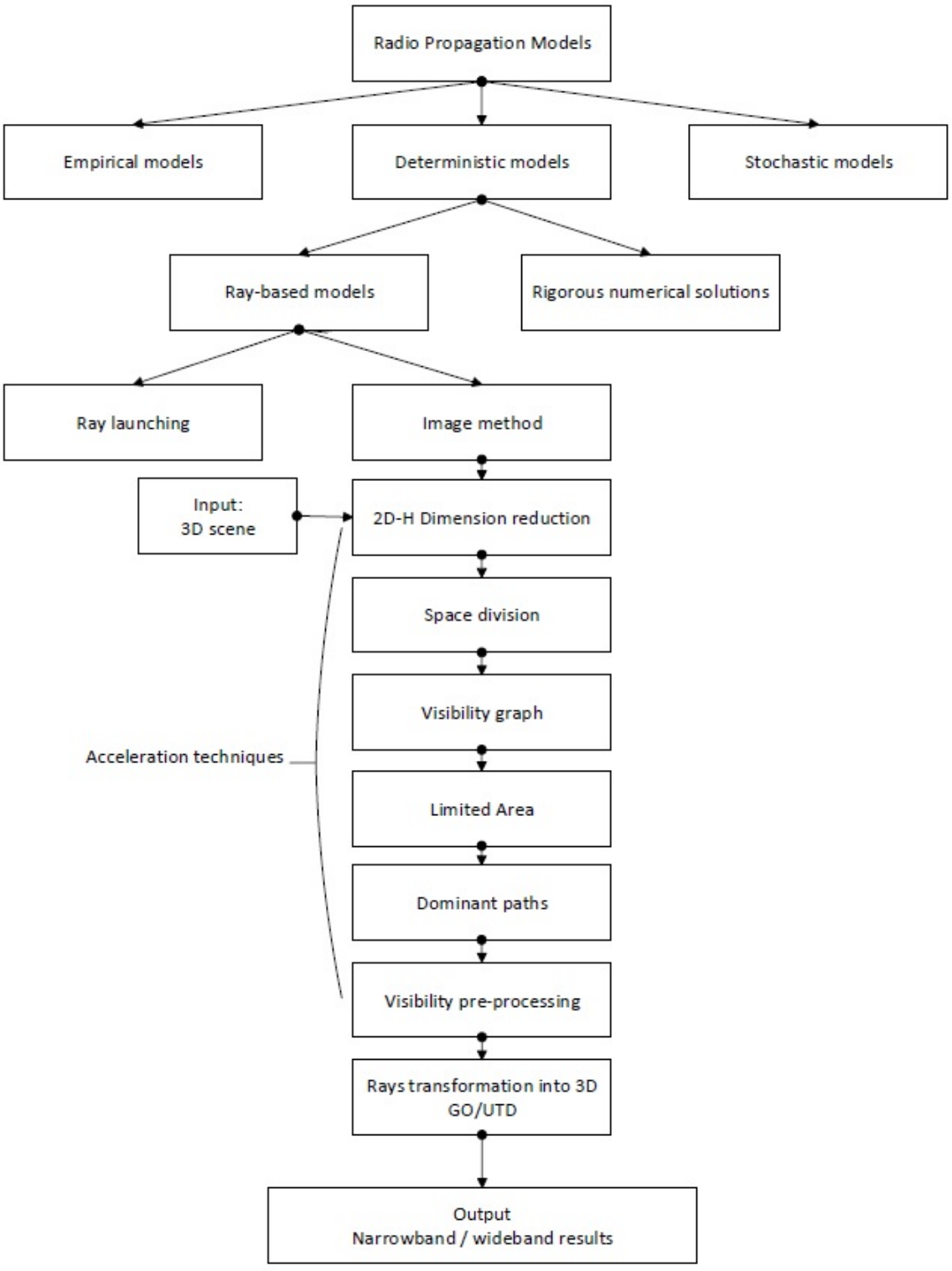

Figure 2.20 – *Proposed solution in the horizontal plane.*

2.10 Conclusion

The radio propagation channel is an unavoidable element in any wireless systems. Signals passing via the radio channel are subjected to impairments and perturbations introduced by the channel. Knowing the channel characteristics is an important element in system design. Four principle interactions encounter the radio wave : reflection, diffraction, transmission, and scattering, this leads to the reception of a set of different paths.

The radio channel is modeled mainly with empirical or deterministic models. An overview of several empirical models for WSNs was provided. They are very fast but they could provide inaccurate results. On the other hand, deterministic modeling was proven to be precise but computationally expensive. Two families of deterministic modeling were presented : models based on ray tracing techniques and other models based on rigorous numerical solutions to Maxwell's equation. Ray tracing techniques are more time-efficient, but still, they are not applicable to the application that needs fast computational times. Many acceleration strategies were suggested to that end. Some of them will be adopted and novel techniques will be proposed in the following chapters to provide fast deterministic models in the horizontal plane and in the vertical plane.

Chapter 3

Visibility tree and acceleration techniques

Contents

3.1 Introduction

The two previous chapters addressed many aspects, mainly the project context, relevant literature, research problem, a proposal and a road map to satisfy the project specifications in the best possible way. Within this road map, chapter 3 will focus on radio modeling in the horizontal plane using the visibility technique along with new innovative techniques in order to accomplish the desired objectives. To this end, chapter 3 will discuss three key issues that are organized as follows :

Implementation phase :

This phase describes the fundamental concepts of the visibility technique and then it illustrates the algorithms that are needed to implement a ray-tracing propagation model based on this technique in an efficient way. The implementation process will be described starting from the first stages of defining the propagation scenes up until the final phases *i.e.* the construction of propagation paths and electrical field computation.

Validation phase :

Model validation was performed against a standard 3D ray-tracing tool and then against a narrow-band measurement campaign that was conducted in an urban configuration. Within the validation phase, model performance will be evaluated in terms of accuracy as well as in terms of execution time through several test scenarios in order to prove that visibility technique can reduce the execution time without introducing loss in accuracy.

Acceleration phase :

After the validation process, new several techniques will be integrated into the visibility-tree based ray-tracing model to further accelerate the simulations. These acceleration techniques will be based on simple hypotheses, then different algorithms will be implemented in order to test the validity of these hypotheses. The validity tests are conducted through several case studies in different urban configurations. Furthermore, the studies will evaluate the impact of these techniques on both accuracy and execution time. On the other hand, other parametric studies are carried out within this phase to evaluate the effect of the number of interactions on various important parameters such as accuracy, time execution, and coverage percentage. These studies provide guidelines on the optimal number of interactions according to the degree of precision required for a certain application and according to the available time resources.

3.2 Input Data Bases

3.2.1 Description of the propagation environment

Ray-tracing algorithms need a detailed geometric description of the propagation environment, it needs also information about the type and position of the transmitter and receiver antennas. The geometric description of the propagation scene could be taken directly from a GIS file (Geographic Information System). However, many ray-tracing software tools define

their own format, hence the description needs to be converted into the format that is supported by that tool. It is important to underline that the proposed models were integrated into a ray tracing tool developed by XLIM research institute. Hence, the proposed models will use the same file format in which the geometric description is defined in an XML file format, as well as transmitters and receivers as follows :

— **Transmitters and receivers :** a list of all transmitters and receivers with their positions (x, y, z), antenna type (which specifies the antenna radiation pattern), polarization, and orientation.

— **Buildings data base and electrical properties :** buildings are defined as horizontal 2D polygons by a set of 2D vertices (x_1, y_1), (x_2, y_2), ... , (x_n, y_n). Heights are then added to create a 3D city model. In addition, permittivity and conductivity values are specified for each building. These values are needed for the physical models that calculate the electric field. Buildings are defined in the following manner :
<building>
<epsilon>9.0</epsilon>
<sigma>0.001</sigma>
<height>017.00</height>
<outline>165.00 009.00 189.00 009.00 188.00 027.00 0164.00 025.00</outline>
</building>

3.2.2 Description of test scenes

In fact, test and validation process is an important step to ensure that each phase is working properly. All the test scenarios that will be used throughout this chapter are based on 3 realistic propagation environments as shown in figure 3.1. The test scenarios are used for illustrating different algorithms and for model validation. In fact, the complexity of a scene is determined mainly by the level of detail that it considers (*e.g.* number of buildings, faces, and edges). The three test propagation scenes have different degrees of complexity as follows :

Environment 1 - Simple 5-building scene : a simple test scenario containing 5 rectangular buildings with different heights as shown in figure 3.1(a). It contains only a limited number of objects (26 faces and 40 edges). This scene will be used for describing and validating different steps such as horizontal profile extraction, discretization, visibility tree technique, searching for the propagation paths, *etc.*

Environment 2 - Campus, University of Poitiers : a relatively simple real test scenario of the University of Poitiers campus as shown in figure 3.1(b). It contains a reasonable number of objects (549 faces and at least 850 edges). This scene will be used for model validation by comparing the proposed models with a full 3D ray-tracing model.

Environment 3 - Charles de Gaulle - Étoile : a scene that models a neighborhood in downtown Paris as shown in figure 3.1(c). It contains a considerable number of objects (10330 faces and about 15504 edges). A field measurement campaign was conducted by France Telecom R&D for this scene. For this reason, it will be used for model validation and perfor-

mance evaluation by comparing the proposed model with the field measurements.

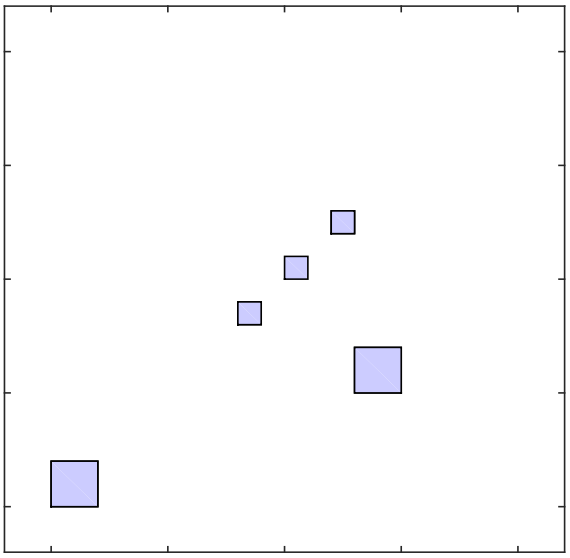

(a) *Environment 1 : Simple 5 building-scene.*

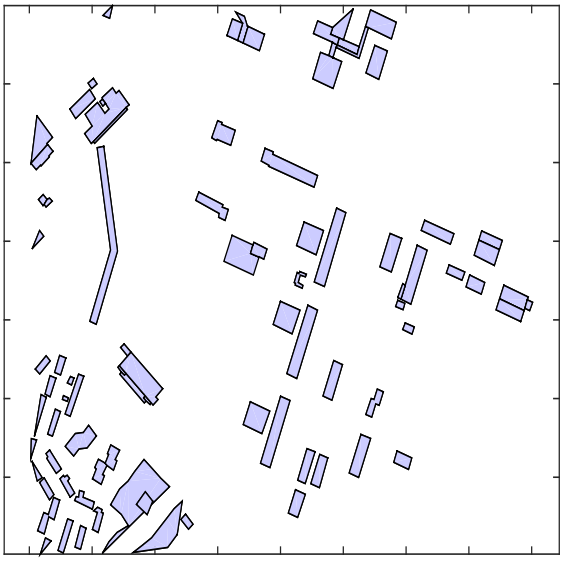

(b) *Environment 2 : Campus, University of Poitiers.*

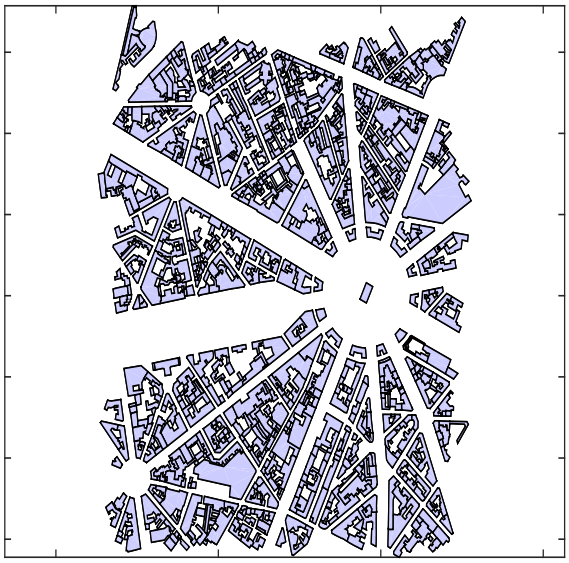

(c) *Environment 3 : Charles de Gaulle - Étoile, Paris.*

Figure 3.1 – *Considered urban environments.*

3.3 Ray-tracing based on the visibility tree

As mentioned previously, a ray-tracing model based on the visibility technique in the horizontal plane is the main building block of the proposed solution. Therefore, the next subsections will discuss the principle of this technique and how it can be used to find the propagation paths in an accurate and fast way.

3.3.1 Creation of a horizontal 2D visibility tree

3.3.1.1 Principle and data structure

The idea is to calculate the visibility relations between a given transmitter and the objects in the propagation environment in a hierarchical manner according to the nature of the propagation phenomena. The idea itself appears fairly simple but an efficient implementation of a hierarchical visibility structure necessitates specific techniques that will be explained briefly, further details are given in [CAVP06, ACVM03, Com04a].

In fact, the visibility relations are calculated for a given number of propagation phenomena called interactions (*i.e.* reflections, diffraction, and transmissions) from a reference point which is the transmitter position. These relations need to be processed in an optimized data structure. One of the best data structure candidates is the tree structure, because it is very easy to move up through the nodes until the root node, which means that history of each branch is known and consequently the intersection tests will be conducted for only the concerned objects (faces or edges) and in the right order. Figure 3.2 shows the adopted tree structure, which is composed of :

— Self : a node that represents a geometric 2D zone computed according to a specific interaction. This node contains all the geometrical data that will be needed for finding propagation paths between the receiver and transmitter (*e.g.* faces, edges, *etc*). Furthermore, the self-node is connected to a parent, a sibling, a child as described just after.
— Parent : a node that is one upper step in the hierarchy, from which the self-node was originated.
— Sibling : a node that shares the same parent, because all siblings are originated from the same node.
— Child : a lower-level node that is generated from the self-node.

It is important to note that the parent, sibling, and child nodes are, at the same time, self-nodes (*i.e.* they have their own parents, siblings, and children).

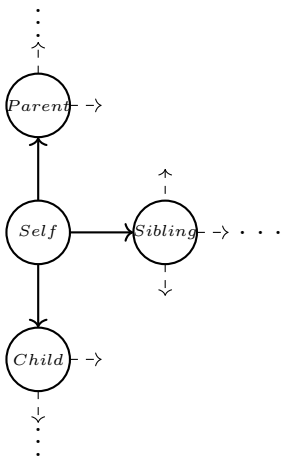

Figure 3.2 – *Tree structure.*

Accordingly, the visibility tree technique can be defined as an algorithm that starts from a transmitter T_x to construct a tree in such a way that the root node corresponds to the transmitter, the first level of the tree represents the visible zones to the transmitter, and the next level consists of new spatial zones that have been generated from the previous level by a propagation phenomena (reflection or diffraction) and so on. The creation of a complete visibility tree will be explained in the next subsections by an example describing the algorithms from the first steps until the final stages for the propagation scene shown in figure 3.1(a).

3.3.1.2 Horizontal plane profile from a 3D city map

It has been illustrated that for short-range communication protocols, propagation occurs mainly in the horizontal plane while the contribution of the vertical propagation is less important because the buildings are high as compared to the antennas' height. Therefore, the dimension reduction technique will be used to exploit this fact, which will significantly reduce the complexity of the propagation scene from a 3D to 2D one. This leads, in turn, to considerably reduce the computational costs.

Consequently, the very first step of the visibility algorithm is to extract a 2D horizontal cross-section of the 3D propagation environment at a specific height. In order to include all the buildings, the horizontal profile is extracted at ground level. Figure 3.3 shows the dimension reduction process where it depicts the propagation scene in 3D (figure 3.3(a)) and the corresponding 2D layout (figure 3.3(b)).

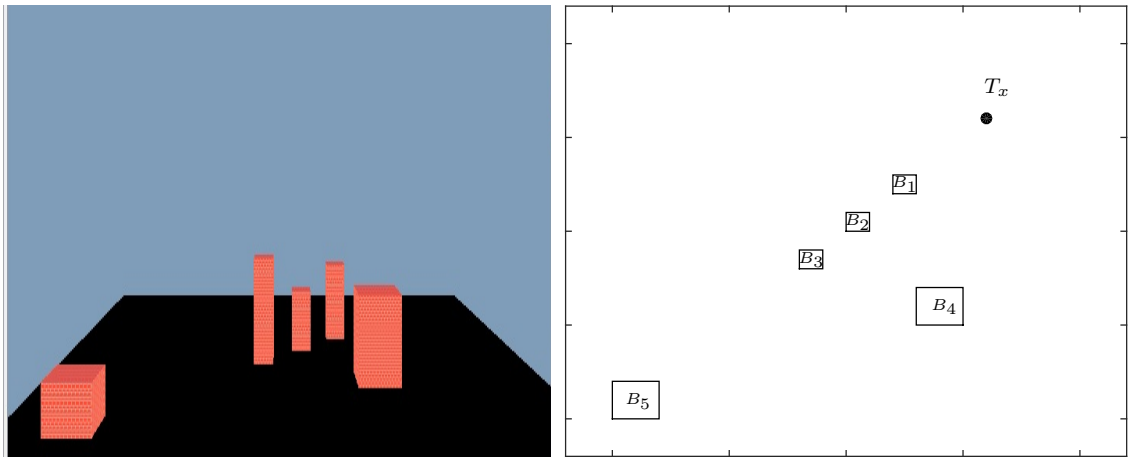

(a) *Environment 1 : simple scene in 3D.* (b) *Environment 1 : simple scene in 2D.*

Figure 3.3 – *Dimension reduction.*

3.3.1.3 Initialization of the visible zones

After extracting the 2D layout of the propagation environment, the algorithm assumes initially that the whole propagation scene is visible without considering any obstacle. As shown in figure 3.4, the visibility algorithm starts from the transmitter position T_x to create four visible zones (*i.e.* nodes) V_1, V_2, V_3, and V_4 from the transmitter T_x to the corner points of the scene. The five buildings of the scene B_1, B_2, ..., and B_5 were initially ignored. It is

worth mentioning that from a programming point of view, the zones are defined as geometrical shapes having only three or four vertices.

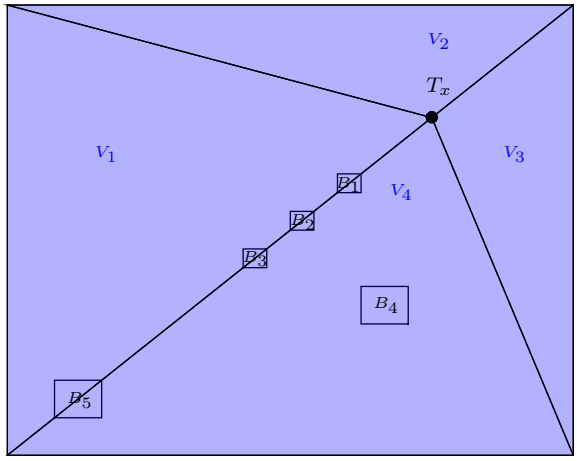

Figure 3.4 – *Initial visible zones.*

The assumption that the whole scene is visible from the transmitter was just an initialization step to set up the starting point of a recursive algorithm aiming to find the real visible zones. Therefore, the next step is how to divide the four initial zones according to the obstacles in such a way that the zones are delimited by the edges of the buildings. A trivial way to that is to perform an intersection test for each zone with every single edge in the 2D propagation scene. This way is a time-consuming process especially for complex scenes that could contain tens of thousands of edges with potentially tens of thousands of zones. A more efficient way is to use a space division strategy to reduce the number of intersection tests as explained in next subsection.

3.3.1.4 Space Division

As just mentioned, the objective of using space division techniques, is to reduce the number of tests. Space division solutions are based on discrete grids. Many space division techniques were discussed in chapter 2. A uniform 2D division of the environment (*i.e.* a 2D discrete grid) will be used for this purpose. Each grid cell is known as a pixel and is defined by a pair of integer coordinates (x, y). In discrete mathematics, geometric objects of the scene are associated with the pixels that intersect these objects. Similarly, spatial zones are represented by all the pixels that include these zones. To achieve this objective, two discretization algorithms are needed : line and zone discretization algorithms.

Line discretization :

Horizontal edges of the buildings need to be discretized on a 2D grid in an optimized manner. Many 2D discretization schemes for lines are found in the literature [BLV03] to convert line points $(x, y) \in \mathbb{R}^2$ into pixels $(P_x, P_y) \in \mathbb{N}^2$. Among these schemes, the super-cover discretization scheme seems to be the most suitable for this purpose because it includes even the ambiguous cases (*i.e.* when the line passes exactly through a point with integer coordinates, the super-cover scheme will include 2 pixels (if either x or y is an integer) or 4

pixels (if both x and y are integers). Mathematically, the super-cover method is defined by all the pixels $(P_x, P_y) \in \mathbb{N}$ that are satisfying the double inequation [CAVP06] :

$$-\frac{(\lfloor a \rfloor + \lfloor b \rfloor)}{2} \leq ax + by + c \leq \frac{(\lfloor a \rfloor + \lfloor b \rfloor)}{2} \tag{3.1}$$

where $(a, b, c) \in \mathbb{R}^3$ are the line coefficients, and $\lfloor\ \rfloor$ is the floor function. Figure 3.5 shows the simple 5-building scene along with its corresponding discretized scene.

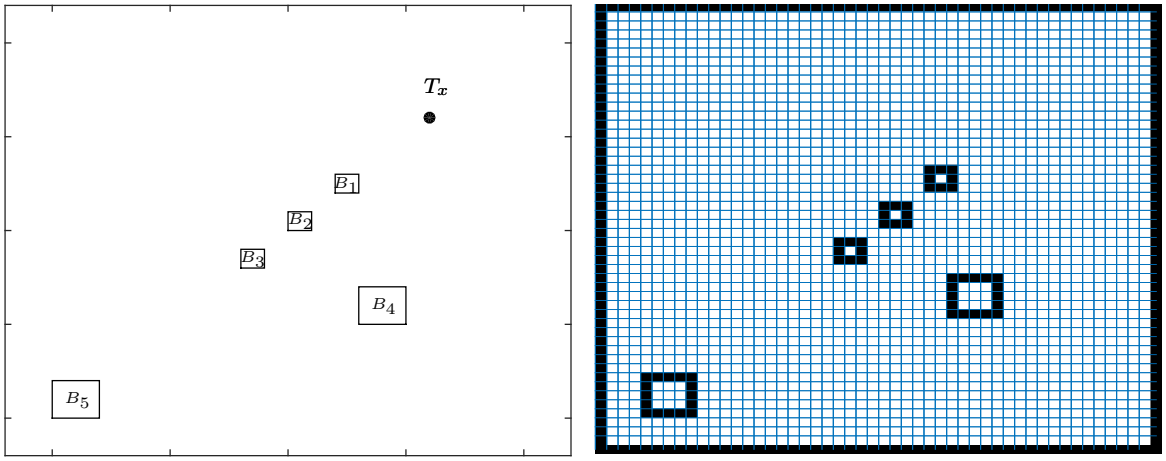

(a) *Environment 1 in 2D.* (b) *Environment 1 discretized.*

Figure 3.5 – *Line discretization.*

Zone discretization :

Like line discretization, the same uniform grid concept is used for zone discretization. It is nevertheless obvious that two issues arise at this stage concerning the zone discretization. Firstly, how to implement an optimal and fast method that does not miss any pixel (i.e. edge) inside the zone in question. Secondly, how to correctly determine the direction of discretization *i.e.* what is the best scan direction to find all the edges inside that zone.

Regarding the first issue, a memory-efficient data structure was proposed in [ACVM03, Com04b]. It is readopted in this algorithm since it is simple and efficient. It is simply a 1D array, the size of the array corresponds to the maximum number of pixels in the scan direction. Each element of this array contains only two integers, which are the end two pixels in the other direction (perpendicular to the scan direction). Using the described data structure, it is possible to scan the whole pixels that are found in the zone in question with only limited parameters (1D array and 2 integers for each array element). According to this algorithm, the 4 initial visible zones of figure 3.4 (without considering the obstacles of the propagation scene) were discretized as shown in figure 3.6. It is important to note that this is the same grid as shown previously in figure 3.5, that means that each pixel of this grid knows also if it contains any edges (if there are any !).

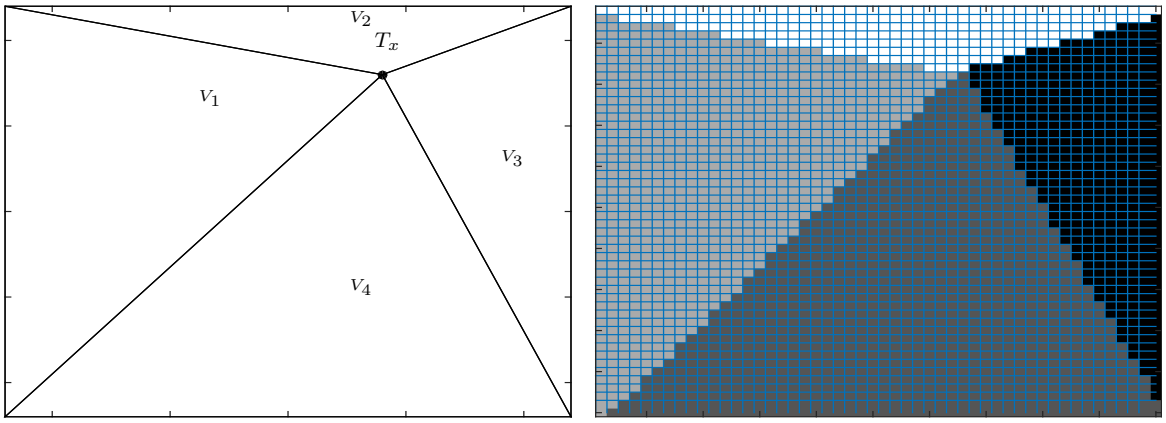

(a) *Initial visible zones.* (b) *Initial visible zones - Discretized.*

Figure 3.6 – *Zone discretization.*

On the second issue regarding the importance of the scan direction, the impact of the discretization direction is illustrated in figure 3.7, where figure 3.7(a) shows only one initial zone from the transmitter to the right scene corners. If the discretization algorithm scans the pixels from the farthest pixel of that zone to its source, it is very possible that the algorithm finds first the edges that are, most probably, shadowed by many other edges as shown in figure 3.7(b). Therefore, unnecessary subdivisions of the zones are noticed. On the other hand, scanning from the source to the farthest pixel guarantees that visible edges are firstly treated, so the final number of zones is optimal as shown in figure 3.7(c). It is shown that for this simple example, the algorithm will produce 9 zones instead of 3 zones according to the scan direction. Even worse, for more complex configurations the number of unnecessary subdivisions would be more significant. In fact, the advantage of reducing the number of zones is that it reduces considerably the size of the visibility tree which, in turn, reduces significantly the execution time for the next levels and it also reduces search complexity. Another advantage of reducing the number of zones is that it occupies less memory. Consequently, 4 privileged scan directions were defined [ACVM03] along x-axis or y-axis as follows : $x_{min} \rightarrow x_{max}$, $x_{max} \rightarrow x_{min}$, $y_{min} \rightarrow y_{max}$, and $y_{max} \rightarrow y_{min}$. In view of the importance of maintaining the minimum possible number of zones, another algorithm was also implemented to make sure that no more than one zone can share the same edge.

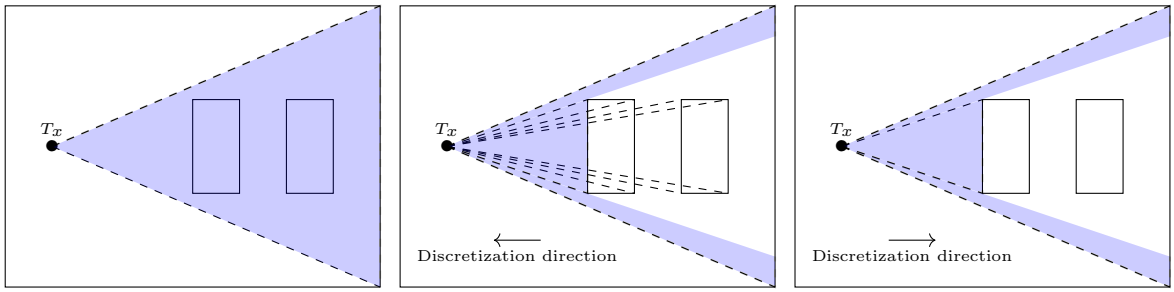

(a) *Initial visible zone.* (b) *Wrong discretization direction.* (c) *Right discretization direction.*

Figure 3.7 – *Discretization direction.*

3.3.1.5 Visible zones

At this stage, the scene edges and the four initial zones of figure 3.4 were discretized on the same grid. This means that each zone knows exactly the edges that are found inside it and in the right direction. Therefore, intersection tests will be limited to those edges instead of searching for all the edges in the scene, this leads to a considerable gain in time. Each one of the initial zones will perform a recursive algorithm to further divide the initial zones in accordance with the visibility rules. At the end of this process, nine visible zones (V_1, V_2, ..., V_9) were generated as shown in figure 3.8. Each zone is limited by an obstacle in such a way that no unnecessary subdivisions were generated.

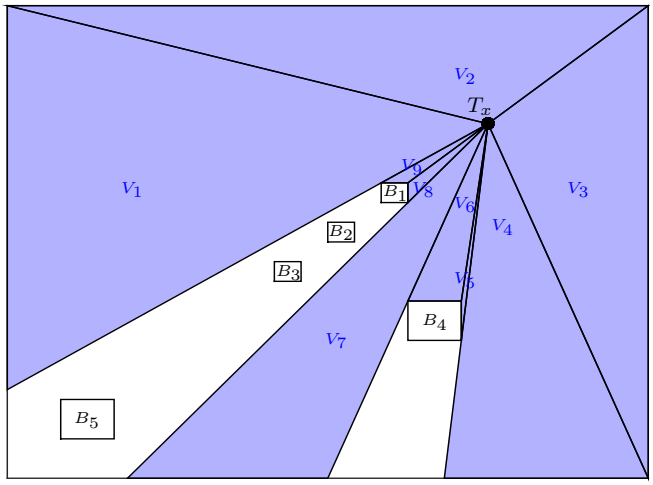

Figure 3.8 – *Visible zones.*

Each one of the visible zones will then be attached to the root node (the transmitter) to create the first level of the visibility tree as shown in figure 3.9. It is important to note that the used tree data structure was designed in a way that each node knows only one child node, one parent, and one sibling. This will not affect the search efficiency for the propagation paths in the final stages since in the search phase, the nodes will be only traced upwards, in addition, this also helps to minimize the memory occupation. Still, a parent node can know the other children nodes through the siblings of its unique child node but it is not needed for any phase the algorithm. The relations between the different nodes can be seen from the direction of the arrows of figure 3.9.

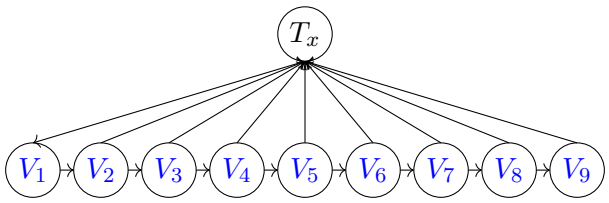

Figure 3.9 – *Visibility tree - layer 1 : visible zones.*

3.3.1.6 Reflected zones

For each zone of the first level of the visibility tree, if it encounters a face in the propagation scene, the algorithm generates the corresponding reflected zones. Figure 3.10 shows all the reflected zones that were generated from the visible zones (V_1, V_2, ..., V_9). To better understand how the reflection algorithm works, let us take an example of how the reflected zones R_2, R_3, R_4 and R_5 that were generated from the visible zone V_6. First, a virtual image of the transmitter with respect to the reflecting face of B_4 (the upper face) is located (T'_x). Then, an initial reflected zone is constructed from the virtual image and from the face of reflection (shown by the dotted zone). Finally, using the same procedure described earlier, this initial reflected zone is then subdivided according to the obstacles in that zone to obtain the real reflected zones R_2, R_3, R_4 and R_5. The same procedure is also applied to the other zones.

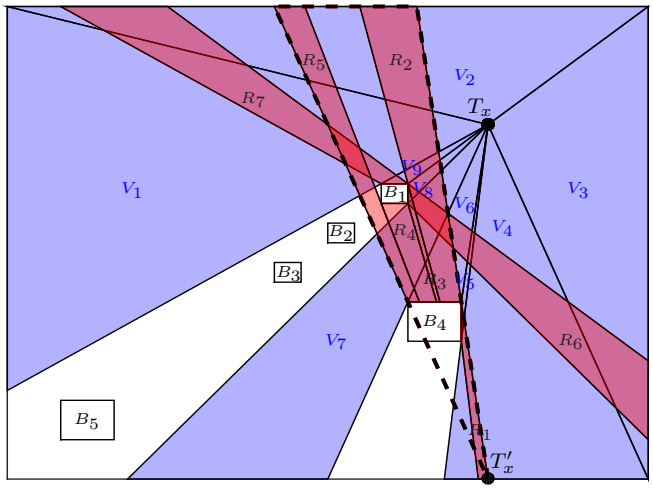

Figure 3.10 – *Reflected zones.*

Once the reflection process is finished, each reflected zone will be attached to its parent node (*i.e.* from which it was generated). Figure 3.11 shows the updated visibility tree after considering one reflection. It important to underline that these nodes contain all the information, which will be needed later on for tracing the propagation paths, such as zones boundaries, reflecting face, the image of the source with respect to that face, its parent node, *etc.*

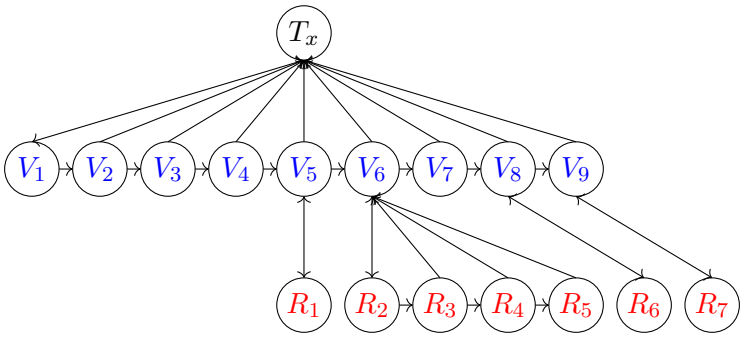

Figure 3.11 – *Visibility tree - with reflection.*

3.3.1.7 Diffracted zones

As regards the diffraction, if any visible zone encounters a vertical diffracting edge in the propagation scene, the algorithm generates the corresponding diffracting zones. In fact, the diffracted zones in a 2D configuration do not depend on the direction of the incident ray because diffracted rays are produced by a ray normally incident on the diffracting edge so the Keller cone becomes simply a plane as shown in figure 3.12.

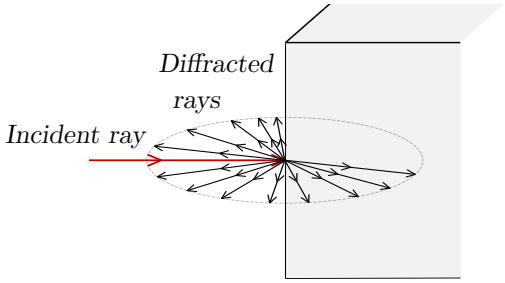

Figure 3.12 – *Keller cone in 2D.*

Returning to the previous example, each corner of the five building is a diffracting edge but for the sake of brevity only one diffracting point P will be treated as shown in figure 3.13. In fact the diffracting zones D_1, D_2, ..., and D_6 were generated using the exact same procedure described earlier. That is to say, four initial zones from the diffracting point P were generated, and then by using the recursive subdivision procedure, the final diffracting zones were obtained (*i.e.* D_1, D_2, ..., and D_6).

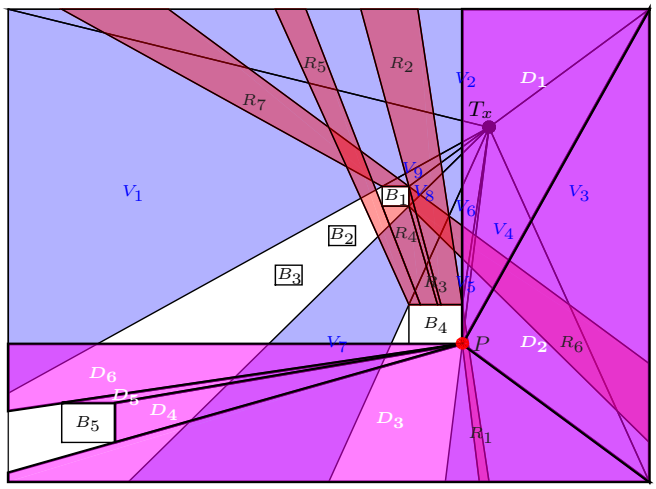

Figure 3.13 – *Diffracted zones.*

Once the final diffracted zones are identified, each diffracted zone will be attached to its parent node. Figure 3.14 shows the updated visibility tree after considering one reflection and the diffraction at point P. Like the reflected nodes, the diffracted nodes contain also the information that will be required to trace the path trajectories such as the diffracting edges.

The other diffracting points are treated in the same manner as point P and then attached to their parent nodes (not shown in figure 3.14). Then, the next levels of the tree are generated by repeating the same procedure until the maximum number of required interactions is reached.

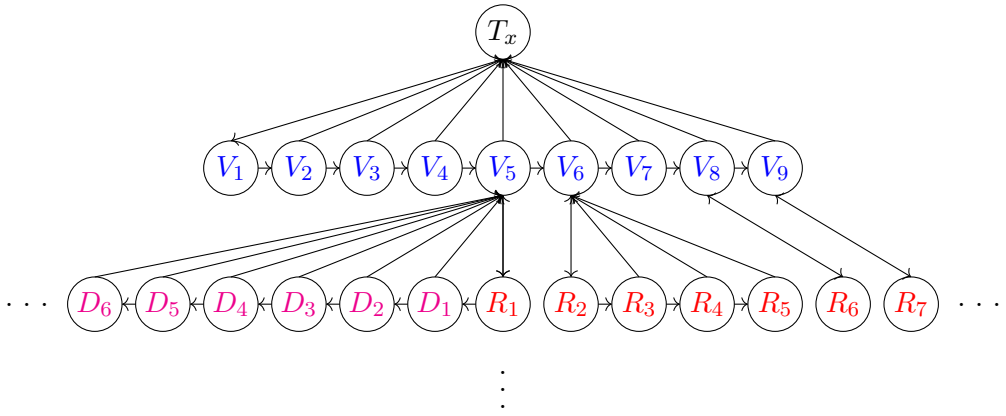

Figure 3.14 – *Visibility tree - with reflection and diffraction at the point P .*

3.3.2 Calculating propagation paths from a visibility tree

3.3.2.1 Propagation paths in the horizontal plane

At this level, the visibility tree is calculated for a certain number of interactions. The next step is, therefore, how to exploit this tree to find all the paths that can be received at the reception point. In order to do that, it is needed first to identify all the nodes (*i.e.* the zones) that include the receiver because each node including the receiver corresponds to a potential geometrical path between the transmitter and receiver. Two approaches can be used to identify the nodes that include the receiver :

Trivial method :

It goes simply through all the nodes of all the levels of the visibility tree to determine if they include the receiver. This trivial solution is efficient only for simple scenes where the number of nodes/zones is limited. However, for complex scenarios with a relatively large number of interactions, an enormous number of zones will be generated (could reach several hundred thousands of zones). Hence, it will be a very time-consuming procedure to perform an exhaustive inclusion test for every single zone. Consequently, a more efficient method is required.

Optimized method :

It has been proven in [ACVM03, Com04b] that more efficient results in terms of execution time can be obtained if a new 2D grid is used in such a way that each pixel of this grid contains a list of all the nodes (*i.e.* zones) that intersect that pixel. This means that two elements are needed. Firstly, the same zone discretization algorithm that was used previously to discretize the zones of the nodes. Secondly, a new 2D grid to associate the tree nodes to the corresponding pixels of this new grid.

As a matter of fact, the objective of using this new grid is for the same reason as the other grids, *i.e.* to reduce the number of inclusion tests. The concept can be better illustrated through the same example as before. Figure 3.15 shows a number of zones (9 visible zones : V_1, ..., V_9 ; 7 reflected zones : R_1, ..., R_7 ; and 6 diffracted zones : D_1, ..., D_6 (for the sake of simplicity, diffracted zones were only shown for one edge (P)). Let us consider the receiver R_x as shown figure 3.15. Instead of conducting inclusion test for more than 20 zones (for this simple configuration, with a limited number of interactions, and without considering all the diffracted zones), the test is conducted only for a very limited number of zones that are found in the pixel containing the receiver. The zoomed portion of the image shows that the pixel containing the receiver includes only four zones, namely V_3, V_4, R_6, and D_2. Therefore, the inclusion test is conducted with only these zones to identify the zones that contain really the receiver, which are V_3, R_6, and D_2.

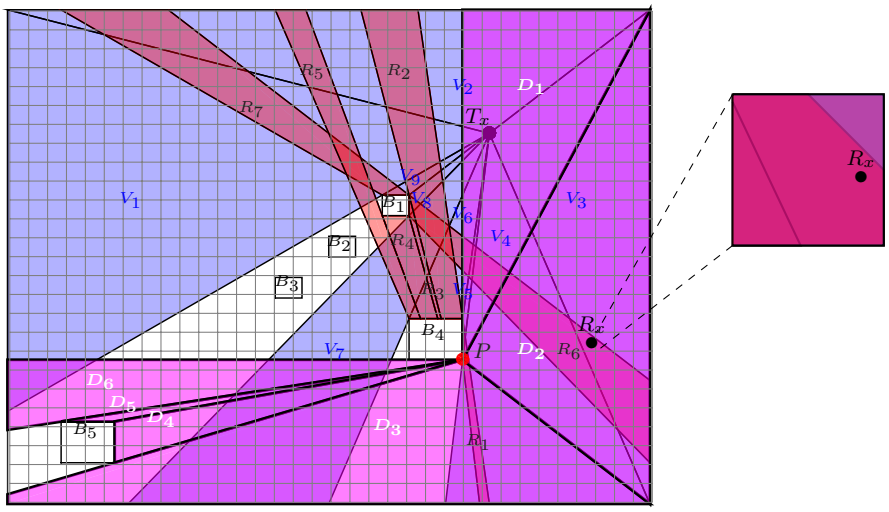

Figure 3.15 – *Diffracted zones.*

Once this process of node identification is finished, the nodes containing the receiver are known as shown in figure 3.16. Consequently, another process is required to go up through

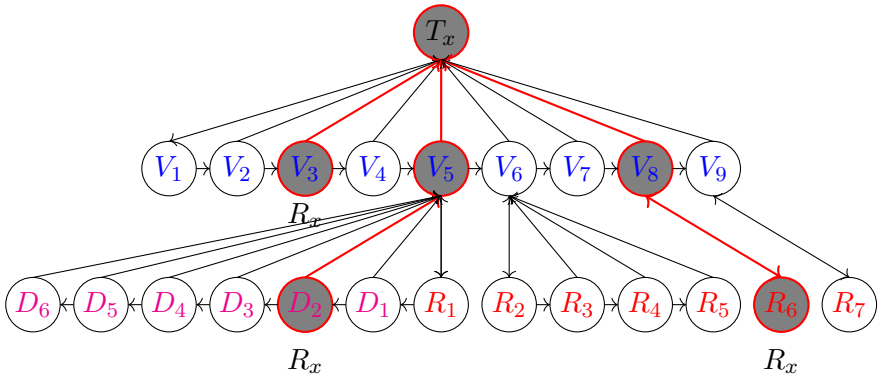

Figure 3.16 – *Visibility tree - nodes including the receiver .*

each identified branch until the root node to find the received paths. In fact, each branch corresponds to a potential geometrical path between the transmitter and receiver. Furthermore, each node stores all the necessary information to construct the received paths (nature of node : reflection or diffraction, object : face or edge, zone boundaries, zone source, *etc.*). Possessing this information from the receiver node up to the transmitter node and in the right order is the key advantage of the visibility tree technique which is the source of the significant gain in term of execution time. Since Rx is included in these zones V_3, R_6, and D_2, three paths (direct, reflected, and diffracted paths) can easily be identified. These paths are constructed in 2D by the source image techniques as shown by red dotted lines in figure 3.17, they are constructed quickly because the order, the type of the interactions, and the objects that generated these interactions are known.

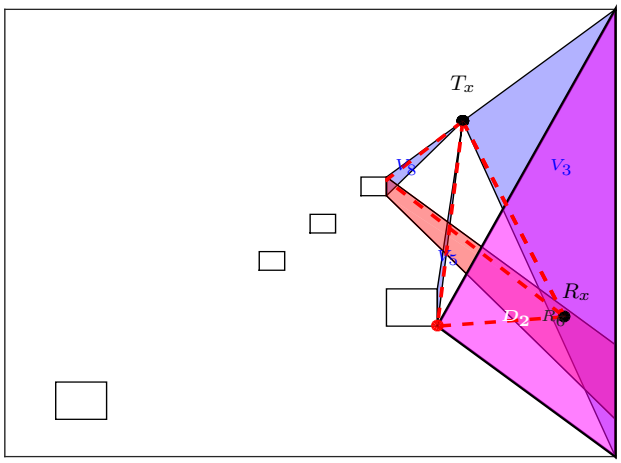

Figure 3.17 – *Zones including the receiver* R_x.

An interesting question that arises is : what is the best pixel size that can provide optimum performance in terms of execution time ? It is not possible to give the sole answer for all configurations, however, in order to find the best answer to this question in general configurations, a complex scene with a relatively reasonable number of interactions is used to precisely assess the impact of the grid resolution.

In fact, pixel size has two contradictory effects on the execution time. To illustrate this point, figure 3.18 shows that for large pixels, zone discretization and association process will be performed quickly but each pixel will contain a long list of candidate zones, which increases the research time (inclusion test time). On the other hand, for the small pixels, zone discretization will take more time but each pixel will contain a limited list of candidate zones, which reduces the research time (inclusion test time). Generally, a range of 5 - 15 m was found to give an optimal range of pixel size for any configuration.

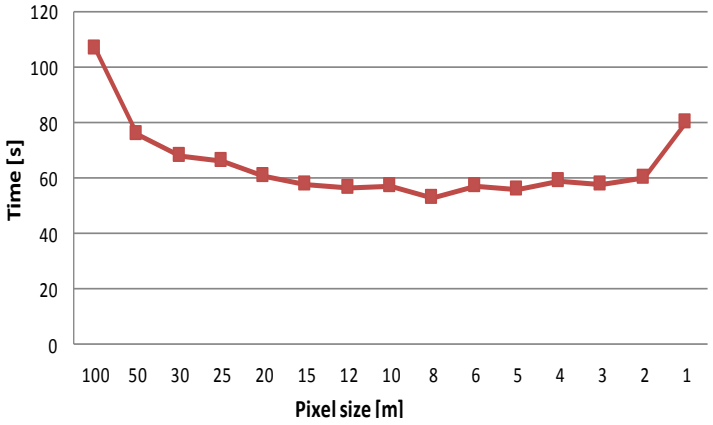

Figure 3.18 – *Grid resolution impact.*

3.3.2.2 Propagation paths in 3D

Up until now, all the propagation paths are found in 2D. However, these paths still need to be transformed into 3D paths. These paths already satisfy the laws of geometrical optics for reflection and diffraction in 2D, hence the paths already have the right coordinates in the x-y plane. However, the paths' trajectories on the z-axis need to be adjusted in order to transform the paths into 3D paths. To achieve this, a simple algorithm was implemented to satisfy Fermat's principle of least time which states that *rays always follow the path that takes least time*. This principle can be satisfied by considering the exact antenna heights of the transmitter and receiver, and then by using simple right triangle formulas to adjust the intermediate reflection and diffraction points through the path. Equation 3.2 and figure 3.19 illustrate this procedure of adjusting the reflection point P. The same procedure still applies for multiple intermediate points of reflection and diffraction.

$$h_p = d_1 \frac{h_r - h_t}{d_1 + d_2} + h_t \tag{3.2}$$

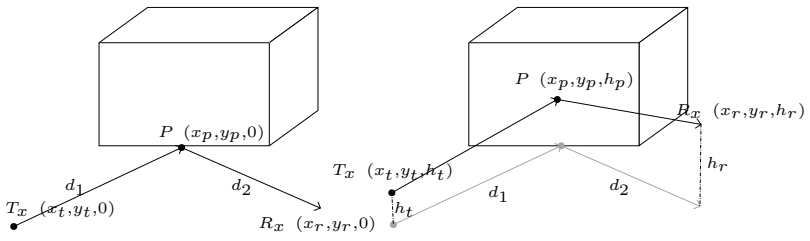

Figure 3.19 – *Paths transformation into 3D.*

Returning to the previous example that has been taken throughout the previous sections (sections 3.3.1 and 3.3.2), all the propagation paths are first found in 2D as shown in 3.20(a) for 1R1D, then the paths are transformed into 3D paths as shown in 3.20(b) using the procedure described above.

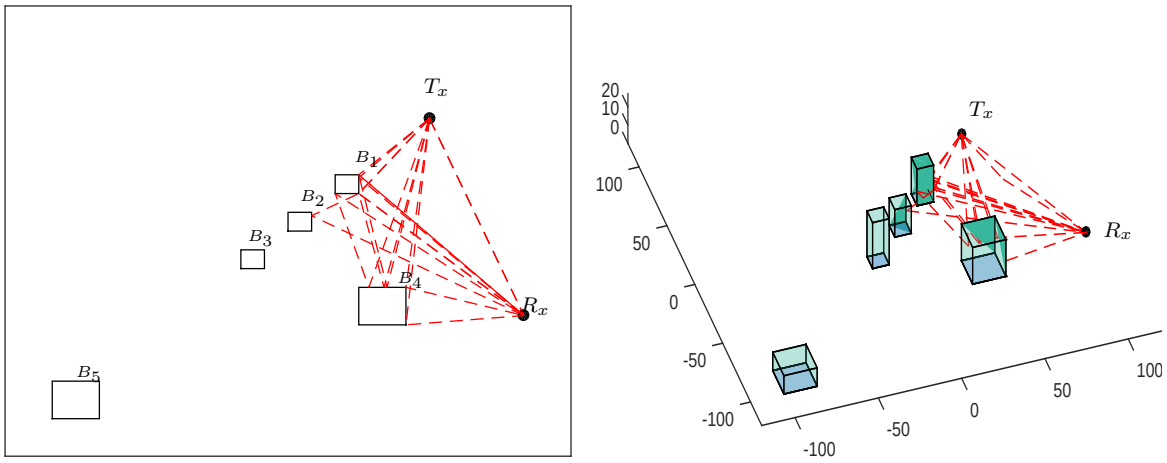

(a) *Paths in 2D.* (b) *Paths in 3D.*

Figure 3.20 – *Paths transformation into 3D.*

3.3.2.3 Ground reflected path

The proposed model was further improved by introducing the ground reflected ray because it has a great impact especially in near ground scenarios [SKPP09b] (this issue will be addressed in section 3.4.1). Despite the fact that this model finds the paths in 3D, it cannot be considered as a full 3D ray-tracing model because it does not include the diffracted rays over the rooftops (horizontal edges).

3.3.2.4 Electric field Computation

At this stage, all the propagation paths are traced geometrically so the last step consists in translating each path into an electromagnetic field using physical models. Correspondingly, the calculation of rays contributions is based on the expressions that are defined by the GO and UTD. It is consequently possible to find at the reception point R_x the electric field carried by each path, the total electric field carried by all the paths, the channel impulse response, or the other wide-band channel parameters.

3.4 Model validation

Model validation is indispensable not just to ensure that the proposed model is working properly, but also to estimate the global performance of the proposed model in terms of accuracy and execution time. Two-step validation process is conducted :

— Punctual model validation (*i.e.* point to point) based on model comparisons with a standard 3D full ray-tracing tool).

— Global model validation based on model comparisons with field measurements.

3.4.1 Punctual validation with a standard 3D full ray-tracing tool

This validation process is based on several test scenarios conducted in the Campus scene of the University of Poitiers that was described in subsection 3.2.2. Single\multiple reflection and diffraction interactions will be considered for the validation. The objective of these point

to point tests is to ensure that the proposed model (compared to a full 3D ray tracing model) is capable of providing all the paths in the horizontal plane, and that the missing paths are only the paths that are in the vertical plane.

3.4.1.1 Reflection

Two test scenarios were conducted to evaluate the model behavior with respect to reflection. The first test scenario is conducted without considering the ground reflection, while the second test scenario integrates the ground reflected ray in order to evaluate the impact of this ray. The test was conducted in the Campus scene where the transmitter and receiver were placed in a direct line-of-sight (LOS) configuration at a distance of about 100 m as shown in figure 3.21 (shown with some reflected rays). The test parameters of the two scenarios (with and without the ground reflected ray) are as follows :

— Frequency = 2.4 GHz.
— Different Transmitter\Receiver heights.
— Considered interactions : 1R, 2R, and 3R.

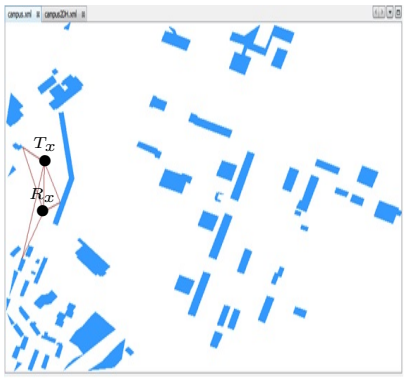

Figure 3.21 – *Punctual model validation - Reflection.*

Table 3.1 shows the simulation results for the first test scenario. It gives a comparison between the proposed model (without considering the ground-reflected ray) and a standard full 3D ray-tracing model (Full 3D RT model). The comparison is conducted in terms of the predicted attenuation between two points, these values can also be regarded as the received power $P_{r[dBm]}$, since the transmit power $P_{t[dBm]}$ is equal to 0 dBm : (ignore the antenna gain is for the moment $\Rightarrow P_{r[dBm]} = P_{t[dBm]} - Att_{[dB]} \quad \Rightarrow \quad P_{r[dBm]} = -Att_{[dB]}$). It can be seen from table 3.1 that in the case of one reflection, 4 paths are obtained by the proposed model *vs.* 5 paths by the full RT model. In fact, the 4 obtained paths are exactly the same as those obtained by the by the full RT model. Furthermore, the missing path is the ground reflected path. Despite the fact that only one path is missing in the case of 1R, this path is still significant ($0 \sim 4$ dB deviation from the full 3D model). For multiple reflections (2R and 3R), the missing paths are the ground reflected path and the ground-wall reflected paths. Although the number of missing paths in the case of multiple reflections is more than those for one reflection, almost the same range of error is noticed ($0 \sim 4$ dB deviation from the full 3D model).

No. of interactions	Transmitter height\ Receiver height	Proposed RT model (without GR)	Full 3D RT model
1 R	**No. of paths**	4	5
	$h_t = h_r = 1.0\,m$	79.79 dB	78.21 dB
	$h_t = h_r = 1.5\,m$		74.94 dB
	$h_t = h_r = 2.0\,m$		76.77 dB
2 R	**No. of paths**	6	10
	$h_t = h_r = 1.0\,m$	80.69 dB	80.81 dB
	$h_t = h_r = 1.5\,m$		76.47 dB
	$h_t = h_r = 2.0\,m$		77.57 dB
3 R	**No. of paths**	7	13
	$h_t = h_r = 1.0\,m$	81.15 dB	81.72 dB
	$h_t = h_r = 1.5\,m$		76.95 dB
	$h_t = h_r = 2.0\,m$		77.90 dB

Table 3.1 – *Model validation - Reflection without ground reflected ray.*

The second reflection test scenario includes the ground reflected ray to assess if the error is mainly caused by the simple ground reflected ray and also to assess to what extent the other ground-wall combinations contribute to the total field. It can be seen from table 3.2 that in the case of one reflection, the exact paths are traced, and hence the same values are obtained. For the case of multiple reflections, the missing paths are the ground-wall reflected paths. They are less significant than the ground reflected ray as it can be seen from the range of error ($0 \sim 2$ dB deviation from the full 3D model). The error becomes more significant as the nodes approach the ground. Given the severe constraints on time, the proposed model includes only the ground reflected ray since the margin of error is within a tolerable range.

No. of interactions	Transmitter height\ Receiver height	Proposed RT model (with ground reflection)	Full 3D RT model
1 R	**No. of paths**	5	5
	$h_t = h_r = 1.0\,m$	78.21 dB	78.21 dB
	$h_t = h_r = 1.5\,m$	74.94 dB	74.94 dB
	$h_t = h_r = 2.0\,m$	76.77 dB	76.77 dB
2 R	**No. of paths**	7	10
	$h_t = h_r = 1.0\,m$	78.17 dB	80.81 dB
	$h_t = h_r = 1.5\,m$	75.31 dB	76.47 dB
	$h_t = h_r = 2.0\,m$	77.90 dB	77.67 dB
3 R	**No. of paths**	8	13
	$h_t = h_r = 1.0\,m$	78.35 dB	81.72 dB
	$h_t = h_r = 1.5\,m$	75.55 dB	76.95 dB
	$h_t = h_r = 2.0\,m$	77.97 dB	77.90 dB

Table 3.2 – *Model validation - Reflection with ground reflected ray.*

3.4.1.2 Diffraction

Two test scenarios were conducted to evaluate the model behavior with respect to the diffraction. Figure 3.22 shows the first test scenario in the Campus scene with the following configurations and parameters :

— Distance $d(T_x, R_x)$ = 100 m.
— Direct line-of-sight (LOS) at 2.4 GHz.
— Considered interactions : 1D, 2D, and 3D.

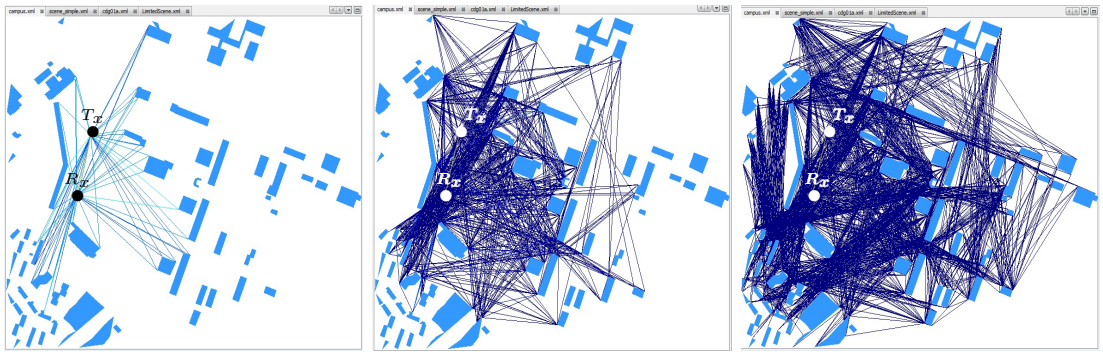

(a) *Campus scene - 1D.* (b) *Campus scene - 2D.* (c) *Campus scene - 3D.*

Figure 3.22 – *Model validation - Diffraction.*

Table 3.3 shows the results obtained for the first test scenario that is shown in figure 3.22. Generally, the proposed model provides the same performance in LOS configurations as the full 3D ray tracing model with regard to the diffraction phenomena. Despite a large number of missing over-rooftop diffracted paths (between the proposed RT model and the full 3D RT model in the case of 2D and 3D), the two models are providing the same performance mainly for two reasons : firstly, in LOS configurations the direct path is predominant so the missing over-rooftop diffracted paths are much less significant, and secondly a large number of the rays have undergone diffraction at more than one edge which means that they can be neglected (very attenuated). Consequently, the main conclusion can be drawn from the table is that in LOS scenarios considering single diffracted rays can provide sufficient accurate estimations, in other words, multiple diffracted rays do not provide any significant contributions (with extra computation time and memory usage).

No. of interactions	Transmitter height\ Receiver height	Proposed RT model	Full 3D RT model
1 D	**No. of paths**	37	39
	$h_t = h_r = 1.0\,m$	82.36 dB	82.39 dB
2 D	**No. of paths**	925	1082
	$h_t = h_r = 1.0\,m$	82.34 dB	82.37 dB
3 D	**No. of paths**	3054	36527
	$h_t = h_r = 1.0\,m$	82.34 dB	82.29 dB

Table 3.3 – *Model validation - Diffraction in LOS configuration.*

In order to better estimate the model performance, a new test in a NLOS scenario was conducted in the Campus scene with the following configuration and parameters (for the sake of brevity, the test scene is not shown as the previous test scenario) :

— Distance $d(T_x, R_x)$ = 151.7 m.
— NLOS configuration at 2.4 GHz.
— Considered interactions : 1D, 2D, and 3D.

Table 3.4 shows the results obtained for the second test scenario. Generally, the proposed model shows comparable performance even in NLOS configurations. Because of the absence of a dominant path, the single-diffracted rays over rooftops (horizontal edges) still have slight contributions to the total field. However, the rays that have undergone diffraction at more than one edge have negligible contributions despite their large number. Moreover, they add intolerable time delays. Consequently, in LOS or in NLOS configurations only the single diffracted rays are sufficient to provide accurate estimations.

No. of interactions	Transmitter height\ Receiver height	Proposed RT model	Full 3D RT model
1 D	**No. of paths**	15	16
	$h_t = h_r = 1.0\,m$	111.78 dB	113.27 dB
2 D	**No. of paths**	581	701
	$h_t = h_r = 1.0\,m$	111.46 dB	112.81 dB
3 D	**No. of paths**	2020	25288
	$h_t = h_r = 1.0\,m$	111.45 dB	112.75 dB

Table 3.4 – *Model validation - Diffraction in NLOS configuration*

In conclusion, point to point validation can overestimate or underestimate the real global performance of the proposed model. Although this validation process showed a good agreement with full 3D RT models, it is not possible to draw a general conclusion on the model performance based on a few test scenarios. In fact, global model validation via field measurements through a long measurement route can fairly evaluate the model performance in terms of its accuracy. Furthermore, model performance in terms of time gain will be evaluated based on comparisons with a full 3D ray-tracing model. Global validation and evaluation process will be addressed in the next subsection.

3.4.2 Model validation with field measurements

3.4.2.1 Scene modeling

Model validation will be based on field measurements that were conducted by France Telecom R&D through a route of 5 km in the (étoile) neighborhood in downtown Paris. The measurement route corresponds to 1651 points of reception at a height of 1.5 m. The transmitter is located at a height of 21 m with a transmit power of 40 dBm at 932 MHz. In

fact, this is a typical urban configuration with quite high buildings where the dominant propagation paths are mainly in the horizontal plane. For the simulation, the macro-geometry of the propagation scene of Charles de Gaulle - Étoile was modeled with 813 buildings (10330 faces and about 15504 edges), and the same measurement route was reproduced on the modeled scene by 1651 equidistant receivers as shown in figure 3.23(a). Figure 3.23(b) shows the averaged measured power in dBm through the real measurement route.

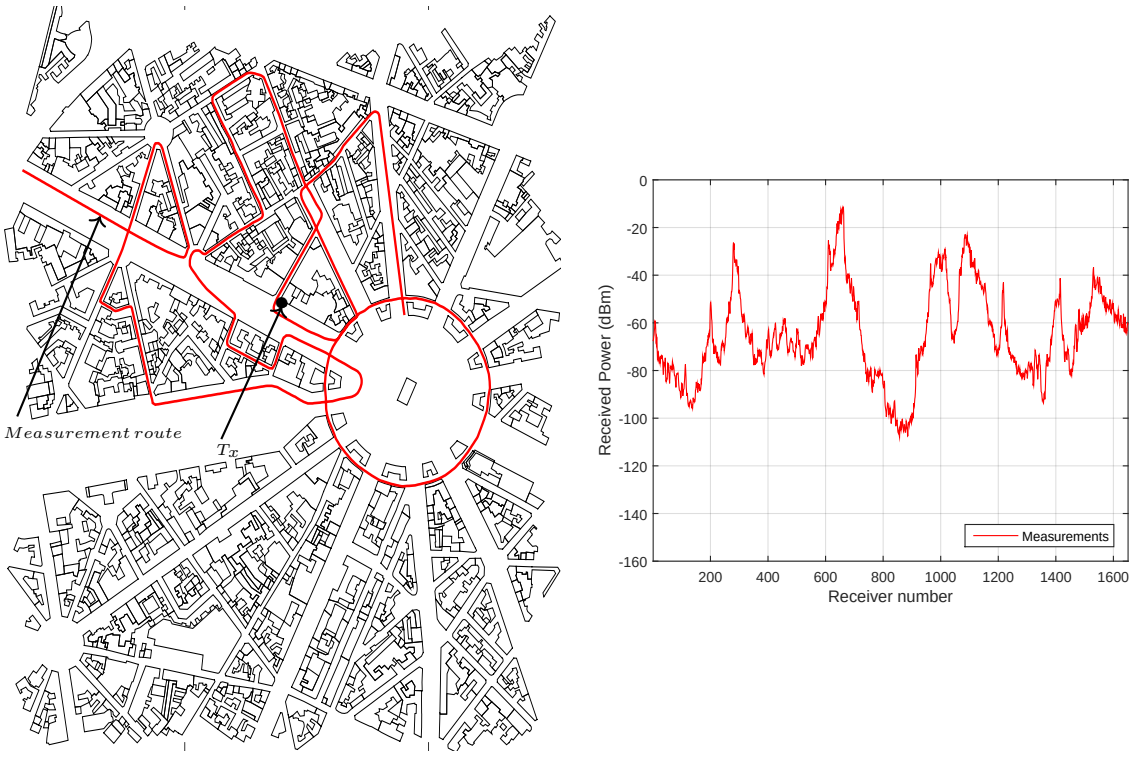

(a) *Measurement route.* (b) *Field measurements.*

Figure 3.23 – *Charles de Gaulle - Étoile, Paris.*

It should be emphasized that the fine details of the propagation environment such as vehicles, vegetation, pedestrians, lamp-posts, billboards *etc.* were not included in scene modeling.

3.4.2.2 Antenna radiation pattern

For the simulations, the transmitter and receiver antennas were considered as vertical dipoles, and therefore they were modeled by the theoretical radiation pattern of a dipole. In fact, the radiation pattern determines how an antenna receives or transmits at any point of the space $P(r, \theta, \varphi)$ as a function of θ, φ. The radiation pattern of a small dipole is given in the E plane by [Sab17] :

$$|E_\theta| = |sin\theta| \tag{3.3}$$

Similarly, the radiation pattern in the H plane is given by [Sab17] :

$$|E_\theta| = 1 \tag{3.4}$$

The modeled radiation pattern was traced as depicted in figure 3.24 in 3D (figure 3.24(a)), in the H - plane (figure 3.24(b)), and in the E - plane (figure 3.24(c)), which gives a donut-shaped radiation pattern.

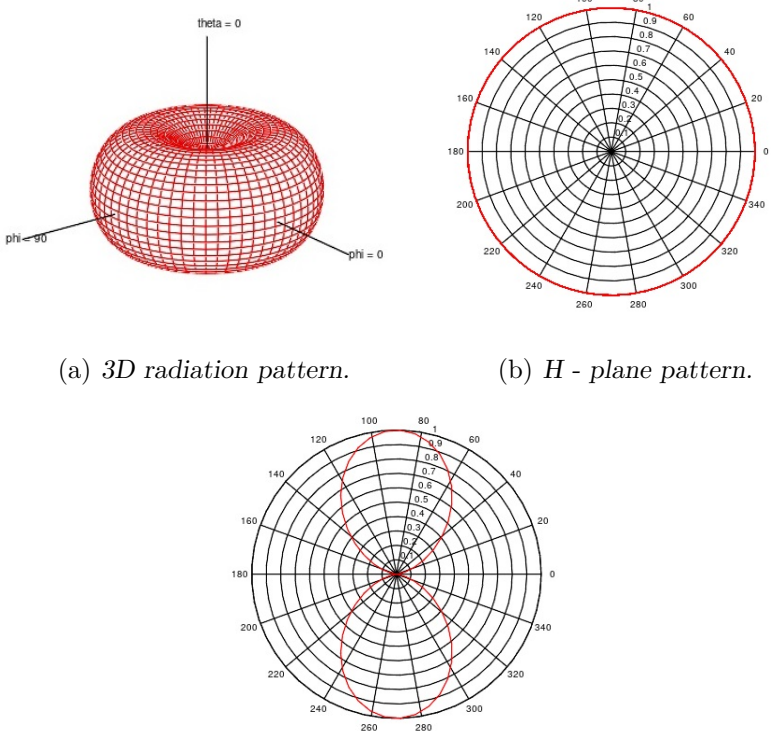

(a) *3D radiation pattern.* (b) *H - plane pattern.*

(c) *E - plane pattern.*

Figure 3.24 – *Radiation pattern of a dipole.*

3.4.2.3 Model performance without power averaging

Simulation results of Charles de Gaulle - Étoile scene were obtained with four different combinations of interactions 1R1D, 2R1D, 3R1D, and 4R1D as shown in figure 3.25. The results of the proposed model show globally a very good agreement with the measurements, even though the simulation results were not locally averaged as the measurements. Globally, it can also be seen from the figures, with a little effort, that higher the number of considered interactions, the more accuracy results. The red bands of the figure will be addressed later on. It is important to underline that the immediate objective of these figures is to give a non-numerical estimation of the model performance. Nevertheless, error evaluation with precise numerical values will be discussed later on using one of the local average power estimation techniques.

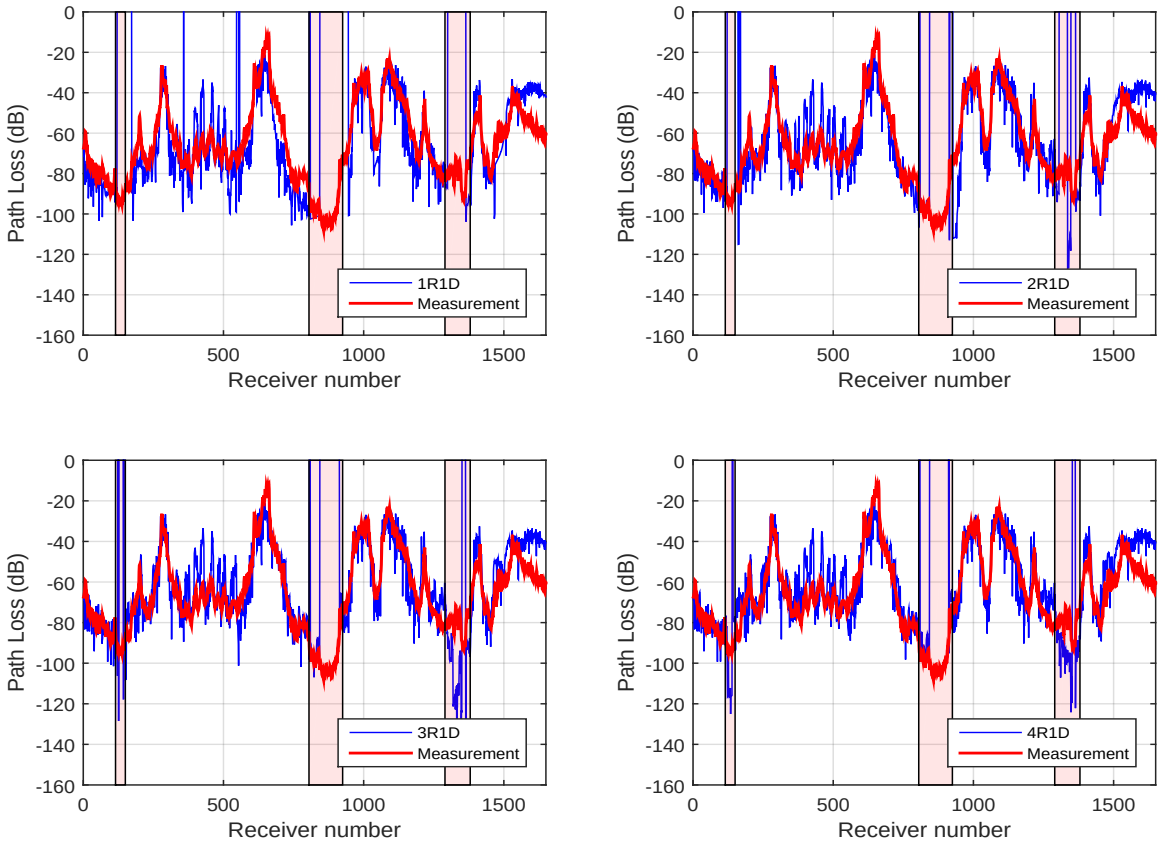

Figure 3.25 – *Global model validation.*

3.4.2.4 Time gain

The gain in time obtained by the proposed ray-tracing model is the most critical element of the research problem. As a matter of fact, the main advantage of the visibility tree technique is not only the time gain that it offers, but also that the execution time is almost independent of the number of receivers (limited dependence). That is to say, for the same transmitter, the same visibility tree can be used for all the receivers to find the propagation paths, whereas a full 3D RT model needs to perform a new calculation for each $T_x - R_x$ pair.

Table 3.5 compares the performance, in terms of execution time, of the proposed model (including the visibility tree calculation) against a conventional full 3D RT model. It shows a considerable gain in time is obtained. For example, to perform a simulation for 1651 receivers for 1R1D, the proposed model takes only about 1 s whereas a full RT model takes more than 2 hours to perform the same simulation. It is even worse if the required number of interactions is more than 1R1D since the full 3D RT model is not even able to perform simulations for 2R1D for all the receivers (the 3D model takes 2 days for only one receiver against 6 s for 1651 receivers with the proposed model!). Still, the proposed model can perform simulations with any number of interactions within a very reasonable time (e.g. for 4R1D it takes about 52 s for 1651 receivers). The term incalculable in the table indicates that it would take a very long time (intolerable). It is important to note that all simulation results were obtained using

an ordinary PC equipped with a 16 GB RAM and 8-core Intel(R) Core(TM) i7-4770 CPU with a clock speed of 3.40 GHz.

No. of interactions	Proposed RT model 1651 receivers	Full 3D RT model per link	Full 3D RT model 1651 receivers
1R,1D	$\sim 1.2\,s$	$\sim 1\,m\,44\,s$	$\sim 2\,h\,12\,m$
2R,1D	$\sim 6.2\,s$	$\sim 2\,d\,3\,h, 56\,m$	incalculable
3R,1D	$\sim 19.8\,s$	incalculable	incalculable
4R,1D	$\sim 52\,s$	incalculable	incalculable

Table 3.5 – *Comparison of computational time.*

3.4.2.5 Local average power estimation of mobile radio signals

One of the main aspects to take into consideration when conducting field measurements or even for simulations is the fast fading. Normally, measurements along a route are averaged by taking N samples over a certain distance (measured in λ) to estimate the local mean power of the received signal and to remove the fast fading effect. Many methods were proposed in the literature to find a valid approach of estimating the local average power. Lee [Lee85] suggests taking at least 36 uncorrelated samples separated by $d = 0.8\ \lambda$ - $1.1\ \lambda$ over a distance of $2L = 40\ \lambda$. Parsons conducted similar studies but distinguished different cases [Par00] : if a linear receiver is used, then the proposed parameters with a 90% degree of confidence are ($2L : 22\lambda$, $N = 57$, d =0,382 λ). For a logarithmic receiver, the proposed parameters are (2L : 33λ, N = 85, d=0,382 λ). For a 95% degree confidence, more samples are taken over a larger distance which yields (2L : 48 λ, N=125 ; d=0,382 λ).

In fact, Lee's averaging method is commonly used and it is also recommended by the European Conference of Postal and Telecommunications Administrations (CEPT) and the International Telecommunications Union (ITU). ITU and CEPT suggest taking the following values (2L = 40 λ, d = 0.8 λ, N= 50) [Par11].

3.4.2.6 Model performance with power averaging

The simulation results of the received radio signal of figure 3.25 were not averaged, so fast fluctuations were present in the simulation curves. Consequently, in order to fairly compare the simulation with the measurements, the same simulations (as the ones in figure 3.25) will be conducted again but with applying Lee's averaging method to estimate the mean values for the simulated signal along the measurement route as shown in figure 3.26. It is obvious that the fast signal fluctuations have disappeared. Globally, It also shows a very good agreement with the measurements especially for high number of interactions *i.e.* 4R1D.

In spite of the good agreement, the error still needs to be quantified with numerical values that can describe the degree of agreement. In order to do that, two error estimation methods are used : the mean error and the mean absolute error. In fact, the mean error is not accurate because negative error values are compensating for positive error values so it often overestimates the model performance so it will not be the main evaluation criterion. Instead, the mean absolute error can give a better perception of the error because it takes the absolute value. Table 3.6 shows the mean error and the mean absolute error between the

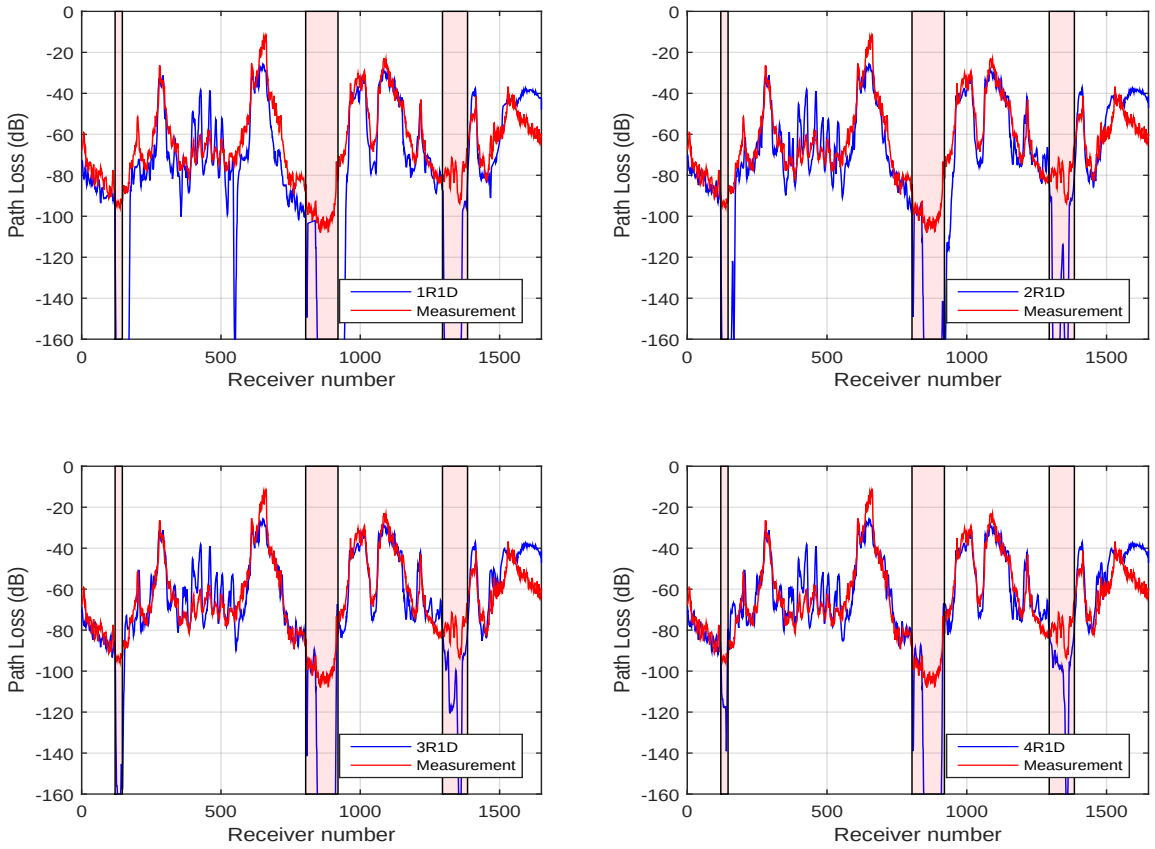

Figure 3.26 – *Model validation - local average power estimation.*

proposed model and the measurements for four different number of interactions (1R1D, 2R1D, 3R1D, and 4R1D). It shows that the mean absolute error for the proposed model is gradually decreasing as the number of interactions increases to reach about 6.7 dB for 4R1D. It shows also that the full 3D model, performs better (for 1R1D) than the proposed model by more than 1 dB (it is important to note that the error value for the 3D model was not averaged due to the time constraints of the 3D models, and because of the same reason, the error for 2R1D, 3R1D, and 4R1D could not be calculated). Another important point is that if more interactions (more than 4R1D) are considered, the error will slightly be improved since the energy of the newly added paths would not be significant. Therefore, this study was limited to 4R1D.

	Proposed RT model		**Full 3D RT model**	
No. of interactions	**Mean Error**	**Mean absolute error**	**Mean Error**	**Mean absolute error**
1R,1D	$\sim -8.04\ dB$	$\sim 12.22\ dB$	$\sim -2.00\ dB$	$\sim 11.40\,dB^*$
2R,1D	$\sim -2.98\ dB$	$\sim 9.13\ dB$	–	
3R,1D	$\sim 1.08\ dB$	$\sim 6.83\ dB$	–	
4R,1D	$\sim 2.73\ dB$	$\sim 6.73\ dB$	–	

Table 3.6 – *Model performance - error evaluation.*

3.4.2.7 Sources of error

Globally, the error can be justified by many facts : the propagation environment does not include all the details of the scene. It should be emphasized that the fine details such as vehicles, pedestrians, lamp-posts, billboards *etc.* were not included in scene modeling. The buildings were modeled as typical concrete blocks (relative permittivity = 9, conductivity = 0.001 S/m) and the ground was modeled as a perfectly flat concrete surface. Another source of error is that the diffracted paths from rooftops were neglected (not a full 3D model).

More specifically, the major sources of error were noticed in some specific places as shown by the gray circular zones in figure 3.27(b), the corresponding receivers were traced on the measurement route as shown in 3.27(a). In fact, the major error areas are located in high vehicular traffic zones (around the Arch of Triumph). This can justify the fluctuations of the power in this area. Besides that, the vegetation was not considered so the additional losses due to the trees are neglected. It is important to notice that pink parts in figure 3.27(b) were, not considered in the error estimation because the receivers in these zones cannot be covered by the horizontal plane even if a higher number of interactions was considered. These receivers are mainly covered by the vertical plane that will be discussed in chapter 4.

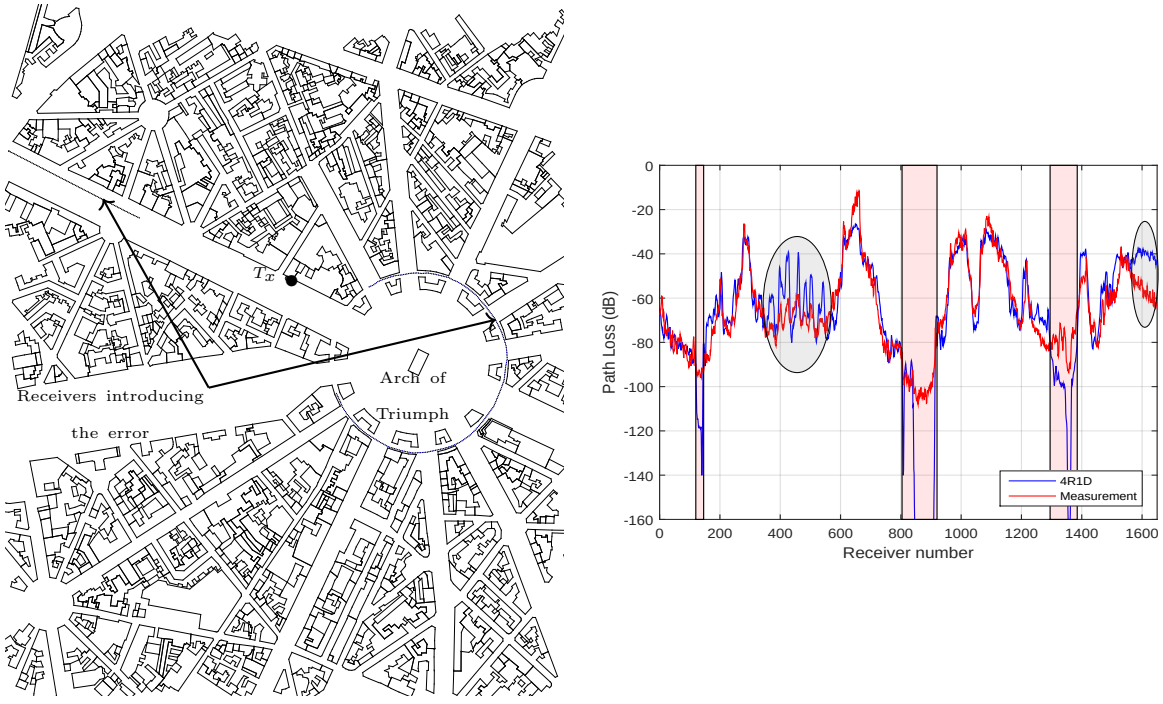

(a) *Major source of error route.* (b) *Major source of error measurement.*

Figure 3.27 – *Major source of error - Étoile, Paris.*

3.4.3 Narrow-band and Wide-band simulations

The model was validated and evaluated in terms of accuracy and execution time. Therefore, this section aims to show some features of the proposed model with no further validation analysis. Since the model is very fast, coverage prediction maps are feasible even with a high

number of interactions. A coverage prediction map (with 4R1D) for Charles de Gaulle - Étoile scene is estimated as shown in figure 3.28. In addition, since the proposed model is a ray-based model, it is also possible to estimate through this model all the wide-band parameters of the radio channel such as the delay spread, channel impulse response, angular spread, angles of arrival, etc. Figure 3.29 estimates the rms delay spread map for the same propagation scene.

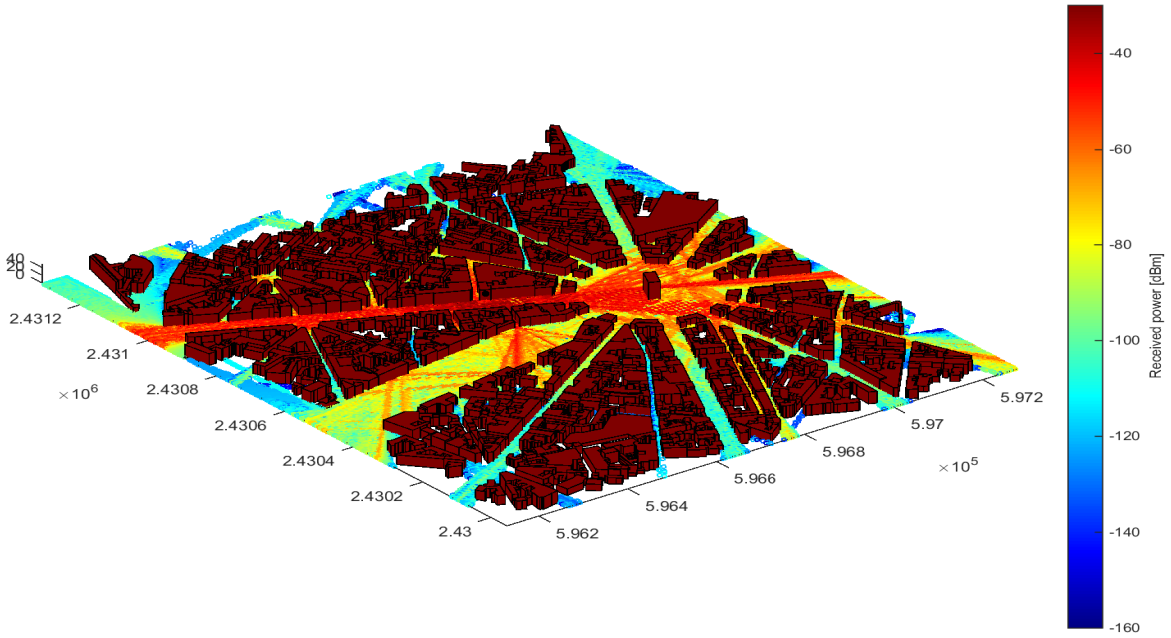

Figure 3.28 – *Coverage prediction.*

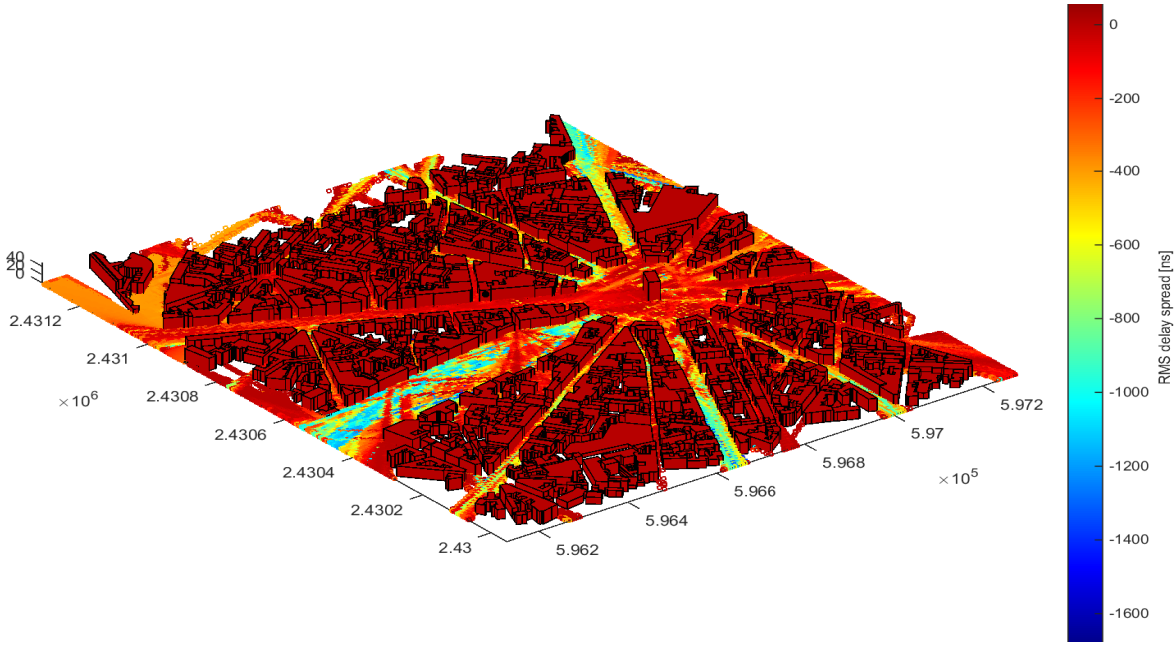

Figure 3.29 – *RMS delay spread.*

3.5 Acceleration techniques

Despite the speed of the currently proposed model, further acceleration techniques are still needed for some application for example in order to support a large number of nodes or even to support mobile nodes. To this end, this section will be proposing some acceleration techniques to the current model.

3.5.1 Scene preparation acceleration algorithms

As a matter of fact, the results shown in table 3.5 include already many acceleration algorithms that are performed with the scene creation phase. They were not mentioned before because it is better to present them in this context. For the sake of brevity, only the main acceleration algorithm will be explained :

— Pre-processing of diffracted zones

Diffracted zones do not depend on the position of the incident ray (independent of the transmitters position), therefore they can be precalculated and then used when needed. To this end, the diffracting edges in the horizontal plane are first identified as shown in figure 3.30. Then the diffracted zones are calculated for each one and saved in the physical memory. In fact, this algorithm helped a lot in reducing the execution time

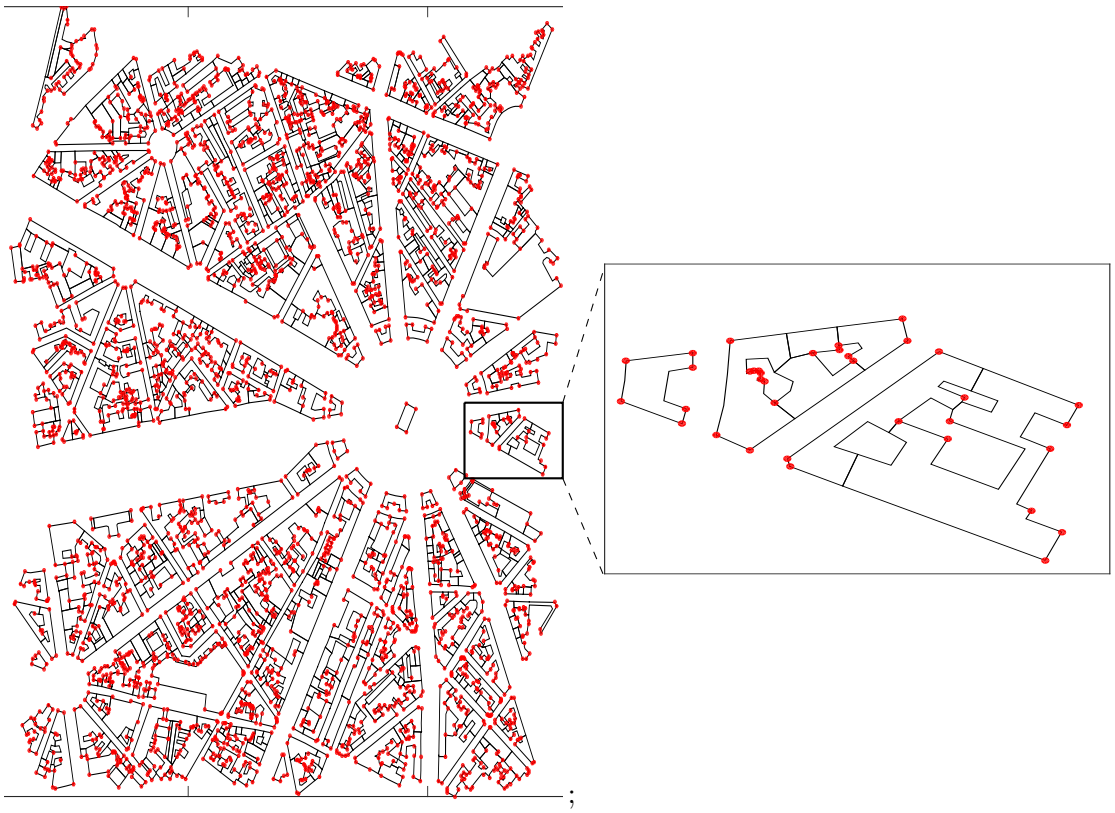

(a) *All the identified diffraction points.* (b) *Zoomed portion.*

Figure 3.30 – *Diffraction Points.*

because the diffracted zones can be used many times without any further calculation because they are already in the memory.

New acceleration techniques will be proposed to further achieve faster simulation results at the cost of introducing negligible loss in accuracy as will be seen in the next subsections.

3.5.2 Maximum number of propagation paths

In many cases, a large number of propagation paths do not contribute to the total field, furthermore, it takes time to find these insignificant paths. Consequently, what is the impact of limiting the maximum number of propagation paths ?

3.5.2.1 Hypothesis

In typical propagation scenarios, only a limited number of propagation paths can contribute significantly to the total field. Consequently, if the proposed model considers a fewer number of propagation paths (the predominant ones), similar simulation results in terms of accuracy can be obtained but with a gain in the execution time.

3.5.2.2 Description of the algorithm

In fact, the nodes in the current structure of the visibility tree are roughly sorted from the most significant node to least significant one, because the tree is structured in levels so the nodes of the level N are normally, but not always, more significant than the next level N+1. The other fact is that the reflected zones were normally placed before the diffracted zones because they are more significant.

Two options are discussed, either to directly use this rough sorting method to select the most significant paths with a small margin. The other option is to implement more effective sorting algorithms that can strictly limit the number of propagation paths to the most significant ones but the problem that an effective sorting method could take more time than considering all the paths. Therefore, the first option was to adopted without any change to the current tree structure.

3.5.2.3 Accuracy and Time gain

In order to evaluate the impact of limiting the number of propagation paths on accuracy and execution time, the same scene of Charles de Gaulle - Étoile, Paris and the same measurements that were shown in figure 3.23 are used. The evaluation study will be conducted through the 1651 receivers of the scene for 4R1D at 932 MHz. Different numbers of propagation paths will be considered each time and the error will be evaluated with respect to the measurements.

In fact, the execution time can be further divided into two parts : the first part is the tree construction time and the other part is for path searching and field calculation time. Limiting the number of paths will not affect the tree construction time (about 42 s for this configuration) but it will surely affect the path search and field calculation time.

Table 3.7 shows the impact of limiting the propagation paths on accuracy and time. It shows that the search time becomes very fast as the number of paths becomes more limited but at the price of a loss in accuracy. For example, if only 5 paths were considered for each receiver, the search time becomes instantaneous but with a considerable loss in accuracy. However, it shows also that limiting the paths to 50 paths can provide the same simulation results in terms of accuracy in about 1 second, instead of 9.7 s. Consequently, the default value of the optimal number of propagation paths is set to 50 paths.

Max. No. of paths	**5**	**10**	**20**	**30**	**50**	**100**	**150**	**200**	**All**
Mean absolute error [dB]	13.55	10.18	7.80	7.34	6.87	6.77	6.81	6.78	6.73
Average number of paths	4.79	9.31	18.19	24.54	43.12	79.82	109.0	130.7	261.6
Time (4R,1D) [s]	0.17	0.33	0.79	0.94	1.2	2.5	3.5	4.7	9.7

Table 3.7 – *Accuracy and gain in time - limited number of propagation paths.*

One might ask about the difference between limiting the number of interactions and limiting the number of paths. In fact, they are not exactly the same thing even if both procedures are limiting the number of paths. Increasing the number of interactions with limiting the number of paths has the advantage that more coverage percentage is achieved.

3.5.3 Limited area

Deterministic models tend to be computationally more expensive as the propagation scene becomes more complex. In micro-cellular configurations, propagation occurs mainly in the horizontal plane. This means that only the surrounding buildings have a considerable impact on radio modeling. Furthermore, in the context of WSN, the nominal transmit power for the protocols that use the IEEE 802.15.4 physical layer is 1 mW (0 dBm) [IEE03], giving a radio range of at most a few hundred meters. This leads to the hypothesis that is formulated in the next subsection.

3.5.3.1 Hypothesis

The significant impact of the propagation environment on radio propagation in micro-cellular configurations is limited to a specified distance smaller than the entire propagation environment. Consequently, the proposed model can provide quite similar simulation results by considering smaller portions of the propagation environment. This area limitation will hopefully bring a considerable gain in time.

3.5.3.2 Description of the algorithm

In order to confirm the stated hypothesis, a new algorithm is needed to limit the propagation scene to a small window with a given size. The concept of the developed algorithm is designed as follows : starting from the transmitter and for a given radius as shown in figure 3.31, the buildings that are found completely within this range will be considered. Partially included buildings will be completely considered by adjusting the window size without including any new building that might exist inside the modified window size. What exists outside this range is completely ignored. Consequently, the visibility tree is only calculated for the window of interest which is much smaller compared to the whole propagation scene.

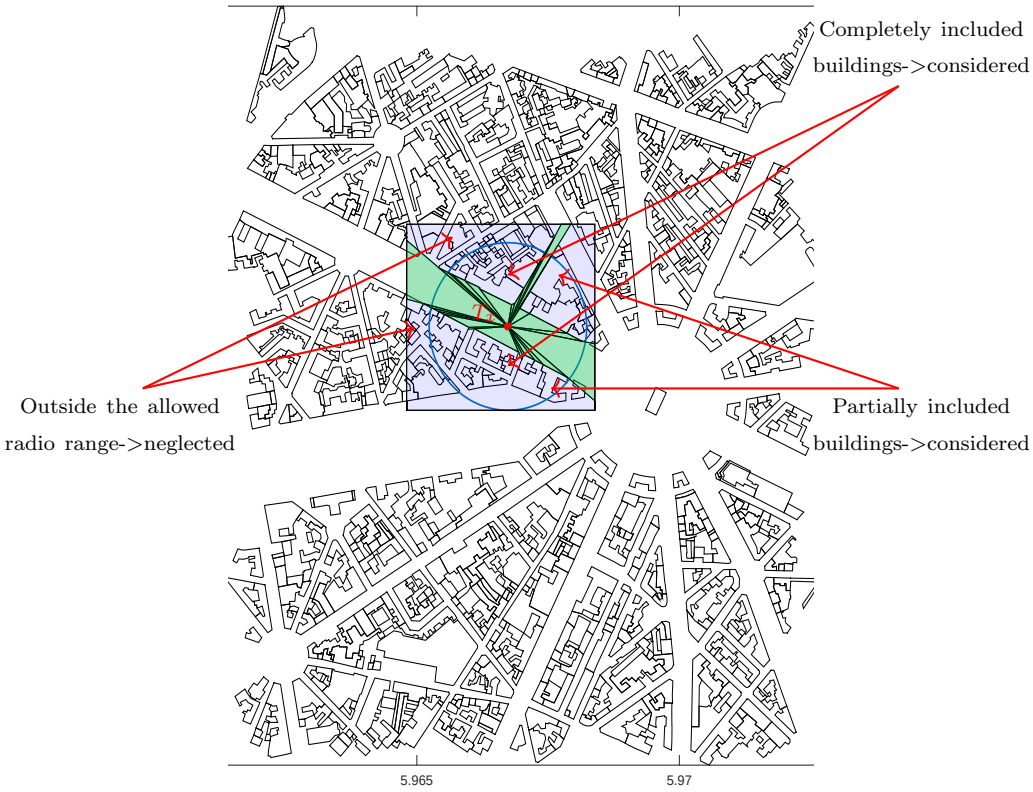

Figure 3.31 – *Limited zone algorithm* .

3.5.3.3 Accuracy and Time gain

This technique allows to limit the calculation to any range but the questions that arise now are : what is the optimum range that we should consider so that there is a negligible impact on the accuracy, and what is the gain of time due to this area limitation ? These questions can be answered thoroughly using several test scenarios as follows :

1. Point to Point test scenarios :

Many point to point tests are conducted to estimate the impact of limiting the scene on the accuracy and on the execution time. Two test categories were distinguished :

— Short communication range scenarios.

— Average communication range scenarios.

1.1 - Point to Point test scenarios - Short communication range :

Three short-range test scenarios were defined in some urban configurations : open area, narrow street (LOS), and narrow street (NLOS). Then, the size of the portion of the propagation scene will be varied (30 m, 40 m, 50 m, 60 m, 80 m, 100 m, 200 m, 300 m, and the whole propagation environment). The parameters of the test scenarios are as follows :

- Open area :
  — Distance $d(T_x, R_x)$ = 20 m.
  — LOS configuration.

- Narrow street (LOS) :
  — Distance $d(T_x, R_x)$ = 22 m.
  — LOS configuration.

- Narrow street (NLOS) :
  — Distance $d(T_x, R_x)$ = 28 m.
  — NLOS configuration.

Table 3.8 shows the results of the three test scenarios for 4R1D at 2.4 GHz. All the three configurations show that limiting to a certain range (50 m $\sim$ 60 m for these test scenarios) has almost no impact on the accuracy. On the other hand, it has a great impact on the execution time. For the three cases, the execution time can be reduced to some milliseconds instead of seconds with a negligible loss. It is important to note that the number of propagation paths is greatly reduced to the significant ones.

Open Area, $d(T_x, R_x)$ = 20 m, 4R1D									
Range [m]	**30**	**40**	**50**	**60**	**80**	**100**	**200**	**300**	**whole**
No. of paths	3	12	130	162	177	196	271	300	521
Att [dB]	61.77	61.77	59.74	59.84	59.83	59.83	59.83	59.83	59.82
Time	$\sim$ ms	$\sim$ ms	$\sim ms$	150 ms	250 ms	500 ms	500 ms	2 s	22 s
Narrow street (LOS), $d(T_x, R_x)$ = 22 m, 4R1D									
Range [m]	**30**	**40**	**50**	**60**	**80**	**100**	**200**	**300**	**whole**
No. of paths	3	10	43	43	67	92	239	348	382
Att [dB]	61.82	67.77	67.11	67.11	67.11	67.14	67.24	67.11	67.21
Time	$\sim ms$	$\sim ms$	$\sim ms$	$\sim ms$	120 ms	200 ms	1 s	4.2 s	9 s
Narrow street (NLOS), $d(T_x, R_x)$ = 28 m, 4R1D									
Range [m]	**30**	**40**	**50**	**60**	**80**	**100**	**200**	**300**	**whole**
No. of paths	8	51	60	65	69	72	79	79	79
Att [dB]	77.84	79.02	79.01	79.01	78.96	78.96	78.96	78.96	78.96
Time	$\sim ms$	$\sim ms$	$\sim ms$	400 ms	500 ms	600 ms	1 s	1.3 s	1.7 s

Table 3.8: *Accuracy vs. gain in time.*

1.2 - Point to Point test scenarios - average communication range :

The same three test scenarios that were previously defined are used but with larger distances between the transmitter and the receiver. Then, the size of the calculation window

will be varied (120 m, 150 m, 200 m, 300 m, and the whole propagation environment). The parameters of the test scenarios are as follows :

- Open area :
  — Distance $d(T_x, R_x)$ = 108 m.
  — LOS configuration.

- Narrow street (LOS) :
  — Distance $d(T_x, R_x)$ = 119 m.
  — LOS configuration.

- Narrow street (NLOS) :
  — Distance $d(T_x, R_x)$ = 100 m.
  — NLOS configuration.

Table 3.9 shows the results of the three test scenarios for 4R1D at 2.4 GHz. The same conclusion can be drawn as the previous test scenario. All the three configurations show the same remarks of the previous cases. It is obvious that limiting to a certain range (120 $\sim$ 150 m for these test scenarios) has a negligible impact on the accuracy with an important impact on the execution time. For the three cases, the execution time was reduced to about 1 s instead of few seconds with a negligible loss.

Open Area, $d(T_x, R_x)$ = 108 m, 4R1D					
Range [m]	**120**	**150**	**200**	**300**	**Complete**
No. of paths	99	212	232	300	855
Att [dB]	78.82	77.97	78.08	78.06	77.85
Time	$\sim$ 100 ms	$\sim$ 1 s	$\sim$ 2 s	$\sim$ 4.7 s	$\sim$ 51 s
Narrow street (LOS), $d(T_x, R_x)$ = 119 m, 4R1D					
Range [m]	**120**	**150**	**200**	**300**	**Complete**
No. of paths	91	115	179	305	311
Att [dB]	74.39	74.38	74.61	74.62	74.62
Time	$\sim$ 280 ms	$\sim$ 780 ms	$\sim$ 1.7 s	$\sim$ 4.8 s	$\sim$ 7.5 s
Narrow street (NLOS), $d(T_x, R_x)$ = 100 m, 4R1D					
Range [m]	**120**	**150**	**200**	**300**	**Complete**
No. of paths	121	122	122	122	122
Att [dB]	88.93	88.93	88.93	88.93	88.93
Time	$\sim$ 1 s	$\sim$ 1.4 s	$\sim$ 2.6 s	$\sim$ 3.7 s	$\sim$ 9.0 s

Table 3.9 – *Accuracy vs. gain in time.*

2. Grid scenarios

Point to point scenarios could be regarded as special case test scenarios. A grid of uniformly distributed receivers is used to obtain more reliable and accurate results. To achieve this objective, three test scenarios, that represent different urban categories, are defined as follows (refer to figure 3.32) :

— **Scenario 1 - an open place :** a grid of 1082 receivers (the blue points in figure 3.32) is distributed in a uniform manner around the transmitter at a distance between 0 - 100 m in an open place. The receivers in this scenario are mainly in direct LOS.

— **Scenario 2 - a narrow street :** a grid of 311 receivers is distributed uniformly around a transmitter in a narrow street. In fact, the environment of this scenario is rich in multipath, and the receivers are mainly in NLOS .

— **Scenario 3 - an intersection :** a grid of 191 receivers is distributed in a uniform manner at a distance between 80 - 100 m (where the error values are higher than the near receivers due to the limitation of the scene in order to assess the worst-case impact due to the area limitation technique). The receivers are both in LOS and NLOS.

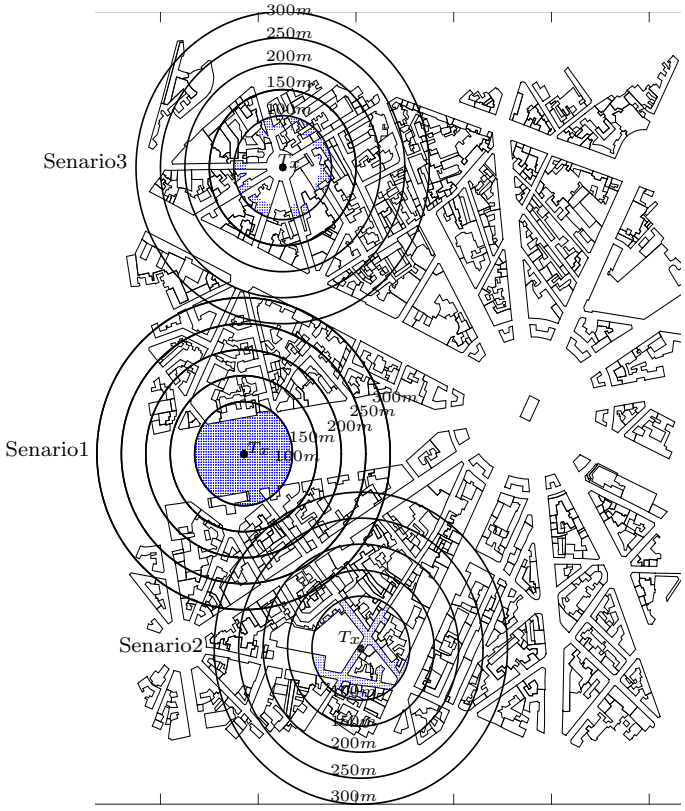

Figure 3.32 – *Limited area test scenarios.*

After defining these scenarios, the size of the portion of the propagation scene will be varied (the circles around the transmitter of 100 m, 150 m, 200 m, 250 m, 300 m, and the whole propagation environment). Table 3.9 shows the mean absolute error and the gain in

time of the three test scenarios for 4R1D at 2.4 GHz. All the three scenarios show the same behavior. It is obvious that limiting the calculation window to a certain range ($\sim$ 150 m for these test scenarios) has a negligible impact on the accuracy with a considerable gain in time. For the three cases, the introduced error when limiting the calculation to 150 m is < 0.6 dB. On the other hand, the execution time is reduced to a few seconds. It is worth noting that this model is used in this table as a self-reference for evaluating the impact of the limited scene *i.e.* the error was evaluated with respect to the configuration where all the propagation scene is considered.

Open place, 4R1D					
Range [m]	**100**	**150**	**200**	**300**	**Whole scene**
No. of covered receivers	1082	1082	1082	1082	1082
Mean absolute error [dB]	0.54	0.086	0.075	0.059	–
Time [s]	$\sim$ 0.2	$\sim$ 2.5	$\sim$ 5.9	$\sim$ 11	$\sim$ 70
Narrow street, 4R1D					
Range [m]	**100**	**150**	**200**	**300**	**Whole scene**
No. of covered receivers	302	311	311	311	311
Mean absolute error [dB]	1.06	0.57	0.04	0.005	–
Time [s]	$\sim$ 2.2	$\sim$ 3.4	$\sim$ 4.2	$\sim$ 5.6	$\sim$ 9.2
Intersection (adapted grid), 4R1D					
Range [m]	**100**	**150**	**200**	**300**	**Whole scene**
No. of covered receivers	178	191	191	191	191
Mean absolute error [dB]	0.34	0.10	0.05	0.011	–
Time [s]	$\sim$ 3.8	$\sim$ 6.6	$\sim$ 7.2	$\sim$ 12.6	$\sim$ 20.8

Table 3.10 – *Gain in time.*

3.5.4 Visibility trees storage (Pre-processing)

Up until now, the proposed model is based on many acceleration techniques. The model can limit the number of paths or even the calculation window to a small portion of the propagation environment leading to a considerable gain in time with a negligible loss of precision. At this stage, the execution time for accurate simulations is in the order of a few seconds for the following parameters (range : 150 m, number of interactions : 4R1D, number of receivers : a few thousands of receivers). Nevertheless, smart cities may contain mobile sensor nodes ; hence the model should be able to support these nodes, *i.e.* the execution time should be further reduced. For this reason, a new acceleration technique that is based on the concept of data pre-processing is proposed. The idea here is to save the visibility trees on the hard disk to use them directly without performing any calculation of the visibility trees.

3.5.4.1 Hypothesis

If a visibility tree is pre-calculated at a specific position, it can be used by a transmitter at the same position to construct the propagation paths without affecting the accuracy, this also brings a very considerable gain in time. However, if the position of the transmitter is not exactly the same as the position of the pre-calculated tree, the nearest one will be used instead, this will not greatly affect accuracy if the distance between the position of the pre-calculated tree and the position of the transmitter is within a limited range.

3.5.4.2 Description of the algorithm

To achieve this goal effectively and efficiently, three issues should be addressed : firstly, what is the best data structure to save the visibility trees in the most compact form possible, in order to reduce the writing time, reading time, processing time, and most importantly, the storage size on the hard disk ? Secondly, what are the positions on the propagation scene that the visibility tree should be pre-calculated at ? Finally, after saving a set of visibility trees, how to find the best visibility tree for a given transmitter and what is the impact on accuracy ?

Data structure

Regarding the first issue of the best data structure, two options are available : either to save the original data structure of the visibility tree as it is, but the size of this structure is not optimized in terms of storage. Thus, a second option is proposed to offer a more compact data structure by saving only the required information to reconstruct the propagation paths, and neglect all other information that was used to build the tree itself.

To better understand the proposed data structure, suppose that the visibility tree of figure 3.33 needs to be saved. In fact, each node of this tree corresponds to a potential propagation path so each node will correspond to a column in the proposed data structure. Since the depth of each node (the number of levels from that node to the root) is not constant, the number of rows for each column is variable. Consequently, the proposed data structure is a two-dimensional integer array, the number of columns is equal to the number of nodes, and the number of rows is variable. The integer type was chosen because it occupies only 4 bytes and gives a range from -2,147,483,648 to +2,147,483,647.

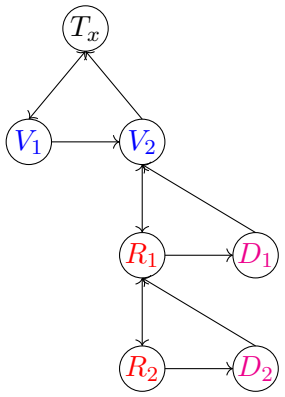

Figure 3.33 – *Simple example of a visibility tree - 2R1D.*

The visibility tree of figure 3.33 is converted prior to saving the tree to a 2D array with variable-length rows, where each node in the tree is represented by a column in this array as follows :

Single interaction node :

- Visible nodes are represented by :
  — 6 integers ($y_3,\ x_3,\ y_2,\ x_2,\ y_1,\ x_1$) because the visible zones are generated from the transmitter point leading to 3-vertex zones (triangles) as V_1 and V_2 in table 3.11.

- Reflected nodes are represented by :
  — 8 integers ($y_4,\ x_4,\ y_3,\ x_3,\ y_2,\ x_2,\ y_1,\ x_1$) because the reflected zones are generated from a face leading to 4-vertex zones as R_1 in table 3.11.
  — An integer ($typeR$) to specify the type of interaction.
  — Two integers ($sourceX, sourceY$) to specify the source point of the reflection.
  — An integer ($indexFace$) to specify the index of the face (just a reference to the face where the reflection has occurred).

- Diffracted nodes are represented by :
  — 6 integers ($y_3,\ x_3,\ y_2,\ x_2,\ y_1,\ x_1$) because the diffracted zones are generated from a diffracting point leading to triangle zones as D_1 and in table 3.11.
  — An integer ($typeD$) to specify the type of interaction.
  — An integer ($indexEdge$) to point to the edge where the diffraction has occurred.

Multiple interactions node :

— for multiple interactions (multiple reflected or diffracted), the same elements for single interaction are saved sequentially except that only the zone of the last level of the tree is saved (*e.g.* R_2 and D_2 in table 3.11). In fact, last-level zone is needed to perform the inclusion tests with the receiver, while the upper zones are not needed anymore.

V_1	V_2	R_1	D_1	R_2	D_2
Int y_3	*Int* y_3	*Int indexFace*	*Int indexEdge*	*Int indexFace*	*Int indexFace*
Int x_3	*Int* x_3	*Int sourceY*	*Int typeD*	*Int sourceY*	*Int sourceY*
Int y_2	*Int* y_2	*Int sourceX*	*Int* y_3	*Int sourceX*	*Int sourceX*
Int x_2	*Int* x_2	*Int typeR*	*Int* x_3	*Int typeR*	*Int typeR*
Int y_1	*Int* y_1	*Int* y_4	*Int* y_2	*Int indexFace*	*Int indexEdge*
Int x_1	*Int* x_1	*Int* x_4	*Int* x_2	*Int sourceY*	*Int typeD*
		Int y_3	*Int* y_1	*Int sourceX*	*Int* x_1
		Int x_3	*Int* y_1	*Int typeR*	*Int* y_1
		Int y_2		*Int* y_4	*Int* x_2
		Int x_2		*Int* x_4	*Int* y_2
		Int y_1		*Int* y_3	*Int* y_3
		Int x_1		*Int* x_3	*Int* x_3
				Int y_2	
				Int x_2	
				Int y_1	
				Int x_1	

Table 3.11 – *Data structure for pre-calculated trees - integer table.*

Pre-calculated visibility tree positions

Regarding the second issue of the positions to save the visibility trees, they should ideally be pre-calculated for every potential position of the transmitter in order to avoid any loss in precision, which is not possible. Instead, two options are implemented as follows :

— The algorithm can create a fictive grid of points (*i.e.* potential transmitters) that goes through the whole propagation scene. The grid consists of N * M equally spaced points separated by a distance defined by the user. Then, the visibility trees are pre-calculated according to this grid. Nevertheless, this option can lead to a large number of positions that are not really needed, large amounts of disk space usage.

— The algorithm asks the user to select a text file that defines the coordinates (x, y) of a route or a set of points. Then, trees are pre-calculated according to this predefined route. This option gives the flexibility to save trees only for the trajectories on which sensor nodes are moving, and therefore, it limits the needed number of visibility trees.

It is important to underline that the impact of the grid spacing, the size of pre-calculated trees, and time gain will be evaluated in subsections 3.5.4.4 and 3.5.4.3.

Tree search process

After saving a set of visibility trees, what is the best one to use for a given transmitter and how to find it ? Figure 3.34 shows a set of points, that each one corresponds to a saved visibility tree. A small range of search around the transmitter is specified by the user to limit the search process to the nearest ones as shown in the figure. In fact, an intelligent search strategy is implemented by using a naming format that contains the position of the tree as *tree_xPosition_yPosition*. This means that the there is no need to read all the saved trees to obtain the position of the tree, but rather it can be directly revealed from the name of the file. Finally, the distance between the transmitter and the candidate trees, which are found the range, is calculated to select only the nearest tree. Hence, only one tree file is read and processed. From this file, the propagation paths are constructed very quickly, and the same procedure as before is used to estimate the electric field.

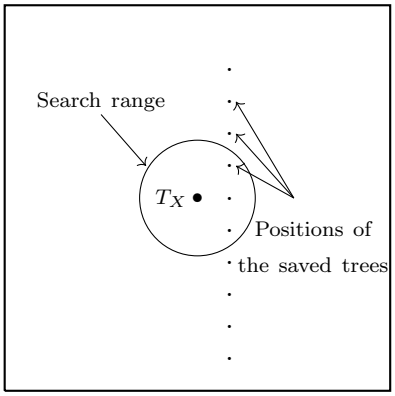

Figure 3.34 – *Search for saved visibility tree.*

3.5.4.3 Time gain and data size

Table 3.12 shows the execution time that is required to search for the pre-calculated tree file, read it, reconstruct the paths from that tree, and to calculate the field strength. As the simulations were conducted for a large number of receivers, the times in table 3.12 were calculated per link (averaged over all the receivers). It shows that, the proposed model, when using the prepossessing technique, can perform very high-speed simulations even for quite a large number of interactions in the order of 1 to 10 milliseconds per link. The data size for the trees depends on the configuration of the surrounding environment, the number of interactions, the considered radio range. Table 3.12 shows also the data size for trees precalculated for a range of 150 m in Charles de Gaulle - Étoile scene. Small file sizes are obtained but the positions of trees must be very carefully selected to reduce the total size.

No. of interactions	Time per link	Size per tree
1R1D	$< 1 \ ms$	50 KB - 250 KB
2R1D	$\sim 2 \ ms$	100 KB - 1.1 MB
3R1D	$\sim 6 \ ms$	200 KB - 2.8 MB
4R1D	$\sim 10 \ ms$	500 KB - 5.0 MB

Table 3.12 – *EXECUTION TIME AND SIZE FOR PRE-CALCULATED VISIBILITY TREES .*

3.5.4.4 Accuracy

As mentioned previously, it is not possible to pre-calculate the visibility trees everywhere, hence two options are implemented (grid or predefined route). In both cases, the transmitter will use the nearest visibility tree if the exact one was not found. Therefore, the final question is : what is the step size to use so that the error is negligible or even acceptable ? Theoretically, the minimum separation between two adjacent receivers in order to be uncorrelated is 0.8λ [Lee85]. As the radio propagation channel is reciprocal, this value could be used for this purpose. However, this value corresponds to 10 cm (at f = 2.4 GHz), which is an extremely small value for a city-scale simulation. For this reason, larger steps are used and the introduced error will be empirically estimated.

Table 3.13 evaluates the error due to the use of the nearest tree instead of the exact one. In order to show the impact of the grid size on the accuracy, visibility trees were pre-calculated using step sizes of 10 m, 5 m, 2 m, and 1 m. Then, 150 transmitters were distributed through a route of 500 m, each transmitter will pick the nearest pre-calculated tree to reconstruct the paths. The mean error was estimated over a grid of receivers (about 150 receivers) around each transmitter. Table 3.13 shows that the error becomes more acceptable for fine discretization

No. of interactions	Step size	Absolute mean error
4R1D	$10 \ m$	4.4 dB
	$5 \ m$	3.2 dB
	$2 \ m$	1.6 dB
	$1 \ m$	0.78 dB

Table 3.13 – *STEP SIZE VS MEAN ERROR.*

(more space on the hard disk). However, the optimum grid size is determined in terms of the required accuracy of the application.

3.6 Optimal number of interactions

3.6.1 Test scenarios

Last section of this chapter will try to answer the last question that could arise : what is the optimum number of interactions that should be considered ? The idea is to search for a trade-off that minimizes the error, minimizes the execution time, and maximizes the coverage percentage. For this reason, this trade-off was proposed using four test scenarios that summarize the main urban cases. In order to get more reliable results, the error and the execution time were evaluated using a large number of receivers (uniformly distributed in a grid. The four test scenarios are shown in figure 3.35) :

— Test scenario 1 : An open place, 1082 receivers (LOS :1067, NLOS :15)
— Test scenario 2 : A narrow street, 347 receivers (LOS :97, NLOS :250)
— Test scenario 3 : An intersection, 613 receivers (LOS :352,NLOS :261)
— Test scenario 4 : A wide street, 537 receivers (LOS : 300, NLOS : 237)

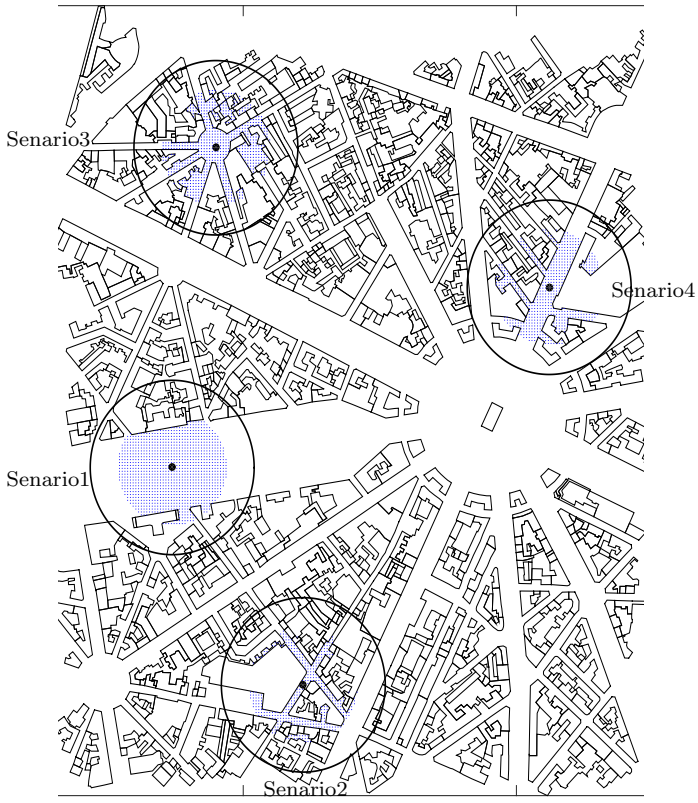

Figure 3.35 – *Test scenarios - optimal number of interactions.*

3.6.2 Parametric study

A parametric study was conducted using the four test scenarios. The study depends mainly on three criteria to find the answer to the addressed question. The main criteria are :

— Accuracy.
— Computational time.
— Coverage percentage.

From the study, it was found that in open scenarios, a ray that has undergone some reflections and diffractions has no significant contribution to the channel estimation. On the other hand, narrow streets are rich in multipath so, even if a ray has undergone some reflections and diffractions, it can contribute significantly to the total electric field.

As a general conclusion, there is no magic number of interactions that is ideal for all scenarios. However, 4R1D could be an acceptable answer to the mentioned question. For this reason, indicative guidelines are given in figure 3.36. Then, according to the application (in terms of accuracy restrictions and time tolerance), the most convenient interaction can be determined.

Figure 3.36 gives a range of values for three parameters : error, execution time, and coverage percentage. The error was estimated with respect to the number of interactions for which the estimation converges, the execution time was estimated for a calculation window of 150 in a complex propagation scene, and finally, the coverage was estimated for the worst case scenario (*i.e.* the narrow street test scenario). Another important point is that the error was evaluated in LOS and NLOS because if the average for both cases was taken, it would hide the higher values of error in NLOS configurations.

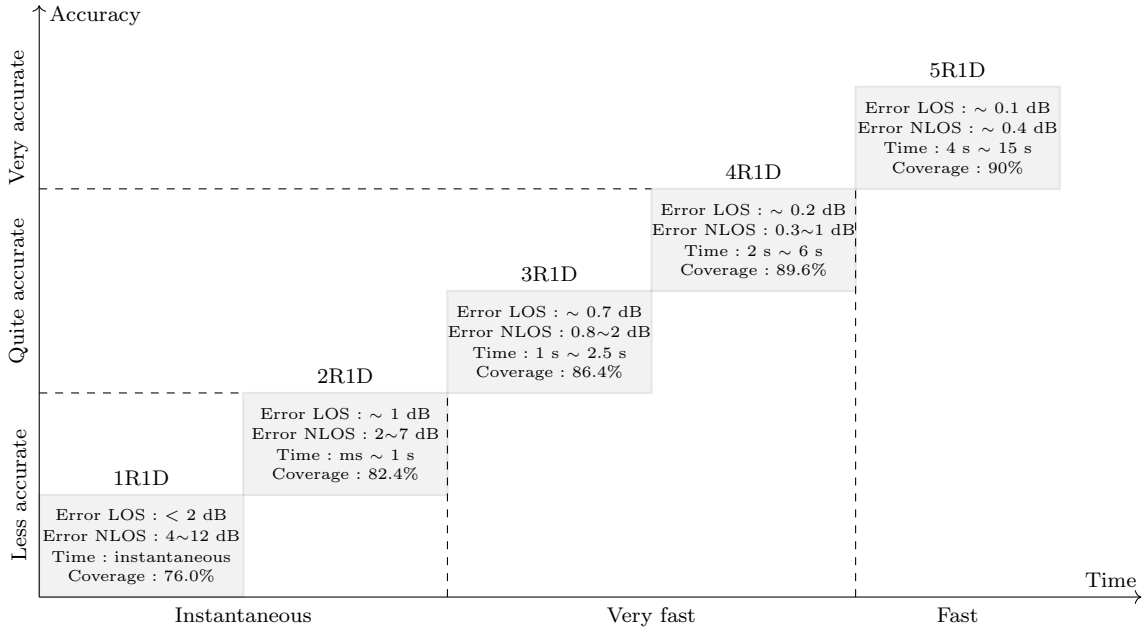

Figure 3.36 – *Guide for the optimum number of interactions - (150 m, grid of receivers).*

3.7 Conclusion

In this chapter, a fast deterministic ray-tracing model for micro-cellular configurations was proposed. The simulation results for this model were compared and validated with a conventional 3D ray-tracing model and then with measurements that were conducted in an urban scenario in Paris. The simulation results corresponded closely to the measurements and to the simulation of the 3D ray-tracing tools.

The first phase of the model was accomplished by implementing a ray-tracing model based on the visibility technique. With the first phase, the model can perform accurate deterministic simulations in the order of tens of seconds (for 4R1D). The second phase was implemented some acceleration techniques, by limiting the propagation scene to a smaller portion and by limiting the number of the propagation paths. With these techniques,accurate deterministic simulations can be performed in the order of a few seconds (for 150 m, 4R1D) with a negligible impact on the accuracy. Finally, it was proposed to pre-calculate a set of visibility trees ; hence channel estimations can be obtained in the order of a few milliseconds per link (for 150 m). However, a fine discretization is required to ensure that the error is small. In fact, the proposed model satisfies the requirements of WSN simulators since it considers the propagation scene, supports a large number of nodes, supports the mobile nodes, and within a reasonable time.

Chapter 4

Propagation in the vertical plane

Contents

4.1 Introduction

Chapter 3 proposed a deterministic ray-tracing model for urban configurations. This model assumes that the principal propagation mechanism occurs in the horizontal plane. However, the vertical propagation (diffraction over rooftops) can be predominant in some configurations. Chapter 4 aims first to investigate the range of validity of the horizontal propagation in a large urban configuration and then it aims to integrate an appropriate deterministic vertical propagation model into the existing model in order to have a complete model valid for all urban configurations.

To this end, chapter 4 is structured as follows : section 4.2 presents Munich site and its measurement routes because these routes will be used throughout this chapter for validation and test purposes. Section 4.3 investigates through some simulations in Munich site (without having the vertical propagation) if the horizontal mode is valid for the whole scene or it is just valid for a certain range around the transmitter. Section 4.4 illustrates briefly the algorithms used to extract the vertical profile from a 3D scene. Section 4.5 aims to present the available options for finding the vertical propagation paths (direct path, all vertical paths, *etc.*). After that, section 4.6 gives the state of the art review for multiple diffraction problems where one edge is in the transition region of the next one. This review is important to evaluate each method, in order to use the most appropriate model candidate that can satisfy the required specifications. In fact, this section will provide a detailed description of two interesting methods : Anderson's method and Capolino-Albani method. Validation and performance evaluation will be discussed in section 4.7. Finally, section 4.8 will verify if the uncovered zones, of the Paris scene (*cf.* chapter 3), is covered by the vertical plane.

4.2 Downtown Munich map and measurements

Researchers of radio propagation modeling need to validate the simulation results of their radio models with a common reference. Munich site is one of the most referenced test scenarios in the literature. Path loss measurement campaigns were conducted at 947 MHz in downtown Munich within the COST231 project [DC99] over three routes (total length of the routes is about 23 km), including different receiver heights. Some authors use one measurement route for model calibration and the other two routes for model validation. Within this chapter, no calibration phase is implemented because, practically, it is not always the case that a measurement campaign is provided for calibration purposes. Therefore, all the measurement routes will be used for validation purposes of the new proposed model. In addition, these measurement routes will be also used for testing the range of validity of the horizontal plane model that has already been implemented.

Munich site has 2088 buildings over an area of about 8 km^2 (about 2400 m × 3400 m) as shown in figure 4.1. It includes a large number of objects (19353 faces and at least 31535 edges). It is important to note that the transmitter is located in the center of the Munich city at a height of 13 m (shown in figure 4.1). The provided database of Munich test site is given in a way such that each building is represented as a polygon and an approximate building height (2.5D format). Furthermore, the site has a fairly flat ground with maximum elevation variation of ± 5 m. Therefore, it was easily converted into an XML file (the format this is used by the internal tool where the proposed models are integrated), and the ground was considered as flat. It must be noted that the reception points of these routes are covered by both the horizontal and vertical propagation mechanisms (each one is predominant in certain regions), therefore, Munich site will be used first for determining the range of validity of the horizontal model in order to show the necessity of integrating a vertical propagation model.

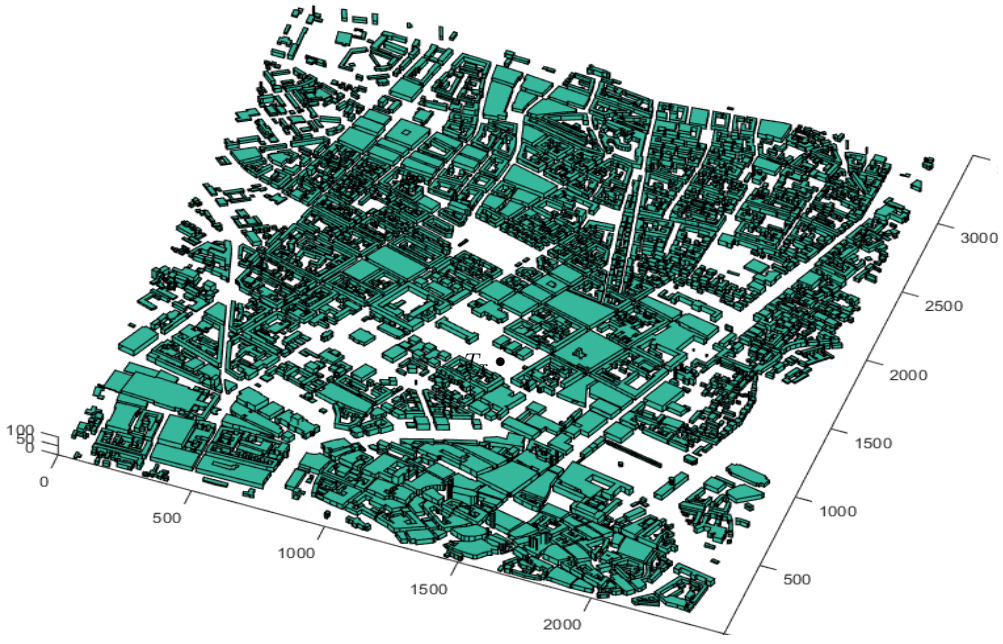

Figure 4.1 – *Munich3D.*

The three routes along with the field measurements will be briefly described in the following subsections as follows :

4.2.1 Measurement path Metro 200

METRO200 measurement route contains 970 reception points extended through 9 km as shown in figure 4.2(a). The average ground height is about 512 m with a slight variation of $\pm$ 4 m. The receivers are placed at a height of 2 m from the ground level. Figure 4.2(b) shows the average path loss through this measurement route. It seems intuitive that not all the reception points are accessible by the lateral propagation.

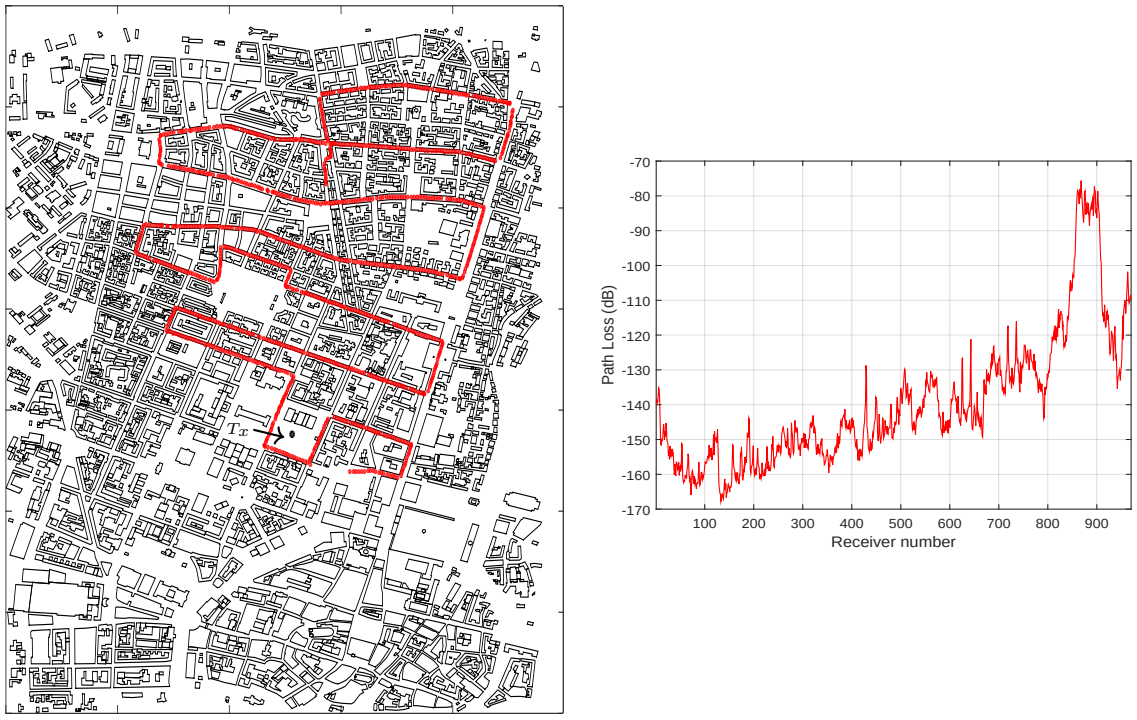

(a) *Measurement route.* (b) *Path loss measurements.*

Figure 4.2 – *Munich site - Metro 200 route.*

4.2.2 Measurement path Metro 201

METRO201 is a short measurement route that contains 355 reception points extended through 3.5 km as shown in figure 4.3(a). The ground height is about 516 m with a small variation of $\pm$ 2 m. The receivers are located at a low height of 1.3 m from the ground level. It is sometimes used for model calibration. Figure 4.3(b) shows the average path loss through this path. It should be noted that although many of the reception points are mainly covered by the lateral propagation mechanism, the vertical mechanism is predominant for the far reception points.

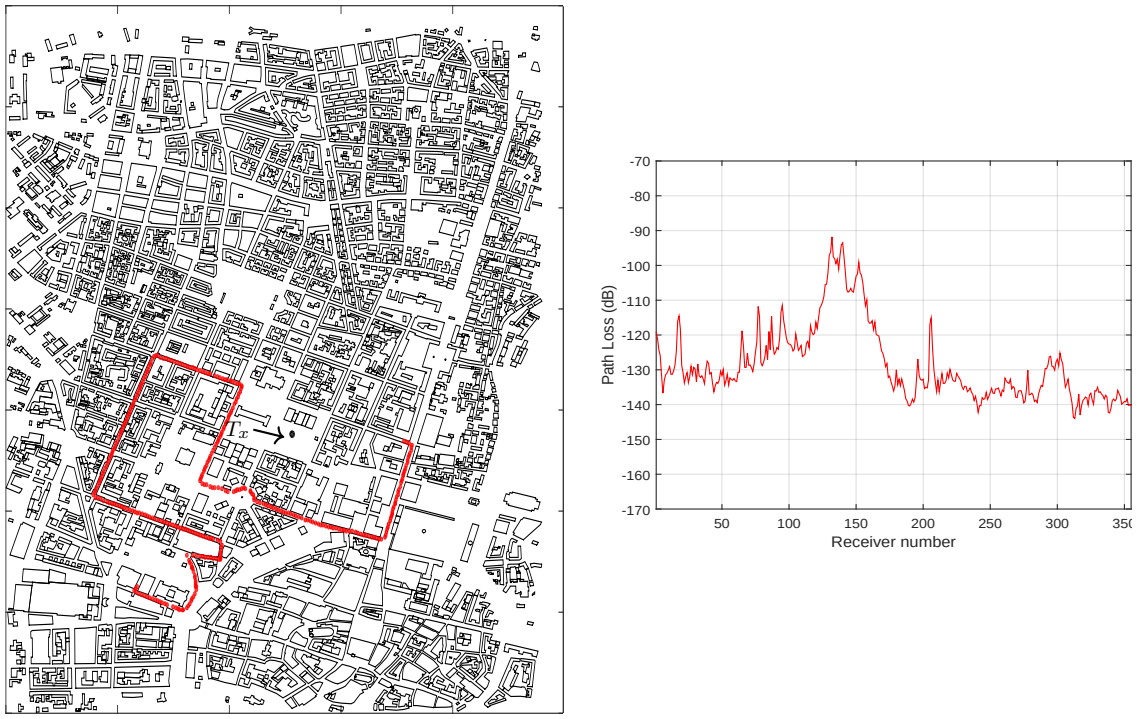

(a) *Measurement route.* (b) *Path loss measurements.*

Figure 4.3 – *Munich site - Metro 201 route.*

4.2.3 Measurement path Metro 202

METRO202 measurement path is the longest route as it contains 1031 reception points extended through 10 km as shown in figure 4.4(a). The average ground height is about 514 m with a slight variation of $\pm$ 5 m. The receivers are placed at a height of 1.9 m from the ground level. Figure 4.4(b) shows the path loss through this route. It seems intuitive that part of the reception points can be covered by the lateral propagation since it is the dominant mechanism, while the other part cannot be reached except by the vertical propagation. This route will be used in the next section to show the range of validity of the lateral propagation.

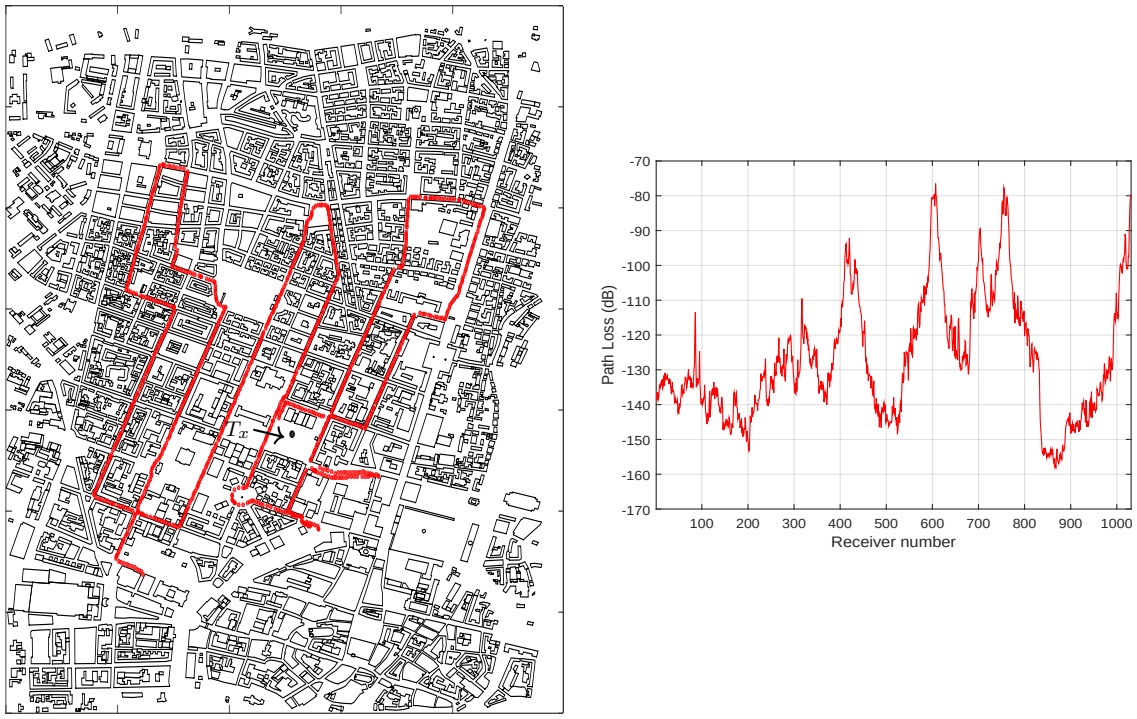

(a) *Measurement route.* (b) *Path loss measurements.*

Figure 4.4 – *Munich site - Metro 202 route.*

4.3 Problem statement

In urban configurations, multi-path contributions of the horizontal propagation are generally limited to several hundreds of meters around the transmitter according to some parameters of the configuration such as the height of the transmitter, height and density of the obstacles around the transmitter, *etc.* After a certain distance, the vertical propagation mechanism becomes more and more predominant [Cor9]. In order to show the validity range of the horizontal plane, the average path loss will be estimated for METRO202 route (presented in figure 4.4(a)), by using only the horizontal model that was described in chapter 3.

Figure 4.5(b) shows the simulation results for several combinations of interactions (1R1D, 2R1D, and 3R1D) against the measured results. It shows a very good agreement with the measurement but just for certain regions (white bands). On the other hand, it gives very inaccurate estimations or even no values for the remaining points of the route (red bands) even if the number of interactions is increased.

In order to estimate the range of validity of the horizontal plane around the transmitter, the reception points for which the horizontal model is valid were traced as shown in figure 4.5(a), where they were marked by the black points (not displayed as points because they are very close, so they appeared as continuous segments). This leads to the conclusion that the horizontal model is only valid over hundreds of meters around the transmitter where the lateral

propagation is predominant. Figure 4.5(b) shows also the necessity to have a comprehensive propagation model that can predict the channel parameters for any urban configuration.

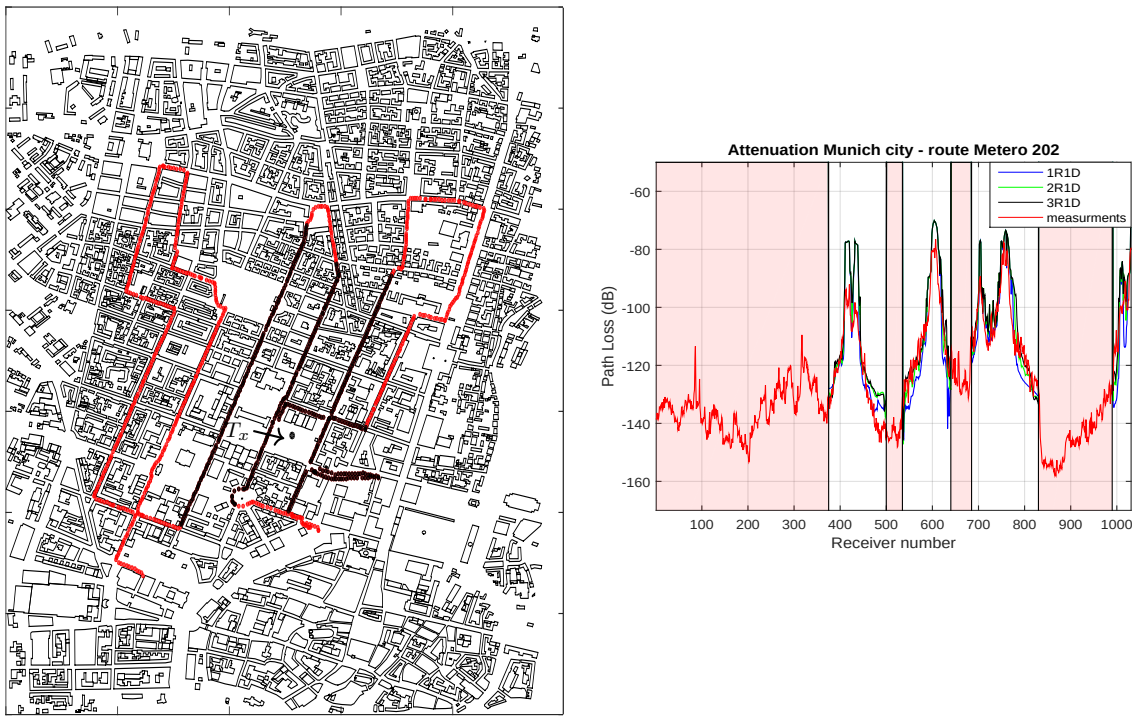

(a) *Measurement route.* (b) *Field measurements.*

Figure 4.5 – *Munich site - Metro 202 route : propagation in horizontal plane .*

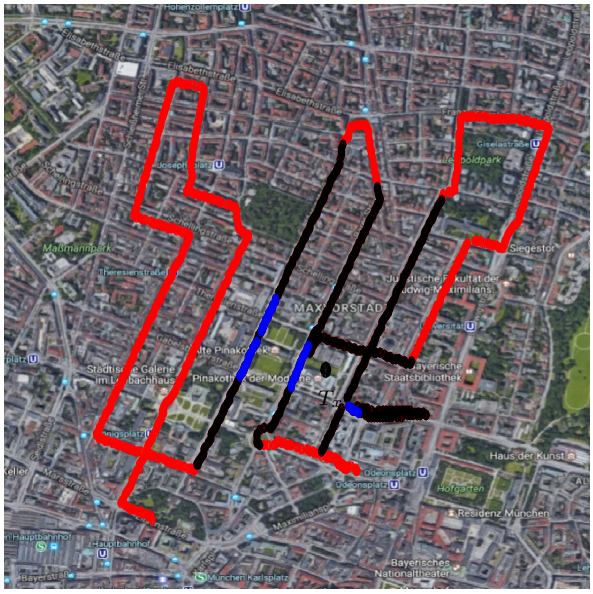

Figure 4.6 – *Google earth view.*

One important point to be mentioned is that, despite the good agreement between the simulation and measurements, some picks were noticed at certain receivers (at the reception points 410-440, 600-620, 700-710, and 755-765 of figure 4.5(b)). These points were traced in a Google earth map as shown by the blue points of figure 4.6. It was revealed that the main reason is the presence of vegetation which obstructs the propagation paths. Some basic vegetation models that add empirical losses in [dB/m] can easily be integrated to model the vegetation loss. However, vegetation information is not provided with the database.

Finally, in order to estimate the radio channel in such scenarios where lateral and vertical propagation mechanism are both present, one possible option is to use a full 3D ray tracing model which can provide good predictions because it considers all the propagation paths. However, this option was excluded as mentioned previously because it is not practically applicable to the project due to the execution time restrictions. Consequently, the adopted solution will be to integrate a deterministic vertical radio model into the existing model, which leads to the so-called 2.5D model. The vertical plane problem will be decomposed in two issues due to the need of two separate models as follows :

— A geometrical model to extract the vertical profile and to find the significant propagation paths in the vertical plane.
— A physical model to estimate the radio channel parameters such as the electric field carried by these propagation paths.

The following sections will address the two provoked issues.

4.4 Vertical plane extraction

As discussed previously in chapter 3, all the horizontal edges were stored in a 2D grid. This grid is still useful for extracting the vertical profile between two points. Figure 4.7 shows a set of buildings that are presented by edges (gray pixels). In order to extract the vertical

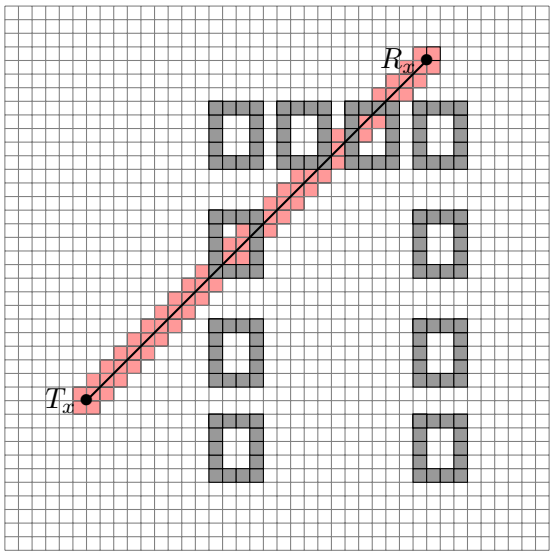

Figure 4.7 – *Vertical plane extraction.*

profile between the transmitter and receiver, a 2D straight line is first drawn between these two points. The line is then discretized according to the supercover scheme as explained in chapter 3 (red pixels of figure 4.7). It is easy now to trace the pixels of the line to check if the line contains an edge. Finally, a set of intersection points (in 2D), where the line and the edges intersect, are determined. The heights of the buildings, to which these edges belong, represent the z-axis of the intersection points.

The above-mentioned algorithm was used to extract the vertical profile between a transmitter and a receiver in Munich site as shown in 4.8(a). The corresponding profile (distance in function of buildings height) is shown in figure 4.8(b), which depicts a cross-section of the buildings inside the vertical plane connecting the transmitter point with the reception point. It must be noted that it takes < 1 ms to extract the vertical thanks to the 2D grid that limited the intersection tests to a few number of edges.

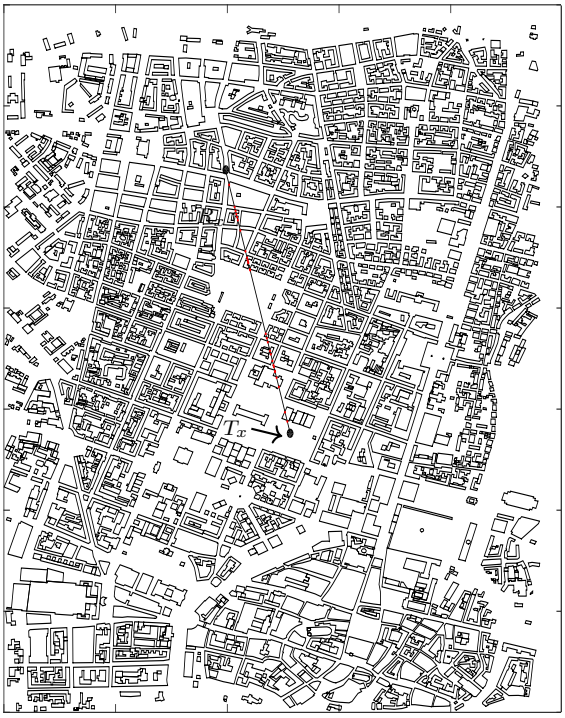

(a) *Transmiter and receiver in Munich city.*

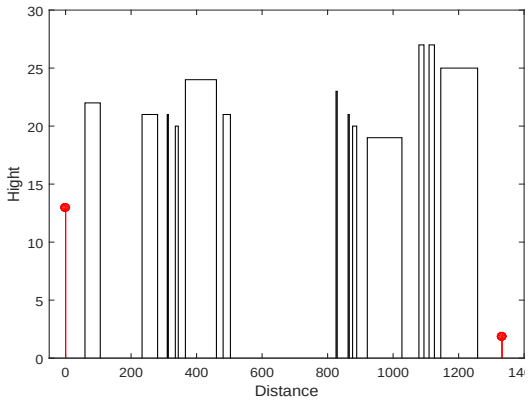

(b) *Vertical profile.*

Figure 4.8 – *Munich city - vertical plane extraction.*

4.5 Vertical Propagation Paths

The next question that arises after extracting the vertical profile is : what are the geometrical propagation paths that should be considered to give the best accuracy-time trade-off. Three options were implemented :

— The direct propagation path which is the shortest path as shown in figure 4.9(a), which is easy and fast to calculate. It assumes that the first Fresnel zone is clear between each two successive diffraction points.

— An exhaustive list of all the possible propagation paths is calculated. In fact, this option necessitates many intersection tests in order to eliminate the paths that are not physically correct. That leads to high calculation time, especially, for a large number of edges. Figure 4.9(b) shows a number of possible propagation path (display limited to 50 paths).
— The direct propagation path with a ground-reflected path as shown in figure 4.9(c). It should be noted that some authors include other options such as reflection between the transmitter and first diffraction or backward diffraction from the building behind the receiver. These options could also be implemented but it would add some extra time.

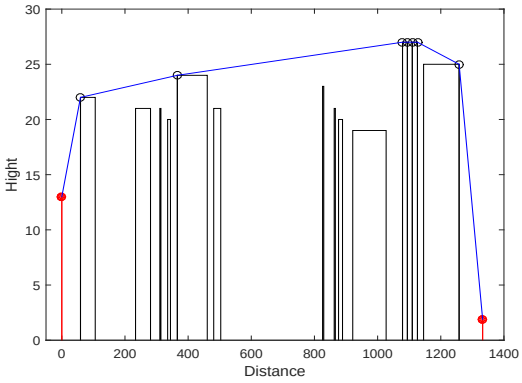

(a) *Direct path.*

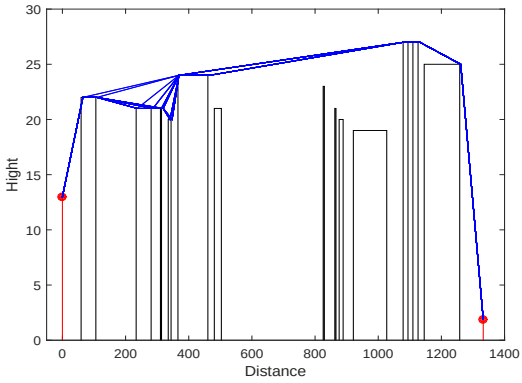

(b) *All possible paths (50 paths shown).*

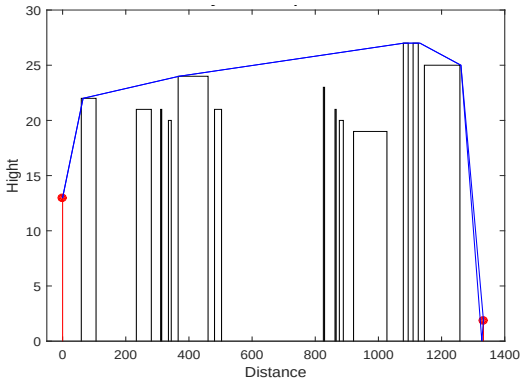

(c) *Direct path with the ground reflected path.*

Figure 4.9 – *Vertical propagation paths - implemented options.*

It should be noted that the direct path option will be adopted not just because it is fast (instantaneous) and easy to be found but also it has mainly the most significant contribution of the total field. The next section will give a brief review of the state of the art of the physical models that address the multiple-diffracted paths in the vertical plane.

4.6 State of the art review

In practical vertical plane cases, more than one obstacle is very likely to be present in the propagation path. Therefore, in order to obtain accurate field estimations, field prediction

models need to take into consideration the behavior of paths obstructed by a number of successive obstacles. In fact, propagation over rooftops in urban scenarios is the dominant phenomenon in the vertical plane. In literature, several solutions were proposed to deal with the multiple diffraction problems. A brief literature review is conducted to find the most adapted physical model that can satisfy the project requirements.

4.6.1 Multiple knife-edge diffraction

In multiple diffraction problems, the diffraction losses from successive obstruction cannot be simply added to find the total loss but rather more sophisticated methods are required. Multiple knife-edge diffraction method is a recursive approach for estimating the overall diffraction loss due to multiple diffraction. By this method, the obstacles are represented by simple geometry as infinitely thin edges (knife-edges). The most used multiple knife-edges methods [SAZ07], which are Deygout [Dey66] and Giovaneli methods, will be briefly presented [Gio84].

Deygout method calculates first the diffraction parameter for each edge as if it was alone. The main edge is identified as the edge with the largest value of the diffraction parameter. Then, the diffraction loss for this edge is estimated. Now, the propagation path is split by the main edge into two segments (*i.e.* two sub-paths). The point at this edge is considered as the receiver point with respect to the first sub-path, and as a new source for the second sub-path. The same procedure is repeated for each sub-path until all the edges are treated. The total loss is calculated by adding the estimated losses from each edge. Giovaneli proposed a similar method but he introduced in the calculation the notion of the effective edge height. It is important to note that the multiple knife-edge solution is quite easy method. It is widely used in rural environments, nevertheless, it is still used in urban environments [CLH02].

It has been shown in [SAZ07] that, the two methods give accurate results as the differences in the heights of the edges become higher. It was also showed that these methods could give a large error at the region of grazing incidence. In fact, multiple building diffraction problems are likely to contain scenarios of grazing incidence. Furthermore, other studies [ML99] show that the knife edge method overestimates attenuation behind tall buildings. Consequently, this solution will not be adopted in the proposed model.

4.6.2 Multiple edge Diffraction Integral

Vogler [Vog82] proposed a general multiple integral solution, valid even at grazing incidence. His work was based on a series originally developed by Furutsu [Fur63] for diffraction propagation problems over different scenarios of inhomogeneous terrain. It was shown that Vogler method [SAZ07] can give reliable results even for cases involving a number of diffracting edges, particularly, at the region of grazing incidence. It is, therefore, used as a reference to compare the performance of the other methods. However, this solution will be excluded because the execution time increases exponentially with the number of edges (*i.e.* intolerable execution time) [Bey04].

4.6.3 GTD/UTD

As introduced in chapter 2, the geometrical theory of diffraction (GTD) [Kel62] and the uniform theory of diffraction (UTD) [KP74] are commonly used to solve diffraction problems over wedges. In addition, the UTD was the adopted solution to estimate the diffracted field for the horizontal propagation as it gives accurate results in that context. Although the UTD is an extension to GTD to solve the singularity problem in the transition region, UTD still gives inaccurate results in the case of multiple diffractions in the transition zone. That therefore means that, it would fail to give the desired accuracy due to the fact that urban configurations are very likely to contain a series of successive buildings having similar or close heights, and also due to the facts that buildings can also be represented by two joined wedges (*i.e.* grazing incidence from the first wedge). Consequently, it is not a recommended physical model for problems involving multiple over-rooftop diffractions.

4.6.4 UTD Slope diffraction

As discussed previously, the UTD has a limitation that multiple diffraction problems cannot be estimated when the wedge is illuminated by fields at the transition region. This could occur when the transmitter position, and/or two or more consecutive wedges, and/or the receiver position are aligned. Therefore, new higher order terms known as the slope diffraction term were introduced in the UTD context in order to deal with the problem of multiple diffractions at the transition region. The diffracted field including the slope diffraction term is given as [SAZ07] :

$$E_d = \left[E_i D + \frac{\partial E_i}{\partial n} d_s \right] A(s) e^{-jks} \tag{4.1}$$

where,

— E_d is the diffracted field,
— E_i is the incident field (defined previously),
— D is the diffraction coefficient (defined previously for wedges, defined in [And97] for knife edges),
— $A(s)$ is the spreading factor (defined previously),
— d_s is the slope diffraction coefficient.

Kouyoumjian [HK74] presented a slope term for perfectly conducting wedges. Luebbers [Lue89] derived a similar slope diffraction coefficient for lossy double-wedges, but with extra terms because of the existence of the reflection coefficient. Holm [Hol96] showed that discontinuities at the shadow boundaries are still present if the second order diffracted field is only considered. Therefore, higher order fields are required to obtain smooth and accurate results. Using the notation of figure 4.10, Holm calculates the diffracted field using a series for higher order diffracted fields as shown by equation 4.2. This expression is valid for diffraction by consecutive perfectly conducting wedges.

$$E_d = \frac{E_0 e^{-jks_T}}{s_T} \sqrt{\frac{s_T}{s_1 s_2 s_3}} \sum_{m=0}^{\infty} \frac{1}{m!} \left(\frac{1}{jks_2} \right)^m \frac{\partial^m}{\partial \phi_1^m} \frac{\partial^m}{\partial \phi_2'^m} D(\phi_1, \phi_1') D(\phi_2, \phi_2') \tag{4.2}$$

where,

— E_d is the diffracted field,

— E_0 the field amplitude from a spherical source,
— $D(\phi, \phi')$ is the diffraction coefficient and the angles ϕ, ϕ' are defined as in figure 4.10,
— k is the wavenumber (defined previously),
— s_1, s_2, s_3, distances defined as in figure 4.10,
— s_T is the total path distance,

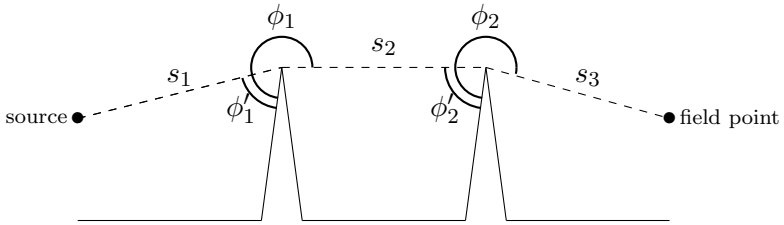

Figure 4.10 – *Geometry for Holm expression.*

Holm showed that in order to have smooth curves (*i.e* no discontinuities at the transition region), the expression of 4.2 should be calculated for an order of 16 in the case of two wedges. Moreover, for the 3 wedges, an order of 30 is required for accurate results. Still, if more wedges are present, more and more terms will be required. For this reason, this solution will not be used for the proposed model because it is not time-efficient. Nevertheless, Holm proposed in [Hol04] a more time-efficient calculation method for higher order diffracted fields. The new optimized expression takes some seconds to predict the field for an order of 100 for a scenario involving 10 edges. Still, this optimization is not enough.

4.6.5 UTD-slope diffraction with distance parameter forcing

4.6.5.1 Principle

As discussed earlier in the previous section, multiple diffractions at the transition zone can be solved by including higher order diffracted fields. Nevertheless, it might be needed to find those diffracted fields for an order of more than 100 (the number cannot be determined for a specific vertical profile). Andersen [And97, And94] proposed a new method within the frame of the UTD to ensure the continuity of the diffracted field at the shadow boundary. The solution will include one higher-order term (the slope diffraction) and will neglect higher order terms. The key principle of the present solution is to enforce the continuity of amplitude and slope by adjusting automatically and separately the length parameters that are present in the diffraction coefficient and in the slope diffraction term. The idea is based on the fact that in order to satisfy the continuity, the diffracted field at the transition boundaries must be one half of the incident field, and hence the method finds the length parameters that satisfy this fact.

Risk [RVCG98] proposed an easier algorithm to implement the method of Andersen by a computer program and validated the obtained results with published reference results. However, the algorithm description was limited to two wedges. Tzaras and Saunders [TS01], proposed to calculate the length parameters for each ray independently leading to added complexity compared to Andersen's method, but it can provide more accurate results. In fact, this method needs a recursive computer algorithm to be generalized. Koutits and Tzaras

[KT06] and Karousos and Tzaras [KT08] provided general expressions for Saunder's method. These expressions will be given in the next subsection.

4.6.5.2 Implementation

The method of Andersen seems to be a good candidate. It is still needed to evaluate if it is realizable from the complexity perspective as well as to evaluate if it is time-efficient from the computational perspective. Figure 4.11 shows the geometry for three wedges with unequal heights. Although figure 4.11 shows only three wedges, the same notation still applies to any number of obstacles. A general expression for the multiple-diffracted field at point N is given by [KT08] :

$$E_N = \left[E_{N-1}D_{N-1} + \frac{\partial E_{N-1}}{\partial n} d_{s_{N-1}}\right] A_{N-1}(S_{N-1}) e^{-jks_{N-1}} \tag{4.3}$$

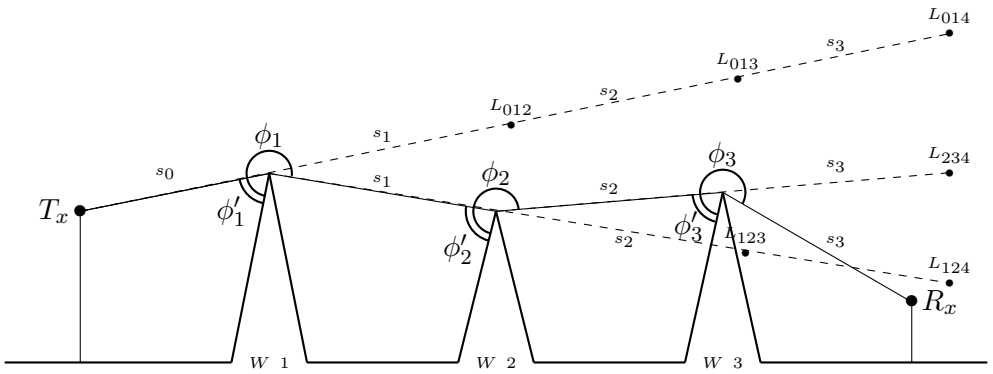

Figure 4.11 – *Propagation path over multiple wedges with unequal heights.*

where,

— E_{N-1} is the field at the wedge N-1,

— D_{N-1} is the diffraction coefficient of the N-1 wedge,

— A_{N-1} is the spreading factor after being diffracted by N-1 wedges, which is given by

$$A_{N-1} = \sqrt{\frac{s_0 + s_1 + ... + s_{N-2}}{s_{N-1}(s_0 + s_1 + ... + s_{N-1})}} \tag{4.4}$$

— $d_{s_{N-1}}$ is the slope diffraction term, which is given by

$$d_{s_{N-1}} = \frac{1}{jk} \frac{\partial D_{N-1}}{\partial \phi'_{N-1}} \tag{4.5}$$

— $\frac{\partial E_{N-1}}{\partial n}$ is the directional derivative of E_{N-1}, which is given by

$$\begin{aligned} \frac{\partial E_{N-1}}{\partial n} = -\frac{A_{N-2}(s_{N-2})}{s_{N-2}} \Bigg[& E_{N-2} \frac{\partial D_{N-2}}{\partial \phi_{N-2}} \\ & + \frac{\partial E_{N-2}}{\partial n} \times \frac{1}{jk} \frac{\partial^2 D_{N-2}}{\partial \phi_{N-2} \partial \phi'_{N-2}} \Bigg] e^{-jks_{N-2}} \end{aligned} \tag{4.6}$$

Let L denote the distance parameter for the diffraction coefficient D, and let Ls denote the distance parameter for the calculation of slope diffraction term ds. The distance parameters use the notation L_{mnk} as shown in figure 4.11, where m is the index of the source of the field, n is the index of the diffracting wedge, and k is the index of the observation point at the shadow boundary. The continuity of the amplitude and slope diffracted field can be guaranteed by finding the values of the distance parameters (L values) that satisfy the following equations [KT08] :

$$L_{mnk} = \left[\frac{E_{mn}(s_{mn} + s_{nk})}{E_{mn}(s_{mn}) A_r(s_{nk}) e^{-jks_{nk}}} \right]^2 \tag{4.7}$$

$$Ls_{mnk} = \left[\frac{s_{nk} \partial E_{mn}(s_{mn} + s_{nk})/\partial n}{\partial E_{mn}(s_{mn})/\partial n A_r(s_{nk}) e^{-jks_{nk}}} \right]^{\frac{2}{3}} \tag{4.8}$$

4.6.5.3 Results and limitations

The distance parameter forcing method was implemented for a limited number of wedges. The results obtained by this method will be validated against some well-known published results. In fact, Holm [Hol96] conducted several tests for many multiple diffraction configurations. These published results are being used by many authors, such as in [RVCG98, TS01], as reference results. Consequently, the validation of this method will be conducted with these results. In particular, the following configurations of Holm [Hol96] will be used :

— Two perfectly conducting wedges with close heights (50 m, 40 m) and with equal interior angles of 60° as shown in figure 4.12(a). The transmitter antenna is at a fixed height of 40 m, while the receiver antenna height varies from -200 m to 200 m (Figure 8 in [Hol96]).
— Two perfectly conducting wedges with the same heights (150 m, 150 m) but with wider interior angles as shown in figure 4.12(c). The transmitter antenna is at a fixed height of 145 m, while the receiver antenna height varies from 0 m to 200 m (Figure 10 in [Hol96]).
— Similar to the first configuration but with three perfectly conducting wedges, two with the same heights and the third one is with a different height (50 m, 50 m, 40 m) respectively. The wedges' interior angles are all equal to 60° as shown in figure 4.12(e). The transmitter antenna is at a fixed height of 40 m, while the receiver antenna height varies from -200 m to 200 m (Figure 9 in [Hol96]).

In the case of two wedges, figures 4.12(b) and 4.12(d) show the diffraction losses obtained by this method for the geometry defined in 4.12(a) and 4.12(c) respectively. These two figures show exactly the same results as those obtained by Holm in [Hol96]. It can be noticed that the diffraction loss is continuous even at the transition regions. Similarly, The diffraction path loss for the three wedges configuration that is defined in figure 4.12(e) is shown in figure 4.12(f). This simulation result shows almost the same result as that obtained by Holm in [Hol96], but with a negligible change in the slope at the shadow boundary (which corresponds to the receiver height of 0 m).

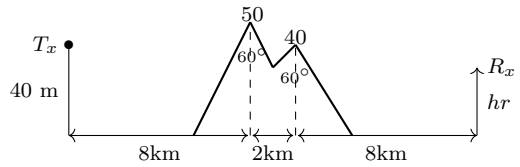

(a) *Geometry for two perfectly conducting wedges (fig. 8 [Hol96]).*

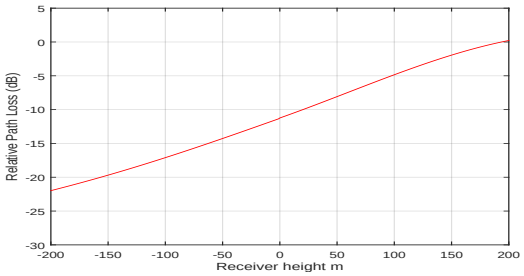

(b) *Diffraction path loss calculated by the distance parameter forcing method for 4.12(a).*

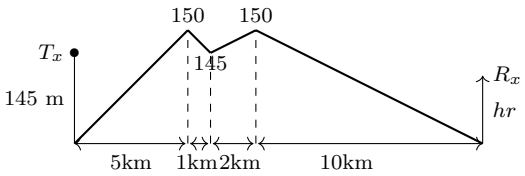

(c) *Geometry for two perfectly conducting wedges with equal heights (fig. 10 [Hol96]).*

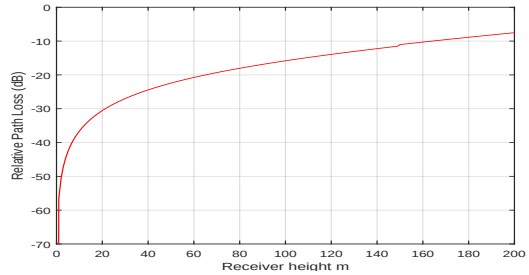

(d) *Diffraction path loss calculated by the distance parameter forcing method for 4.12(c).*

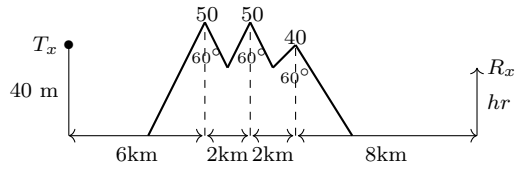

(e) *Geometry for three perfectly conducting wedges (fig. 9 [Hol96]).*

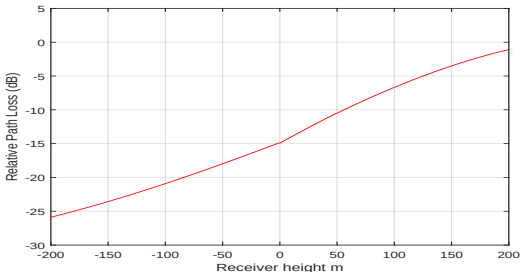

(f) *Diffraction path loss calculated by the distance parameter forcing method for 4.12(e).*

Figure 4.12 – *Validation of the distance parameter forcing method.*

It is important to note that the advantage of this method over the method of Holm [Hol96] is that this method requires only the slope diffraction term (but with choosing the values of L and L_s that ensure the continuity), whereas the method of Holm requires at least 16 higher-order terms for two wedges, 30 higher-order terms for three wedges, and even more terms if the number of wedges increases.

Although the method of forcing the distance parameter is an interesting candidate, it was not used for many reasons. First, in order to generalize the method for any number of wedges with arbitrary heights, a recursive algorithm is required [TS01], which could lead to extra computational loads. The other reason is that, this method is restricted to the case of diffraction by two or more separate wedges [Mik10], and therefore it is not adopted for the case of two joint wedges (flat-plate buildings), which means that the buildings must be represented as wedges.

4.6.6 Capolino and Albani Method

Capolino, Albani, *et al.* [ACMT97] proposed a closed-form solution for high-frequency diffraction problems by a perfectly-conducting thick screen. Capolino and Albani formulated their closed-form expression in a 2D geometry illuminated by a line source. This solution was validated against results obtained from the method of moment (MoM). Furthermore, It was shown that this solution is still applicable when the thickness becomes vanishingly small.

4.6.6.1 Geometry and double diffraction coefficient

Capolino and Albani derived their closed-form expression using the geometry that is shown in figure 4.13. The figure depicts simply a screen of thinness l, which consists originally of two wedges sharing a common face. The second wedge is located in the transition region of the first one. The interior angles of the wedges are $(2 - n_1)\pi$ and $(2 - n_2)\pi$ respectively.

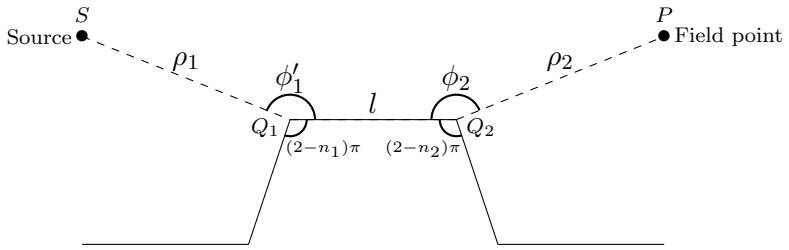

Figure 4.13 – *Geometry for Capolino and Albani Method.*

The double diffracted field $E^d_{12}(P)$ at the observation point P and originated from the source point S is given by :

$$E^d_{12}(P) = E^i(S, Q_1)A(\rho_1, l, \rho_2)D^{s,h}_{12} \tag{4.9}$$

where,

— $E^i(S, Q_1)$ is the incident field at the point Q_1 (the first wedge) from the source point S, and is given as :

$$E^i(S, Q_1) = \frac{e^{-jk\rho_1}}{4\pi\rho_1} \tag{4.10}$$

— $A(\rho_1, l, \rho_2)$ denotes the spreading factor, and is defined as :

$$A(\rho_1, l, \rho_2) = \sqrt{\frac{\rho_1}{l\rho_2(\rho_1 + l + \rho_2)}}e^{-jk(l+\rho_2)} \tag{4.11}$$

— $D^{s,h}_{12}$ denotes the double diffraction coefficient for the soft and hard polarization respectively. It important to note that perpendicular polarization is sometimes referred as soft polarization, and parallel polarization is called hard polarization. The soft and hard diffraction coefficients are given by :

$$D^h_{12} = \frac{1}{4\pi jk}\sum_{p,q=1}^{2}\frac{(-1)^{p+q}}{n_1 n_2}\cot\left(\frac{\Phi^p_1}{2n_1}\right)\cot\left(\frac{\Phi^q_2}{2n_2}\right)\tilde{T}(a_p, b_q, w) \tag{4.12}$$

$$D_{12}^{s} = \frac{-1}{16\pi k^2 l} \sum_{p,q=1}^{2} \frac{(-1)^{p+q}}{(n_1 n_2)^2} \csc^2\left(\frac{\Phi_1^p}{2n_1}\right) \csc^2\left(\frac{\Phi_2^q}{2n_2}\right) \tilde{\tilde{T}}(a_p, b_q, w) \tag{4.13}$$

Equations 4.12 and 4.13 involve the transition functions $\tilde{T}(a,b,w)$ and $\tilde{\tilde{T}}(a,b,w)$, which are defined as :

$$\begin{aligned} \tilde{T}(a,b,w) = \frac{2\pi jab}{\sqrt{1-w^2}} \Bigg[& \mathcal{G}(a, \frac{b+wa}{\sqrt{1-w^2}}) + \mathcal{G}(b, \frac{a+wb}{\sqrt{1-w^2}}) \\ & + \mathcal{G}(a, \frac{b-wa}{\sqrt{1-w^2}}) + \mathcal{G}(b, \frac{a-wb}{\sqrt{1-w^2}}) \Bigg] \end{aligned} \tag{4.14}$$

$$\begin{aligned} \tilde{\tilde{T}}(a,b,w) = \frac{-4\pi (ab)^2}{w\sqrt{1-w^2}} \Bigg[& \mathcal{G}(a, \frac{b+wa}{\sqrt{1-w^2}}) + \mathcal{G}(b, \frac{a+wb}{\sqrt{1-w^2}}) \\ & - \mathcal{G}(a, \frac{b-wa}{\sqrt{1-w^2}}) - \mathcal{G}(b, \frac{a-wb}{\sqrt{1-w^2}}) \Bigg] \end{aligned} \tag{4.15}$$

The transition functions involve three arguments, namely w, a, and b. It also involves the function $\mathcal{G}(x,y)$ that will be defined just after. The arguments are defined as follows :

$$w = \sqrt{\frac{\rho_1 \rho_2}{(\rho_1 + l)(l + \rho_2)}} \tag{4.16}$$

$$a_p = \sqrt{2k \frac{\rho_1 l}{\rho_1 + l}} \sin\left(\frac{\Phi_1^p - 2n_1 N^p \pi}{2}\right) \tag{4.17}$$

$$b_q = \sqrt{2k \frac{\rho_2 l}{\rho_2 + l}} \sin\left(\frac{\Phi_2^q - 2n_2 N^q \pi}{2}\right) \tag{4.18}$$

where, the angles Φ_1^p and Φ_2^q are given as :

$$\Phi_1^p = \phi_1' + (-1)^p \pi \tag{4.19}$$

$$\Phi_2^q = \phi_2 + (-1)^q \pi \tag{4.20}$$

N_p and N_q in equations 4.17 and 4.18 are the integers that can satisfy the following ratios :

$$N_p = \frac{\Phi_1^p}{2\pi n_1} \tag{4.21}$$

$$N_q = \frac{\Phi_2^q}{2\pi n_2} \tag{4.22}$$

Finally, the introduced transition functions were expressed in terms of the Generalized Fresnel Integrals (GFI) $\mathcal{G}(x,y)$. It is an analogue of the ordinary Fresnel integral that is used in the UTD. (Its role is to account for the contribution of the slope term coming from the first diffraction [ACMT97]). The GFI is given by :

$$\mathcal{G}(x,y) = \frac{y}{2\pi} e^{jx^2} \int_x^{\infty} \frac{e^{-j\tau^2}}{\tau^2 + y^2} d\tau \tag{4.23}$$

A simple closed-form and algorithm was described in [FS95]. This algorithm was implemented and the results of the GFI are shown in figure 4.14. These results were validated by comparing them with reference published results (figure 3 in [FS95]).

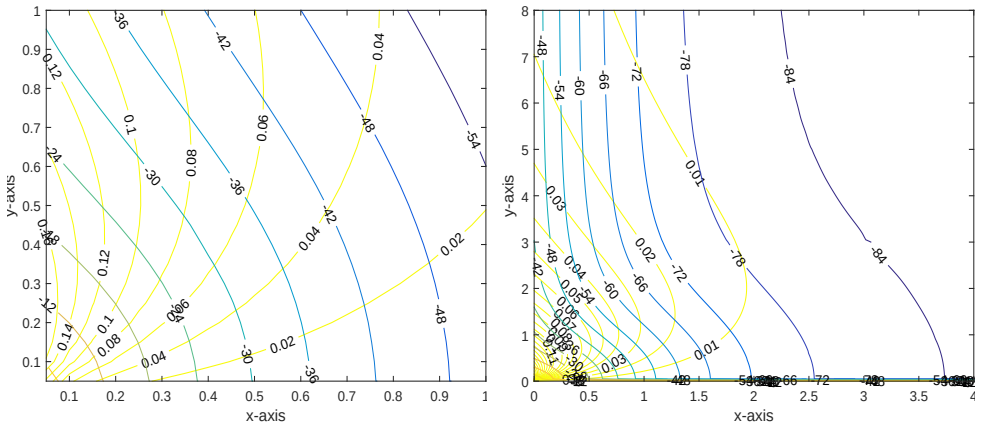

(a) *Amplitude (yellow lines) and phase (blue lines) - level lines of $\mathcal{G}(x, y)$. for a window of (1×1)*

(b) *Amplitude (yellow lines) and phase (blue lines) - level lines of $\mathcal{G}(x, y)$ for a window of (4×8)*

Figure 4.14 – *Generalized Fresnel Integrals validation.*

4.6.7 Application to 2D configurations

Let us verify the behavior of the Capolino and Albani diffraction coefficient in 2D configurations, particularly in the transition zone. To this end, a 2D test configuration as shown in figure 4.15 is used. In this configuration, the second diffracting edge is in the transition zone of the first one. The observation point angle ϕ_2 will vary from 270° to 90° (according to the angle notation of figure 4.15) passing by the transition zone which corresponds to 180°. The study will be conducted for four different source positions *i.e.* ϕ_1' 180°, 185°, 210°, and 240°. The results of the Capolino and Albani diffraction will be compared to those obtained from the UTD method.

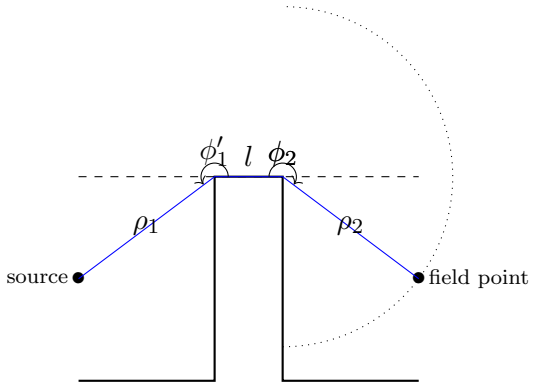

Figure 4.15 – *Geometry for double diffraction by a flat plate.*

Table 4.1 defines all the test parameters, namely the distances from the source point to the first diffraction point (ρ_1), the thickness of the diffracting flat screen (l), the distance from the second diffraction point to the observation point (ρ_2).

It should be noted that the values of ρ_1, ρ_2, l were transposed from acoustic propagation study conducted in [Mik10] in order to use the results as a reference.

Parameter	Value
ϕ'_1	180°, 185°, 210°, 240°
ϕ_2	270° - 90°
ρ_1	26.448λ (3.303 m)
ρ_2	35.264 λ (4.404 m)
l	13.224λ (1.651 m)
$Freq$	2.4 Ghz
Methods	Capolino-Albani and UTD

Table 4.1 – *Test parameters*

The simulation results of figure 4.16 show that Capolino-Albani coefficient has a continuous curve even at the transition boundary. UTD coefficient shows discontinuous behavior at the transition region. The same results were obtained in [Mik10].

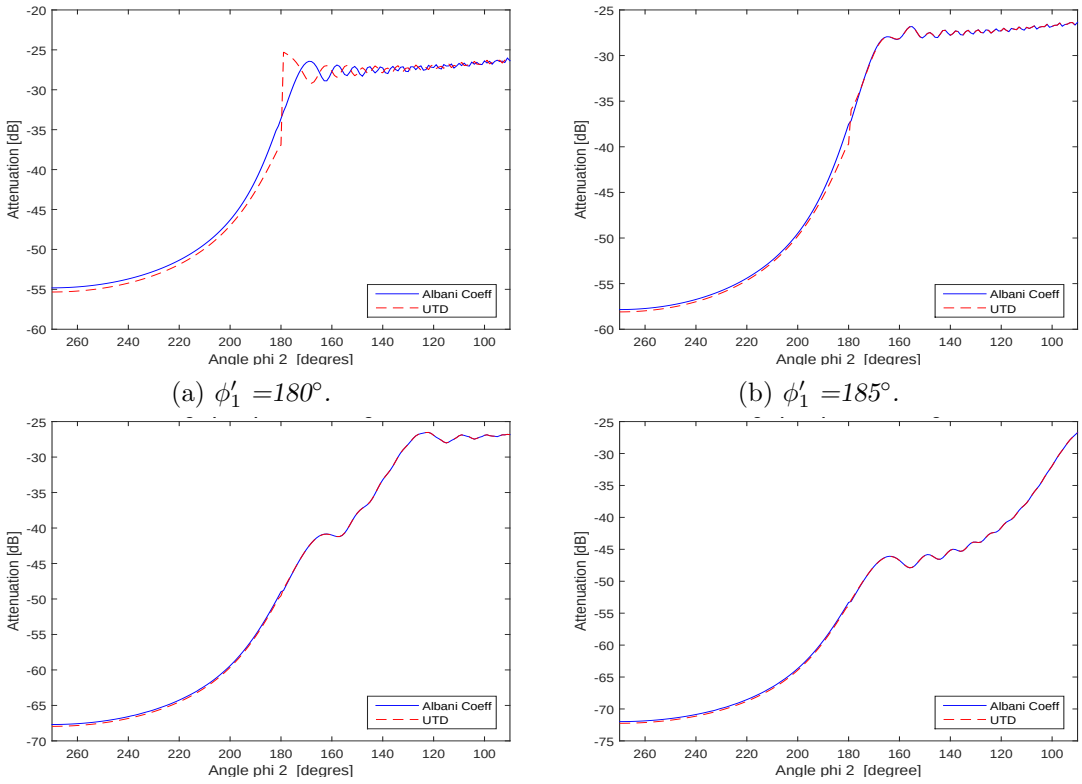

(a) ϕ'_1 =180°.

(b) ϕ'_1 =185°.

(c) ϕ'_1 =210°.

(d) ϕ'_1 =240°.

Figure 4.16 – *Capolino-Albani vs. UTD coefficients in 2D configurations.*

The previous results showed the continuity for a single value of ρ_2. Nevertheless, it is important to ensure the smooth continuity for any value of ρ_2. Figure 4.17(a) shows a 2D configuration containing one building and a grid of receivers distributed behind the building. The transmitter was placed in a way that generates three regions of interest :

— Region 1 : behind the building and below the double diffraction boundary which will have double diffracted rays.
— Region 2 :between the single and double diffraction boundaries.
— Region 3 : above the single diffraction boundary.

The results presented in 4.17(b) show that the attenuation varies smoothly as it can be noticed from the smooth color transition even the at regions' boundaries which confirms, in turn, the continuity of Capolino-Albani diffraction coefficient.

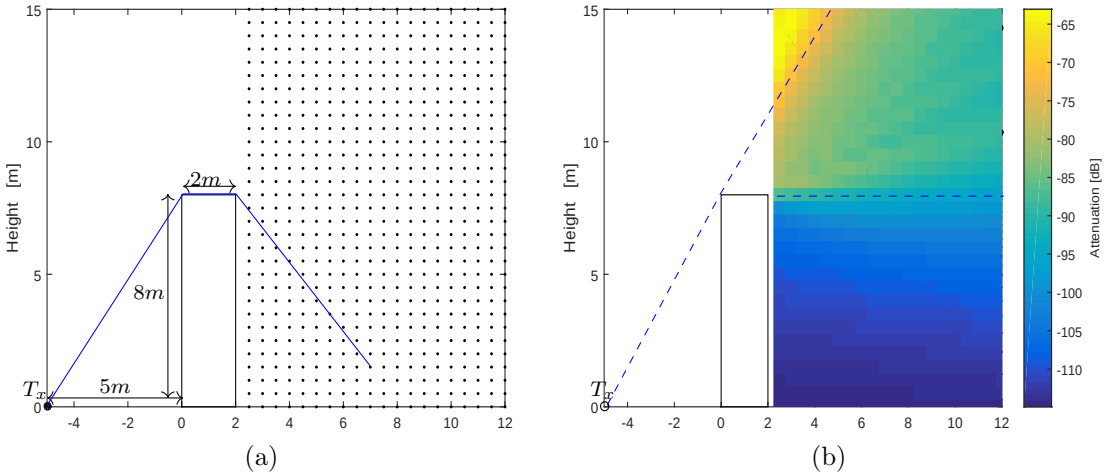

Figure 4.17 – *Continuity of Capolino-Albani diffraction coefficient.*

Until now, it has been shown the continuous behavior of Capolino-Albani diffraction coefficient. However, in order to conclude this set of validation tests in 2D configurations, a new study is conducted to ensure the continuity for any width of the screen. For this purpose, five different widths will be considered : thin screen, $\frac{1}{4}\lambda$, $\frac{1}{2}\lambda$, λ, and $\frac{3}{2}\lambda$. Figure 4.18 shows the geometry used for this test configuration.

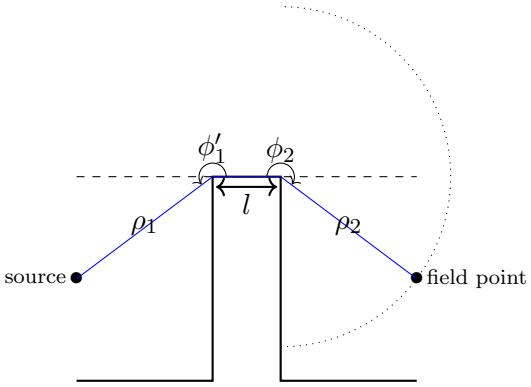

Figure 4.18 – *Geometry for double diffraction by a plate - different plate widths.*

Table 4.2 shows the test parameters, namely the angles of incidence and diffraction (ϕ'_1 and ϕ_2), the distances from the source point to the first diffraction point (ρ_1), the thickness of the diffracting screen (l), the distance from the second diffraction point to the observation point (ρ_2).

Parameter	**Value**
ϕ'_1	210°
ϕ_2	270° - 90°
ρ_1	26.448λ (3.303 m)
ρ_2	35.264 λ (4.404 m)
l	thin screen, $\frac{1}{4}\lambda$, $\frac{1}{2}\lambda$, λ, $\frac{3}{2}\lambda$
$Freq$	2.4 Ghz
Method	Capolino and Albani method

Table 4.2 – *Test parameters*

The results of this study are presented in figure 4.19. It presents the attenuation level due to the diffraction. Different attenuation curves are traced in function of ϕ_2 for different thicknesses of the screen. The position of the receiver varies from 270° to 90°. It can be observed that Capolino and Albani method remains valid, in particular at the transition boundary, for any thickness of the plate. It is also noted that more attenuation is experienced as the plate thickness increases.

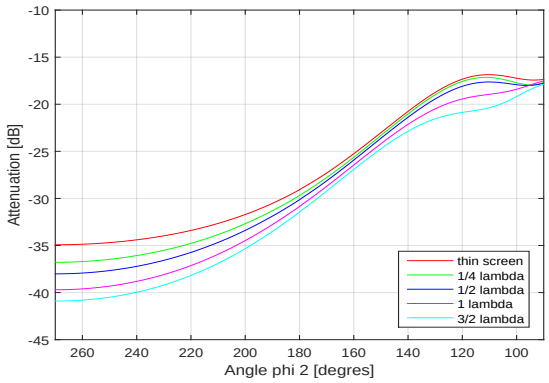

Figure 4.19 – *Simulation results of different thicknesses.*

4.6.8 3D Double diffraction coefficient

Capolino and Albani method was extended in [Mik10] and [ACMT97+] to handle 3D diffraction problems. New formulas will be derived for a 3D general configuration as shown in figure 4.20. Similar equations as those derived in subsection 4.6.6.1 will be presented for 3D configurations.

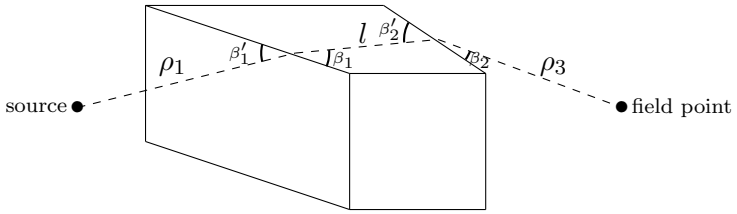

Figure 4.20 – *3D Geometry for Capolino-Albani method.*

The double diffracted field is given by :

$$E^d(P) = E^i(Q)A(\rho_1, l, \rho_2)D_{12}^{s,h} \tag{4.24}$$

$A(\rho_1, l, \rho_2)$ denotes the spreading factor, and is defined as :

$$A(\rho_1, l, \rho_2) = \sqrt{\frac{\rho_1}{l\rho_2(\rho_1 + l + \rho_2)}}e^{-jk(l+\rho_2)} \tag{4.25}$$

$D_{12}^{s,h}$ denotes the double diffraction coefficient for the soft and hard polarization respectively, and is defined as [Mik10, ACMT97+] :

$$D_{12}^{s,h} = \frac{1}{4\pi jk \sin\beta_1' \sin\beta_2} \sum_{p,q=1}^{2} \frac{(-1)^{p+q}}{n_1 n_2} \cot\left(\frac{\Phi_1^p}{2n_1}\right) \cot\left(\frac{\Phi_2^q}{2n_2}\right) \tilde{T}(a_p, b_q, w) \tag{4.26}$$

where, a_p and b_q are defined as :

$$a_p = \sqrt{2k\frac{\rho_1 l}{\rho_1 + l}} \sin\beta_1' \sin\left(\frac{\Phi_1^p - 2n_1 N^p \pi}{2}\right) \tag{4.27}$$

$$b_q = \sqrt{2k\frac{\rho_2 l}{\rho_2 + l}} \sin\beta_2 \sin\left(\frac{\Phi_2^q - 2n_2 N^q \pi}{2}\right) \tag{4.28}$$

4.6.9 Application to 3D configurations

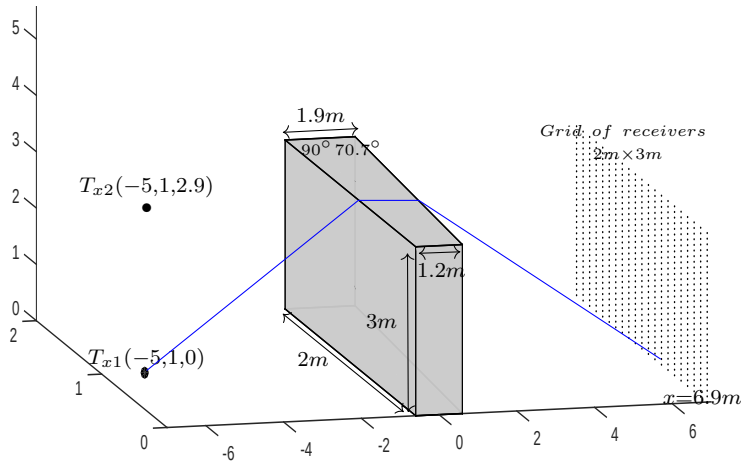

Figure 4.21 – *Capolino and Albani 3D test configuration.*

Capolino and Albani 3D coefficient will be tested in a 3D configuration as shown in figure 4.21. Two transmitter positions were placed in this test configuration. The first one (T_{x_1}) is located away from the transition region and the other one (T_{x_2}) is placed close to the transition boundary. A grid of receivers will be used to estimate the attenuation using Capolino-Albani and the UTD methods. Figure 4.22(a) shows the attenuation results for T_{x_1} using Capolino-Albani and the UTD. The difference between the two methods is zero everywhere except at the transition region. Similarly, figure 4.22(b) shows the attenuation results but for T_{x_2}, this time the difference is greater than zero especially as one moves towards the transition region. This is due to the discontinuity of the UTD at the transition boundary.

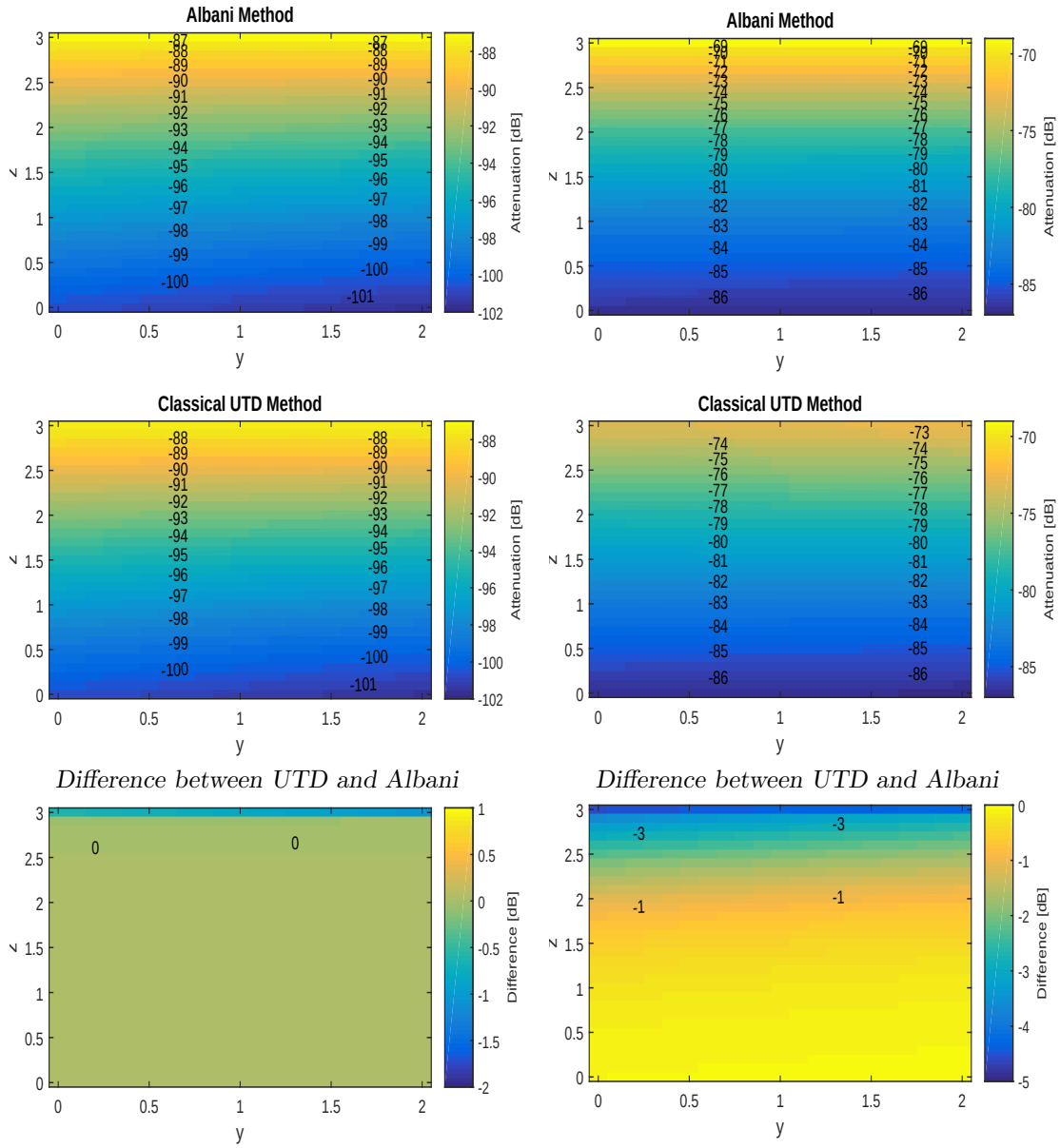

(a) *Results for* T_{x_1} (b) *Results for* T_{x_2}

Figure 4.22 – *Capolino and Albani 3D coefficient validation.*

4.7 Model Validation

Vertical propagation was integrated into the existing horizontal model to obtain a 2.5D model that considers the lateral propagation as well as the propagation in the vertical plane. Capolino and Albani method was adopted for estimating the electric field in the vertical plane. Global model validation is now required for the model to ensure that it provides good estimations.

4.7.1 Global validation via Munich measurements

It was shown previously through Munich site that lateral propagation is predominant only for a certain area around the transmitter so it fails to predict the field outside this range. Therefore, the same test scene will be used to validate and estimate the performance of the new model in terms of accuracy and execution time after introducing the vertical plane to the model. In fact, this validation phase can fairly reflect the model performance because it is conducted against field measurements through long measurement routes. Before addressing the model validation, next section will discuss the averaging method to get the mean radio signal power for Munich site.

4.7.1.1 Local average power estimation

COST231 project specifies that the measured signal was averaged over a sector of approximately 10 m, the center of this sector corresponds roughly to the location of the receiver. However, it does not give further details of the relevant parameters such as the number of considered samples, the minimum distances between the samples, if a sliding window or a filter was further used to smooth the measurement curves. Therefore, the following averaging parameters were adopted for the simulation results :

- Averaging sector = 10 m (corresponds to 31.57 λ).
- Minimum distance (L) = 0,88 m (corresponds to about 2.78 λ).
- Number of samples (N) = 98 samples/receiver (grid of receivers).
- Number of receivers :
  - Metro200 : 970×98 = 95060 receivers.
  - Metro201 : 355×98 = 34790 receivers.
  - Metro202 : 1031×98 = 101038 receivers.

Figure 4.23 shows that the reception point is surrounded by an averaging sector of 10 m composed of a grid of 98 receivers distributed according to the above-mentioned parameters. The average power of these receivers will be considered. It should be noted that these parameters respect the Lee criteria [Lee85].

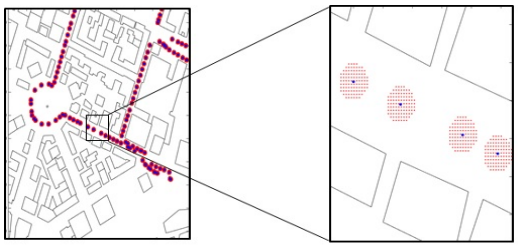

Figure 4.23 – *Averaging sector - Munich site.*

4.7.1.2 Model performance

The test scene of Munich site and the three measurement routes were modeled in XML files. Then, simulation were conducted for each routes with the following parameters :

— Frequency : 947 MHz.
— 3R1D in the horizontal plane.
— Direct path in the vertical plane.
— Averaging sector of 10 m.

The simulation results are then compared with the measurements as shown in figures 4.24(a), 4.24(b), and 4.24(c). The results of the final model for the three routes show globally a very good agreement with the measurements but with some fluctuations around the mean value. Nevertheless, it should be noted that the simulation curves of figure 4.24 were not smoothed as proposed by some authors [RVF+98, TPHB14, dah] to remove the fast fading fluctuations as shown later on.

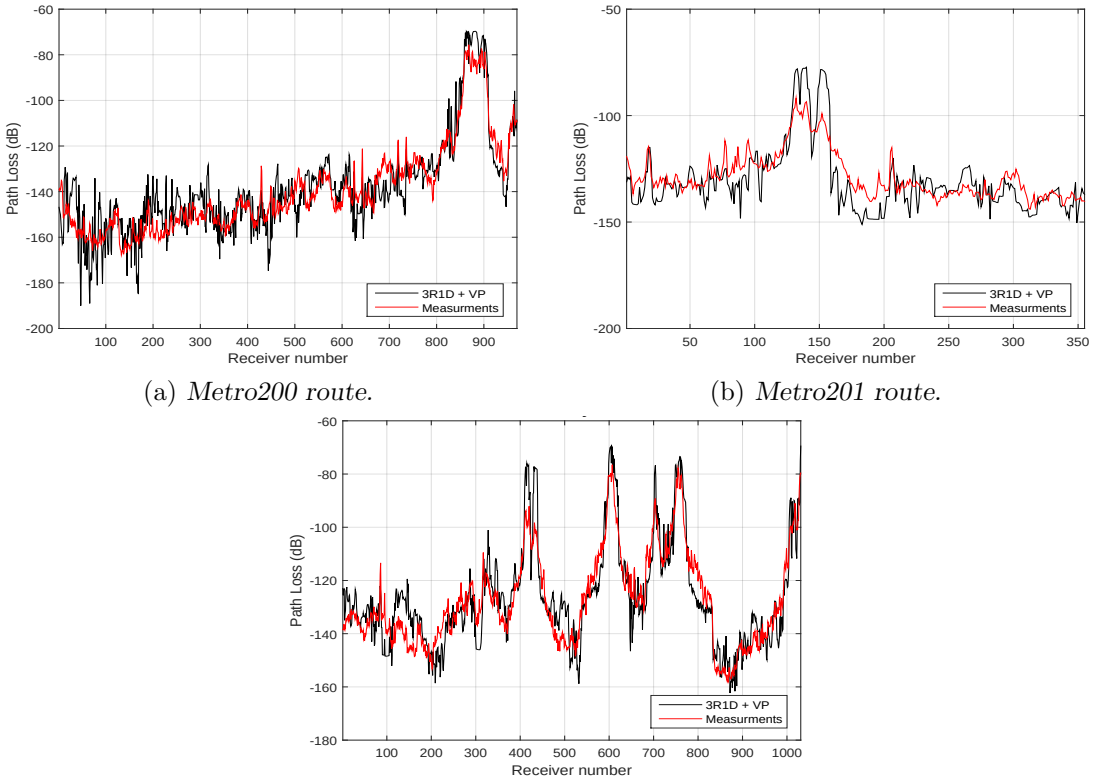

(a) *Metro200 route.*

(b) *Metro201 route.*

(c) *Metro202 route.*

Figure 4.24 – *Model performance.*

In spite of the good agreement, it is important to evaluate the model performance with numerical values. To this end, some error indicators were calculated, namely : the mean error η[dB] , mean absolute error Abs η[dB], and the standard deviation σ [dB]. Table 4.3 presents these error indicators between the measurements and predictions for the three measurement routes. In fact, the mean error gives small values because negative values are compensating for positive values but it is widely used in the literature as a global error indicator. Table 4.3

shows also the mean absolute error that is about 7 dB for the three measurements routes, which means that the vertical model performs well because it is the predominant propagation mechanism for the majority of the reception points.

	Metro 200	**Metro 201**	**Metro 202**
η[dB]	0.84	-2.3	0.65
Abs η [dB]	7.55	7.03	6.94
σ [dB]	9.38	8.76	8.48

Table 4.3 – *Error between the measurements and model prediction (HP : 3R1D, VP : Capolino and Albani Method)*

In order to compare the Capolino and Albani method with the classical UTD method, the same error indicators were calculated for the three routes with the same simulation parameters as before. Table 4.4 shows that the error values are intolerable for all the measurement routes. For example, for the first route (Metro 200), the mean error is -10.5 dB and the mean absolute error is about 13 dB.

	Metro 200	**Metro 201**	**Metro 202**
η[dB]	-10.5	-7.04	-4.81
Abs η [dB]	13.34	10.79	9.39
$\sigma[dB]$	14.8	11.74	11.30

Table 4.4 – *Error between the measurements and model prediction (HP :3R1D, VP : classical UTD)*

4.7.1.3 Sources of error

Many sources of error have contributed to the overall error. Globally, a large part of the error is due to the fact that the vegetation losses are not considered which leads to the peaks (overestimation) as shown earlier in section. Another important source of error is that the geometrical representation of the city models all the buildings with a flat roof which is not always the case (triangle shaped roofs are considered as flat). Furthermore, not all the vertical paths were considered due to the time restrictions.

It should be mention that part of the error is due to the physical model as Capolino-Albani model is for perfectly conducting materials, therefore the buildings were considered as perfectly conducting. For the sake of comparison, the UTD model in table 4.4 was also computed for conducting materials.

4.7.1.4 Curve smoothing

It is proposed by many authors to smooth the curves to remove the local variation and local peaks of the received signal, therefore, it enhances the accuracy of the prediction. In [dah], an averaging distance of 80λ was proposed. Risk *et al.* [RVF$^+$98] used a moving window of 20 points to smooth the lateral and vertical predictions. This value was empirically chosen because the lowest standard deviation was achieved for this value. In [TPHB14] an averaging window of 21 samples was used. In fact, 20 points is a very large averaging distance because it corresponds to 760λ.

Although some published results in the literature are using a wide averaging window, the simulation results of figures 4.24 will be smoothed by a small window of 3 samples (one before and one after). Table 4.5 shows that smoothing reduces the mean absolute error to about 6 dB and the standard deviation to about 7 dB for all the routes as the local fluctuations are removed, however, the mean error remains unchanged. It should be noted that better results can be achieved by smoothing over larger sliding windows or by using the window size that minimizes the error as proposed in [RVF+98] (leads to large averaging distance). Anyway, the smoothing process is independent of the model because it is a post-processing action. Therefore, the end-user can use the sliding window as needed.

	Metro 200	**Metro 201**	**Metro 202**
η[dB]	0.84	-2.3	0.65
Abs η [dB]	6.66 - 5.85	6.46 - 5.77	6.52 - 5.95
$\sigma[dB]$	8.37 - 7.42	8.06 - 7.15	7.98 - 7.32

Table 4.5 – *Error between the measurements and model prediction (HP : 3R1D, VP : Capolino and Albani Method) with curve smoothing.*

Figures 4.25 reproduce the same curves 4.24 but they were smoothed with a small averaging window of 3 samples. Local peaks and local fluctuations are almost removed leading to better agreement with the measurements and lower error values.

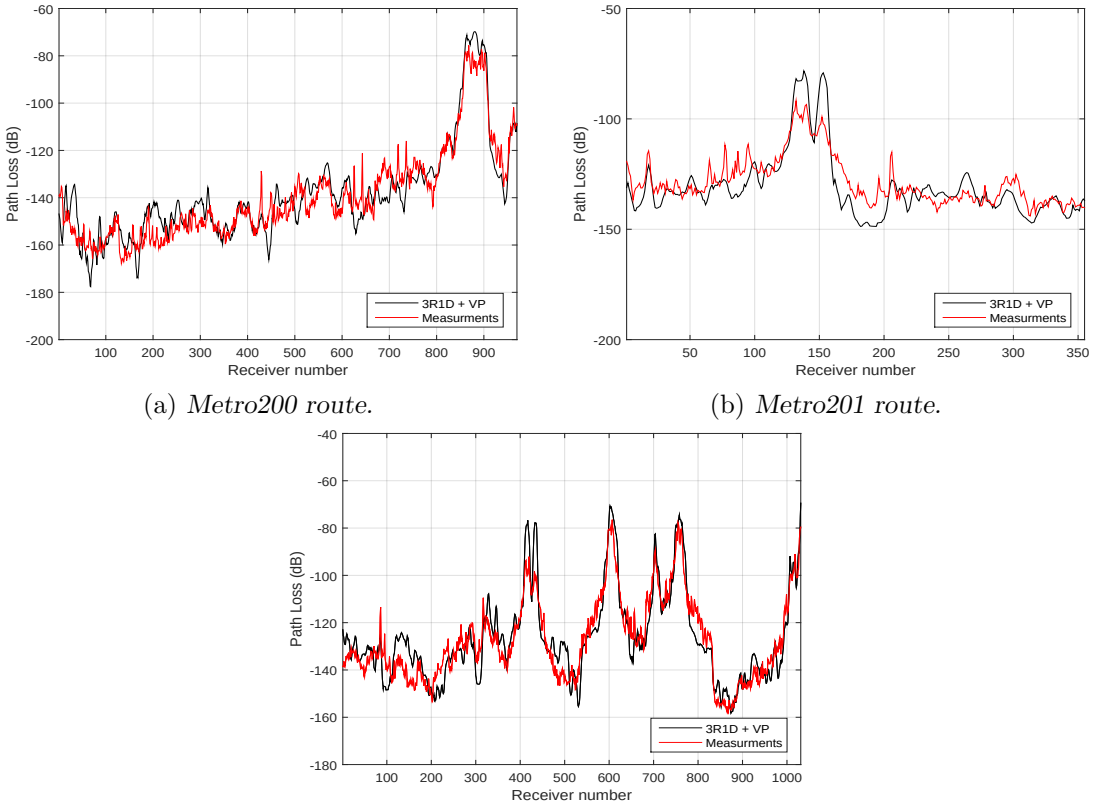

(a) *Metro200 route.*

(b) *Metro201 route.*

(c) *Metro202 route.*

Figure 4.25 – *Model performance - curve smoothing.*

4.7.2 Computational time

Table 4.6 presents the overall model performance in terms of execution time. It shows that the vertical model adds very slight extra computational loads to the overall computational time as it takes less than 1 ms per link for extracting the vertical profile, finding the vertical path, and for estimating the electrical field (according to Capolino and Albani model). The execution time for the vertical plane was also calculated for all the receivers for the three measurement routes, the model takes less than 1 s for all the receivers as shown in table 4.6.

The horizontal model performance for Munich site was also calculated to show that the overall model is fast even for large scenarios. In fact, the three routes show similar behavior in terms of execution time because the computational time of the visibility technique is almost independent of the number of receivers (the same visibility tree is used for all the receivers). Table 4.6 shows that the combination 1R1D takes about 1s for all the receivers, 7 s for the combination 2R1D, while the combination 3R1D takes about 30 s. It should be noted that it is still possible to obtain very fast performance through the preprocessing mode and through limiting the simulation areas as discussed in chapter 3. Table 4.6 does not include the execution time per link for the horizontal plane because it is not very dependent on the number of receivers.

Propagation mode	**Execution Time**	**Metro 200 970 receivers**	**Metro 201 355 receivers**	**Metro 202 1031 receivers**
Vertical plane	All receivers	870 ms	480 ms	820 ms
	Per link	0.9 ms	1.3 ms	0.8 ms
Horizontal plane 1R1D	All receivers	1.1 s	1.2 s	1.2 s
	Per link	–	–	–
Horizontal plane 2R1D	All receivers	7.4 s	7.6 s	7.8 s
	Per link	–	–	–
Horizontal plane 3R1D	All receivers	30.7 s	32.0 s	30.6 s
	Time : per link	–	–	–

Table 4.6 – *Computational time*

4.8 Vertical propagation impact on Charles de Gaulle - Étoile scene

Lateral propagation was mainly the predominant mechanism for Charles de Gaulle - Étoile scene (*cf.* chapter 3). Consequently, the horizontal model was able to provide fairly accurate estimation for the majority of the receivers as shown in figure 4.26(b). Nevertheless, there were some reception points that were not accessible (covered) even for a large number of lateral interactions because the waves propagate predominantly vertically for these points. In order to confirm this, the electric field is estimated via the final model using the following simulation parameters : 4R1D in the horizontal plane and the direct vertical path. Figure 4.26(a) shows globally a good agreement with the measurements for the whole route. It should be noted that the main source of error is due to the geometrical model and because it misses the full 3D propagation paths that can contribute to the total electric field.

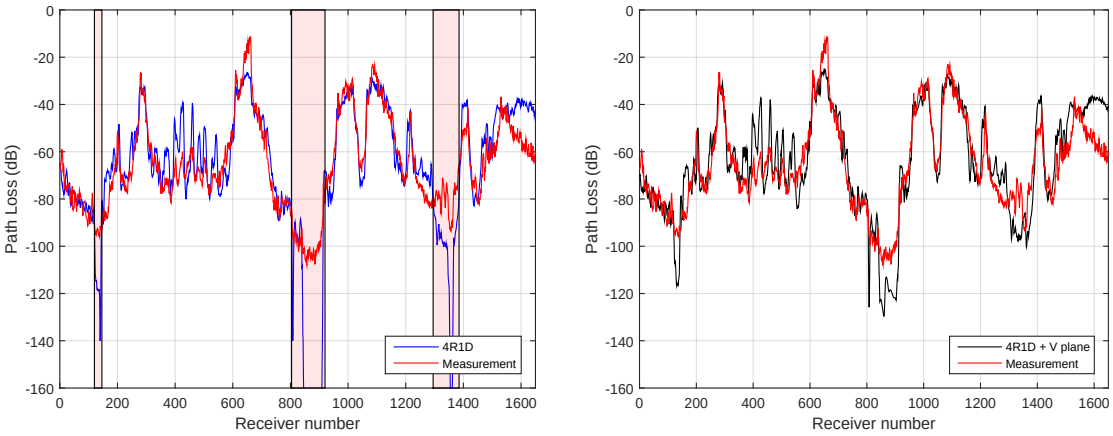

(a) *Simulation resuts - lateral propagtion.* (b) *Simulation resuts - lateral + vertical propagtion.*

Figure 4.26 – *Simulation results of Charles de Gaulle - Étoile, scene with/without the vertical plane.*

4.9 Conclusion

This chapter started by describing Munich site and its three measurement routes in order to assess if the model that considers only the lateral propagation is valid for any urban configuration. It has revealed that the horizontal model is only valid over a certain range of distances around the transmitter. Good agreement was obtained within this range of validity, however, beyond this range, the model is not valid anymore because the contributions of the vertical paths are becoming more dominant in these regions. That is the reason why a propagation model in the vertical plane should be added to complete the existing model to be valid in all urban configurations (2.5D model).

In urban scenarios, multiple diffractions over rooftops are very likely to occur between a series of buildings having similar or close heights, which means that one edge could be in the transition region of the next one. In this case, the classical UTD fails to predict correctly the electric filed. Therefore, a literature review of the most common models that address the mentioned issue was given. The review revealed that the UTD-slope diffraction with distance parameter forcing (Andersen's method) and Capolino and Albani method were the most two relevant methods. These two models were evaluated. Capolino and Albani diffraction coefficient was integrated to the existing model and then validated against some published results.

Finally, the global model performance was evaluated by comparing the simulation results with the three measurement routes of Munich site. The simulation results were averaged over a sector of 10 m. The overall model showed good performance when comparing to the measurements. The absolute mean error of the simulation was found to be about 6 dB compared to the measurements. It should be noted that the vertical propagation model has no extra time loads since it has a negligible computational time (execution time for the direct vertical ray *i.e* < 1 ms per link). In fact, we can say that the final model satisfies the project's requirements since it gives fairly accurate results, considers the propagation scene, supports a large number of nodes, can deal with the mobile nodes, and within a reasonable time.

Chapter 5

Integration and case study

Contents

5.1 Introduction

Chapter 3 and 4 proposed radio propagation models along with algorithms and techniques that made these models fast and sufficiently accurate at the same time. Chapter 5 will discuss many key points about the integration of the implemented radio module into the final platform. To this end, chapter 5 was structured as follows : section 5.2 will give a brief overview of CupCarbon in which the radio module will be integrated. Then, it illustrates the procedure followed to integrate the radio models into Cupcarbon. Section 5.3 discusses the encountered problems during the integration phase mainly because of the geometry databases and how they can be resolved. Section 5.4 aims to re-validate the radio models but this time within the final platform and with using a free source of geometry (OpenStreetMap data). Finally, section 5.5 presents a real case study of a number of moving sensors in an urban configuration in order to show the importance of using realistic channel models that take into account the propagation environment.

5.2 Integration into CupCarbon

5.2.1 CupCarbon

As presented in chapter 1, CupCarbon is the main kernel of PERSEPTEUR Project. CupCarbon is a Smart City and Internet of Things Wireless Sensor Network (SCI-WSN) simulator for both scientific and educational purposes. Its objective is to provide reliable simulations for WSNs, mainly in terms of propagation and interference of signals. It is very useful for designing, visualizing, validating, and debugging distributed algorithms for real projects such as environmental data surveillance. It also supports engineers and researchers to test their wireless topologies, protocols, *etc.* in a 3D urban environment.

Networks can be easily designed with CupCarbon's user interface because it is possible to deploy sensors directly on the map. CupCarbon uses the OpenStreetMap (OSM) framework, which will be the geometry source for the deterministic radio propagation models. Two simulation environments are offered by CupCarbon. The first simulation environment enables the design of mobility scenarios and the generation of events. The other simulation environment represents a discrete event simulation which takes into consideration the mobility scenarios defined in the first environment.

Besides that, CupCarbon includes many interesting features such as : the ability to simulate the interferences of signals, energy consumption model, easy script language (SenScrip) to program sensor nodes, intelligent mobility, user-friendly graphical interface, ability to split nodes into separate networks, clear visualization of the network and the working environment *etc.* It also includes some WSN protocols such as ZigBee, LoRa, and WiFi. Figure 5.1 shows Cupcarbon's graphical interface with a number of static and moving sensor nodes in Brest city.

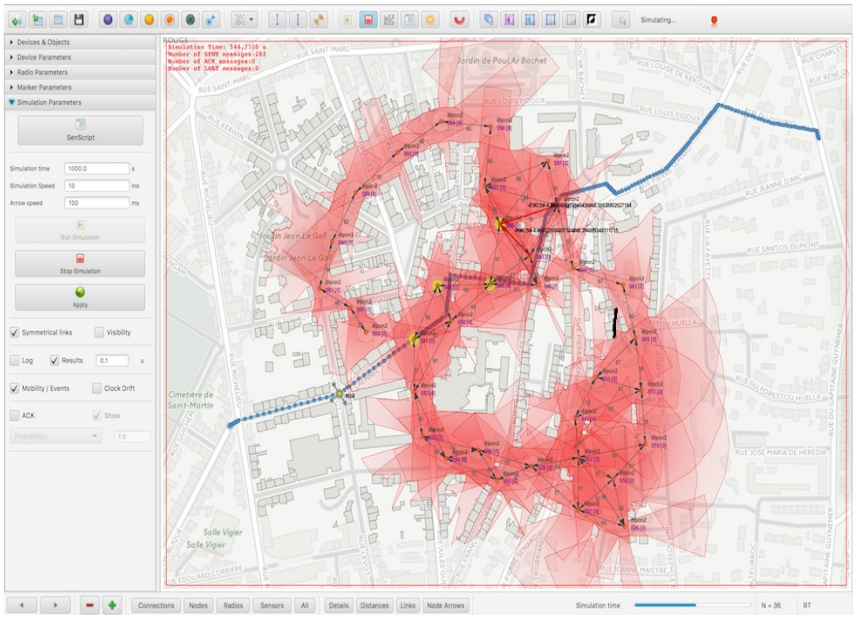

Figure 5.1 – *CupCarbon user interface.*

5.2.2 Integration procedure

The developed radio propagation models were validated previously in order to ensure the optimal performance both in terms of accuracy and computation time. Therefore, the final stage is to integrate the developed algorithms into CupCarbon without affecting or degrading the performance. The integration process will pass through many steps as explained in the next subsection.

5.2.2.1 Application Programming Interface

The radio models were integrated as an Application Programming Interface (API). This choice makes it easier to integrate the radio models into CupCarbon because the API abstracts the underlying implementation and performs all the internal steps for fetching the output without requiring to integrate the source code into that platform.

Accordingly, the radio API was designed to take only the required simulation parameters and the geometry database to launch the computation and delivers back the required channel estimations without having access to the operations occurring behind the scenes. The end-user can define (through CupCarbon) the simulation parameters for the API (for the horizontal and vertical plane) as follows :

```
/* --- Horizontal plane parameters --- */
int nbRefl=1, nbRefr=0, nbDiff=1; /* No. of reflexions, refractions, diffractions */
VTSim.setInteractions(nbRefl,nbRefr,nbDiff); /* Setting the No. of interactions */
VTSim.range = 200;                /* Maximum horizontal range [m] */
VTSim.maxNoHorizonatlPaths = 100; /* Maximum number of paths (horizontal plane) */
```

```
/* --- Preprocessing parameters of the visibilty tree --- */
VTSim.saveTrees = false;         /* Option to preprocess and save visibilty trees */
VTSim.step_size = 5.0;           /* Step size between preprocessed trees*/
VTSim.preCalculated = false;     /* Option to use the saved trees */

/* --- Vertical plane parameters --- */
VTSim.addVerticalPath = false;    /* Option to include the vetical paths */
VTSim.all_Vertical_Paths = false; /* Option to find all or just the direct path */
VTSim.groundReflexion = false;    /* Add a ground reflection before the receiver */
VTSim.maxNoVericalPaths = 1;      /* Maximum number of paths (verticalplane) */
```

It is important to note that the API outputs the channel estimation as text files with extensions : *.BE for narrow-band simulations and *.RI for wide-band simulation (Complex Impulse Response).

5.3 Geometry databases

CupCarbon uses OpenStreetMap (OSM) framework to obtain the geometry databases, that is why the API is still not ready to be used at this stage since the algorithms developed in the API requires geometry databases described in units of meters. In fact, the metric system was strongly required in the algorithms in order to facilitate the calculation of many channel parameters such as attenuation, phases *etc.* This means that the OSM geometry needs to be processed before using the API, which will be discussed in the following subsections.

5.3.1 GPS coordinate system conversion

OpenStreetMap data are defined as polygons having a number of points, each point consists of a pair of values (latitude and longitude). Therefore, the first encountered issue is to how to convert the exported GPS coordinates into the Cartesian coordinate system. Many conversion methods can be found in the literature but the adopted solution is the Lambert93 projection method because it is the official map projection in France since 2000. The details of the conversion method will not be discussed because it is beyond the scope of this chapter.

5.3.2 Geometry database simplification

The polygons defined in the geometry database contain a large number of points (please note that now geometry database is taken from OpenStreetMap and converted to the Cartesian coordinate system). Many of them add almost nothing or, at best, contribute very little to the precision. On the other hand, these unnecessary details reduce considerably the performance of the visibility tree method and they take a huge amount of memory as well. Therefore, in order to ensure the best performance of the API, it is necessary to simplify the outlines that are defined in the geometry database before using it as an input for the API.

The idea is how to simplify the contours to the maximum possible extent but without deforming the shape. Douglas-Peucker method is the best candidate for this purpose [XWW11]. It is a simple recursive algorithm that maintains the shape of the contour but with much fewer points. The degree of tolerance is defined by a user-defined parameter ϵ. The algorithm starts initially with the two endpoints. It marks always these two points to be kept. It then finds the point that is furthest from the line segment connecting the two endpoints. If the furthest point is within the value of ϵ from that line segment, then this point will be removed from the contour, otherwise, the point must be kept. The algorithm recursively calls itself until all the points are treated. Therefore, the simplified contour consists of a subset of the points that defined the original one.

To better understand Douglas-Peucker method and its effect on a given contour, it will be applied to a complex building as shown in figure 5.2(a). Table 5.1 shows that the unsimplified building consists initially of 138 face (which is a considered as a large number of faces for a single building). Then, the simplification was applied using several values of ϵ : 0.30, 0.40, 0.50, 0.75, 1.0, 1.5, and 2.0. The geometry was considerably simplified by this method as shown in figures 5.2(b) - 5.2(g). This can be confirmed by table 5.1 that presents the number of faces for each value of ϵ. The number of faces is reduced considerably from 138 faces to only 12 faces as the tolerance increases.

This simplification is a very important step because it has a great impact on the performance in two ways, less memory usage, considerable gain in time. It was found empirically that a tolerance value of about 0.50 - 1.0 gives a good simplification and maintains the same original shape as well. However, a higher value than the proposed range can be used according to the required degree of accuracy but it could lead to shape distortion as can be noticed in figure 5.2(g) with $\epsilon = 1.5$.

Epsilon value	**No. of Faces**
Unsimplified coordinates	138
Epsilon = 0.30	30
Epsilon = 0.40	27
Epsilon = 0.50	26
Epsilon = 0.75	23
Epsilon = 1.00	23
Epsilon = 1.50	18
Epsilon = 2.00	12

Table 5.1 – *Geometry simplification.*

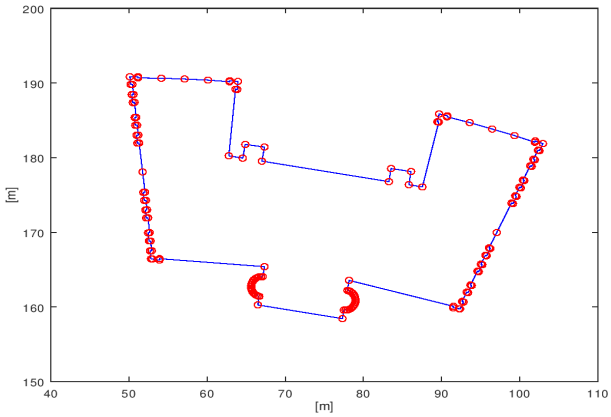

(a) *Unsimplified coordinates.*

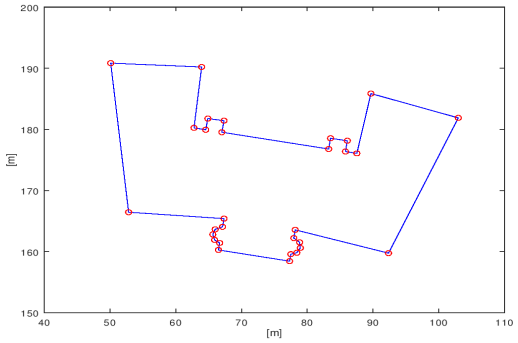

(b) *Epsilon 0.3.*

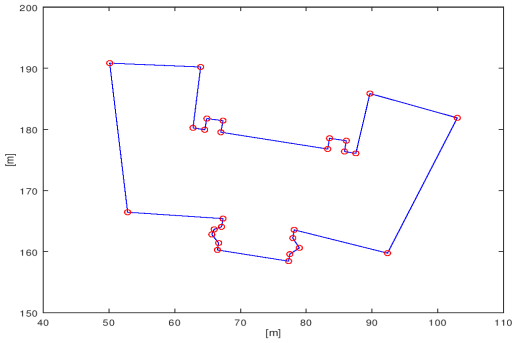

(c) *Epsilon 0.4.*

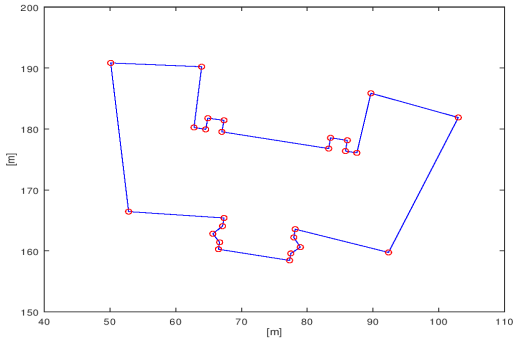

(d) *Epsilon 0.5.*

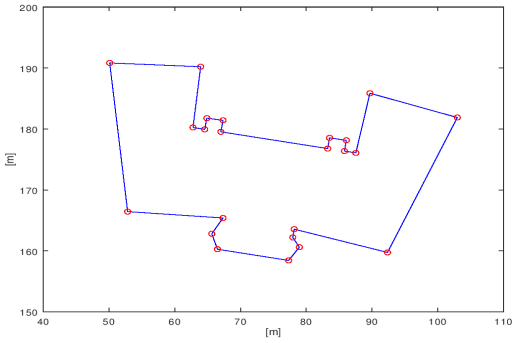

(e) *Epsilon 0.75*

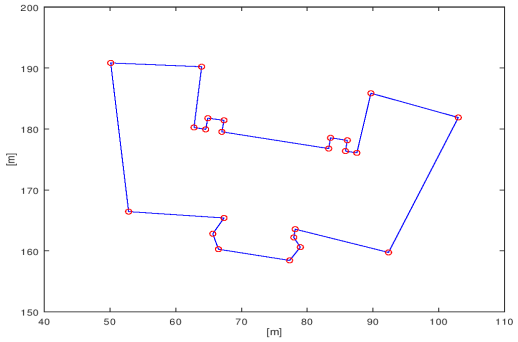

(f) *Epsilon 1.0.*

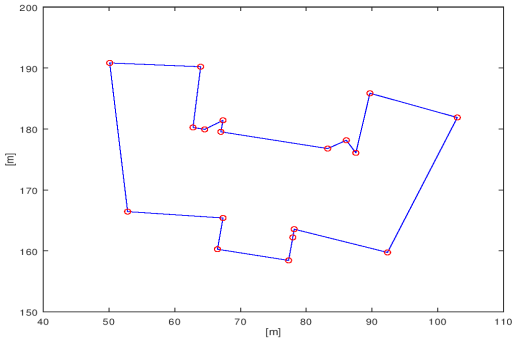

(g) *Epsilon 1.5.*

Figure 5.2 – *Geometry simplification.*

5.3.3 Precision of geometry databases

OpenStreetMap is one of the major sources of geometry databases. The major two issues were resolved in the previous two subsections. However, many other issues regarding OpenStreetMap geometry databases cannot be easily resolved. The main important points that were noticed are :

— OSM databases do not export all the geometrical data so some buildings are missing in the exported file. This will certainly have an impact on accuracy.
— OSM databases do not give accurate building heights for some geographical areas.
— OSM databases may have inaccuracies in the GPS coordinates which leads to uncertainty in the converted Cartesian coordinates.

It should be noted that the API is ready at this stage to be used in CupCarbon, therefore the objective of the next section is to validate and to evaluate the performance of the API.

5.4 API validation

The radio algorithms have been already validated and the performance has been assessed as discussed in chapters 3 and 4. However, it is still important to ensure that the API still gives similar performance as before. For this purpose, the propagation scene of Charles de Gaulle - Étoile, Paris, that was used in chapter 3, will be reused again but this time the scene geometry will be taken directly from CupCarbon user interface as it is shown in figure 5.3.

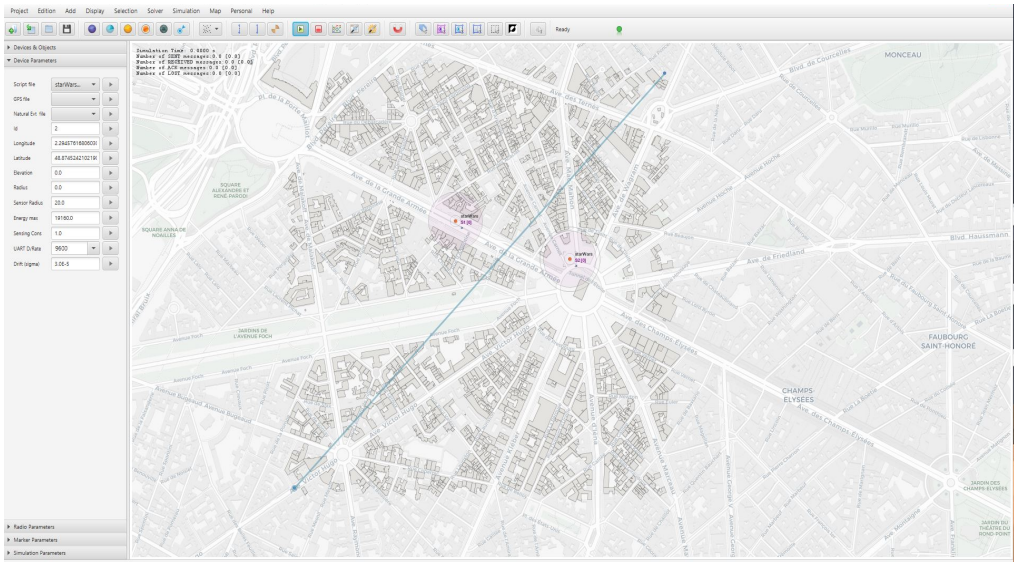

Figure 5.3 – *API validation - CupCarbon user interface.*

The geometry of this scene will go internally through the simplification process and then it will be used as an input for the integrated API. Figure 5.4 shows the differences between the modeled scene of chapter 3 (figure 5.4(a)) and the extracted scene from OpenStreetMap (figure 5.4(b)). It can be noticed that they are fairly similar but the latter misses some building which will surely have an impact on the estimation accuracy.

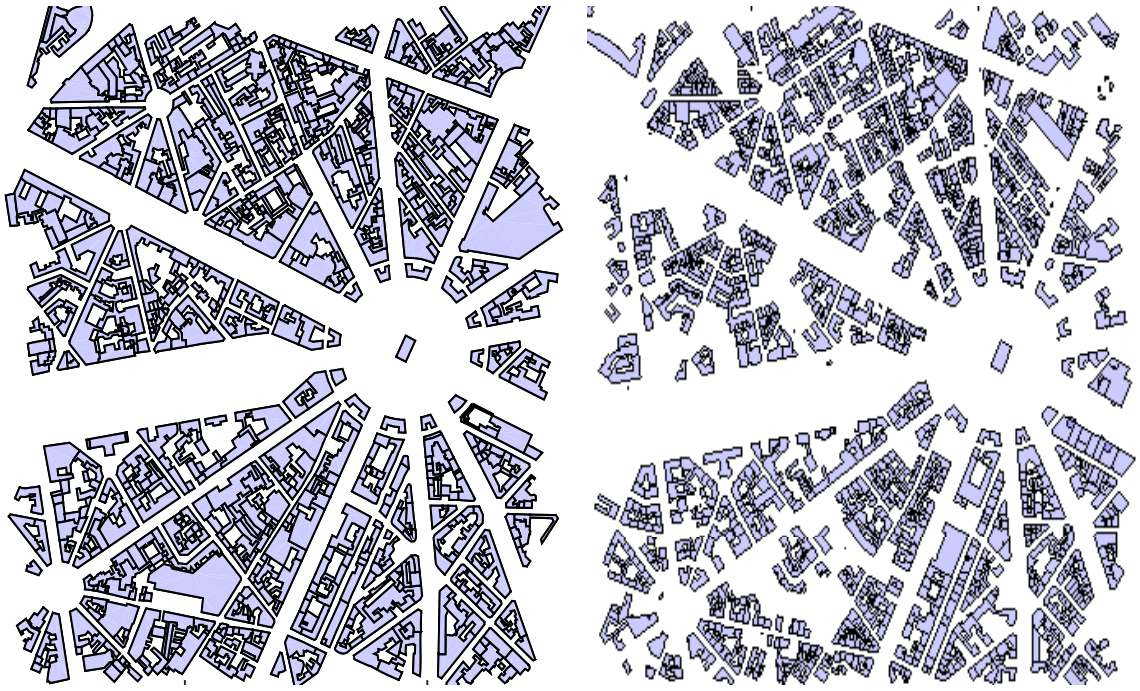

(a) *Modeled sence.* (b) *Scene etxracted from OpenStreetMap.*

Figure 5.4 – *Charles de Gaulle - Étoile, Paris.*

The performance of the integrated API will be tested for several values of ϵ : 0.30, 0.40, 0.50, 0.60, 0.75, 1.0, and 1.5. The obtained simulation results are shown in figures 5.5(a) - 5.5(g). They show very good agreement with the measurements (for the valid zones as discussed in chapter 3). It can be noticed that they have comparable behavior for all the values of ϵ. In order to get numerical error values, table 5.2 evaluates the mean absolute error for each case. It must be noted that the error values are greater than the values that were obtained in chapter 3 because that these results were not averaged according to Lee criterion as the results in chapter 3. Another important source of error is the missing buildings and the inaccuracies of the geometry databases. The minimum error for this particular configuration was found for $\epsilon = 0.5$.

Scene	**No. of Faces**	**Avg. No. Of Paths**	**Mean absolute error**
Modeled scene	10302	132.53	6.83 (*cf.* ch. 3)
OSM, $\epsilon = 0.3$	17170	130.86	8.00[1]
OSM, $\epsilon = 0.4$	16642	129.80	7.88[1]
OSM, $\epsilon = 0.5$	16137	129.56	7.86[1]
OSM, $\epsilon = 0.6$	15771	129.54	7.91[1]
OSM, $\epsilon = 0.75$	15244	129.00	8.00[1]
OSM, $\epsilon = 1.0$	14424	127.99	7.90[1]
OSM, $\epsilon = 1.5$	13148	124.74	7.84[1]

Table 5.2 – *API validation - error estimation for different values of* ϵ.

1. value was not averaged according to Lee criterion

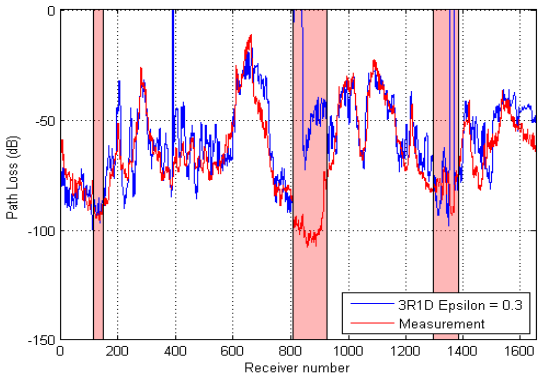

(a) *Epsilon 0.3.*

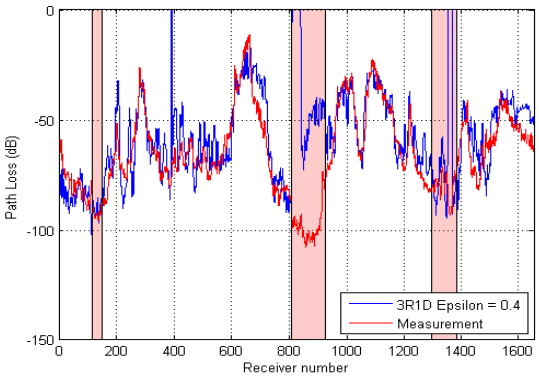

(b) *Epsilon 0.4.*

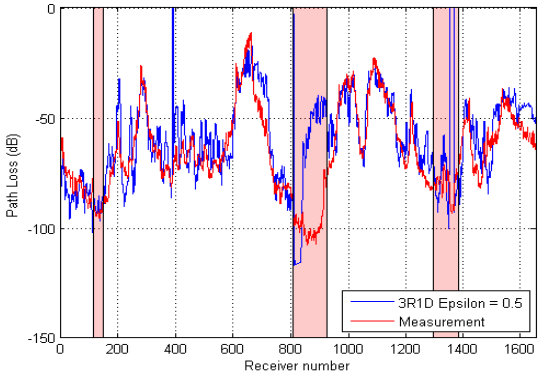

(c) *Epsilon 0.5.*

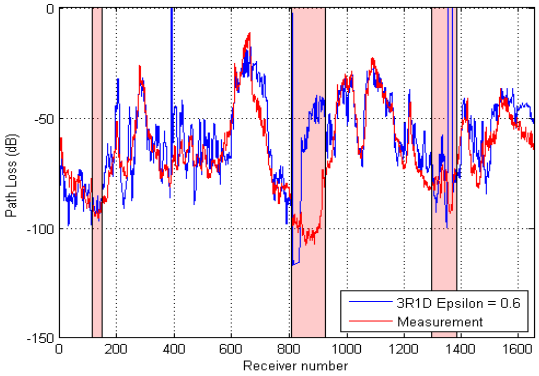

(d) *Epsilon 0.6*

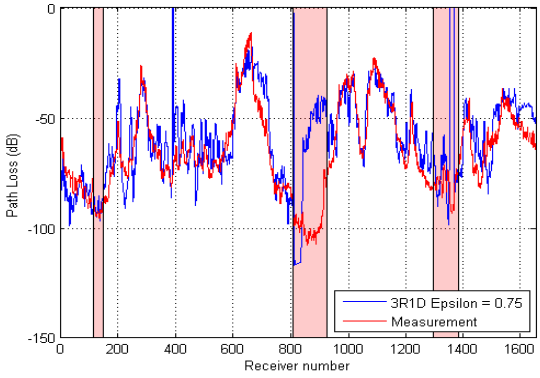

(e) *Epsilon 075.*

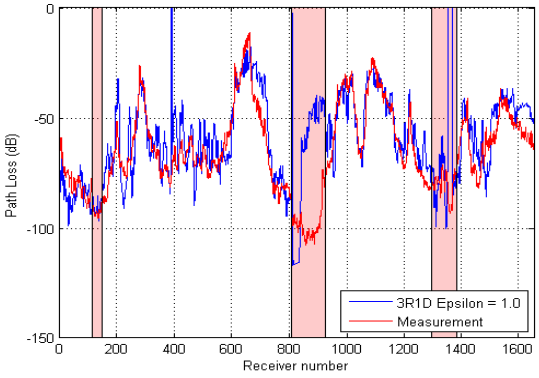

(f) *Epsilon 1.0.*

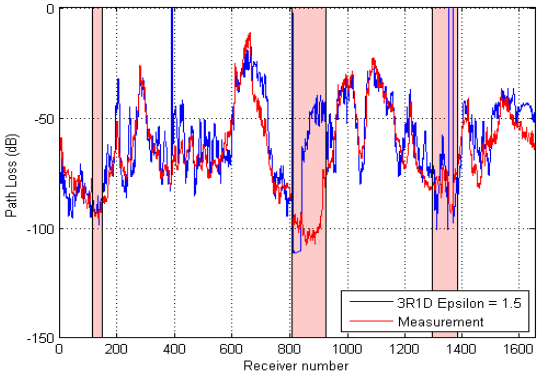

(g) *Epsilon 1.5.*

Figure 5.5 – *Epsilon effect on accuracy.*

5.5 Mobility case study

This section defines a case study carried out in Brest city, where the project is initially planned. The test scenario consists of a small WSN having 10 sensor nodes (s_1, s_2, ... , s_{10}) as shown in figure 5.6. All the sensors are moving along predefined trajectories presented by the red-dotted paths in figure 5.6. The sensors move at a constant speed along these paths and reach the end of their trajectories in 60 seconds, therefore, it is convenient to trace the behavior at a step of one second, leading to 60 snapshots for each sensor.

The main simulation parameters are presented below. However, it should be noted that the transmit power and Rx sensitivity values are not the theoretical values defined by the standard but rather, they were taken from a commercial ZigBee module (Ember EM357 Transceiver - ZICM357P2) in order to extend the link budget.

- **Configuration :** Urban.
- **Location :** Downtown, Brest.
- **Simulation area :** 800 m × 800 m
- **Protocol :** ZigBee.
- **Transmit power :** 20 dBm.
- **Frequency :** 2.4 GHz
- **Sensitivity level :** -100 dBm.
- **Channel estimation mode :** Horizontal mode.
- **Number of interactions :** 3R1D

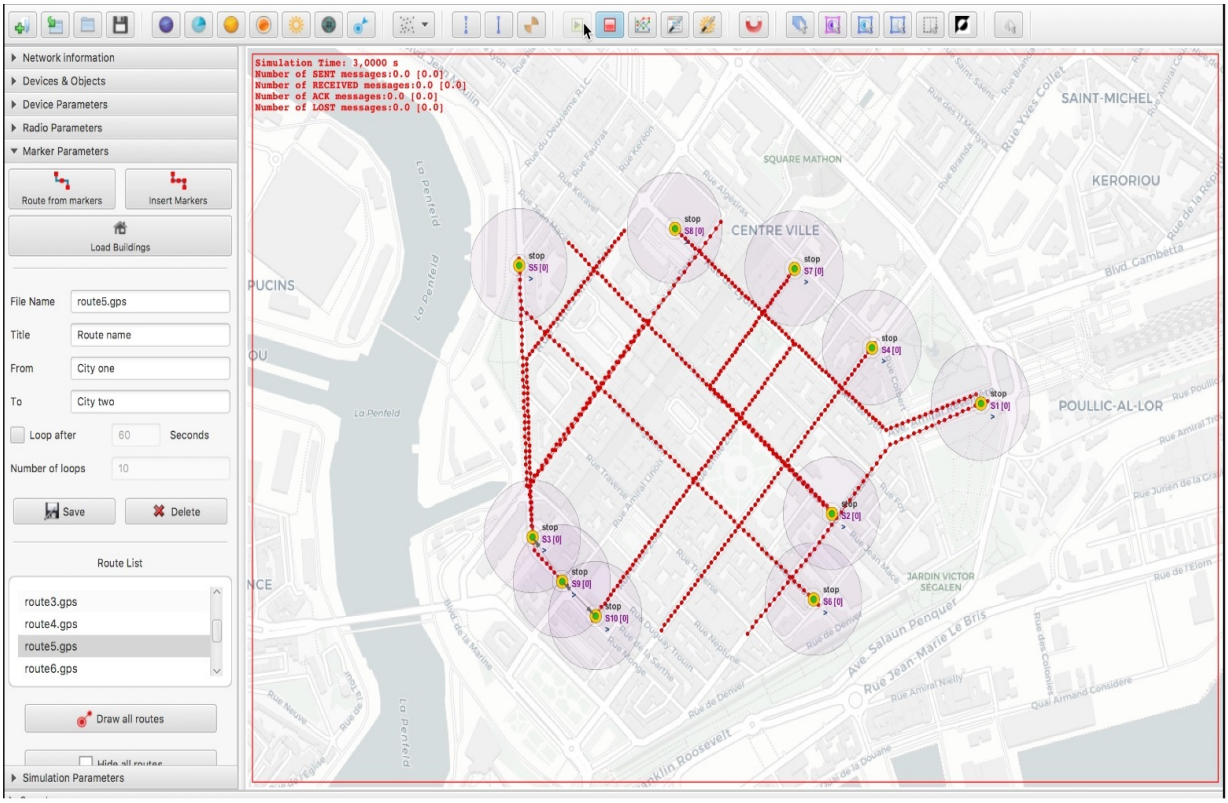

Figure 5.6 – *Mobility scenario.*

The results are given in a matrix format. One channel matrix is given for each sensor node for all the time instants, giving a matrix of 600 channel elements (10 sensors × 60 seconds = 600 elements). This means also that if one wants both narrowband and wideband simulations to be considered, 600 channel elements for narrowband results and other 600 elements for wideband results). At a specific instant, the channel information is presented by a row (from the global matrix) that contains 10 elements(C_{x-y}), which represent the channel information between the sensor node in question and the other 9 sensors at that instant. For example, the channel information for the first sensor node at a specific instant is given in the following form :

$$ChannelMatrix(s_1, t) = \begin{bmatrix} - & C_{1-2} & C_{1-3} & \dots & C_{1-9} & C_{1-10} \end{bmatrix}$$

where, C_{1-2} denotes the channel information between S_1 and S_2 at a specific instant (t = 1 - 60 s). Similarly, the channel information for the second, third, and tenth sensor nodes at a specific instant are given in the following forms :

$$ChannelMatrix(s_2, t) = \begin{bmatrix} C_{2-1} & - & C_{2-3} & \dots & C_{2-9} & C_{2-10} \end{bmatrix}$$

$$ChannelMatrix(s_3, t) = \begin{bmatrix} C_{3-1} & C_{3-2} & - & \dots & C_{3-9} & C_{3-10} \end{bmatrix}$$

$$ChannelMatrix(s_{10}, t) = \begin{bmatrix} C_{10-1} & C_{10-2} & C_{10-3} & \dots & C_{10-9} & - \end{bmatrix}$$

The attenuation values of s_{10} with respect to the other sensors (*i.e.* $ChannelMatrix(s_{10}, t)$) are traced graphically as shown in figure 5.7 at different time instants : t = 1 s, t = 10 s, t = 20 s, t = 30 s, t = 40 s, t = 50 s, and t = 60 s. The simulation parameters are already described above. A dashed line connecting S_{10} (the cyan-dotted trajectory of figure 5.7) with the other 9 sensor nodes is drawn to make it easier to spot the link in question. It must be mentioned that the dashed lines connecting S_{10} with the other nodes do not represent the physical path between this two nodes but rather a representative path. The attenuation value is then displayed next to each sensor. It is easy to notice that attenuation values do respect the propagation environment since the radio model is deterministic. Another related point, the wideband results were also extracted (not shown here) because these results will be used for interference analysis by another project partner.

In order to show the importance of using a realistic channel model which takes into account the propagation environment. A comparison of some network parameters will be conducted, these parameters will be obtained by using the deterministic model and then by using a statistical Log-Normal shadowing model. However, the Log-Normal model parameters should first be determined to in order to get good results from the model.

(a) $t = 1$ *s.*

(b) $t = 10$ *s.*

(c) $t = 20$ *s.*

(d) $t = 30$ *s.*

(e) $t = 40$*s.*

(f) $t = 50$*s.*

(g) t= *60s.*

Figure 5.7 – *Attenuation values for* S_{10} *at different time instants.*

Log-Normal shadowing model parameters :

Log-Normal shadowing model can be used for a wide range of environments. It consists of two parts ; the first part is in function of distance and the relation is controlled by the path loss exponent n. The second part is the shadowing part which reflects the variation of the received power around the first part as given by its general form :

$$L(d_i) = L(d_0) + 10n \log\left(\frac{d_i}{d_0}\right) + X_\sigma \tag{5.1}$$

There are some typical values of the path loss exponent and shadowing deviation that are defined in the literature (*cf.* table 2.3). These values can be used, however, it is more accurate to use adapted values for this specific environment. Since there are no field measurements for this configuration, the deterministic attenuation values will be used for this purpose. To this end, the deterministic attenuation values are traced in function of distance as shown in figure 5.8.

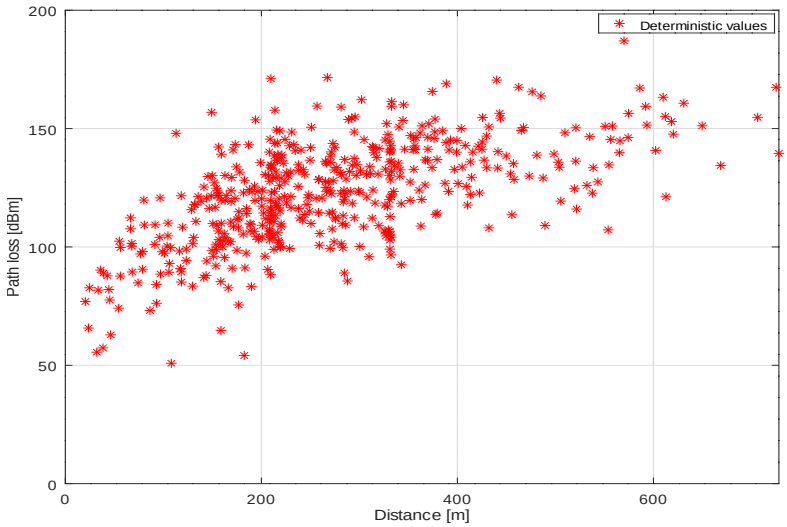

Figure 5.8 – *Deterministic attenuation in function of distance.*

The attenuation samples were used to find the parameters of the log-normal distribution, the obtained parameters were found as follows :

$$L_{dB}(d[m]) = -14.27 + 10 * 5.7 \log\big(d[m]\big) + X_{\sigma=16dB} \tag{5.2}$$

Figure 5.9 shows the Log-Normal model without shadowing (black curve), and it also shows the shadowing variation around the black curve (the blue points). Although it is true that the parameterized Log-Normal model follows the deterministic values (the red points), the shadowing part is random and does not depend on the propagation environment (only global environment dependency represented by the path exponent and shadowing deviation values). Moreover, a dotted-green line is drawn in figure 5.9, it represents the link budget level, which means that if a packet is sent between a pair sensors having a path loss value below this threshold, the packet would probably be received correctly.

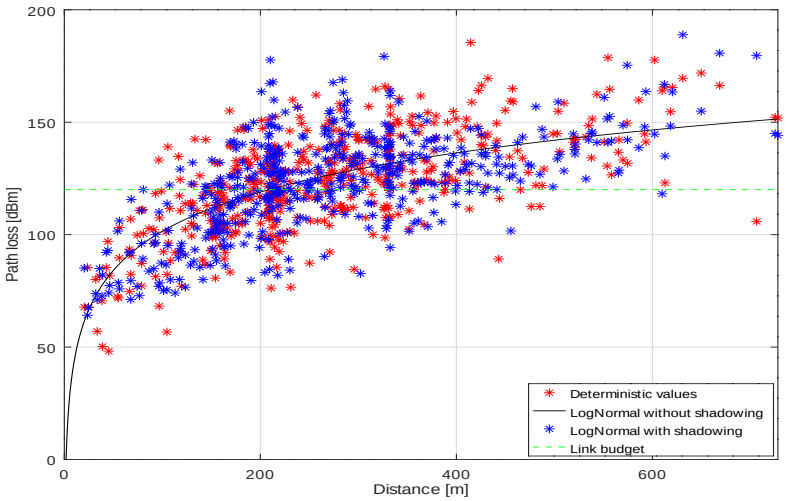

Figure 5.9 – *Deterministic vs. Log-Normal model.*

Packet error rate :

One of the important WSN parameters is the Packet Error Rate (PER). In ZigBee sensor networks, if the packet was not received correctly, the receiving node requests a retransmission (with a maximum number of retransmission requests). Therefore, the PER parameter is a good parameter to show the importance of the radio channel. In other words, to show the impact of the radio channel on the PER.

Random data were generated and formatted as ZigBee Payloads, then they were added to the ZigBee preamble to form a ZigBee frame as defined by the physical layer of the protocol. All the other physical layer parameters such as (center frequency, sampling frequency, bit rate, chip rate, *etc.*) were also considered. The ZigBee frames will be sent to the receiver node, via the radio channel : first with the deterministic radio model of the API and then with the adapted Log-Normal model. It should be noted that a white Gaussian noise was added to the channel. At the receiver side, the received signal was decoded with a maximum of three retransmission requests.

Figure 5.10(a) shows the PER for the deterministic channel model in function of distance. It can be shown that for distances less than 100 m, the success rate is always 100%. For the distances between 100 m - 400 m, the packets are sometimes received correctly and other times, they could not be received (depending on the sensor's location and on the propagation environment). For large distances, the packet reception always fails. Figure 5.10(b) shows the PER of the deterministic model in function of the attenuation. As expected, the packets were received if the received power is more than the link budget threshold (- 120 dBm).

The binary behavior of the success rate (either 0% or 100%) is due to the fact that package is considered as received, even if it fails for two retransmission attempts and succeeds in the third retransmission attempt. If the package fails in all the three retransmissions, it is then considered as unreceived.

Similar global behavior for the Log-Normal channel model could be noticed through figures 5.10(c) and 5.10(d). Moreover, table 5.3 shows relatively close PER percentages for the two models. Although figures 5.10(c) , 5.10(d) and table 5.3 showed similar global behavior of the Log-Normal model compared to the deterministic model, they (figures 5.10(c) , 5.10(d) and table 5.3) do not really show the inaccuracy because of the error compensation (due to the random part of the Log-Normal distribution). This issue will be discussed in the next paragraph.

Model	**PER**
Deterministic model	52%
Log-Normal model	48.3%

Table 5.3 – *PER.*

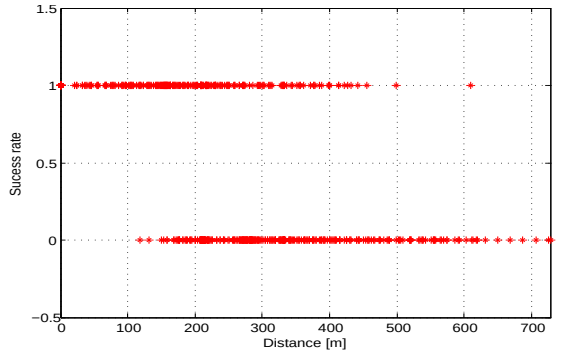

(a) *Error rate in function of distance - deterministic model.*

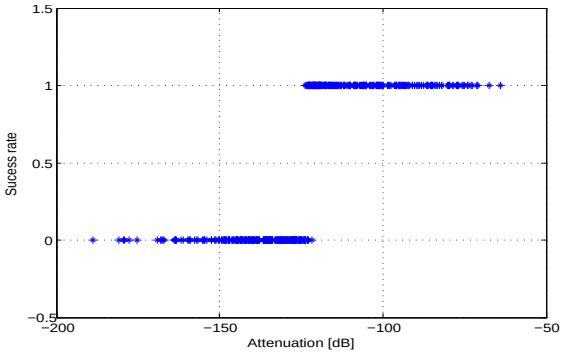

(b) *Error rate in function of attenuation - deterministic model.*

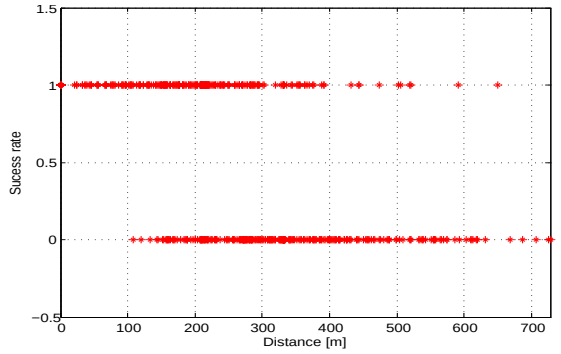

(c) *Error rate in function of distance - Log-nomal model.*

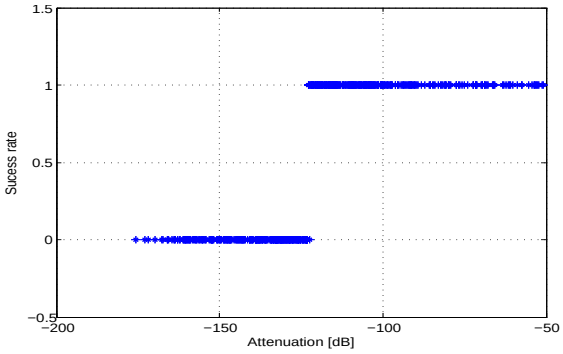

(d) *Error rate in function of attenuation - Log-nomal model.*

Figure 5.10 – *Package error rate.*

In order to show that the Log-Normal model gives inaccurate PER, the difference between the PER obtained by the deterministic model and the PER obtained by the Log-normal model is shown in figure 5.11. The three obtained values in the figure mean :

— 1 : the packet was received correctly by the deterministic model but it was not received by the Log-normal model.
— 0 : the packet was received or not received by the two models.

— -1 : the packet was not received by the deterministic model but it was received correctly by the Log-normal model.

Table 5.4 shows that 188 packets out of 600 (31.33%) were considered as received by the Log-normal model whereas, they were not received correctly by the deterministic model or vice versa. This difference confirms that : although the global behavior seems to be similar, the parametrized Log-Normal is not accurate enough.

	Difference
Deterministic model PER - Log-Normal PER	(188/600) 31.33%

Table 5.4 – *Deterministic vs. Log-Normal model success rate difference.*

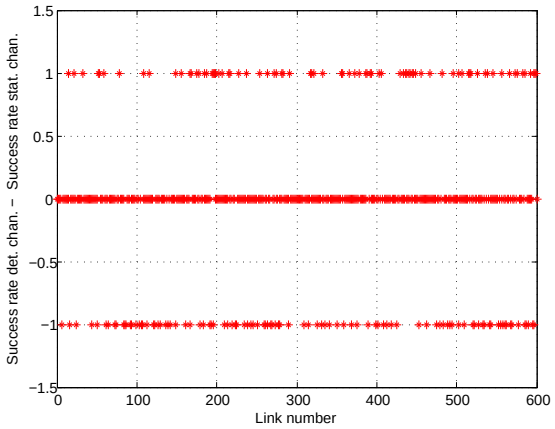

Figure 5.11 – *Difference between deterministic and Log-Normal model in terms of PER.*

5.6 Conclusion

In this chapter, many points were discussed regarding the integration of the radio propagation models to the wireless network simulator platform (CupCarbon). Chapter 5 started by presenting briefly the main features of CupCarbon. Then, it illustrated the integration process in many steps. In fact, the radio models were integrated as an API, this choice made it easy to integrate the radio module as a black box. However, many problems were encountered during the integration phase. Most of the faced problems were because of the geometry databases since OpenStreetMap is the geometry source for the API. The main two issues were, firstly, the conversion from the GPS coordinates to the Cartesian coordinate system. Lambert93 projection was used for the conversion between these two systems. The second issue was the simplification of the geometry. Douglas-Peucker method was the best fit for the contour simplification. Then, the API was tested on Charles de Gaulle - Étoile, Paris scene because it has field measurements. The results of the API showed very good agreement with the measurements. Finally, the last part of this chapter presented a real case study of ten moving sensors in Brest city to emphasize the importance of realistic radio channel models that consider the propagation environment. That was achieved by tracing the PER using the deterministic radio model versus a statistical model.

General Conclusion and Perspectives

The smart city concept was introduced in chapter 1 of this thesis. It was shown that it covers several interesting applications in many diverse domains that aims to facilitate people's everyday life. Some example of those applications were listed in this chapter. In fact, wireless sensor networks and the Internet of things are the main technologies of the smart cities. A large number of communication protocols is dedicated to WSNs. Each protocol has a projected application. The main widely-used protocols are : the IEEE 802.15.4 derived standards (i.e. Zigbee, WirelessHart, 6LoWPAN, ..., *etc.*) for short-range communications, and Lora, Sigfox for wide-range communications. Since real experiments are costly and time-consuming, simulation tools are highly required to simulate, test, and validate the behavior of these network before the real deployment. For this reason, they should be reliable, precise, and quick, that was the main motivation for PERSEPTEUR project.

The objective of PERSEPTEUR project which was to develop a realistic, accurate, and fast 3D wireless network simulator. Different tasks to build the final platform were assigned to the project partners. Modeling the radio channel was the targeted task for this thesis. In fact, it was shown that existing well-known WSN simulators offer simple-inaccurate or complex, time-consuming radio models. On the other hand, the propagation models that are in the literature are not directly adopted because they do not satisfy the project's requirements mainly in terms of time constrains. Consequently, this thesis aimed to propose a set of accuracy-time trade-offs to answer the research problem.

Chapter 2 provided an overview of the relevant literature about the radio channel fundamentals. Two main modeling approaches were discussed : empirical and deterministic radio modeling. An overview of the radio models that are integrated into the well-known WSNs was provided. This survey showed that these WSNs are using either empirical models so they could provide inaccurate results because they are not site-specific models, or they are using deterministic models which are computationally expensive.

Since the project necessitates a site-specific model, the deterministic option was further investigated. Two families of the deterministic modeling were presented : the ray-based models and the numerical methods that try to solve Maxwell's equation. Although ray-tracing techniques are more time-efficient, they are still not directly applicable to the simulator because of the computational time, which means that they still need to be accelerated.

Since the predominant propagation mechanism for the short-range communication protocols and Low-Power Wide-Area Network (LPWAN) protocols are not necessarily the same, the research problem was subdivided into two modes :

— Lateral propagation mode : which addresses the configurations where the propagation occurs mainly in the horizontal plane. This mode was covered in chapter 3.
— Vertical propagation mode : which treats the configurations where the propagation occurs mainly over rooftops. This mode was discussed in chapter 4.

Consequently, a ray-tracing model based on the visibility technique in the horizontal plane was developed in chapter 3. It was shown that the visibility tree has introduced a very significant gain in terms of execution time. Moreover, the model was evaluated in terms of accuracy with the measurements that were conducted in Paris. The evaluation showed that the model can perform accurate simulations with a mean absolute error of about 6 dB in 50 s for 4R1D (for 1651 receiver). A new acceleration technique was implemented by limiting the propagation scene to smaller areas and by selecting the most significant propagation paths. It was shown through some test scenarios that limiting the propagation area to an adequate range reduces the execution time with a negligible impact on accuracy. Many examples were given in chapter 3 showing that the model after limiting the area of interest can perform simulation in the order of a few seconds for a range of 150 m (for 4R1D). It was shown through these examples that the accuracy very slightly affected due to the acceleration technique. Finally, in order to support the mobile nodes, it was proposed to pre-process a set of visibility trees over a predefined route. Therefore, instead of calculating the visibility trees, the algorithm will use the pre-processed ones. This acceleration technique has made it possible to obtain the channel estimations in the order of a few milliseconds per link (for 150 m). However, an adequate discretization is required to ensure that the error is within an acceptable range and to ensure that the size on the hard disk is not that large.

Chapter 4 started by evaluating the implemented model (in the horizontal plane) through the measurements that were carried out in Munich site. It showed that the horizontal model is valid only over a certain range of distance around the transmitter. Over this distance, the model showed a good agreement with the measurements. However, beyond this distance, the contribution of the vertical paths become more and more predominant so the model was not valid anymore. That proved that is mandatory to consider also the propagation in the vertical plane. However, in such urban scenarios, multiple diffractions over rooftops are very likely to contain a series of buildings having similar or close heights, which means that one edge could be in the transition region of the other. A review of the most relevant physical models that consider the above-mentioned problem was given. The review revealed that the UTD-slope diffraction with distance parameter forcing method (Andersen's method) and Capolino and Albani method were the best two relevant models. These two methods were evaluated and then Capolino and Albani diffraction coefficient was integrated. Finally, the model perfor-

mance was evaluated by comparing the simulation results with the three measurement routes of Munich. The overall model was found to be capable to perform simulations with an absolute mean error of about 6 dB. It should be mentioned that the vertical propagation model has a very low computational time $i.e < 1$ ms per link (for the direct vertical ray). In fact, we can say that the final model satisfies the project's requirements since it gives fairly accurate results, considers the propagation scene, supports a large number of nodes, can deal with the mobile nodes, and within a reasonable time.

Chapter 5 discussed the integration process of the developed radio propagation model in CupCarbon. It started by giving an overview of the main features of CupCarbon. Chapter 5 showed that the radio models were integrated as an API, which means that it takes from the end user the required simulation parameters and the geometry database to launch a new simulation. It delivers back the channel prediction without giving the simulator access to the operations occurring behind the scenes. This choice made the integration easier. Nevertheless, several issues were encountered during the integration process. Most of them were because of the geometry databases that were provided by OpenStreetMap. Conversion from the GPS coordinates to the Cartesian coordinate system was the first main issue. This issue was resolved by using Lambert93 projection. The other issue was the complexity of the geometry. Douglas-Peucker method was used to simplify the outline of the buildings. Then, the API was tested on Charles de Gaulle - Étoile, Paris scene. The results of the API showed very good agreement with the measurements. Finally, the last part of chapter 5 presented a real case study of ten moving sensors in Brest city to emphasize the importance of realistic radio channel models that consider the propagation environment. That was achieved by tracing the PER using the deterministic radio model versus a statistical model. It showed that the empirical model reported wrongly that about 30% of the packets are received or unreceived.

This work can be further improved in many different ways. Some of the topics that can enhance the performance in term of accuracy are : a simple empirical model that adds additional losses to account for the vegetation loss, a statistical model for describing the temporal variation of the radio channel, consideration of the topography of the propagation environment since the ground is considered as flat, model calibration with measurements carried out for smart city applications. Furthermore, the performance of the final model can be largely enhanced in term of execution time by simplifying the geometry of the propagation environment (*e.g.* by grouping a number of adjacent buildings that have close heights to form one block). This work can also be improved with considerable effort to include the smart cities within the 5G vision.

Bibliography

[AAFA+12] A. Abuarqoub, F. Al-Fayez, T. Alsboui, M.Hammoudeh, and A.Nisbet. Simulation issues in wireless sensor networks : A survey. *SENSORCOMM 2012 : The Sixth International Conference on Sensor Technologies and Applications*, 2012.

[ACMT97] M. Albani, F. Capolino, S. Maci, and R. Tiberio. Diffraction at a thick screen including corrugations on the top face. *IEEE Transactions on Antennas and Propagation*, 45(2) :277–283, Feb 1997.

[ACMT97+] F. Capolino and I. M. Albani and S. Maci and R. Tiberio. Double diffraction at a pair of coplanar skew edges. *IEEE Transactions on Antennas and Propagation, Aug 1997.*

[ACVM03] *L. Aveneau, P. Combeau, R. Vauzelle, and M. Meriaux. Efficient computation of radio coverage zone using a spatial partitionment approach. In* 2003 IEEE 58th Vehicular Technology Conference. VTC 2003-Fall (IEEE Cat. No.03CH37484)*, volume 1, pages 65–68 Vol.1, Oct 2003.*

[AFAHN13] *F. Al-Fayez, A. Abuarqoub, M. Hammoudeh, and A. Nisbet. Wireless sensor network simulation : The current state and simulation tools.* Sensors and Transducers Journal*, 18 :145–155, January 2013.*

[And94] *J. B. Andersen. Transition zone diffraction by multiple edges.* IEE Proceedings - Microwaves, Antennas and Propagation*, 141(5) :382–384, Oct 1994.*

[And97] *J. B. Andersen. Utd multiple-edge transition zone diffraction.* IEEE Transactions on Antennas and Propagation*, 45(7) :1093–1097, Jul 1997.*

[Ban06] *R. Bansal.* Engineering Electromagnetics : Applications*. CRC Press, 2006.*

[Bel63] *P. Bello. Characterization of randomly time-variant linear channels.* IEEE Transactions on Communications Systems*, 11(4) :360–393, December 1963.*

[Beu12] *R. Beuran.* Introduction to Network Emulation*. Pan Stanford Publishing, 2012.*

[Bey04] *J. Beyer. An approximate approach to predict multiple screen diffraction in the case of grazing incidence.* Radio Science*, 39(4) :1–6, Aug 2004.*

[BLV03] *A. Braquelaire, J.O. Lauchaud, and A. Vialard.* Discrete Geometry for Computer Imagery : 10th International Conference, DGCI 2002, Bordeaux, France, April 3-5, 2002. Proceedings. *Lecture Notes in Computer Science. Springer Berlin Heidelberg, 2003.*

[Cas13] *Castalia user's manual : A simulator for wireless sensor networks and body area networks. Technical report, May 2013.*

[CAVP06] *Pierre Combeau, Lilian Aveneau, Rodolphe Vauzelle, and Yannis Pousset. Efficient 2-d ray-tracing method for narrow and wideband channel characterisation in microcellular configurations.* IEE Proceedings-Microwaves, Antennas and Propagation*, 153(6) :502–509, 2006.*

[CDB04] *Zhongqiang Chen, Alex Delis, and Henry L. Bertoni. Radio-wave propagation prediction using ray-tracing techniques on a network of workstations (now).* Journal of Parallel and Distributed Computing*, 64(10) :1127 – 1156, 2004.*

[CIS15] *Fog computing and the internet of things : Extend the cloud to where the things are. Technical report, San Jose, CA, USA, 2015.*

[CLH02] *Y. Corre, Y. Lostanlen, and Y. Le Helloco. A new approach for radio propagation modeling in urban environment : knife-edge diffraction combined with 2d ray-tracing. In* Vehicular Technology Conference. IEEE 55th Vehicular Technology Conference. VTC Spring 2002 (Cat. No.02CH37367)*, volume 1, pages 507–511 vol.1, 2002.*

[CNE] *Cnet tutorial available from.* `http://www.csse.uwa.edu.au/cnet/wlans.html/`*. Accessed : 2017-11-30.*

[Com04a] *P. Combeau.* Simulation efficace et caractérisation du canal radiomobile en enironnement réel. Application aux systèmes sans fil*. PhD thesis, 11 2004.*

[Com04b] *P. Combeau.* Simulation efficace et caractérisation du canal radiomobile en enironnement réel. Application aux systèmes sans fil.*. PhD thesis, Novembre 2004.*

[Cor9] *Y. Corre and Y. Lostanlen.* Three-Dimensional Urban EM Wave Propagation Model for Radio Network Planning and Optimization Over Large Areas*. IEEE Transactions on Vehicular Technology, 2009.*

[dah]

[Cor10] *L.M. Correia.* Mobile Broadband Multimedia Networks : Techniques, Models and Tools for 4G*. Elsevier Science, 2010.*

[dah]

[DC99] *E. Damosso and L.M." Correia.* COST Action 231 : Digital Mobile Radio Towards Future Generation Systems : Final Report*. EUR (Series). European Commission, 1999.*

[Dey66] *J. Deygout. Multiple knife-edge diffraction of microwaves.* IEEE Transactions on Antennas and Propagation*, 14(4) :480–489, 07 1966.*

[DS16] *N. DuPuis and E. Stahl. Trends in smart city development : Case studies and recommendations. Technical report, American University Department of Public Administration and Policy with the National League of Cities, 2016.*

[Ers17] *Aksel Ersoy. Smart cities as a mechanism towards a broader understanding of infrastructure interdependencies.* Regional Studies, Regional Science*, 4(1) :26–31, 2017.*

[FCF07] *A. Fraboulet, G. Chelius, and E. Fleury. Worldsens : Development and prototyping tools for application specific wireless sensors networks. In* 2007 6th

International Symposium on Information Processing in Sensor Networks, *pages 176–185, April 2007.*

[FS95] *Capolino F. and Maci S. Simplified closedâform expressions for computing the generalized fresnel integral and their application to vertex diffraction.* Microwave and Optical Technology Letters, *9(1) :32–37, 1995.*

[Fur63] *Kōichi Furutsu.* On the theory of radio wave propagation over inhomogeneous earth, *volume 67D. 1963.*

[Gio84] *C. L. Giovaneli. An analysis of simplified solutions for multiple knife-edge diffraction.* IEEE Transactions on Antennas and Propagation, *32(3) :297–301, Mar 1984.*

[GMM+17] *O. Gervasi, B. Murgante, S. Misra, G. Borruso, C.M. Torre, A.M.A.C. Rocha, D. Taniar, B.O. Apduhan, E. Stankova, and A. Cuzzocrea.* Computational Science and Its Applications – ICCSA 2017 : 17th International Conference, Trieste, Italy, July 3-6, 2017, Proceedings. *Number ptie. 5 in Lecture Notes in Computer Science. Springer International Publishing, 2017.*

[God01] *L.C. Godara.* Handbook of Antennas in Wireless Communications. *Electrical Engineering & Applied Signal Processing Series. CRC Press, 2001.*

[Ham13] *J.R. Hampton.* Introduction to MIMO Communications. *Cambridge University Press, 2013.*

[HBVP17] *B. Hilt, M. Berbineau, A. Vinel, and A. Pirovano.* Networking Simulation for Intelligent Transportation Systems : High Mobile Wireless Nodes. *Network and Telecommunications. Wiley, 2017.*

[HHC06] *Mohsen Guizani Hsiao-Hwa Chen.* Next Generation Wireless Systems and Networks. *John Wiley & Sons, 2006.*

[HK74] *Y. M. Hwang and R. G. Kouyoumjian. A dyadic diffraction coefficient for an electromagnetic wave which is rapidly varying at an edge. 1974.*

[Hol96] *P. D. Holm. Utd-diffraction coefficients for higher order wedge diffracted fields.* IEEE Transactions on Antennas and Propagation, *44(6) :879–888, Jun 1996.*

[Hol04] *P. D. Holm. Calculation of higher order diffracted fields for multiple-edge transition zone diffraction.* IEEE Transactions on Antennas and Propagation, *52(5) :1350–1354, May 2004.*

[Hol00] *P. D. Holm. A new heuristic UTD diffraction coefficient for nonperfectly conducting wedges.* IEEE Transactions on Antennas and Propagation, *48(8) :1211–1219, 2000.*

[IEE03] *Ieee standard for information technology telecommunications and information exchange between systems local and metropolitan area networks specific requirements - part 15.4 : Wireless medium access control (mac) and physical layer (phy) specifications for low-rate wireless personal area networks (lr-wpans). Technical report, New York, NY 10016-5997, USA, 2003.*

[Inc17] *Scalable Network Technologies Inc.* QualNet 8.0 Model Library Index, *qualnet 8.0 edition, May 2017.*

[IY02] *M. F. Iskander and Zhengqing Yun. Propagation prediction models for wireless communication systems.* IEEE Transactions on Microwave Theory and Techniques, *50(3) :662–673, Mar 2002.*

[Jac15] *Martin Jacobsson. Using software-defined networking principles for wireless sensor networks. 11th Swedish National Computer Networking Workshop (SNCNW 2015) Karlstad, May 2015.*

[Jin15] *J.M. Jin.* The Finite Element Method in Electromagnetics*. Wiley - IEEE. Wiley, 2015.*

[JZD09] *Miloš Jevtić, Nikola Zogović, and Goran Dimić. Evaluation of wireless sensor network simulators. In* Proceedings of the 17th Telecommunications Forum (TELFOR 2009), Belgrade, Serbia*, pages 1303–1306, 2009.*

[KAMH17] *H. I. Kobo, A. M. Abu-Mahfouz, and G. P. Hancke. A survey on software-defined wireless sensor networks : Challenges and design requirements.* IEEE Access*, 5 :1872–1899, 2017.*

[Kel62] *Joseph B Keller. Geometrical theory of diffraction.* JOSA*, 52(2) :116–130, 1962.*

[KGNM06] *G. Kloos, J. E. Guivant, E. M. Nebot, and F. Masson. Range based localisation using rf and the application to mining safety. In* 2006 IEEE/RSJ International Conference on Intelligent Robots and Systems*, pages 1304–1311, Oct 2006.*

[Kli51] *Morris Kline. An asymptotic solution of maxwell's equations.* Communications on Pure and Applied Mathematics*, 4(2-3) :225–262, 1951.*

[KM16] *M.B. Krishna and J.L. Mauri.* Advances in Mobile Computing and Communications : Perspectives and Emerging Trends in 5G Networks*. CRC Press, 2016.*

[KMF+14] *S. Karnouskos, P.J. Marrón, G. Fortino, L. Mottola, and J.R.M. Dios.* Applications and Markets for Cooperating Objects*. SpringerBriefs in Electrical and Computer Engineering. Springer Berlin Heidelberg, 2014.*

[KMHMP16] *K. Klem-Musatov, H.C. Hoeber, T.J. Moser, and M.A. Pelissier.* Classical and Modern Diffraction Theory :*. SEG Geophysics Reprint Series. Society of Exploration Geophysicists, 2016.*

[KP74] *R. G. Kouyoumjian and P. H. Pathak. A uniform geometrical theory of diffraction for an edge in a perfectly conducting surface.* Proceedings of the IEEE*, 62(11) :1448–1461, Nov 1974.*

[KSW+08] *A. Köpke, M. Swigulski, K. Wessel, D. Willkomm, P. T. Klein Haneveld, T. E. V. Parker, O. W. Visser, H. S. Lichte, and S. Valentin. Simulating wireless and mobile networks in omnet++ the mixim vision. In* Proceedings of the 1st International Conference on Simulation Tools and Techniques for Communications, Networks and Systems & Workshops*, Simutools '08, pages 71 :1–71 :8, ICST, Brussels, Belgium, Belgium, 2008. ICST (Institute for Computer Sciences, Social-Informatics and Telecommunications Engineering).*

[KT06] *G. Koutitas and C. Tzaras. A slope utd solution for a cascade of multi-shaped canonical objects.* IEEE Transactions on Antennas and Propagation*, 54(10) :2969–2976, Oct 2006.*

[KT08] *A. Karousos and C. Tzaras. Multiple time-domain diffraction for uwb signals.* IEEE Transactions on Antennas and Propagation*, 56(5) :1420–1427, May 2008.*

[KT13] *S. Kurt and B. Tavli. Propagation model alternatives for outdoor wireless sensor networks. In* 2013 IFIP Wireless Days (WD)*, pages 1–3, Nov 2013.*

[LB98] *G. Liang and H. L. Bertoni. A new approach to 3-d ray tracing for propagation prediction in cities.* IEEE Transactions on Antennas and Propagation*, 46(6) :853–863, Jun 1998.*

[LCL89] *H. Ling, R. C. Chou, and S. W. Lee. Shooting and bouncing rays : calculating the rcs of an arbitrarily shaped cavity.* IEEE Transactions on Antennas and Propagation*, 37(2) :194–205, Feb 1989.*

[Lea17] *Rodger Lea. Smart cities : An overview of the technology trends driving smart cities. Technical report, March 2017.*

[Lee85] *W. C. Y. Lee. Estimate of local average power of a mobile radio signal.* IEEE Transactions on Vehicular Technology*, 34(1) :22–27, Feb 1985.*

[Lee10] *W.C.Y. Lee.* Mobile Communications Design Fundamentals*. Wiley Series in Telecommunications and Signal Processing. Wiley, 2010.*

[LH64] *R.K. Luneburg and M. Herzberger.* Mathematical Theory of Optics*. University of California Press, 1964.*

[Lib] *Libelium world : Smart parking project in montpellier to relieve traffic congestion and reduce car parking search.* `http://www.libelium.com/smart-parking-project-in-montpellier-to-relieve-traffic-congestion-and-reduce-car-parking-search/`*. Accessed : 2017-11-30.*

[LL00] *W. C. Y. Lee and D. J. Y. Lee. Microcell prediction by street and terrain data. In* VTC2000-Spring. 2000 IEEE 51st Vehicular Technology Conference Proceedings (Cat. No.00CH37026)*, volume 3, pages 2167–2171 vol.3, 2000.*

[LL13] *Y.T. Lo and S.W. Lee.* Antenna Handbook : Theory, Applications, and Design*. Springer US, 2013.*

[Lor15] *A technical overview of lora and lorawan. Technical report, November 2015.*

[Lue89] *R. J. Luebbers. A heuristic utd slope diffraction coefficient for rough lossy wedges.* IEEE Transactions on Antennas and Propagation*, 37(2) :206–211, Feb 1989.*

[Man] *Mannasim web site.* `http://www.mannasim.dcc.ufmg.br/`*. Accessed : 2017-11-30.*

[Mik10] *VERMET Mikael.* Simulations par l'acoustique géométrique en présence de surfaces courbes avec prise en compte de la diffraction*. PhD thesis, mars 2010.*

[MiX] *Mixim simulator website.* `http://mixim.sourceforge.net/`*. Accessed : 2017-11-30.*

[ML99] *H. Mokhtari and P. Lazaridis. Comparative study of lateral profile knife-edge diffraction and ray tracing technique using gtd in urban environment.* IEEE Transactions on Vehicular Technology*, 48(1) :255–261, Jan 1999.*

[MLBK14] *Kamal Mehdi, Massinissa Lounis, Ahcène Bounceur, and Tahar Kechadi. Cupcarbon : A multi-agent and discrete event wireless sensor network design and simulation tool. In* Proceedings of the 7th International ICST Conference on Simulation Tools and Techniques*, SIMUTools '14, pages 126–131, ICST, Brussels, Belgium, Belgium, 2014. ICST (Institute for Computer Sciences, Social-Informatics and Telecommunications Engineering).*

[np16] *ns3 project.* ns-3 Model Library*, release ns-3.26 edition, October 2016.*

[ns2a] *The network simulator ns-2 available from.* `http://www.isi.edu/nsnam/ns/`. *Accessed : 2017-11-30.*

[ns2b] *Radio propagation models implemented in ns-2 available from.* `https://www.isi.edu/nsnam/ns/doc/node216.html/`. *Accessed : 2017-11-30.*

[NS15] *A. Nayyar and R. Singh. A comprehensive review of simulation tools for wireless sensor networks (wsns).* Journal of Wireless Networking and Communications, *5(1) :19–47, 2015.*

[omn] *Omnet++ website.* `https://www.omnetpp.org/intro/`. *Accessed : 2017-11-30.*

[Par00] *J. D. Parsons.* The Mobile Radio Propagation Channel. *John Wiley Sons LTD, 2nd. edition edition, 2000.*

[Par11] *J. D. Parsons. Field-strength measurements along a route with geographical coordinate registrations - recommendation itu-r sm.1708-1. Technical report, September 2011.*

[PC15] *A. Patel and T. A. Champaneria. Study and comparision of various internet of things protocols.* International Journal of Advance Engineering and Research Development, *2(12) :22–32, December 2015.*

[PRG15] *R. M. Pereira, L B Ruiz, and M L A Ghizoni. Mannasim : A ns-2 extension to simulate wireless sensor network.* ICN 2015 : The Fourteenth International Conference on Networks, *April 2015.*

[RVCG98] *K. Rizk, R. Valenzuela, D. Chizhik, and F. Gardiol. Application of the slope diffraction method for urban microwave propagation prediction. In* Vehicular Technology Conference, 1998. VTC 98. 48th IEEE, *volume 2, pages 1150–1155 vol.2, May 1998.*

[RVF+98] *K Rizk, R Valenzuela, S Fortune, D Chizhik, and F Gardiol. Lateral, full-3d and vertical plane propagation in microcells and small cells. In* Vehicular Technology Conference, 1998. VTC 98. 48th IEEE, *volume 2, pages 998–1003. IEEE, 1998.*

[RWG97] *K. Rizk, J. F. Wagen, and F. Gardiol. Two-dimensional ray-tracing modeling for propagation prediction in microcellular environments.* IEEE Transactions on Vehicular Technology, *46(2) :508–518, May 1997.*

[Sab17] *A. Sabban.* Novel Wearable Antennas for Communication and Medical Systems. *CRC Press, 2017.*

[SAZ07] *S. Saunders and A. Aragón-Zavala.* Antennas and Propagation for Wireless Communication Systems : 2nd Edition. *John Wiley & Sons, 2007.*

[SD11] *Christoph Sommer and Falko Dressler. Using the right two-ray model ? a measurement-based evaluation of phy models in vanets. 2011.*

[SEGD11] *C. Sommer, D. Eckhoff, R. German, and F. Dressler. A computationally inexpensive empirical model of ieee 802.11p radio shadowing in urban environments. In* 2011 Eighth International Conference on Wireless On-Demand Network Systems and Services, *pages 84–90, Jan 2011.*

[SH10] *C. Saeidi and F. Hodjatkashani. Modified angular z-buffer as an acceleration technique for ray tracing.* IEEE Transactions on Antennas and Propagation, *58(5) :1822–1825, May 2010.*

[Sig] *Sigfox technology overview available from.* `https://www.sigfox.com/en/sigfox-iot-technology-overview/`. *Accessed : 2017-11-30.*

[SJK07] *C. Suh, J. E. Joung, and Y. B. Ko. New rf models of the tinyos simulator for ieee 802.15.4 standard. In* 2007 IEEE Wireless Communications and Networking Conference*, pages 2236–2240, March 2007.*

[SKPP08] *T. Stoyanova, F. Kerasiotis, A. Prayati, and G. Papadopoulos. Communication-aware deployment for wireless sensor networks. In* 2008 Second International Conference on Sensor Technologies and Applications (sensorcomm 2008)*, pages 217–222, Aug 2008.*

[SKPP09a] *T. Stoyanova, F. Kerasiotis, A. Prayati, and G. Papadopoulos. A practical rf propagation model for wireless network sensors. In* 2009 Third International Conference on Sensor Technologies and Applications*, pages 194–199, June 2009.*

[SKPP09b] *T. Stoyanova, F. Kerasiotis, A. Prayati, and G. Papadopoulos. A practical rf propagation model for wireless network sensors. In* 2009 Third International Conference on Sensor Technologies and Applications*, pages 194–199, June 2009.*

[SON10] *S. Soni and A. Bhattacharya. New Heuristic Diffraction Coefficient for Modeling of Wireless Channel.* Progress In Electromagnetics Research C*, 12 :125–137, 2010.*

[S.R10] *Theodore S.Rappaport.* Wireless Communications : Principles And Practice, 2nd Edition. *Prentice Hall, 2010.*

[SRK+09] *A. Schmitz, T. Rick, T. Karolski, L. Kobbelt, and T. Kuhlen. Beam tracing for multipath propagation in urban environments. In* 2009 3rd European Conference on Antennas and Propagation*, pages 2631–2635, March 2009.*

[SRK+11] *A. Schmitz, T. Rick, T. Karolski, T. Kuhlen, and L. Kobbelt. Efficient rasterization for outdoor radio wave propagation.* IEEE Transactions on Visualization and Computer Graphics*, 17(2) :159–170, Feb 2011.*

[SS99] *Simon R. Saunders and Saunders R Simon.* Antennas and Propagation for Wireless Communication Systems*. John Wiley & Sons, Inc., New York, NY, USA, 1st edition, 1999.*

[ST12] *W.L. Stutzman and G.A. Thiele.* Antenna Theory and Design*. Antenna Theory and Design. Wiley, 2012.*

[STW17] *D. Shi, X. Tang, and C. Wang. The acceleration of the shooting and bouncing ray tracing method on gpus. In* 2017 XXXIInd General Assembly and Scientific Symposium of the International Union of Radio Science (URSI GASS)*, pages 1–3, Aug 2017.*

[SWS12] *Mariusz Słabicki, Bartosz Wojciechowski, and Tomasz Surmacz. Realistic model of radio communication in wireless sensor networks. In Andrzej Kwiecień, Piotr Gaj, and Piotr Stera, editors,* Computer Networks*, pages 334–343, Berlin, Heidelberg, 2012. Springer Berlin Heidelberg.*

[Tan16] *Parnika Tandon. Internet of things : The next evolutionary step- a review.* International Journal of Students' Research in Technology & Management*, 4(2) :30–34, 2016.*

[TH05] *A. Taflove and S.C. Hagness.* Computational Electrodynamics : The Finite-difference Time-domain Method. *Artech House antennas and propagation library. Artech House, 2005.*

[TOSa] *Building a network topology for tossim.* `https://github.com/tschmid/tinyos-2.x/blob/master/doc/html/tutorial/usc-topologies.html/`. *Accessed : 2017-11-30.*

[TOSb] *Tossim simulator web site.* `http://tinyos.stanford.edu/tinyos-wiki/index.php/TOSSIM/`. *Accessed : 2017-11-30.*

[TPHB14] *D. Trinh, V. Pham, S. Hussain, and C. Brennan. Integral equation based path loss modelling for propagation in urban environments. In* 2014 International Conference on Electromagnetics in Advanced Applications (ICEAA)*, pages 738–741, Aug 2014.*

[TS01] *C. Tzaras and S. R. Saunders. An improved heuristic utd solution for multiple-edge transition zone diffraction.* IEEE Transactions on Antennas and Propagation*, 49(12) :1678–1682, Dec 2001.*

[TT96] *S. Y. Tan and H. S. Tan. A microcellular communications propagation model based on the uniform theory of diffraction and multiple image theory.* IEEE Transactions on Antennas and Propagation*, 44(10) :1317–1326, Oct 1996.*

[TWCM10] *K. Tan, D. Wu, A. Chan, and P. Mohapatra. Comparing simulation tools and experimental testbeds for wireless mesh networks. In* 2010 IEEE International Symposium on "A World of Wireless, Mobile and Multimedia Networks" (WoWMoM)*, pages 1–9, June 2010.*

[Vog82] *L. E. Vogler. An attenuation function for multiple knife-edge diffraction.* Radio Science*, 17(06) :1541–1546, Nov 1982.*

[WGG10] *K. Wehrle, M. Günes, and J. Gross.* Modeling and Tools for Network Simulation. *Springer Berlin Heidelberg, 2010.*

[WH06] *I. Wald and V. Havran. On building fast kd-trees for ray tracing, and on doing that in o(n log n). In* 2006 IEEE Symposium on Interactive Ray Tracing*, pages 61–69, Sept 2006.*

[WSKZ12] *Daihua Wang, Linli Song, Xiangshan Kong, and Zhijie Zhang. Near-ground path loss measurements and modeling for wireless sensor networks at 2.4 ghz.* International Journal of Distributed Sensor Networks*, 8(8) :969712, 2012.*

[WSN] *The models included in the wsnet distribution.* `http://wsnet.gforge.inria.fr/models.html/`. *Accessed : 2017-11-30.*

[XWW11] *Z. Xie, H. Wang, and L. Wu. The improved douglas-peucker algorithm based on the contour character. In* 2011 19th International Conference on Geoinformatics*, pages 1–5, June 2011.*

[XZS16] *W. Xiang, K. Zheng, and X. Shen.* 5G Mobile Communications*. Springer International Publishing, 2016.*

[Yee66] *Kane Yee. Numerical solution of initial boundary value problems involving maxwell's equations in isotropic media.* IEEE Transactions on Antennas and Propagation*, 14(3) :302–307, May 1966.*

[YI15] *Z. Yun and M. F. Iskander. Ray tracing for radio propagation modeling : Principles and applications.* IEEE Access*, 3 :1089–1100, 2015.*

[Yur16] *S. Yurish.* Advances in Sensors : Reviews, Vol. 3 : Chapter 14 : A Survey on Wireless Sensor Networks Simulation Tools and Testbeds*. Advances in sensors : review. CONCHA BOOKS, 2016.*

[YZI02] *Zhengqing Yun, Zhijun Zhang, and M. F. Iskander. A ray-tracing method based on the triangular grid approach and application to propagation prediction in urban environments.* IEEE Transactions on Antennas and Propagation*, 50(5) :750–758, May 2002.*

[ZBC+14] *A. Zanella, N. Bui, A. Castellani, L. Vangelista, and M. Zorzi. Internet of things for smart cities.* IEEE Internet of Things Journal*, 1(1) :22–32, Feb 2014.*

[ZYI00] *Z. Zhang, Z. Yun, and M. F. Iskander. Ray tracing method for propagation models in wireless communication systems.* Electronics Letters*, 36(5) :464–465, Mar 2000.*

Abstract :

Modeling the radio channel in an accurate way is a key element in any wireless systems. Deterministic models offer a good degree of precision at the cost of high computational complexity, which is prohibitive for wireless sensor network (WSN) simulators because the test scenario could involve many sensor nodes in a city-wide scale. Within this context, the objective of this thesis is to propose efficient, fast, and accurate deterministic methods for modeling electromagnetic waves by finding the best time-accuracy trade-offs that guarantee accuracy under tight time constraints. The study was first subdivided into two modes according to the dominant propagation mechanism. In microcell configurations, the proposed approach is a ray-tracing model based on the visibility technique. It adopts a set of acceleration techniques to reduce the complexity with a minimal loss of precision. To the same end, the vertical propagation was addressed to include the most significant contributions. Finally, these models were integrated into a WSN simulator to provide realistic and accurate results for smart city applications. The importance of using precise models in WSN simulators is illustrated in terms of some network parameters.

Keywords : ray-tracing, visibility tree, acceleration techniques, vertical profile propagation, WSN simulator, smart cities.

Resumé :

Le canal de propagation est un élément important pour la fiabilité des simulations et la conception des systèmes sans fil. Les modèles déterministes offrent un bon niveau de précision au prix d'une complexité croissante de calcul, ce qui les rend prohibitifs pour les simulateurs de réseaux de capteurs sans fil (RdC) car ils impliquent de nombreux nœuds distribués à l'échelle d'une ville. Dans ce contexte, l'objectif de cette thèse est de proposer des méthodes déterministes rapides et précises pour modéliser le comportement des ondes électromagnétiques en garantissant le juste compromis entre la précision et le temps de calcul. L'étude a d'abord été subdivisée en deux modes selon le mécanisme dominant de propagation. Dans une configuration microcellule, l'approche proposée est basée sur un modèle de lancer de rayons reposant sur la technique de la visibilité qui adopte un ensemble de techniques d'accélération pour réduire la complexité sans perte significative de la précision. Dans ce même but, la propagation verticale a été abordée en incluant les contributions les plus significatives. Enfin, ces modèles ont été intégrés dans un simulateur de RdC pour fournir des résultats réalistes dans le contexte d'une "smart city". L'impact des modèles précis dans les simulateurs est illustré par évaluer certains paramètres du réseau.

Mots-clés : arbre de visibilité, techniques d'accélération, propagation plan vertical, simulateur RdC, villes intelligentes.